Photoelectron Spectroscopy of Polarons

in Molecular Semiconductors

D i s s e r t a t i o n

zur Erlangung des akademischen Grades

d o c t o r r e r u m n a t u r a l i u m

(Dr. rer. nat.)

im Fach Chemie

eingereicht an der

Mathematisch-Naturwissenschaftlichen Fakultät

der Humboldt-Universität zu Berlin

von

M.Sc. Stefanie Winkler

Präsident der Humboldt-Universität zu Berlin

Prof. Dr. Jan-Hendrik Olbertz

Dekan der Mathematisch-Naturwissenschaftlichen Fakultät

Prof. Dr. Elmar Kulke

Gutachter: 1. Prof. Dr. Klaus Rademann
2. Prof. Dr. Norbert Koch
3. Prof. Dr. Thomas Chassé

Tag der mündlichen Prüfung: 2.11.2015

Electrons, after all, know only a few tricks.

Frank Weinhold, *Nature, News and Views*, 2001

Understanding the nature of charge carriers in molecular semiconductors, typically summarized by the term "polaron", is indispensable for rational material design targeting future superior (opto-)electronic device performance. Despite intense experimental efforts, however, prevalent perceptions on the energy levels associated with polarons could previously only be assessed for the occupied states of negative polarons, while the spectral signature of positive polarons could never be observed by photoelectron spectroscopy.
The present work addresses this fundamental issue in order to derive a comprehensive picture of polarons in organic semiconductors.
Conceptual work is dedicated to identifying a sample structure, which allows both, deliberately generating charged molecules and applying the complementary photoemission techniques X-ray photoelectron spectroscopy (XPS), ultraviolet photoelectron spectroscopy (UPS), and inverse photoelectron spectroscopy (IPES) in order to assess the polaron energetics. The sample concept is based on the fact that molecular layers exhibiting an ionization energy lower than the work function of the supporting substrate show Fermi-level (E_F) pinning. There, as the substrate E_F is moved into the occupied density of states of the molecular adsorbate, electron transfer occurs from the molecules to the substrate. In previous related spectroscopic studies, metals were employed as substrates, where strong electron coupling between the molecules and clean metal surfaces inevitably occurs. As this might mask or, at least, significantly alter the spectral information of excess charge carriers, such interaction needs to be inhibited by implementation of an ultrathin passivating interlayer.
Fulfilling a number of essential requirements regarding the sample concept, metal oxides were chosen as potential candidates to serve as interlayer. In this regard, the nature of interactions at organic/metal-oxide interfaces, at which E_F-pinning is established, is thoroughly tested by performing a number of studies on various material combinations. These studies revealed that monolayer formation can be significantly affected by, in this context, undesired chemical interactions, which cannot be rationalized by simple electrostatic considerations. In conjunction with literature, it was derived that chemical interactions are not a general phenomenon at such interfaces, but critically depend on the specific molecular structure and, in particular, the presence of reactive functional groups. As such interactions can be avoided by an appropriate choice of (essentially) inert molecules, metal oxides are implemented as passivating interlayer in the carefully designed sample concept, which finally ensures the generation of "pure" molecular ions, i.e., polarons, which the current work aims to investigate.
This approach allows the unambiguous experimental observation of the full spectral signature (XPS, UPS, IPES) of positive polarons for the first time. The comprehensive results provide evidence that the highest occupied molecular orbital level is split into an upper unoccupied and a lower occupied sub-level due to strong on-site Coulomb interaction. This finding is in marked contrast to what has been assumed for decades, where a singly occupied level was proposed to lie within the gap of the neutral molecular semiconductor, which is valid only for molecular monolayers on metals, where excess charges are widely delocalized. In this case, observing the precise energetics associated with polarons is, indeed, impossible. If, instead, delocalization due to (weak) intermolecular or molecule/substrate interaction is dominated by charge localization - which is actually rather the rule than the exception in molecular materials, molecular monolayers can comprise integer-charged molecules. Moreover, taking into account the inter-site Coulomb interaction between molecular cations and surrounding neutral molecules, as well as energy-level bending, finally, a complete picture of the energetics associated with polarons in molecular semiconductors could be derived, which aims at replacing well-established common perceptions.

Das fundamentale Verständis von Ladungsträgern in molekularen Halbleitern, die typischerweise als Polaronen bezeichnet werden, ist unverzichtbar, wenn es um das Design besonders leistungsfähiger künftiger (opto)elektronischer Bauelemente geht. Trotz intensiver experimenteller Bemühungen, konnten entsprechend der etablierten Vorstellung der Energieniveaus von Polaronen bisher nur die besetzen Zustände von negativen Polaronen tatächlich experimentell zugänglich gemacht werden. Insbesondere vom positiven Polaron gibt es keine eindeutigen Studien mittels Photoelektronenspektroskopie.
In der vorliegenden Arbeit geht es im Wesentlichen darum, diesen Missstand aufzuheben, um so ein umfangreiches Bild von Polaronen in organischen Halbleitern zu erhalten. Zunächst geht es darum einen Probenaufbau zu finden, der es nicht nur ermöglicht Ladungsträger zu generieren, sondern auch ihre elektronische Struktur unter Verwendung von komplementären Photoemissionsechniken - X-ray Photoelektronenspektrospopie (XPS), Ultraviolette Photoelektronenspektroskopie (UPS) und inverse Photoelektronenspektroskopie (IPES) - aufzuklären. Das Probenkonzept basiert darauf, dass molekulare Filme, die eine niedrigere Ionsierungsenergie als die Austrittsarbeit des zugrunde liegenden Substrates aufweisen, Fermi-level (E_F) Pinning zeigen. In diesem Fall wären die höchsten besetzten Zustände der neutralen molekularen Schicht energetisch oberhalb des E_F des Substrats angeordnet, wodurch zum Erhalt des elektronischen Gleichgewichts die Notwendigkeit für einen Ladungstransfer gegeben ist. In ähnlichen spektroskopischen Studien, kam es bei der Verwendung von metallischen Substraten zwangsläufig zur starken elektronischen Kopplung zwischen den Molekülen und den Metalloberflächen, die die spektrale Information verbergen bzw. deutlich verändern kann. Um diese Kopplung zu verhindern, kommt eine ultradünne passivierende Zwischenschicht zur Anwendung, die die Erzeugung „reiner“ Molekülionen - jener Polaronzustände, die es zu untersuchen gilt - gewährleisten kann. Da Metalloxide eine Reihe von wesentlichen Bedingungen im Zusammenhang mit dem Probenkonzept erfüllen, wurden sie als potentielles Zwischenschichtmaterial ausgewählt. Die tatsächliche Eignung von Metalloxiden in diesem Zusammenhang wird dann in einer Reihe von grundlegenden Studien an Organik/Metalloxid-Grenzflächen, die Fermi-niveau Pinning aufweisen, überpfrüft. Dabei stellt sich heraus, dass die Bildung einer molekularen Monolage deutlich von starken elektronischen Kopplungen bzw. chemischen Wechselwirkungen beeinflusst werden kann, die nicht auf Grundlage einfacher elektrostatischer Überlegungen erklärt werden können. Weiterhin kann jedoch festgehalten werden, dass diese chemischen Wechselwirkungen kein allgemeingültiges Phänomen für Organik/Metalloxid-Grenzflächen darstellen, sondern stark von der Struktur des entsprechenden Moleküls, insbesondere aber von reaktiven funktionellen Gruppen, abhängt. Durch die geeignete Wahl eines besonders reaktionsträgen Materials kann dies jedoch vermieden und Metalloxide folglich als passivierende Zwischenschicht in dem Probenaufbau verwendet werden.
Diese Herangehensweise ermöglicht nun erstmalig den experimentallen Zugang der spektralen Signatur (XPS, UPS, IPES) von positiven Polaronen. Wegen der vorliegenden starken on-site Coulomb Repulsion kommt es zur Aufspaltung des höchsten besetzen molekularen Niveaus in ein besetzzes und ein unbesetztes Sub-niveau. Dieses Ergebnis steht im Widerspruch zur seit Jahren etablierten Vorstellung von einem einfach besetzten Niveaus in der Bandlücke des neutralen molekularen Halbleiters, was nur für molekulare Monolagen auf Metallen zutrifft, in denen Überschussladungen stark delokalisiert sind. Folglich ist die Untersuchung der Energetik von Polaronen unmöglich. Dominiert Ladungs-Lokalisation über Ladungs-Delokalisation, was eher die Regel als die Ausnahme in molekularen Materialen darstellt, existieren einfach-geladene Moleküle in der Monolage. Unter zusätzlicher Berücksichtigung der inter-site Coulomb Repulsion zwischen Molekülionen und neutralen Molekülen, sowie der Energieniveau Verbiegung kann schließlich ein vollständiges Bild entwickelt werden, das die etablierte Vorstellung bezüglich der Energieniveaus von Ladungsträgern in molekularen Halbleitern ersetzen soll.

Contents

List of Symbols and Abbreviations

Symbols	
a	lattice constant
A	area
β	overlap Integral
c_m	coefficient with index m
d	layer thickness
e	elementary charge
E	energy
E_{at}	atomic electronic ground state energy
$E_{1,2,3}$	eigenvalues of the Hamiltonian matrix
E^0	ground state
E^1	excited singlet state
E^3	excited triplet State
E_B	binding energy
E_{chem}	minimal potential energy for chemisorption
E_{phys}	minimal potential energy for physisorption
E_F	Fermi level
$E_{initial/final}$	energy attributed either to the initial or final state
E_{kin}	kinetic energy
E_{pass}	pass energy
E_{vac}	vacuum level
$\mathfrak{h}$	1-electron Hamiltonian
$\mathfrak{h}_{at}$	atomic 1-electron Hamiltonian
h	Planck constant
$h\nu$	photon energy
H	Hamiltonian
H_S	perturbation operator
H_2	hydrogen molecule
I	intensity
k_B	Boltzmann constant
n	charge carrier concentration
N	number of electrons
n_D	packing density
$P^{(+/-)}$	(positive/negative) polarization energy
$P(E)$	probability distribution

$p_{initial \to final}$	transition probability between an initial and a final state
PB_{rem}	remaining pushback effect
Q	amount of charges
q	charge
r	distance
r_s	Wigner-Seitz radius
$R_{A,B}$	positions of proton A and B
t	transfer integral
T	temperature
U	on-site Coulomb repulsion
$V(r)$	inter-site Coulomb interaction/electrostatic potential
V_{at}	atomic potential well
V_{OC}	open-circuit voltage
W	band width
Δ_e	electron-injection barrier
Δ_h	hole-injection barrier
Δ_{opt}	optical gap
Δ_{trans}	transport gap
Δ_{cond}	conductivity gap
$\Delta E_{exciton}^{Frenkel-CT}$	energy difference between a Frenkel and a charge-transfer exciton
$\Delta E_{adsorption}$	adsorption enthalpy
ΔH_{dis}	disproportions enthalpy
$\Delta\Phi$	work function shift
$\Delta\Phi_{ID}$	work function shift caused by an interface dipole
$\Delta\Phi_{dip}$	work function shift caused by dipolar layer formation
$\Delta\Phi_{chem}$	work function shift caused by chemical bond formation
$\Delta\Phi_{PB}$	work function shift caused by the pushback effect
$\Delta\Phi_{pin}$	work function shift caused by E_F-pinning
∇^2	kinetic energy of an electron
ϵ_0	vacuum permittivity
ϵ_r	relative permittivity
θ_e	emission angle
θ	nominal coverage
λ	geometrical reorganization energy
$\lambda^{(+/-)}$	geometrical relaxation energy upon (+/-)-ionization
λ_1	geometrical relaxation energy upon ionization
λ_2	geometrical relaxation energy upon returning from ionised to neutral state
μ	mobility
μ_{chem}	chemical potential
$\mu_\perp$	vertical contribution of the intramolecular dipole moment

$\rho(x)$	charge density
σ	conductivity
$\sigma_{g/u}$	even (g) and uneven (u) *sigma*-orbitals
ϕ_{elec}	electrostatic field
Φ	work function
Φ_{spec}	electron gun work function
Φ_{spec}	analyzer work function
Φ_{sub}	substrate work function
Φ_{crit}	critical Φ_{sub}, at which E_F-pinning sets in
Φ^{pin+}	critical Φ_{sub}, at which E_F-pinning of HOMO sets in
Φ^{pin-}	critical Φ_{sub}, at which E_F-pinning of LUMO sets in
χ	atomic orbital
$\chi_{A/B}$	atomic orbital of atom A or atom B
φ	molecular orbital
$\uparrow\downarrow$	indices: spin-up and spin-down
$\Psi_{intial/final}$	initial or final state referring to a N or N-1 electron system
$\psi_{intial/final}$	initial or final state referring to the photoexcited electron
Υ_0	atomic contribution of the ground-state configuration
$\Upsilon_{1,2}$	ionic contributions of the ground-state configuration
z	distance between components in a multi-particle system
z_{chem}	effective molecular diameter in a multi-particle system for chemisorption
z_{phys}	effective molecular diameter in a multi-particle system for physisorption
Z	atomic number of a nucleus A

Abbreviations

$\alpha - NPD$	N-N'-Bis-(1-naphthalenyl)-N,N'-bis-phenyl-(1,1'-biphenyl)-4,4'-diamine
AES	auger electron spectroscopy
Ag	silver
Al	aluminum
Ar^+	argon ion
Au	gold
BE	binding energy
BHJ	bulk hetero junction
C_{60}	$(C_{60} - I_h)$[5,6]fullerene
CB	conduction band
Cu	copper
Cs	cesium
CT	charge transfer
CNL	charge neutrality level
DFT	density functional theory
DOS	density of states
DSSCs	dye-sensitized solar cells
EA	electron affinity
EDC	energy distribution curve
F_4TCNQ	2,3,5,6-Tetrafluoro-7,7,8,8-tetracyanoquinodimethane
FWHM	full width at half maximum
HATCN	1,4,5,8,9,12-Hexaazatriphenylene-hexacarbonitrile
HF	Hartree-Fock
HOMO	highest occupied molecular orbital
HSAB	hard and soft acids and bases
HTL	hole-transport layer
IDIS	induced density of interface states
IE	ionization energy
ICT	integer charge transfer
IMFP	inelastic mean free path
IPES	inverse photoelectron spectroscopy
ITO	indium tin oxide
K	potassium
LCAO	linear combination of atomic orbitals
LEED	low energy electron diffraction
LUMO	lowest unoccupied molecular orbital
Li	lithium
MED	mean escape death
ML	monolayer

MO	molecular orbital
MoO_3	molybdenum trioxide
NaCl	sodium chloride
NEXAFS	near edge X-ray absorption fine structure
OFET	organic field-effect transistor
OLED	organic light emitting diodes
OPVC	organic photovoltaic cell
P3HT	Poly(3-Hexylthiophene-2,5-Diyl)
PES	photoelectron spectroscopy
QMS	quadrupole mass spectrometer
Rb	rubidium
S	screening parameter
S_{AB}	overlap matrix
SAM	self-assembled monolayer
SECO	secondary electron cut-off
SCLS	surface core-level shift
SD	surface dipole
SrF_2	strontium fluoride
Sm_2O_3	samarium trioxide
STM	scanning tunneling microscopy
TiO_2	titanium dioxide
UHV	ultra-high vacuum
UPS	ultraviolet photoelectron spectroscopy
UV	ultraviolet
VdW	van-der-Waals
VB	valence band
XPS	X-ray photoelectron spectroscopy

I. Introduction

Since the discovery of high conductivity in doped polyacethylene by Shirakawa, MacDiarmid and Heeger in 1977,[1,2] which has been honoured by the Nobel Prize in Chemistry 2000,[3–5] the interest in the field of organic electronics has strongly increased. This interest is driven by the rich chemistry of organic semiconducting materials, as it enables the wide tunability of key material properties, such as the optical gap, which is a crucial parameter in organic light-emitting device (OLED) applications. In particular, applications employing organic semiconductors in organic photovoltaic cells (OPVCs) benefit from their high absorption cross sections. Finally, this material class offers high potential for low-cost and large-area processability.[6,7] At the same time, however, the performance of today's organic electronic devices often suffers from the relatively low charge-carrier mobility in the molecular semiconductors, as compared to their inorganic counterparts.

To address this major drawback of low charge-carrier mobility on a fundamental level, a detailed understanding of the processes by which individual charge carriers propagate through an organic semiconductor is of utmost importance. In this regard, key parameters that enter current models for hole-transport, e.g., the geometrical reorganization energy λ[8–10] and the transfer integral t[11–13] have been shown to be accessible by probing the occupied manifold of single-particle states, in particular the highest occupied molecular orbital (HOMO) in neutral molecules employing ultraviolet photoelectron spectroscopy (UPS)[14–25](see section 1.1).

Concomitantly, a model for the single-particle energy levels associated with excess charge carriers, that is so-called *polarons*, has been developed; the core message of this model for positive polarons is illustrated in Fig. I.1: Removing an electron from the HOMO of a neutral molecule leads to an energetic relaxation of the now singly occupied state into the gap of the semiconductor. While doubly occupied states are experimentally accessible by employing UPS and unoccupied states by employing inverse photoemission spectroscopy (IPES), this singly occupied state should be observable by both UPS and IPES. However, despite immense experimental effort, clear experimental evidence for the HOMO-derived, singly occupied state of the cation is still missing in UPS, even though, in reverse, LUMO-derived, singly occupied states have been clearly observed for the anion.[26–29] Clearly, this indicates that common perceptions on the polaron energetics are to be challenged.

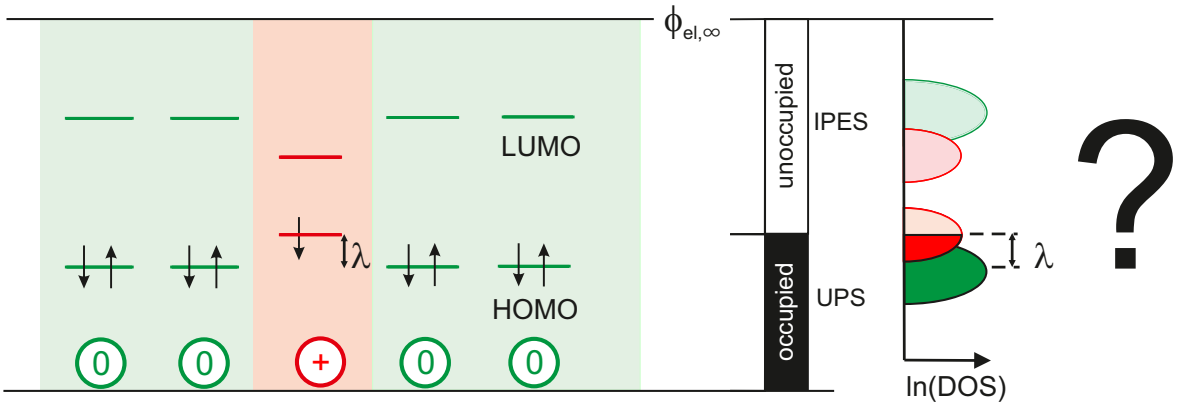

Figure I.1.: From left to right: common perception on the single-particle energy levels for neutral molecules (green) surrounding a cation (red) with respect to a common vacuum level ($\phi_{el,\infty}$), their experimental accessibility to (inverse) photoelectron spectroscopy depending on their occupancy and the resulting density of states (DOS) on a logarithmic scale, ln(DOS), as proposed according to Ref.[30]. This view is to be challenged on the basis of new experiments.

In order to evaluate the appropriateness of the standard model, the unambiguous experimental observation of the spectral signature of positive polarons is of key importance. However, one easily realizes that it is a highly challenging task to even *generate* this species of interest, i.e., molecular ions in a matrix of neutral, but otherwise identical molecules: On the one hand, if cations are generated by application of chemical dopants, the new doping-induced states can hardly be distinguished from the occupied LUMO of the dopant.[31] Likewise, strong electronic coupling, i.e., hybridization, between these two energy levels is reasonable to occur.[32,33] [MHW+15] On the other hand, cations can be generated by employing a metallic substrate with a work function (Φ) larger than the ionization energy (IE) of the molecular adsorbate. Thereby, the Fermi level (E_F) of the underlying metal is moved into the occupied density of states (DOS) of the molecules, which induces electron transfer from the molecules into the metal to establish electronic equilibrium (E_F-pinning),[34–38] [ANW+13] as shown in Fig. I.2. Unfortunately, however, strong electronic coupling to atomically clean metal surfaces is well known to *not* yield integer-charged molecules but, rather, to result in a pronounced mixing of metal and molecular states.[39] [HDS+13]
This process of *hybridization with the metallic substrate*, however, can be inhibited by deliberately inserting a passivating layer between metal and molecular adsorbate, as depicted in Fig. I.2.
To further ensure the detectability of these charge carriers, *the amount of charges* (Q) per area (A) in the organic-semiconductor portion of the heterostructure can be increased by employing a dielectric interlayer (between the molecules and the metallic ground) either of large permittivity (ϵ_r), of small thickness (d), or both.[34]

$$\frac{Q}{A} = (\Phi - IE) \cdot \frac{\epsilon_0 \epsilon_r}{d}, \qquad \text{for} \quad IE < \Phi$$

In order to fulfil these experimental requirements, wide-gap metal oxides were chosen as best candidates to serve as passivating interlayers: (i.) metal oxides are moderately conductive, which is required for (inverse) photoelectron spectroscopy techniques, (ii.) they can provide a large substrate-Φ needed to electrically generate cations, (iii.) they can be prepared in the form of thin films, and (iv.) strong electronic coupling to organic adsorbates is expected to be significantly reduced compared to the pristine metal surface. In this regard, the validity of the underlying expectation of molecule/metal-oxide interactions being negligible needs to be experimentally confirmed.

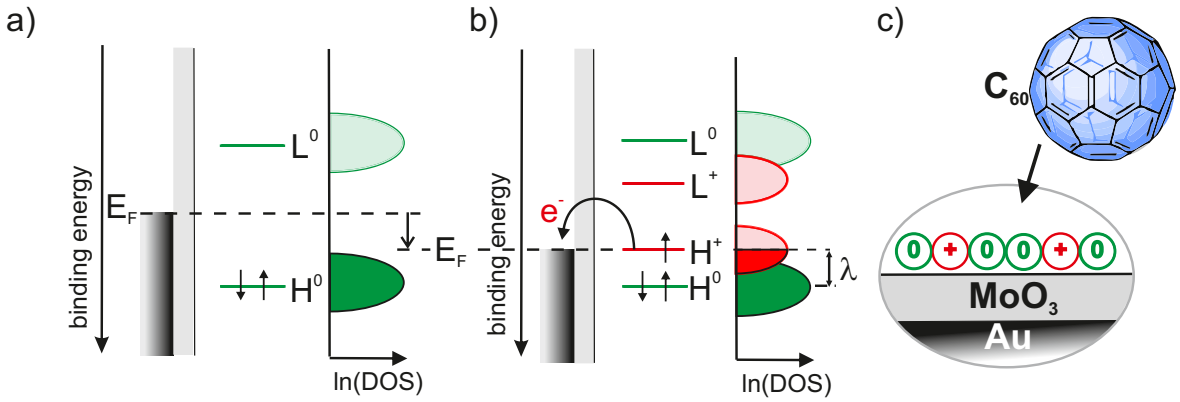

Figure I.2.: Sample concept for obtaining the spectral signature of positive polarons: Single-particle energy-level diagrams for a neutral molecule on (a) an intermediate and (b) a high work-function substrate inducing electron transfer, which results in the formation of a cation.[26,30,31,35,40,41] The latter is experimentally realized employing the Au/MoO_3/C_{60}-heterostructure (c).

To that end, a selection of organic/metal-oxide interfaces was studied by photoemission spectroscopy in order to sufficiently cover the interplay between the charge transfer induced by extreme substrate work functions and potential further phenomena, which are well established to occur upon metal-organic interface formation.[41–45](section 1.2) In particular, the interface formation between metal oxides and N-N'-Bis-(1-naphthalenyl)-N,N'-bis-phenyl-(1,1'-biphenyl)-4,4'-diamine (α-NPD), strong molecular acceptors like 1,4,5,8,9,12-Hexaazatriphenylene-hexacarbonitrile (HATCN) and 2,3,5,6-Tetrafluoro-7,7,8,8-tetracyanoquinodimethane (F_4TCNQ), or strongly dipolar molecules like merocyanines is investigated in chapter 4. From these results it could finally be deduced that, if the energy-level alignment upon interface formation cannot be explained by simple electrostatic considerations, it is related to bond formation involving reactive side-groups of the molecules employed. Consequently, undesired molecule/metal-oxide interactions are not a general phenomenon, but, rather, can be avoided by the appropriate choice of an inert molecular material.

The resulting overall sample concept based on E_F-pinning, which successfully accounts both for sufficient charge carrier quantity and for negligible molecule-substrate hybridization, is illustrated in Fig. I.2(c): An Au-supported, 1.2 nm thin "passivating" MoO_3 layer (Φ = 6.8 eV) was implemented to serve as substrate to C_{60} (IE = 6.4 eV), which was employed as hole-accumulation layer due to its essentially inert molecular structure without reactive sidegroups.
Employing a combination of direct and inverse photoelectron spectroscopy, the full spectral signature of positive polarons was then obtained for the first time and is comprehensively discussed in chapter 5. Based on these results, the well-established model for the electronic structure of molecular semiconductors comprising excess charge carriers[26,27,30,31,35,40,41,46,47] is consequently revised.
Finally, a comprehensive summary and an outlook is given in part IV, which is based upon the results obtained within this work.

II. Fundamentals

Chapter 1. The electronic structure of (electrically doped) organic materials is outlined on two levels:

- The electronic structure is related to the charge transport mechanisms in organic materials supported by considering the concepts of localization and delocalization of charges. Furthermore, those insights are linked to the transfer integral t and the Coulomb repulsion U, that are in principle accessible by photoemission.
- The energy-level alignment at interfaces is outlined. Particularly E_F-pinning at interfaces is introduced, as it is the mechanism serving as overall sample concept in order to generate charges. Moreover established origins for the occurrence of (undesired in the sample concept) interface dipoles are outlined.

Chapter 2. An overview of the theoretical background of the employed photoemission techniques XPS, UPS and IPES is given, as well as some basic remarks on their strong points and experimental limits.

Chapter 3. The used materials and setups, for which the theoretical background has been given, are introduced.

Chapter 1.

Organic Semiconductors and Their Interfaces

In this chapter, the fundamentals of charge transport in organic semiconductors is outlined.[48–51] The transport of a charge q through an organic semiconductor is characterized by two key quantities, charge carrier concentration n and mobility μ, that give the electrical conductivity σ.

$$\sigma = nq\mu \tag{1.1}$$

This relation simply indicates that n and μ need to be increased to establish large conductivity and electrical current. To address this issue it is of paramount importance to have a detailed understanding of the process of how individual charge carriers propagate through an organic semiconductor. Therefore the intrinsic electronic structure of organic semiconducting materials and its implication on μ is outlined in section 1.1. Afterwards strategies to increase n extrinsically are outlined in section 1.2. Particularly E_F-pinning is introduced as mechanism to generate additional charges in the organic material, as this is employed as concept in order to obtain the spectral signature of polarons, the current work aims at investigating.

1.1. Hopping Transport and Band Transport

The principal origin of μ relies on either band or hopping conduction. The hopping mobility, that is generally lower than the band mobility, is dominated by the charge reorganization energy λ,[8,9,52], whereas the band mobility is dominated by the transfer integral t.[14,53]
The low dielectric constant of organic semiconductors ($\epsilon_r = 3$) places them in between both limiting cases. Considering the temperature dependence of μ in pure and perfect low molecular weight aromatic organic crystals,[50] the carrier transport has to be described by coherent transport in a band with substantial width W and with high mobilities at low temperatures.[54–56] When

the temperature is raised, a charge carrier gets more frequently scattered with a mean free path of about the distance between two adjacent molecules, resulting in a decrease of its mobility. Also, the charge carrier delocalisation is reduced, which can be observed by a decreasing or vanishing bandwidth. In consequence of this charge carrier localisation, the charge carriers are is increasingly more coupled to the polarisable crystal environment leading to successively slower band conduction and thermally assisted hopping comes into play and finally dominates. Understanding the nature of this thermally assisted hopping transport mechanism and furthermore a detailed description of the transition where both mechanisms come into play is still under debate. This is also related to the fact, that the observation of band dispersion in simple (and therefore neither highly ordered nor clean) device-relevant organic electronic heterostructures is rather the exception than the rule.

A brief introduction on the mentioned counteracting effects of charge localization and delocalization in an organic semiconductor is given with respect to the transfer integral t ($t \sim \frac{W}{4}$) and the Coulomb repulsion U. To do so, the electronic structure of molecular semiconductors is introduced considering the limiting cases of incoherent coupling (*atomic limit*) and coherent coupling between the molecular units (*band limit*).[12]

1.1.1. The Electronic Structure of Matter

Hydrogen-like atom and molecule

In order to describe an electron bound in a hydrogen-like atom,[57] one refers to a 1-electron hamiltonian $\mathfrak{h}_{at}$ covering the kinetic energy $\frac{1}{2}\nabla^2$ of the electron, that feels the nucleus attraction formed by the nucleus with atomic number Z in a distance r:

$$\mathfrak{h}_{at} = -\frac{1}{2}\nabla^2 - \frac{Z}{r} \tag{1.2}$$

With respect to an electronic wave function $\chi(r)$, one obtains the corresponding Schrödinger equation, whereas E_{at} is the atomic electronic ground state energy:

$$\mathfrak{h}_{at}\chi(r) = E_{at}\chi(r) \tag{1.3}$$

In a next step, the complexity is extended by discussing the situation of *one* electron in a potential of *two* protons in a finite distance r_{AB}, the case of a H_2^+-ion.[58]

Due to the repulsion between both nuclei, and the electron-nuclei attraction, the atomic description of the atomic potential well V_{at} within the H_2^+-ion is only appropriate close to the protons and shows, however, significant deviations in between both hydrogen protons, as depicted in Fig. 1.1(a). Accounting for this potential modification, one uses a perturbative treatment,[59] replacing $\mathfrak{h}_{at}$ by $\mathfrak{h} = \mathfrak{h}_{at} + V_1(r)$ (Tight Binding Approach[60,61]).

The respective molecular orbitals φ can be described by a linear combination of both atomic hydrogen orbitals, referred to as LCAO approach[62–65]:

$$\varphi = \sum_{m=A}^{N} c_m \chi_m \tag{1.4}$$

In this regard, the coefficients $(c_m, m = A, ..., Z)$ are the constants to be determined using the variational principle:

$$\frac{\delta E}{\delta c_m} \stackrel{!}{=} 0 \quad \text{with} \quad E = \frac{\int \varphi^* \mathfrak{h} \varphi dr}{\int \varphi^* \varphi dr} \tag{1.5}$$

Considering the hydrogen molecule, each hydrogen atom is described in the spatial representation by an electronic wavefunction χ_A and χ_B, respectively:

$$\varphi = c_A\chi_A + c_B\chi_B \tag{1.6}$$

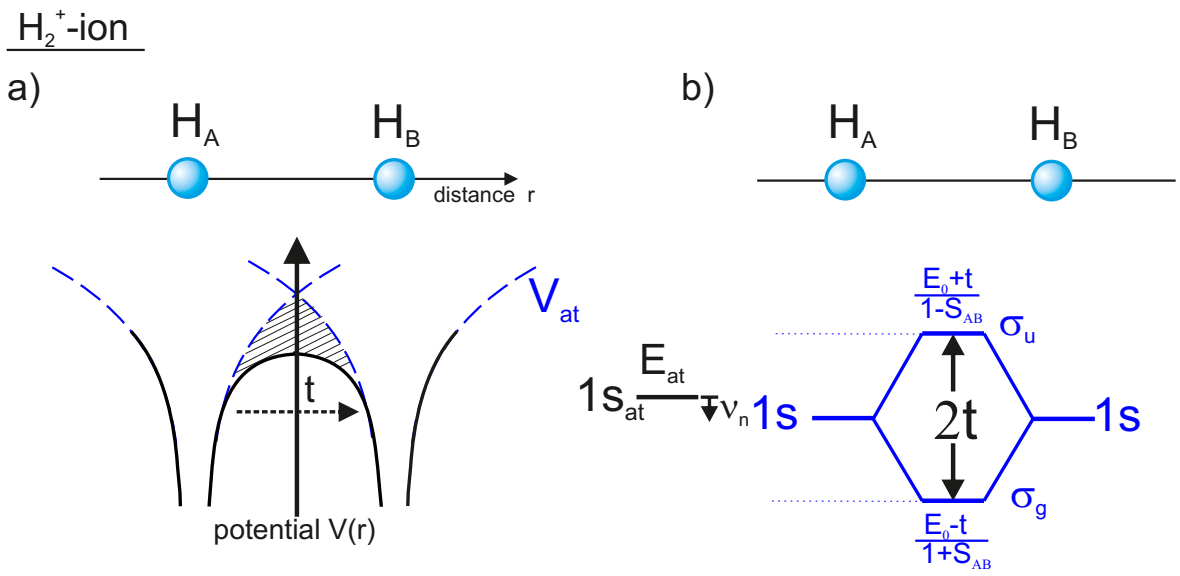

Figure 1.1.: (a) Illustration of the cross section of the attractive potential due to two protons at R_A and R_B in the H_2^+-ion; the atomic potential V_{at} is significantly modified in between both atoms. (b) MO-scheme of a hydrogen molecule adapted for non-interacting electrons according to the LCAO approach. The relation between the eigenvalues of the Hamilton matrix, given in eq.(1.9), is moreover illustrated.

Their overlap matrix $\int \chi_A \chi_B dr$ is replaced by S_{AB} in order to simplify equation (1.5). Furthermore, the amplitude for electron transfer between both sites (hydrogen atoms) is represented by the transfer integral t:

$$\int \chi_A^* \mathfrak{h} \chi_B dr = \int \chi_B^* \mathfrak{h} \chi_A dr = -t \tag{1.7}$$

Additionally, the energy associated with finding the electron either at R_A or at R_B is E_0, that is E_{at} modified by ν_n, as depicted in Fig. 1.1(b):

$$\int \chi_A^* \mathfrak{h} \chi_A dr = \int \chi_B^* \mathfrak{h} \chi_B dr = E_0 \tag{1.8}$$

Taking these expressions into account when solving eq.1.5, one obtains the Hamiltonian matrix:

$$\begin{bmatrix} E_0 - E & -t - ES_{AB} \\ -t - ES_{AB} & E_0 - E \end{bmatrix} \tag{1.9}$$

The respective ground state energy yields accordingly $\frac{E_0 - t}{1+S_{AB}}$, corresponding to the bonding σ_g-orbital, as depicted in the MO-scheme in Fig. 1.1(b). The energy associated with the anti-bonding orbital σ_u is accordingly $\frac{E_0+t}{1-S_{AB}}$.

If the probability of finding the electron in between both hydrogen atoms and S_{AB} is zero, there is no driving force for forming a covalent bond between these hydrogen atoms. In consequence, the electronic ground state recovers the atomic

energy E_{at} for each individual atom, corresponding to an electron occupying an atomic 1s orbital.

For the H_2^+-ion and a non-zero probability of finding an electron in between both hydrogen atoms, the corresponding molecular orbitals can be determined from the secular equations:

$$\sigma_g = \frac{1}{\sqrt{2(1-S_{AB})}}(\chi_A + \chi_B) \qquad \sigma_u = \frac{1}{\sqrt{2(1+S_{AB})}}(\chi_A - \chi_B) \tag{1.10}$$

Meanwhile, it is reasonable to neglect the overlap integral S_{AB}, as it is known to be very small for $r_{AB} \neq 0$. This leads to the simplification of the molecular orbitals and corresponding energies in further discussions [see Fig. 1.2(a)].

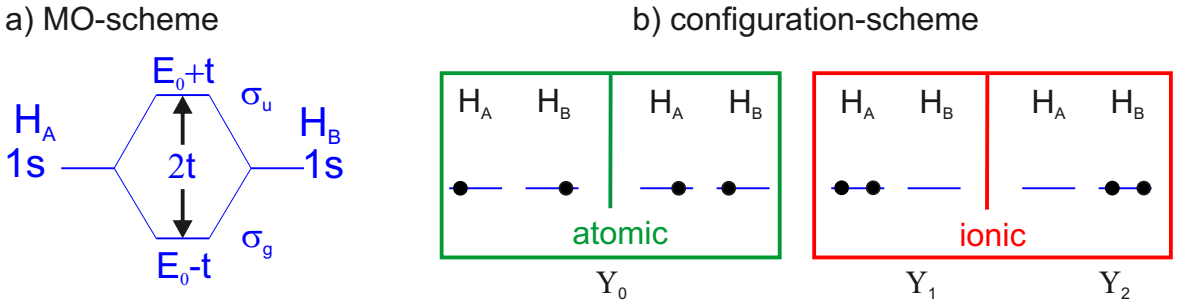

Figure 1.2.: (a) MO-scheme of a hydrogen molecule according to the LCAO approach assuming S_{AB} to be very small and negligible, as compared to Fig. 1.1(b). (b) Illustration of the atomic and ionic configurations summing up (weighted) to the ground-state wave function, as referred to in eq.(1.11) and (1.12).

Adding a second electron with opposite spin (Pauli principle) into this system, both electrons reside in the one-electron levels of the lowest energy (σ_g), which correspondingly results in a total energy of $2(E_0 - t)$ on the basis of *non interacting* electrons (free electrons like in the case of metals) for the singlet spatially symmetric ground state.*

In order to account, however, for the *electron interaction*, it is suitable to rely on a multi-configuration description of the eigenfunction, as will be shown in the following. In particular, one uses both the atomic and the ionic contributions of the ground state configuration in order to describe two interacting electrons in the field of two protons (H_2), as depicted in Fig. 1.2(b):

* Other non ground-state electron configurations are conceivable, i.e. (i) $\chi_{A,\downarrow}\chi_{B,\uparrow}$ or $\chi_{A,\uparrow}\chi_{B,\downarrow}$ corresponding to $2E_0$ and (ii) both electrons residing in σ_u corresponding to $2(E_0 + t)$.

- Atomic contributions considering the antisymmetric *singlet state*†, whereby the spatial ground state is symmetric towards the exchange due to Pauli exclusion: Electron 1 resides in χ_A and electron 2 resides in χ_B or vice versa:

$$\Upsilon_0 = \frac{1}{\sqrt{2}}(\chi_{A,\downarrow}\chi_{B,\uparrow} + \chi_{B,\uparrow}\chi_{A,\downarrow}) \tag{1.11}$$

- Ionic contributions: Both electrons reside either in χ_A or χ_B; consequently both configurations are singlet states due to Pauli exclusion.

$$\Upsilon_1 = \chi_{A,\uparrow}\chi_{A,\downarrow} \qquad \Upsilon_2 = \chi_{B,\uparrow}\chi_{B,\downarrow} \tag{1.12}$$

For the ionic contributions Υ_1 and Υ_2 one has to respect the on-site Coulomb repulsion energy U arising between two electrons, if they are found on the same proton. To account for this, the full 2-electron Hamiltonian can be written as the sum of the two individual one-electron Hamiltonians plus U.

$$H = \mathfrak{h}_1 + \mathfrak{h}_2 + U \tag{1.13}$$

The energy associated with the ionic contributions is accordingly $2E_0 + U$, as the last additional positive energy U represents the intra-atomic (on-site) Coulomb repulsion between the two localized electrons.
Hence, the full 2-electron Hamiltonian has the matrix form in the space of the singlet states, as follows. The diagonal terms referring to the atomic contributions (eq.(1.11)) of 2 independent electrons in the potential given by the atoms yield $H_{00} = 2E_0$, as referred to in eq.(1.8). Those diagonal terms associated with the ionic contributions (eq.(1.12)) yield $H_{11} = 2E_0 + U$ and $H_{22} = 2E_0 + U$, respectively:

$$\begin{bmatrix} H_{00} & H_{10} & H_{20} \\ H_{01} & H_{11} & H_{21} \\ H_{02} & H_{12} & H_{22} \end{bmatrix} = \begin{bmatrix} 2E_0 & -\sqrt{2}t & -\sqrt{2}t \\ -\sqrt{2}t & 2E_0 + U & 0 \\ -\sqrt{2}t & 0 & 2E_0 + U \end{bmatrix} \tag{1.14}$$

The off-diagonal terms as, for instance, $H_{10} = \langle \Upsilon_1 | H | \Upsilon_0 \rangle = \frac{1}{\sqrt{2}}(\langle \chi_A | \mathfrak{h}_1 | \chi_A \rangle \cdot \langle \chi_A | \chi_B \rangle + \langle \chi_A | \mathfrak{h}_1 | \chi_B \rangle \langle \chi_A | \chi_A \rangle + \langle \chi_A | \mathfrak{h}_2 | \chi_A \rangle \langle \chi_A | \chi_B \rangle + \langle \chi_A | \mathfrak{h}_2 | \chi_B \rangle \langle \chi_A | \chi_A \rangle = -\sqrt{2}t$ represent the gain in energy, throughout the delocalization of an electron at proton R_A over both protons. In the same manner, this applies to H_{01}, H_{20} and H_{02} $(= -\sqrt{2}t)$.

† Due to chemical intuition and to be more descriptive in the following discussion the (excited) *triplet-states* are neglected.

The probability of changing in between both ionic contributions, that is 2 electrons residing on one site being transferred simultaneously to the other site, is expected to be rather small and in consequence assumed to be zero; $H_{21} = H_{12} = 0$.

Solving the respective secular equations, one obtains the eigenvalues of the Hamiltonian matrix:

$$\begin{aligned} E_1 &= 2E_0 + U \\ E_{2,3} = E_{\pm} &= 2E_0 + \frac{1}{2}U \pm \sqrt{4t^2 + \frac{1}{4}U^2} \end{aligned} \tag{1.15}$$

Most importantly, the lowest eigenvalue is the ground state energy $E_{Hubbard}$ of the Hamiltonian.

$$E_{Hubbard} = 2E_0 + \frac{1}{2}U - \sqrt{4t^2 + \frac{1}{4}U^2} \tag{1.16}$$

Obviously the ground state energy $E_{Hubbard}$ is a function of t and U which pictorially means it is an interplay of the competing trends of delocalization of the electrons, which is associated with an energy gain of t, and of localization of two electrons on one single atom, for which an energy U is required.

Regarding the question whether the energy cost of double occupation exceeds the energy gain throughout delocalization, one can thusly derive: For $U/t << 1$ both electrons are independent and delocalized and for $U/t >> 1$ each electron is well localized on each individual atom.

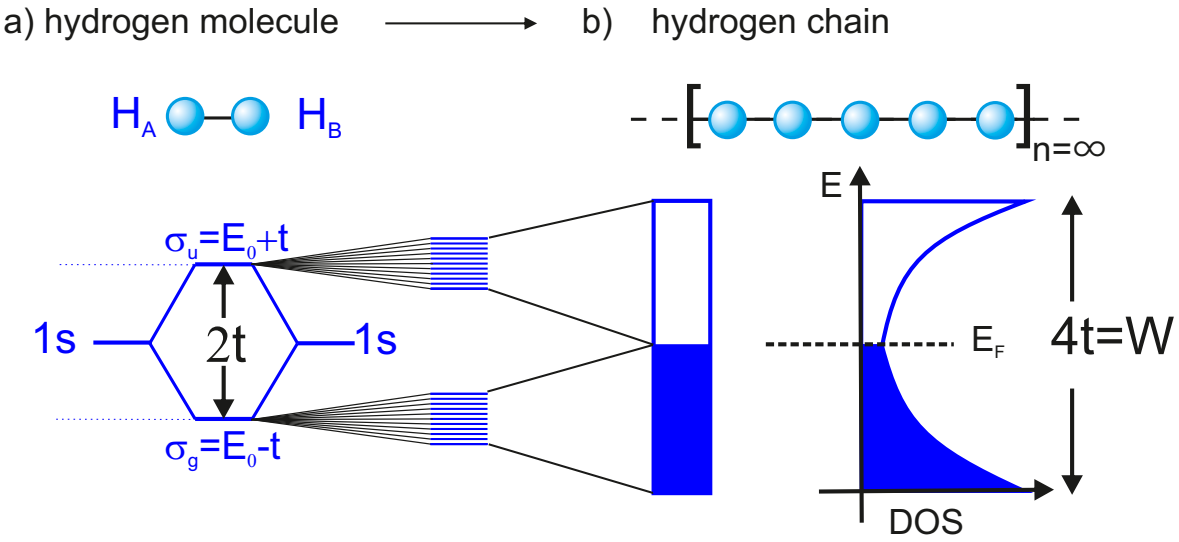

Figure 1.3.: Illustration of the evolution of the DOS depending on the number of hydrogen atoms between the limiting cases (a) hydrogen molecule and (b) hydrogen chain.

Condensed Matter

Applying the concept of these competing effects, i.e. localization and delocalization of charges, to condensed matter,[11,12] the band model[66–69] is the most relevant treatment for $t >> U$. For $U >> t$ the Hubbard model[70–72] recovers the value of the Heitler-London prediction[62], in which the electrons are well localized on a particular atom.
Recycling the introduced model system of the isolated molecule (H_2), it is now to turn to the artificial case of a hydrogen chain, comprising an infinite number of H-atoms arranged with an inter-atomic distance a representing a simplified picture towards the solid hydrogen modification[73,74]. Starting out with the limiting case of $U = 0$, this chain is a 1D-solid with one atom (1 electron) per unit cell and all atomic 1s-levels give rise to the 1s-band, which has a size-able width ($W = 4t$) and is half-filled. The half-filled band is moreover cut in half by E_F, and characterized as a metal with a non-vanishing density of states at E_F (band limit).
If the lattice constant a is increased within the hydrogen chain to larger inter-atomic separation, the 1s-band becomes narrower, as depicted in Fig. 1.4. Meanwhile, it remains half-filled and therefore the hydrogen chain should be a metal even at very large inter-atomic distance, where $t \to 0$.
Here, the Coulomb repulsion comes into play, as at large enough atom-atom distance the hydrogen chain is not a metal but an array of isolated neutral hydrogen atoms, which are known to be a non-conductor (atomic limit).
For $U \neq 0$ and small values of t, one refers to the so-called Mott-insulators, which are characterized by two split Hubbard-subbands instead of one half-filled band. These Hubbard-subbands are occupation number dependent, i.e. the upper (empty) subband depends on the presence of the electrons in the (occupied) lower subband. In contrast to the independent electron treatment, where each band

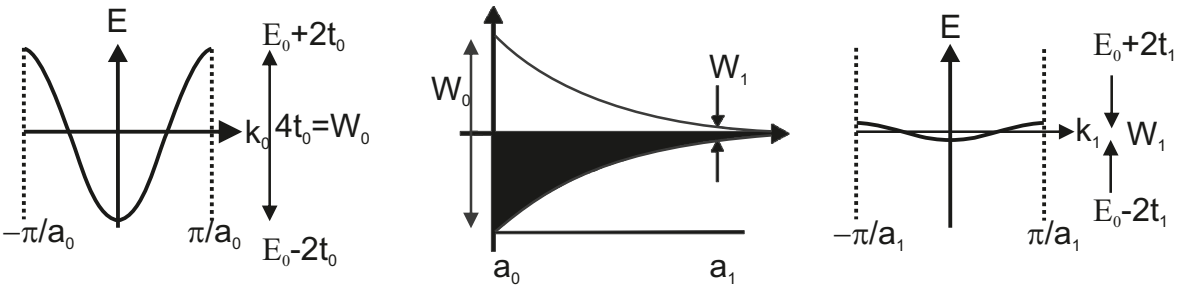

Figure 1.4.: Schematic representation of t ($= \frac{1}{4}W$) as a function of the lattice constant a. Left: For a small a_0, t_0 is large, as can be experimentally observed in a pronounced band dispersion; Right: for large a_1, t_1 is small resulting in a neglecting probability of a hopping event.[adapted from Ref.[75]]

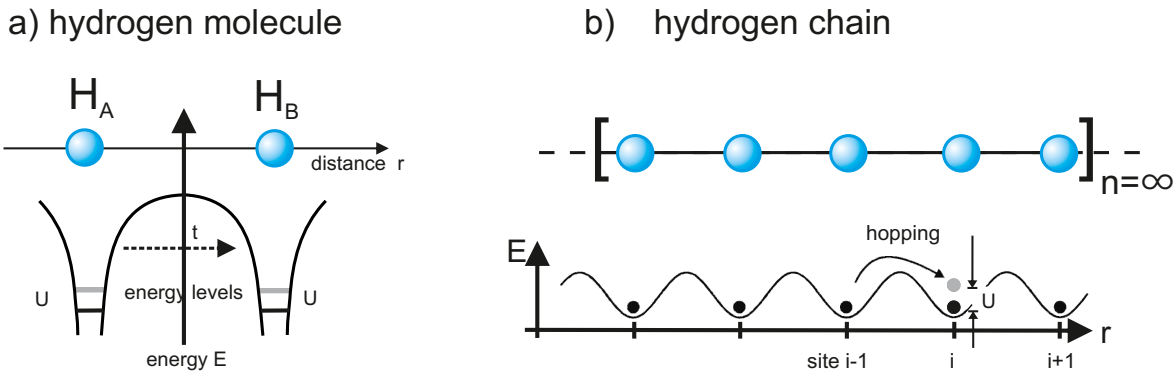

Figure 1.5.: (a) Qualitative illustration of the cross section of the attractive potential due to protons H_A and H_B in the hydrogen molecule; the position of the energy levels indicates the possibility of tunneling from one proton to the other; and the Coulomb repulsion required to populate two electrons on the same atom. [adapted from Ref.[58]](b) Analogous to (a) in order to illustrate the situation for the hydrogen chain [adapted from Ref.[75]]

can hold $2n$ electrons, the lower Hubbard subband can only hold n electrons as the upper Hubbard subband only has place for n electrons. For the movement of an electron from one site to the next, depicted in Fig. 1.5, the occupation of the upper subband is necessary and requires an additional Coulomb-repulsion energy U. Effectively, this "hopping"-process is the *oxidation* of one site and *reduction* of a neighboring site, summing up to the Hubbard U in solid state physics and being reminiscent to the disproportions enthalpy ΔH_{dis} in the chemist's language. If referred to the vacuum level E_{vac}, the Hubbard U can be considered as the difference between the ionization energy IE and the electron affinity EA of a "half-filled band" (Hubbard subbands), and equals zero if the investigated material is a metal.

This concept can be applied to semiconducting molecular systems, where the values for U and t need to be determined in order to comprehensively characterize the nature of charge transport.

The hopping (transfer) integral t is connected to the bandwidth $W(= 4t)$, which can be determined by studying the band dispersion of the valence band (HOMO) or conduction band (LUMO), as depicted in Fig. 1.4.

Even though delocalization has been tried to look for extensively in organic semiconductors employing UPS since the first experimental determination of intermolecular band dispersion,[19] it has been shown, however, to be appreciable only in rare cases. Obviously molecules generally interact only by weak van der Waals forces, yielding to narrow intermolecular energy bands of approximately <0.2 eV.[14,21,76] Only in rather exceptional cases, however, one might find $W \approx 0.4$ eV[53] or even ≈ 0.7 eV[77]. Consequently, the electronic structure of the individual molecule is basically preserved in the organic solid.[78]

In clear contrast, the observation of non-vanishing spectral intensity of states at E_F has led to its classification as metallic. Meanwhile this has been shown to be suitable under certain circumstances,[HDS+13] [39] in particular for the first organic monolayer adsorbed on a metal. Here the dispersion has been observed to be significantly enhanced within a molecular monolayer film due to strong substrate-mediated coupling.[79] Indeed the organic monolayer formed on a metal is the best studied system, and thusly the intrinsic electronic properties characterizing organic semiconductors, i.e. beyond the "metallic" monolayer,[HDS+13] [39,79] have accordingly not been thoroughly accessed by photoemission. Moreover, it is self-evident that the first organic layer inevitably provides rather different properties, particularly regarding U, than those intrinsic properties associated with the bulk crystal. Accordingly, the substrate-molecule interaction determines whether the intrinsically semiconducting molecular monolayer conserves the semiconducting behaviour or becomes metallic.

The direct access of U by determining the EA and the IE of the respective Hubbard subbands is usually not possible when studying molecules in the context of organic electronics.‡ These molecules generally provide a closed-shell configuration, whereby one "only" has access to the transport gap comprising both an energy term attributed to the Couloumb interaction, i.e. the exciton binding energy E_{exiton}, and one energy term attributed to the molecular-orbital[80], i.e. the optical gap Δ_{opt}.

At this point it is worth mentioning that Coulomb repulsion and attraction are frequently treated as equivalent and not distinguished in literature.[80,86] In the following the addressed Coulomb repulsion is always assigned to the Hubbard U and any other Coulomb interaction is stated separately.

However, an ingenuous usage of both terms equivalently is not advisable, even if a certain relation is not denied at this point, as will be elucidated in further detail in section 5.2.

Due to the wealth of different terms to define energy gaps in organic semiconductors, depending on whether e.g. these Coulomb interactions are involved or not, a selection of widely used terms is given in the following section.

‡ To date U has been assessed indirectly, as for instance for C_{60} via Auger photoelectron spectroscopy[80,81] scanning tunneling microscopy[82], two-photon photoemission[83], X-ray adsorption near-edge structure spectroscopy[84] and resonant inelastic soft x-ray scattering[85].

1.1.2. The Types and Nature of Energy Gaps

For closed-shell systems, including most application-relevant organic molecules, the gas-phase values IE_g and EA_g and the corresponding energy gap Δ_{gas} are connected to the analogoue bulk phase properties via the polarization energies. The polarization energy of the cation (P^+) is defined as the difference in energy between the ionization energy of the molecular system in the crystal (IE) and the ionization energy of the molecular system in the gas phase (IE_{gas}).[87] In analogy, the anion polarization energy (P^-) is obtained by using the electron affinities in the solid and gas phase. In general, the chosen conventions result in negative cation and anion polarization so as to reflect the stabilizing nature of the interaction in the condensed phase, which provides a permittivity larger than vacuum $\epsilon_r = \frac{\epsilon}{\epsilon_0} > 1$.[88]

$$\begin{aligned} P^+ &= IE - IE_g \\ P^- &= EA - EA_g \end{aligned} \tag{1.17}$$

Involved contributions to P^+ or P^- can be structured according to their process-time.[48] If the ionization time is small as e.g. the time from the photoexcitation to the photoelectron detection, the very rapid electron rearrangement might be the sole contribution. If there are slower ionization processes such as charge-hopping, polarization associated with deformation of the geometrical structure of the molecular ion and of surrounding molecules contributes.

1. The summation of all electronic polarization effects is denoted "electronic polaron".

2. Intramolecular geometrical polarization is denoted "very small polaron".

   Taking and electron from a π-orbital *or* adding it to a π^* orbital alters the spatial distribution of electrons in the more strongly bound σ-orbitals, which might result in a change of the bond lengths of the molecule. The energy associated with this geometrical change in the molecular structure is known as the geometric relaxation energy λ_1, and the charge traveling through the molecular crystal, that comes along with the geometric distortion of the molecules, is commonly referred to as "polaron". In conjunction, one refers to λ_2, considering the process of returning from the ionized state $(N-1,\ N+1)$ to the neutral one.§ In essence the reorganization energy,

§ The relaxation energies $\lambda_1^{+/-}$ of an isolated molecule (in solid phase) can be determined employing gas phase (high resolution) UPS and analyzing the vibrational modes, as illustrated in Fig. 1.7(a).

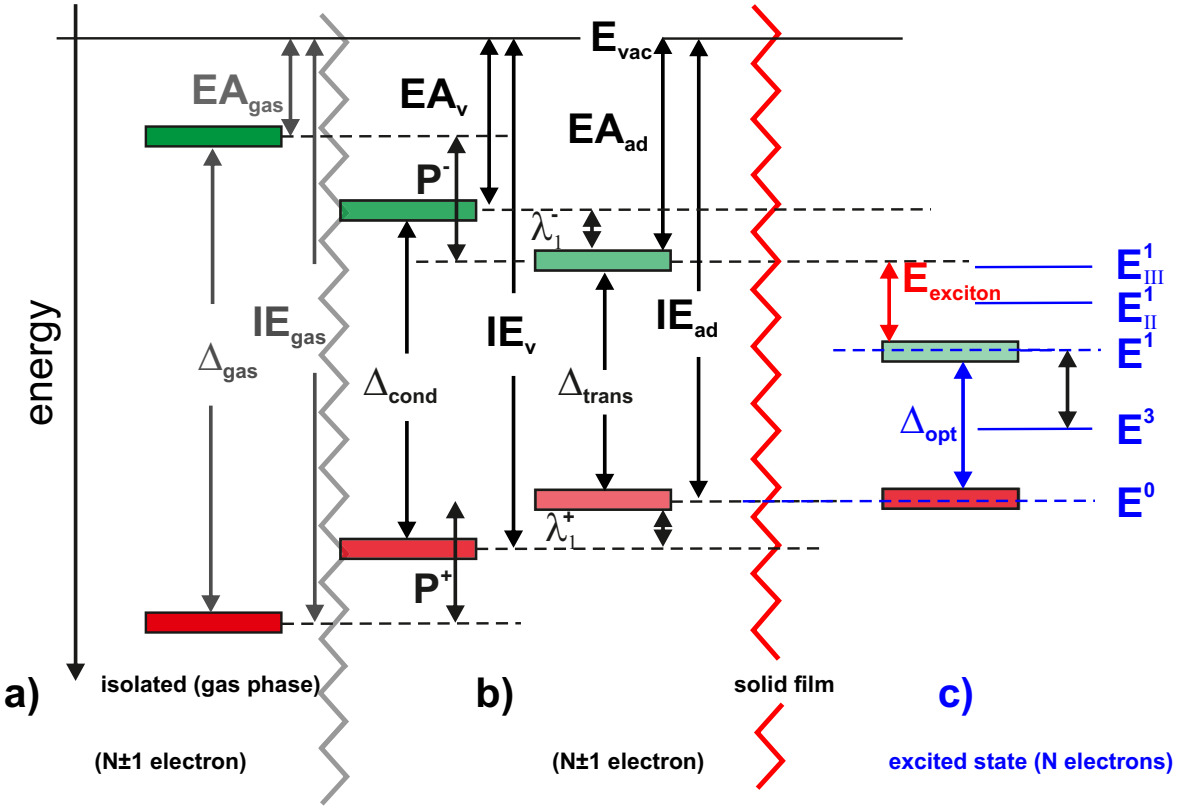

Figure 1.6.: Schematic frontier energy levels of (a) an isolated molecule in the gas phase, with IE_{gas}, EA_{gas} and the energy gap Δ_{gas}. (b) Respective energy levels of a molecule in a solid (condensed film), where the polarization of the surrounding media decreases IE_{gas} by the positive polarization energy P^+ and increases EA_{gas} by the negative polarization energy P^-. The energetic difference between both energy levels is the conductivity gap Δ_{cond}. Moreover, the geometrical reorganization energy $\lambda^{+/-}$ further decreases/increases the vertical IE/EA resulting in an energy gap of Δ_{trans}. In (c) the fundamental optical transition $E^0 \rightarrow E^1$ [triplet (E^3) or higher excitations (E^1_{II}, E^1_{III}) are indicated] yields the optical band gap Δ_{opt}. Comparing Δ_{trans} and Δ_{opt} yields an energy difference corresponding to the exciton binding energy ($E_{exciton}$). [inspired by Ref.[89]]

corresponds to the sum of the geometrical relaxation energies (see Fig. 1.7) and can be written as[9,16,17,90]

$$\lambda = \lambda_1 + \lambda_2 \approx 2\lambda_2 \quad \text{if} \quad \lambda_1 \approx \lambda_2 \tag{1.18}$$

3. Intermolecular or lattice geometrical polarization is called (i) "small polaron", if the lattice deformation is in the order of the crystal's unit cell and (ii) is called "large polaron", if it is a larger scale deformation.

For oligoacenes the 2^{nd} as well as the 3^{rd} (2 meV[91]) contributions in general are small. While the 3^{rd} contribution is neglected from now on, high resolution UPS has been shown to provide access to the geometrical relaxation and reorganization

energies,[9,16,89] which are depicted in Fig. 1.6 separately.

For determination of Δ_{cond} only the electronic polaron is involved in response to separating an electron-hole pair into "free" charge carriers, that can then travel through the organic semiconductor. This is associated with the vertical electron affinity (EA_v) and ionization energy (IE_v), corresponding to the 0-2'-transition (IE_v) and 0'-2-transition (EA_v) in Fig. 1.7(a). Both vertical transitions are often associated with the most intense feature in the vibronic progression.

$$\Delta_{cond} = IE_v - EA_v \tag{1.19}$$

In contrast, Δ_{trans} is determined by considering the onsets of HOMO and LUMO. This is because in addition to the fast electronic polarization of the local surrounding, the transport of the photo electron to the surface to emit is accomplished by hopping via "very small polaron states". During the lifetime of such a polaron state a (nearly fully) relaxation of the molecular ion occurs. Fig. 1.7(a) shows a simplified picture of the origin of the vibrational satellites intensity I_n in a valence-level spectrum. The lowest energy 0-0'-transition between the neutral and photoionized state, both in relaxed configuration, commonly has a low cross section, as the 0-2'-transition (IE_v) commonly has a high cross section. In essence, the photoemission onset of the experimental observable envelope-function of all vibrational modes yields the 0-0'-transitions (IE_{ad} and EA_{ad}) and accordingly Δ_{trans} in good approximation.

$$\Delta_{trans} = IE_{ad} - EA_{ad} \tag{1.20}$$

Δ_{trans} is the essential one for charge transport equal to the conduction band gap reduced by the relaxation energies $\lambda_1^{+/-}$.

The minimal energy required for the first fundamental optical transition $E^0 \rightarrow E^1$ is the optical gap Δ_{opt}, that can be determined from e.g. absorption spectra.

While UPS and IPES-transitions create "dressed" charges (polarons) as final states, the optical transition creates a Frenkel exciton (bound electron-hole pair) located on one site, i.e. molecule, as final state. As can be deduced from Fig. 1.6, the difference between Δ_{trans} and Δ_{opt} is the Coulomb attraction between electron and hole, called exciton-binding energy ($E_{exciton}$), which is substantial in organic semiconductor materials due to the low relative dielectric constant. $E_{exciton}$ has been reported to be as large as 1.5 eV[92–94] in strong contrast to inorganic semiconductor materials, where the charge separation energy is generally below k_BT.[95] Noteworthy, even though the Coulomb attraction between a hole located in the former HOMO and an electron located in the former LUMO, that is

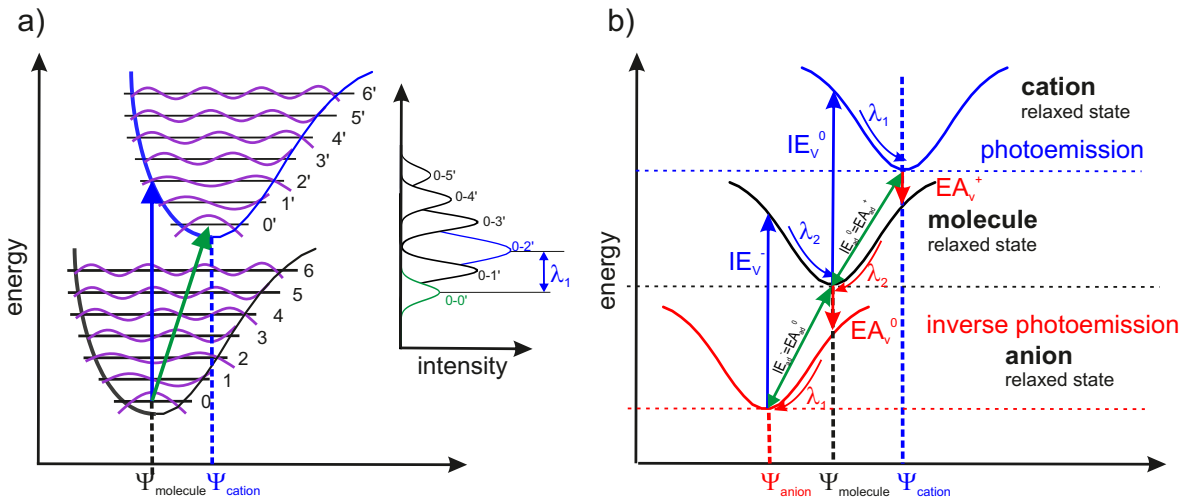

Figure 1.7.: (a) Illustration of the franck-condon principle for photoemission. Since electronic transitions are very fast compared with nuclear motions, vibrational levels are favored that correspond to a minimal change in the nuclear coordinates. The potential wells are shown favouring 0-2'-transition, that is the vertical ionization energy (IE_v). The UPS intensity of vibration satellites I_n on photoionization is shown: for this example the peak maximum of the envelope-function should give IE_v, as the photoemission-onset yields the lowest possible energy transition IE_{ad} (b) (inverse) photoionization (anion EA_v/cation IE_v) of a neutral state and geometrical relaxation by an energy λ_1, as well as the returning process from ionic to neutral state and the geometrical relaxation energy λ_2 are illustrated according to the franck-condon principle.[89]

$E_{exciton}$, is widely established to be large in organic semiconductors, the Coulomb repulsion term (U) for either pairing two holes in the former HOMO or two electrons in the former LUMO is rarely considered. Meanwhile it is reasonable to summarize both values to the on-site Coulomb interaction, which is discussed in more detail in section 5.2.

Beside the mentioned effects on the energetic positions, there are in particular several peak-broadening mechanisms at play that can influence the determination of e.g. the transport levels, which will be briefly summarized when discussing photoelectron spectrocopy in chapter 2.

1.2. Energy-Level Alignment at Interfaces

Recalling eq.(1.1), strategies to increase the charge carrier concentration n in an organic semiconducting material rely on effective injection of charges from electrodes (OFET) or/and exciton-dissociation at heterojunctions (OPVC). Although the intrinsic organic bulk properties remain unaffected, when different materials come into intimate contact, this might not be true at their interfaces. In this regard some general remarks on interface formation are worth mentioning considering the adsorption channels of an organic molecule, i.e. *physisorption* and *chemisorption*.[96]

Upon a small adsorption enthalpy gain $\Delta E_{adsorption} (< 50$ kJ/mol) corresponding to physisorption, which is mainly mediated by van-der-Waals (vdW) interactions, the electronic structure of the adsorbate as well as of the substrate remain mostly unaffected. For example, the noble gases bind to surfaces by physisorption.[97]

For a large enthalpy gain (> 50 kJ/mol), one most commonly refers to chemisorption. Here the adsorption process results in significant sharing of electrons between the adsorbing molecule/atom and the solid substrate. The driving force for chemisorption is in the simplest case the formation of a covalent bond. This involves a splitting of the levels into molecular bonding and anti-bonding orbitals, that is essentially characterized as compromise between the cost of Coulomb repulsion and energy gain of delocalization of energy levels.[98] Depending on the magnitude of asymmetry of the electron density distribution along the bonding axes - as generally the case for hetero-atomic coupling - the bonding might also be denoted as ionic.

Instead of dealing with the full electronic structure of adsorbate and surface, the interaction can be described semi-empirically by combining two Lennard-Jones potentials, one for each adsorption channel, chemisorption and physisorption:

$$V(r) = 4E_0 \left[\left(\frac{z_{eff}}{z} \right)^{12} - \left(\frac{z_{eff}}{z} \right)^{6} \right] \tag{1.21}$$

where E_0 (i.e., E_{chem} or E_{phys}) is the minimal potential energy, z_{eff} (referring to either z_{chem} or z_{phys} according to Fig. 1.8) the corresponding effective molecular diameter in a multi-particle system and z the distance between the components. The first term is due to short range repulsive forces, which occur because of the Pauli exclusion principle and the Coulomb repulsion, while the second term includes the long range attractive vdW-forces due to induced dipoles. If - as often the case for non-interacting closed-shell systems - Coulomb repulsion predominates, adsorption is physical, even though charge transfer occurs in order

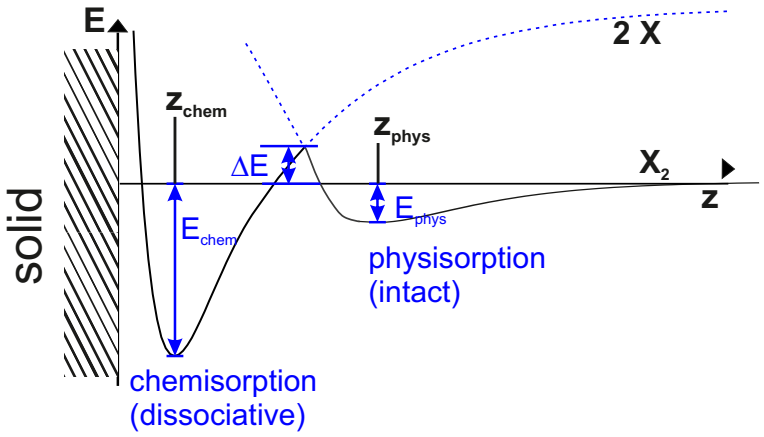

Figure 1.8.: The combination of Lennard-Jones potentials illustrating both adsorption channels: physisorption and chemisorption. If a molecule X_2 adsorbs physically and intact, the corresponding adsorption height z_{phys} is usually larger and the adsorption enthalphy E_{pyhs}usually smaller than for chemisorption. If the activation barrier (ΔE) for the transition from physisorption to chemisorption is small enough, chemisorption occurs leading to e.g. molecular dissociation or significant mixing of molecular and substrate states.

to establish electronic equilibrium (E_F-pinning).
In this frame of mind, it is now to consider how adsorption induces electron density rearrangements that might induce interface dipoles and consequently determines the energy-level alignment at interfaces. Prior to discussing these interface dipoles in more detail, two rather simple models describe the energy-level alignment mechanisms at organic/inorganic and organic/organic interfaces: the Schottky-Mott limit, where the energetic positions of the molecular levels are strictly determined by the work function of the underlying substrate involving vacuum-level alignment (section 1.2.1); and Fermi-level pinning, where the energetic positions of the molecular levels are pinned relative to the Fermi level of the substrate by charge transfer between the substrate and the adsorbate (section 1.2.2).

1.2.1. Vacuum-Level Alignment

In the first limiting case of vacuum-level alignment (Schottky-Mott limit) the formed interface is essentially free of gap states and any adsorbent would simply align its vacuum level with respect to the substrate work function Φ_{sub}, i.e. the difference between the substrate E_F and the vacuum level (E_{vac}).
The adsorbents' vacuum level is commonly referred to the intrinsic molecular or atomic energy levels (IE, EA). Consequently charge-injection barriers for holes Δ_h or electrons Δ_e at organic/electrode interfaces can be predicted by simply

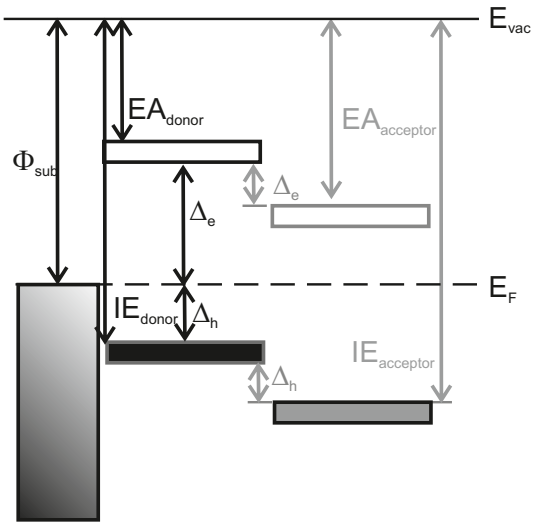

Figure 1.9.: Schematic energy-level scheme of a heterojunction in the Schottky-Mott-limit. The energy levels of all involved materials are aligned to the vacuum level of the underlying substrate.

taking the difference between the Φ_{sub} of the electrode and the IE (EA) of the organic semiconductor. For organic/organic interfaces one refers to the difference between the energy levels of the involved materials, in which one is commonly characterized as the acceptor-type and the other one as the donor-type, i.e. $IE_{acceptor} > IE_{donor} > EA_{acceptor} > EA_{donor}$.

$$\begin{aligned} \Delta_h &= IE - \Phi & \Delta_h &= IE_{donor} - IE_{acceptor} \\ \Delta_e &= \Phi - EA & \Delta_e &= EA_{acceptor} - EA_{donor} \end{aligned} \tag{1.22}$$

Even though the charge injection barrier termination exists for those energy differences, it is likewise applicable for charge extraction. Here, the direction of electron transfer is reversed, Δ_h/Δ_e have negative values and denote the "overpotential". This term is the driving force to transport the charges to the electrodes, respectively.
Although it has been often observed for organic/organic interfaces, in general vacuum-level alignment is rather the exception than the rule at interfaces between conjugated organic materials and clean metal surfaces, because an interface dipole ($\Delta\Phi_{ID}$, see section 1.2.3) results in almost every case from the "push back" of electron density.[99,100]

1.2.2. Fermi-Level Pinning and Band Bending

As there is no pushback involved, for most conductive polymers and ambient-contaminated metal and conducting metal-oxide electrodes, it was found ex-

perimentally that vacuum-level alignment holds for a certain range of Φ_{sub} values,[101,102] which is specific for every organic semiconductor.[41] Exceeding the limits of this range, referred to as critical work functions Φ^{pin+} or Φ^{pin-}, vacuum-level alignment would place the electrode E_F below the HOMO level or likewise above the LUMO level of the organic semiconductor, corresponding to an electronic non-equilibrium situation. In response, charge is transferred, and work function shifts $\Delta\Phi_{pin}$ form such that E_F comes to lie within the HOMO-LUMO gap of the organic semiconductor and equilibrium is re-established; this phenomenon is commonly referred to as E_F-pinning.
Further increase (decrease) of Φ_{sub} beyond the critical limit $\Phi^{pin+}(\Phi^{pin-})$ would

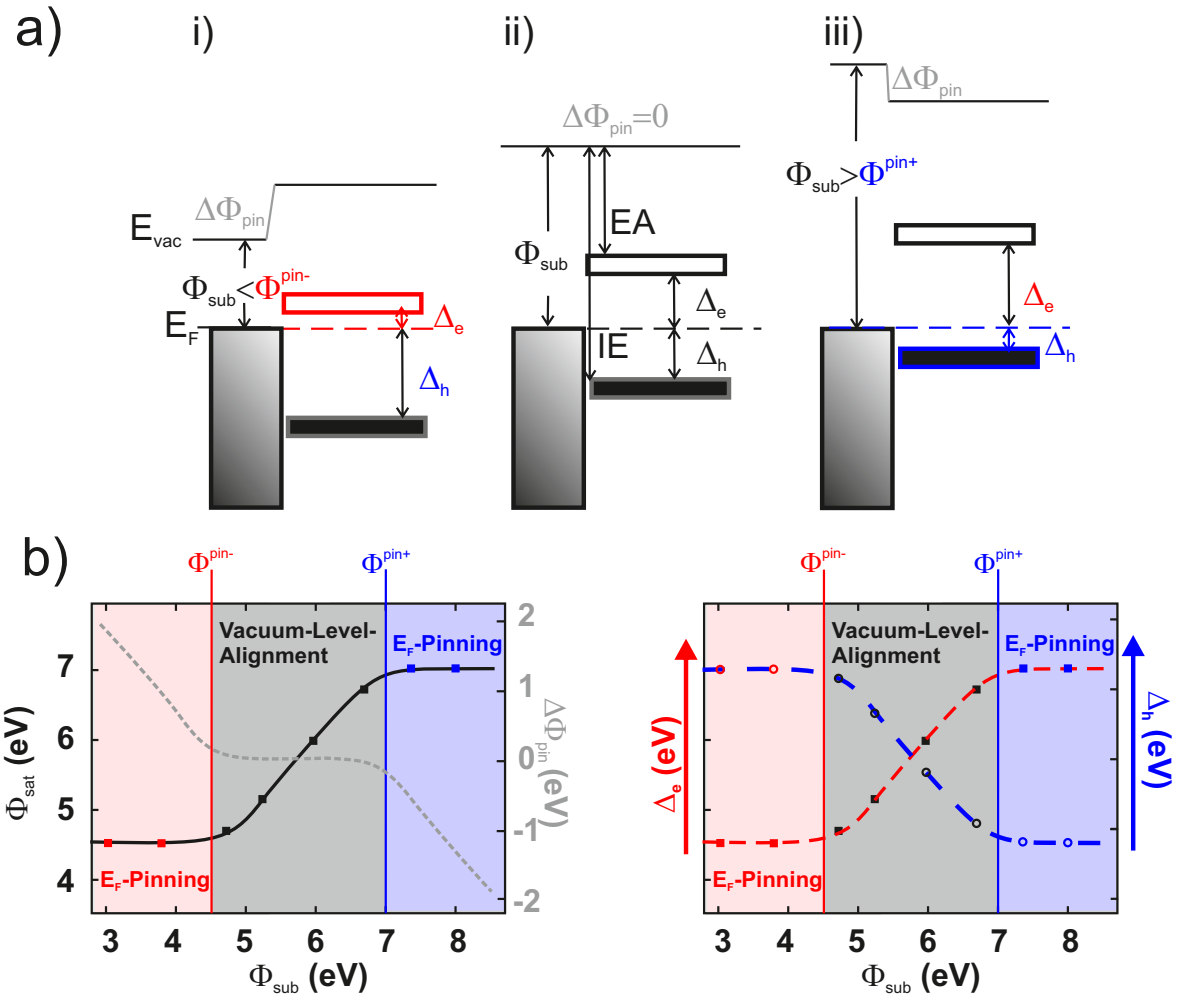

Figure 1.10.: (a) Schematic energy-level diagrams of a heterojunction with the organic material to illustrate the situation of Fermi-level pinning. (i) LUMO-level pinning at E_F, (ii) vacuum-level alignment, (iii) HOMO-level pinning at E_F. (b) Corresponding evolution of the saturated work function Φ_{sat}, the work function shift $\Delta\Phi$ and the injection barriers Δ_h and Δ_e in dependence of the substrate work function Φ_{sub}. The transitions point between E_F-pinning and vacuum-level alignment are marked by the critical substrate work functions Φ^{pin+} and Φ^{pin-}.

not change the energy-level alignment of the organic semiconductor, therefore the injection barriers Δ_h and Δ_e become independent of Φ_{sub} and reach their minimal/maximal values. Instead, the amount of transferred charge and in conjunction the resulting work function shift is increased to the amount necessary for establishing electronic equilibrium in the respective consecutive layers.

To describe the occurrence of E_F-pinning properly, several models have been proposed. The so-called integer charge transfer (ICT) model[35,41] predicts that new states may be induced in the organic molecules/polymers at weakly interacting interfaces. Those states are discrete charge-transfer states within the adsorbate layer, as the degree of mixing between the adsorbate and substrate states is negligible. These interfaces are characterized by the absence of an interface dipole ($\Delta\Phi_{ID}$) and instead one observes the "pure" band bending phenomenon[103].

1.2.3. Interface Dipoles

When the interaction strength between substrate and molecule is increased, partial charge transfer and/or the formation of covalent bonds occurs. Then the energy-level alignment should consider the vacuum-level discontinuity, which is associated with an interface dipole $\Delta\Phi_{ID}$ resulting from charge rearrangement upon interface formation.[42]

Collapse of Band Bending

In order to describe E_F-pinning at strong interacting interfaces, the *Induced Density of Interface States* (IDIS) model[104] can be considered. Here the driving mechanism is the tendency of the Charge Neutrality Level (CNL) to align with the metal Fermi level. The CNL is defined as the boundary energy at which states in the gap state continuum change from donor-type to acceptor-type character with increasing energy. It is originally given by the mid-gap position of a semiconductor[105].

$$CNL = \frac{IE + EA}{2} \tag{1.23}$$

Taking all but not only the frontier orbital contributions into account transforms the initial "discrete" distribution into a continuum density of interface states (IDIS) with non-negligible values in the former energy gap. By modeling this induced DOS and populating them in a continuous manner, starting with the lowest state, with the number of electrons N of the isolated and neutral molecule/polymer,

the position of the CNL can be determined implicitly.

$$N = \int_{-\infty}^{CNL} IDIS(E)dE \tag{1.24}$$

In general the CNL does not come to lie at the energy of the peak associated with the broadened HOMO (LUMO) of the isolated molecule but is located within the semiconductor's energy gap.
The actual energy difference of the CNL and the substrate's E_F prior to the establishment of electronic equilibrium can be further modified by a screening parameter S[104,106] ranging between 0 and 1, and by the exact nature of charge distribution within the molecular monolayer.
If the IDIS or gap states are significantly present, caused by a mixing between adsorbate and substrate states, the band-bending region "collapses" into a localized interface dipole.[103] In consequence, for generation of the integer-charged molecules, whose spectral signature is aimed for within this thesis, a clearing of the energy gap, and subsequent confirmation, has proved to be a rather challenging task. On the one hand, non-interacting/insulating materials would clear the energy gap but prevent them to be experimental accessible if e.g. photoemission techniques are employed, which are dependent on electrical contact. On the other hand, good electrical contact can be established employing strong interacting, metallic materials that are known to induce a rather large amount of IDIS. This is in line with the rare observations of band bending in organic semiconductors in the past. In many studies, the adsorption of strong electron acceptor or donor materials on metal surfaces was usually accompanied by the formation of hybrid states between the metal continuum states and specific molecular levels. This interfacial charge transfer induces interface dipoles, whose magnitude have been proven to be tunable by varying the coverage of donor or acceptor molecules in the (sub)monolayer.[107,108] In consequence, the vacuum-level discontinuity upon this (sub)monolayer surface modification can be tailored. This facilitates controlling the energy-level alignment of a subsequently deposited organic semiconductor.
In this regard a further strategy to control the energy-level alignment can be considered, one that relies on introducing a monolayer of suitable molecules between substrate and organic semiconductor. The difference lies in how the required vacuum-level discontinuity ($\Delta\Phi_{ID}$) is realized.

Dipolar Layer Formation

An interface dipole (Φ_{ID}) can be caused by adsorption of molecules that exhibit a functional group, which anchors to the substrate through the formation of a

covalent bond. Under certain conditions this process can lead to a densely packed ordered molecular assembly in the first monolayer, denoted as "self-assembled monolayer" (SAMs). Prominent examples are thiol-anchoring groups for SAMs on coinage-metal surfaces[109–111] or carboxyl groups on metal-oxide surfaces[112]. Here, the bond is formed e.g. upon hydrogen elimination:
2 R-SH+ 2 Au $\rightarrow$ 2 R-S-Au + H_2 &
R-COOH + $O_{oxide} + M_{oxide} \rightarrow R - COO - M_{oxide} + O_{oxide} - H$.
Because the resulting bond upon chemisorption is usually formed between atoms of different electronegativity, it can already induce an interface-dipole contribution $\Delta\Phi_{chem}$.[38,113,114]
The rich chemistry of organic molecules, however, facilitates to equip a SAM with dipolar chemical substituents pointing away form the surface. Depending on the strength of the electron-withdrawing or electron-donating group and their exact position, the intra-molecular dipole moment can be tuned. This allows the adjustment of the energy-level alignment between the transport states in a subsequent deposited organic material and E_F by introducing an interface-dipole contribution $\Delta\Phi_{dip}$ in a rather controlled fashion.[38,113–117] $\Delta\Phi_{dip}$ can be estimated assuming a vertical contribution of the intra-molecular dipole moment ($\mu_\perp$) of a compact layer of such molecules, via the Helmholtz equation:

$$\Delta\Phi_{dip} = \frac{e n_D \mu_\perp}{\epsilon_r \epsilon_0} \tag{1.25}$$

where e is the elementary charge, ϵ_0 is the vacuum permittivity, ϵ_r the relative permittivity of the organic material and n_D is the molecular packing density.
Summing up both contributions ($\Delta\Phi_{chem}$,$\Delta\Phi_{dip}$) yields the total interface dipole $\Delta\Phi_{ID}$ obtained upon SAM-formation:

$$\Delta\Phi_{ID} = \Delta\Phi_{chem} + \Delta\Phi_{dip} \tag{1.26}$$

Importantly, the subsequently deposited material is electronically decoupled from e.g. the clean metal surfaces and a mixing of metallic and molecular-overlayer states is inhibited, thus corresponding to a clearing of the overlayer's transport gap. Instead this applies to the interlayer. In the same manner, the interlayer is responsible for the pushback effect $\Delta\Phi_{PB}$, a further contribution to the interface dipole formation that remains to be discussed.

Pushback Effect

Most importantly, in contrast to the previously discussed contributions $\Delta\Phi_{chem}$ and $\Delta\Phi_{dip}$, the pushback effect does not affect the molecular density of states.

Instead it is a pristine substrate-surface effect.

For illustration of this phenomenon, the electronic structure of the metal surface needs to be described in more detail first. Fig. 1.11(a,i) depicts the charge density $\rho(r)$ across the metal surface. Due to the non-vanishing probability of electrons residing outside the metal, a finite charge density spills out into the vacuum, whereas negative charge density is missing inside the metal due to the requirement of overall charge neutrality. The uniform background model[118] is considered to separate the positive charge density ($n(r)$) created by the nuclei from the electronic density. It is approximated as a step-like function that drops from a constant value inside the metal to zero at the interface.

Concomitantly, Fig.1.11(a,ii) depicts the electrostatic potential $\phi(r)$ when going from the bulk across the interface into the vacuum. μ_{chem} is the bulk chemical potential of the electrons relative to the mean electrostatic potential in the metal interior. If the Fermi level is set to 0, the difference between the electrons' inner potential and E_F equals the bulk chemical potential μ_{chem}. The difference between the vacuum level E_{vac} and E_F is the work funtion (Φ). Φ depends on μ_{chem} and the shape of $\phi(r)$. As a consequence of $\phi(r)$'s asymmetry across the surface, the difference between the absolute values of μ_{chem} and Φ defines the absolute change of the electron potential energy. This is referred to as "Dipole Barrier"[119], "Double Layer"[120] or "Surface Dipole" (SD)[121].

$$\Phi = \mathrm{SD} - \mu_{chem} \tag{1.27}$$

Being a bulk property, μ_{chem} is not changed by adsorbates, however, the SD, as determined by the spill-out of electrons into vacuum, can easily be modified by adsorbed species. Particularly, the surface electron density spilling out into the vacuum is pushed back into the metal by Coulomb (Pauli) repulsion of the adsorbates' electron density, as has been shown for physisorption of xenon (Xe) on various metal substrates in Ref.[123].

Interestingly, the amount of SD is dependent on the specific metal surface. For alkali metals this SD is close to 0 eV and accordingly the work function change upon Xe adsorption is negligible. In contrast, for the noble metals, Cu, Ag, Au, SDs of several eV are reported. In conjunction, adsorption of Xe changes the work function significantly by about 0.5-0.8 eV. To elucidate the difference between alkali metals and noble metals in this context, one can consider the particle density of valence electrons. The Wigner-Seitz radius (r_s), which denotes the radius of a sphere that equals the mean volume per atom in a solid, is proportional to the cube root of the inverse particle density of valence electrons. In Tab. 1.1 r_s-values for a selection of metals are listed. For large r_s-values (K,

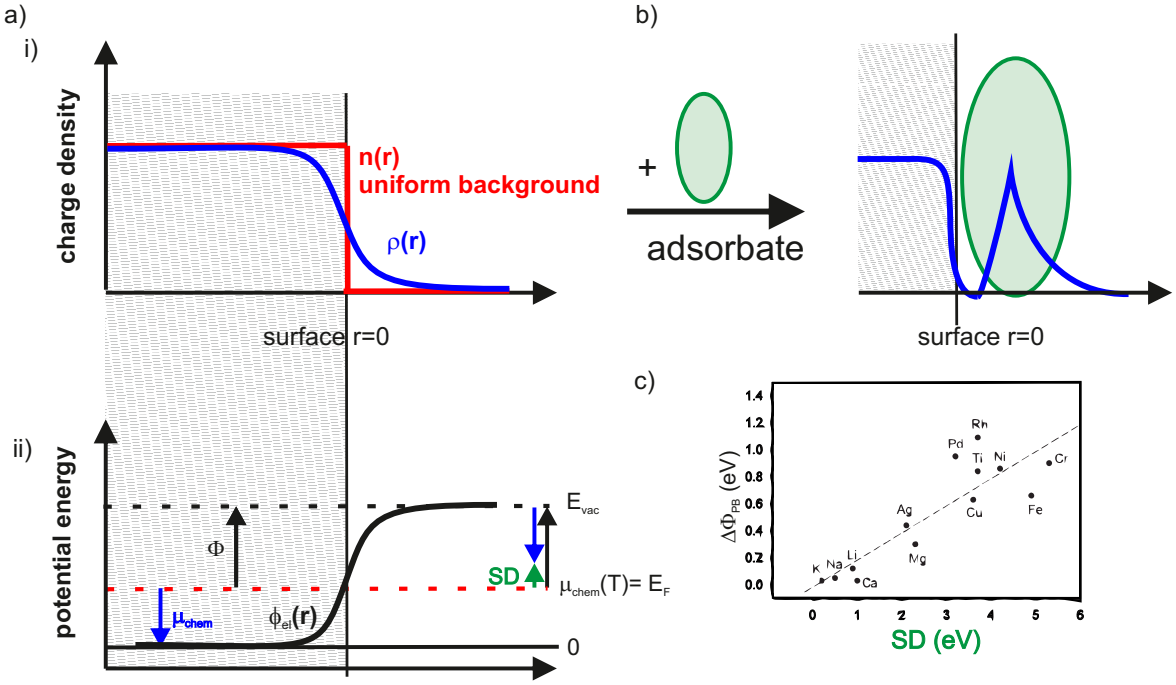

Figure 1.11.: (a) Illustration of the uniform background model [122]: (a,i) the positive charge density $n(r)$ is approximated as a step-like function, whereas $\rho(r)$ denotes the electron charge density . (a,ii) From the respective evolution of the electrostatic potential $\phi_{el}(r)$ across the interface, one can derive μ_{chem}, which describes the chemical potential of the metal. States are filled from zero potential energy up to the energy which corresponds to the Fermi level, a value only theoretical accessible. Φ describes the energy necessary to remove an electron from the E_F to the vacuum. This value is experimental accessible and is related to μ_{chem} but needs to be modified according to the electrostatic potential arising at the interface due to the field of the ionic atoms which cannot be canceled out outside the bulk material. This electrostatic potential is denoted as "Surface Dipole". b) Illustration of the "pushback effect" induced by the electron density of an adsorbate pushing the electron density spilling out the metal back into the metal. This is largest for large metal valence electron densities. (c) Correlation between observed work function shift upon Xe-adsorption SD (adapted from Ref.[41]). Noteworthy, for low electron density metals $|\phi_{chem}| = |\Phi|$ approximately holds. For large electron density metals, however, large deviations resulting from large dipole barriers are found. In consequence with increasing SD, one finds a linear increasing pushback effect.

Rb and Cs), the SD is small, whereas $\phi(r)$ is sharp and symmetric. For small values of r_s, as for noble metals, the line shape of $\phi(r)$ is less sharp and can be asymmetric. Most likely $\phi(r)$ is extending exponentially in vacuum, i.e. electrons spill out into the vacuum.[122] Therefore we find much larger SDs, which are significantly affected by the presence of an adsorbed molecule. In consequence, one finds a significant interface-dipole contribution $\Delta\Phi_{PB}$.

Prior to giving an outline of the organic/metal-oxide interfaces, some *concluding remarks* are given on the different contributions to the interfacial charge rearrangement that have been presented. Noteworthy, the possibility to clearly distinguish each of these contributions from each other is rather the exception

Table 1.1.: Surface Potential characteristics of selected metals. Wigner Seitz radius r_s according to Ref.[124] is compared to the dipole barrier SD according to Ref.[125].

Element	r_s	Dipole barrier	Element	r_s	Dipole barrier
Li	3.26	1.55	Cu	2.12	2.91
Na	3.99	0.794	Ag(100)	–	xx
K	4.95	0.386	Ag(110	2.39	1.99
Rb	5.31	0.327	Ag(111)	–	–
Cs	5.75	0.258	Au	2.22	2.01

than the rule. Only for a SAM-molecule whose molecular structure is composed of dipolar groups that are electrically decoupled from the anchoring groups, it does come naturally to sum the bonding dipole ($\Delta\Phi_{chem}$) and a dipolar layer ($\Delta\Phi_{dip}$), as referred to in eq.(1.26). In general, different interfacial phenomena come not only along with each other, but also affect each other, yielding a rather complex interplay. For instance, intra-molecular charge rearrangements upon charge transfer have been shown to alter the intra-molecular dipole moment and thereby $\Delta\Phi_{dip}$ of strongly dipolar molecules employed in a SAM.[126]

1.2.4. Organic/Buffer-Layer Interfaces

The need to overcome the critical issue of the rare observation of band bending in organic semiconductors is obvious, as the underlying generation of integer-charged molecules is essential to obtain their spectral signature, the current work aims at investigating. Due to the fact that this generation of charged molecules is inhibited by the strong electronic coupling between adsorbates and clean metal surfaces, which have been employed as prototypical substrates for decades, thin passivating interlayers can be introduced. These interlayers can decouple the organic semiconductors from strong interacting substrates while conserving the electrical contact to the substrate's E_F.[ANW+13,NAW+12] [127]
This concept applies to the employment of strong molecular acceptors/donors and monolayers comprising strong intramolecular dipoles as well as to more typical dielectrics, i.e. salts[103], serving as "passivating" interlayers.
Suitably fulfilling a number of experimental requirements, semiconducting metal oxides were chosen: (i.) They are conductive, as required by (inverse) photoelectron spectroscopy, (ii.) they can provide rather large work function values in order to electrically generate cations, (iii.) they can be prepared in thin films and (iv.) their likeliness for strong electronic coupling to organic adsorbates should be significantly reduced compared to the pristine metal surfaces.

Organic/Metal-Oxide Interfaces

Organic/metal-oxide interfaces are present in hybrid and organic photovoltaic cells, as well as in low-resistance contacts in OLEDs, where one hopes to benefit from the combination of the favourable properties of both of those distinct material classes. On the organic side one finds excellent absorption cross sections whereas the inorganic side provides higher charge carrier mobilities and stability against, e.g. photo-induced degradation. In order to establish a desired functionality in application of optoelectronic devices (e.g. efficient charge carrier injection), control of the energy-level alignment is required. In order to address this issue, different strategies can be pursued, as have been introduced in the previous subsections. Furthermore, a detailed understanding of the nature of these interfaces is expected to not only inspire but also promote the efforts.
In 2012 Greiner et al. postulated the *Universal Energy-Level Alignment of Molecules on Metal Oxides.*[37] Thereby the necessity of electronic equilibrium was elaborated to be the driving force governing the energy-level alignment according to the considerations outlined in section 1.2.2. It was concluded that the energy-level alignment is properly described by invoking the effect of E_F-pinning, obtained for the deposited material employing a substrate work function beyond the critical

values. Furthermore, a pushback effect, that universally accounts for 0.3 eV was considered. The pushback effect[128–130] at organic/metal-oxide interfaces is rationalized by invoking the following reasoning. As previously discussed, the pushback effect occurs upon interface formation between two materials with significantly different valence electron densities per volume. In this context, the noble metals have been characterized by large valence electron densities per volume, termed to be "soft" in association with the HSAB-principle[131]. In comparison to metals, metal-oxide surfaces should be rather termed "hard" in association with the HSAB-principle but not as "hard" as the deposited molecule. Indeed, the metal oxide's valence electron density at the surface is pushed back, even if this effect is not as prominent as the one obtained for organic/metal interfaces, where the difference between the "hard" and "soft" matter is obviously more pronounced.[132]

It needs to be pointed out, that the study by Greiner et al.[37] focused on the variation of metal oxides and their surface configuration rather than aiming at completely covering the diversity of organic materials. Noteworthy, for the selected molecular materials no chemical interface formations and accordingly no interface dipoles occur. If, however, one aims at extending this generalization to other molecules, the energy-level alignment of molecules on metal oxides is found to be far from being able to be termed "universal". Indeed, phenomena like e.g. the formation of phosphonic[133–136] or carboxylic-acid-based[112,137,138] SAMS on metal-oxide surfaces show significant deviations from those phenomena considered so far: E_F-pinning and an interface dipole contribution assigned to the pushback effect.[37]

This emphasizes the importance of functional groups, which potentially serve as molecular anchoring moieties of the organic molecules and thereby drive the adsorption process on metal-oxide surfaces in a non-physical manner.

Chapter 2.

Spectroscopic Methods

Photoemission spectroscopy was the investigation technique used in this study, allowing not only the chemical analysis and thickness estimation [XPS, Fig. 2.1(b)], but also the electronic characterization of the occupied valence states [UPS, Fig. 2.1(a)] as well as the unoccupied states [IPES, Fig. 2.1(c)]. Indeed, a complete picture of the electronic properties that are related to charge-injection and charge-transport processes can only be achieved when UPS and IPES are employed in combination.

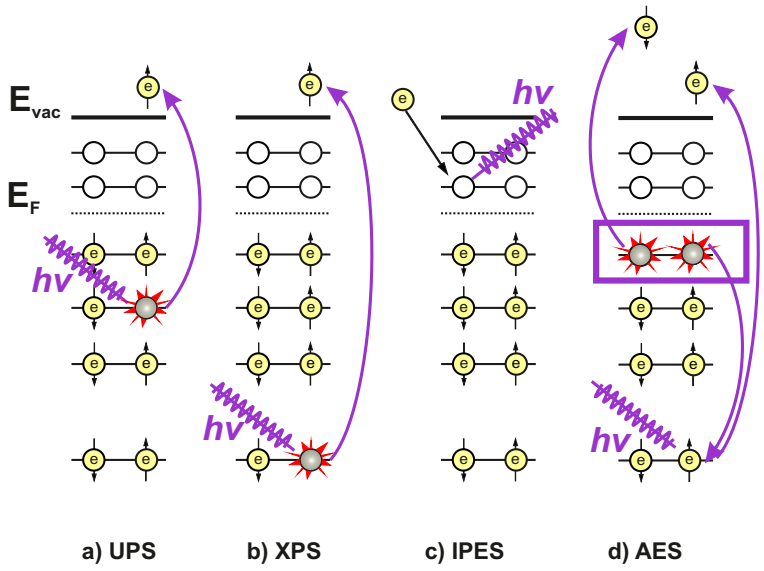

Figure 2.1.: Comparison of photoelectron techniques at the molecular level (based on Ref.[139]); (a) UPS, (b) XPS, (c) IPES, (d) AES.

2.1. Basic Principle

Photoemission spectroscopic methods are characterized by the process of electrons undergoing an irradiated/radiative ($h\nu/-h\nu$) transition from an initial state with an energy ($E_{initial}$) to a final state with an energy (E_{final}). These transitions are briefly discussed for both direct and inverse photoemission techniques,[140–142] using E_F as the reference level corresponding to zero electron binding energy, as illustrated in Fig. 2.2.

$$\underbrace{E_{final} - E_{initial} = h\nu}_{PES} \qquad \underbrace{-E_{final} + E_{initial} = -h\nu}_{IPES} \tag{2.1}$$

Photoelectron spectroscopy

In photoelectron spectroscopy (PES) a sample is irradiated with (monochromatic) light $h\nu$, generating photoelectrons via the external photo effect ($A + h\nu \rightarrow A^+ + e^-$). For an N-electron system, an initial state $|\Psi_{initial}\rangle$ with an energy $E_{initial}(N)$ is photoexcited to a final state $\langle\Psi_{final}|$ with an energy $E_{final}(N)$. The transition probability $p_{initial\rightarrow final}$ can be treated perturbatively according to Fermi's Golden Rule:

$$p_{initial\rightarrow final} \propto |\langle\Psi_{final}|H_S|\Psi_{initial}\rangle|^2 \delta(E_{final}(N) - E_{initial}(N) - h\nu) \tag{2.2}$$

whereas the perturbation operator H_S is given by the product of the dipole moment and the electric field in the dipole approximation.

Separating the excited electron, denoted as $|\psi_{initial}\rangle$ and $\langle\psi_{final}|$ with the respective energies $E_{initial}$ and E_{final}, the remaining N-1-electron system is accordingly denoted by $|\Psi'_{initial}\rangle$ with an energy $E_{initial}$(N-1) and $\langle\Psi'_{final}|$ with an energy E_{final}(N-1). In consequence, eq.(2.2) is transformed to:

$$p_{initial\rightarrow final} \propto |\langle\psi_{final}|H_S|\psi_{initial}\rangle|^2 |\langle\Psi'_{final}(N-1)|H_S|\Psi'_{initial}(N-1)\rangle|^2 \delta(E_{final} + E_{final}(N-1) - E_{initial}(N) - h\nu) \tag{2.3}$$

Relying on the frozen orbital approximation, where $E_{final}(N-1) = E_{initial}(N-1)$, one obtains the electron's binding energy E_B as $-E_{initial}$ and E_{final} corresponds to the kinetic energy E_{kin} of the free electron, which already has passed the barrier attributed to the work function Φ leaving a photohole in the investigated material.

Accordingly eq.(2.1) can be rewritten:

$$\underbrace{\Phi + E_{kin}}_{E_{final}} + \underbrace{E_B}_{-E_{initial}} = h\nu. \tag{2.4}$$

For the theoretical description of this photoemission process the single particle picture shall be used here rather than the complex many-body treatment. Many-body effects necessary to evaluate the spectra will be briefly discussed in the following section. According to the single-particle picture, one assumes that the removal of the electron from the remaining N-1 electron system is so fast that there is only negligible interaction between the two systems during ejection. In order to describe the origin of the spectral features, the so-called three-step model [see Fig. 2.2(a)] is considered albeit the separation is somewhat artificial[143]. In this model, the photoemission process is divided into:

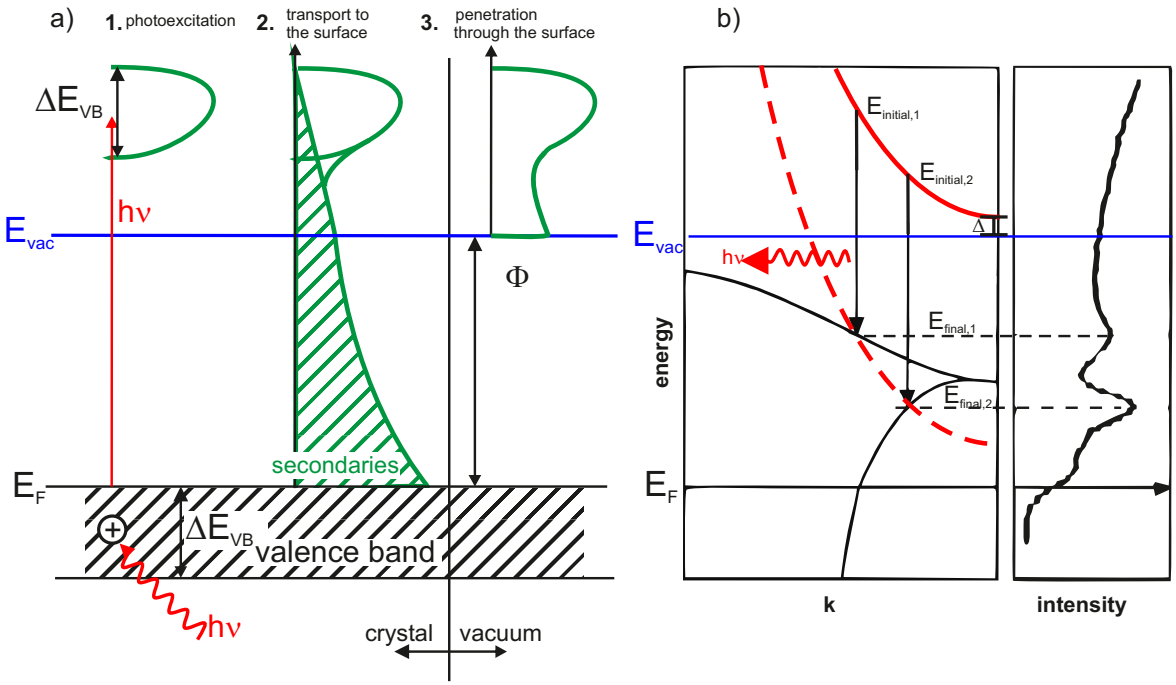

Figure 2.2.: (a) PES as a three-step process: 1. photoexcitation of electrons; 2. non-elastic travel to the surface with concomitant production of secondaries; 3. penetration through the surface (barrier) and escape into the vacuum (adapted from Ref.[140]) (b) Schematic illustration of inverse (radiative) transition with respect to the momentum-dependence.(adapted form Ref.[144])
Even if presented separately for the sake of simplicity, the three-step model and momentum dependence are equally applicable for both techniques.

1. **Photoexcitation of an electron in the solid**
   Depending on the excitation photonenergies, PES is subdivided into ultraviolet (energy range: 10 eV to 100 eV) and X-Ray (100 eV and above) photoelectron spectroscopy - UPS and XPS, respectively. The quantum chemical probability of absorption of high-energy X-ray radiation is highest for electrons in the inner orbitals ("core shells") during photoionization.

2. **Traveling of the excited electron to the surface of the solid**
   Caused by inelastic scattering processes, the excited electrons may loose kinetic energy on their way to the surface and thus contribute to the secondary electron background, as can be seen in Fig. 2.2(a).

3. **The escape of the electron from the solid into the vacuum through the surface**
   Electrons with an energy E_{final} smaller than necessary to overcome the sample work function Φ cannot escape from the surface into the vacuum; the sharp low-energy cut off (secondary electron cutoff - SECO) is thus a direct measure of the local vacuum level (E_{vac}), see Fig. 2.2(a). To ensure the detection of the escaped photoelectron's E_{kin}, E_{kin} further needs to be at least as large as $\Phi_{spec} - \Phi$ (for $\Phi_{spec} > \Phi$) as indicated in Fig. 2.3(a).

The generated (core) hole can be refilled with an electron from energetically higher shells. The resulting energy difference is either radiatively emitted or used for another ionization process of an electron in outer shells [Auger process, see Fig. 2.1 (d)]. The latter process causes further secondary electrons and dominates for elements with small nuclei number.[145]

Inverse Photoelectron Spectroscopy

To study the unoccupied states, inverse photoemission spectroscopy (IPES) is employed.[144,146,147] Electrons with a well defined energy $E_{initial}$ (typical: 5-20 eV) impinge on a surface and may occupy previously empty states above E_{vac} thus generating excited states. Via radiative ($h\nu$) transitions these electrons fall into lower lying unoccupied states below E_{vac} with an energy $-E_{final}$, given in eq.(2.1), that is rewritten in analogy to eq.(2.4):

$$\underbrace{-\Phi - E_{kin}}_{E_{initial}} \underbrace{-E_B}_{-E_{final}} = -h\nu \tag{2.5}$$

In the (here) used *isochromatic* mode, $E_{initial}$ and accordingly E_{kin} is varied and the emitted photons of only one particular energy $h\nu$ are detected employing

bandpass detectors. In particular the ionization threshold for the NaCl-covered photocathode as high-pass and the transmission cutoff of an SrF_2-window as low-pass (photon energy:9.5 eV) have shown to be a good compromise between quantum efficiency (up to 2.5%) and UV-energy-resolution (FWHM: 0.42 eV).[148] Accordingly, the detection is limited to a certain photon energy and the detectability is ensured only if E_{kin} of the electrons generated by the electron gun is at least as large as $\Phi - \Phi_{gun}$. Then a "free electron state" (above E_{vac}) can fall into a formerly unoccupied state, as illustrated in Fig. 2.3(b). From eq.(2.5), it further follows that E_{kin} needs to be at least as large as $h\nu - \Phi$.[140]

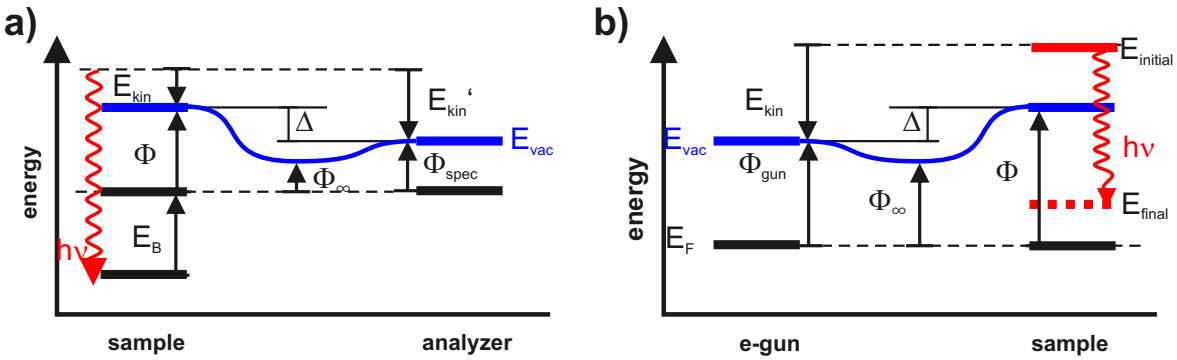

Figure 2.3.: Schematic correlation between the sample and (a) analyzer energy levels, or (b) electron gun energy levels.

For both techniques, energy conversion as well as the momentum conversion are the underlying principles as illustrated in Fig. 2.2(b). This further enables to employ these techniques in order to study momentum-dependent properties, like electronic band dispersion[77] and a preferential (molecular) orbital orientation, because in particular non-spherical π-orbitals only resonate with certain photon wave vectors.[149]

2.2. Content of Information

A typical energy distribution curve (EDC) obtained in a PES study is shown in Fig. 2.4, where the number of counted photoelectrons are plotted against their kinetic and binding energy, respectively. The binding energy (E_B) is referenced to the Fermi level (E_F), which has been aligned between sample and spectrometer/gun due to electrical contact, following eq.(2.4) and eq.(2.5), and in accordance to Fig. 2.3(a,b). Then E_B is given by:

$$E_B = h\nu - E_{kin} - \Phi \qquad -E_B = E_{kin} + \Phi_{gun} - h\nu \tag{2.6}$$

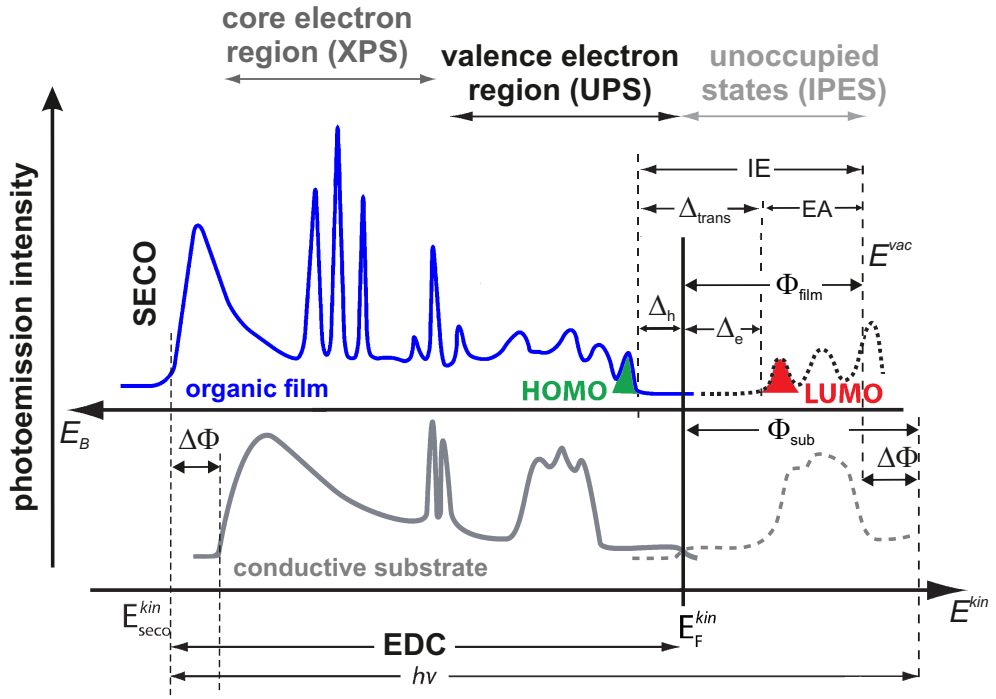

Figure 2.4.: Energy distribution curve (EDC) obtained in a comprehensive photoemission experiment (XPS, UPS, IPES) for a conductive substrate (bottom) and a subsequently deposited organic film. Apart from the determination of the substrate (film) work function and accordingly $\Delta\Phi$, a detailed analysis of the valence-level region and the unoccupied states of the organic film provides the hole (Δ_h) and electron (Δ_e) injection barriers, as well as the IE, EA and consequently the transport gap (Δ_{trans}). [inspired by Ref.[150, 151]]

2.2.1. Effective Binding Energy

According to Koopman's theorem E_B is the negative orbital energy and thusly characteristic for each atom an orbital type. Consequently, it allows quantitative elemental analysis with the number of detected photoelelectrons being related to the concentration of the specific element in the sample.
As E_B is sensitive to the local chemical environment, the so-called chemical shift ΔE_{chem} is obtained with respect to the elemental line position. From the sign and magnitude of ΔE_{chem} one can deduce details about oxidation states and electron donating or withdrawing substituents, as illustrated in Fig. 2.5(a). However, while non-equivalent atoms, with different substituents, always have different binding energies, these differences are often not detectable because of the limited resolution of the spectrometer (0.6 eV at synchrotron facilities, see section 3.2). With respect to the sum of effects, that are subdivided into 1. initial-state and 2. final-state effects at play during the photoemission process, the effectively detected binding energy $E_{B,eff}$ is obtained[152]:

$$E_{B,eff} = E_B - \underbrace{\Delta E_{chem} - \Delta E_{Madelung}}_{\text{1. initial state effect}} - \underbrace{P^{+/-}}_{\text{2. final state effects}} \tag{2.7}$$

Besides ΔE_{chem} also $\Delta E_{Madelung}$ - arising from the electrostatic energy in an ionic crystal - is summed up to the initial state effects, which reflect intrinsic material properties. Instead, any contributing polarization effect, induced by the perturbation of the system in the ground state created by photohole generation (P^+) or an impinging electron (P^-), is summed up to final state effects. The impact of $P^{+/-}$ on the determination of the semiconductors energy gap, being critically dependent on the permittivity of the surrounding medium, is discussed in section 1.1.2. This discussion reasons in favour of taking the onsets into account rather than the peakmaxima to obtain the parameters of interest IE, EA, Δ_h, Δ_e and Δ_{trans} (see section 1.2) from the obtained EDC curve as shown in Fig. 2.4.
E_F of a metal is used as zero binding energy reference and from the secondary electron cutoff (SECO), where the intensity drops rather abruptly due to zero kinetic energy, effectively hampering further electron extraction and detection, Φ is derived. Fig. 2.4 illustrates that this is possible by subtracting the full width of the EDC from the applied photon energy:

$$\Phi = h\nu - (E^{kin}_{SECO} - E^{kin}_F) \tag{2.8}$$

Usually an additional bias is applied to detect the cutoff decay clearly, obtained

for zero-kinetic energy. The region just below the SECO, which originates from secondary electrons during the non-elastic travel of the photoelectrons to the surface, is typically very strong and dominates the spectrum in case of carbon contaminations present on a surface, which enhances the probability of non-elastic interaction.[153,154]

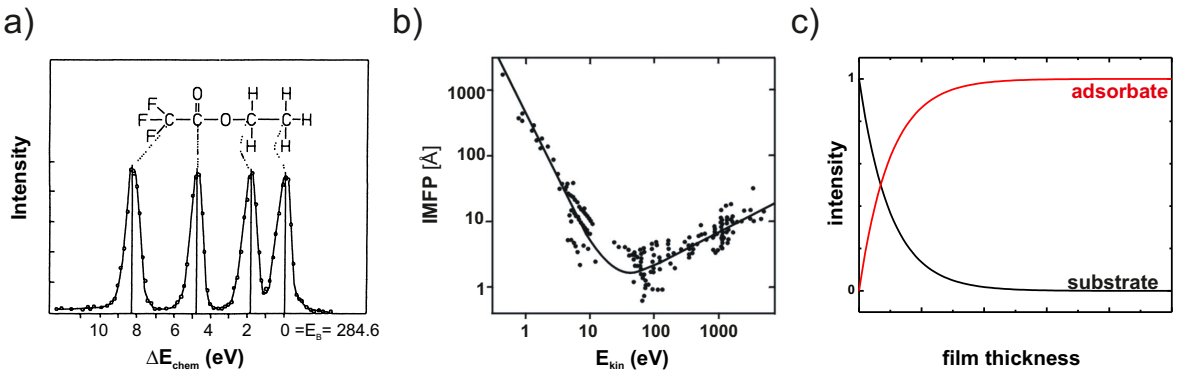

Figure 2.5.: (a) Four separated C1s-features referring to different carbon oxidation-states in ethyltrifluoroacetate, adapted from Ref.[152]. (b) Inelastic mean free path (IMFP) as a function of incident photoelectron's kinetic energy, as in Ref.[155]. (c) Substrate- and adsorbate-feature intensities as a function of film thickness according to layer-by-layer growth mode, a prominent growth mode observed for organic molecules.[156,157]

2.2.2. Surface Sensitivity

The surface sensitivity of the techniques is given by the (photo)electrons interacting with the surrounding substrate or adsorbate during their travel to/from the surface from/into the solid (2^{nd}-step in 3-step model). The mean escape depth (MED) is the depth from the surface at which the probability of an electron escaping/penetrating without significant energy loss has dropped to $\frac{1}{e}$.* To estimate the inelastic mean free path (IMPF), different empirical formulas have been proposed which dependend on the lattice constant of the investigated compound and the photoelectron's E_{kin},[155,158] the latter being depicted in Fig. 2.5(b). The curve's minimum is located at about 50 eV, corresponding to the largest surface sensitivity. For larger values of E_{kin}, the cross section with lattice atoms is large, but the E_{kin} after the collision is still large enough to escape (penetrate into) the solid. For lower values of E_{kin} the cross section is effectively reduced, as well as the surface sensitivity.
The surface sensitivity can be enhanced by employing lower kinetic energies or tilting the sample ($MED = IMPF \cdot cos(\theta_e)$,[159,160] where θ_e denotes the emission

* MED equals the inelastic mean free path, IMPF, considering normal emission.

angle) thereby enabling to obtain depth-profiles via energy-resolved/angular-resolved XPS (ERXPS/ARXPS[161]).
Likewise a comprehensive film-thickness d dependent analysis of spectral intensities $I(d)$ of the substrate and the organic material has proven to be a powerful tool to investigate the growth mode of the organic material derivable from Beer-Lambert law.[162]

$$I(d) = I_0 \cdot e^{\frac{-d}{IMPF(E_{kin})\cdot cos(\theta_e)}} \tag{2.9}$$

This simple relation validates the superposition of qualitatively pristine substrate's and organic layer's spectral intensities in order to reproduce a thin film spectra, if one deals with essentially non-interacting interfaces. This procedure is applied in chapter 5.

2.2.3. Angular & Orientation Dependence

Performing a photoemission experiment in angular dependence, enables the study of intra- and intermolecular band dispersion,[20,77] i.e. monitoring the evolution of certain peak positions with the photoelectron take-off angle. Analyzing the intensity evolution of certain peak positions† with the angle of photon incidence, the average orientation in a preferential oriented molecular conglomerate can be revealed.
In this regard, multiple ionization energy values for molecules in ordered assemblies are obtained. This is caused by an electrostatic aspect at play: the existence of a surface dipole built into molecular layers‡, that might drastically change depending on the molecular layer's orientation with respect to the surface.[163]
The simplest approach to study this phenomenon for organic materials utilizes oriented molecules exhibiting strong intrinsic dipole moments in an ordered assembly (SAMs, see section 1.2.3 or Ref.[38]).

2.2.4. Peak Broadening Mechanisms

In the following a brief overview of the peak broadening mechanisms arising from the photoemission process is given.

1. Lifetime
   The lifetime τ of a state is related to an energy uncertainty of a measurement

† as referred to non-spherical molecular orbital.

‡ This effect is reminiscent of the various surface dipoles for different single crystal surfaces. As a consequence, one obtains different work functions, as referred to in section 1.2.3. Here, this is conceptually adapted for the ionization energy.

and results in a Lorentz peak with a width $\delta E = \frac{2\hbar}{\tau}$. All investigated peaks in this work did neither show a Lorentzian shape nor a convolution of a Lorentzian with a Gaussian peak (Voigt profile). In general, lifetime effects have been shown to be very small (50-90 meV[17]) in organic semiconductors.

2. Experimental resolution
   The experimental resolution is limited by the photon (electron) source on the one hand and the electron energy analyzer (photon detector) on the other hand.

3. Band dispersion
   The electron analyzer is limited in resolving the angular dependence and therefore collects data from a certain range of angles. The investigated part of the Brillouin zone is thus rather a volume than a point. As the valence levels of thin organic films have only a very weak dispersion because of the weak interaction, this contribution is known to be very small[14,21,76].

4. Structural disorder
   In thin organic semiconducting films, the individual molecules weakly interact with each other. Most of the molecules do not exhibit spherical symmetry and therefore their ionization energies might differ, as already discussed. Moreover, the molecule's interactions are local and depend on their orientation with respect to each other. Variations of these local interactions might alter the screening process of a photo-hole and therefore the kinetic energy of the photoemitted electron. This site-specific polarization screening can induce a shift of up to 1 eV.[51,164,165] Accordingly, the energetic position of the orbitals is distributed over a range due to the different arrangements of the molecules, as sketched in Fig. 2.6(a). If this broadening effect contributes, the onset of the peaks mark the lowest LUMO and the highest HOMO. Charge transport will most likely occur through such states, justifying to account for the onset positions to determine Δ_{trans} once more (see section 1.1.2).

5. Band bending
   Closely related to the effect of structural inhomogeneity is the effect of band bending. The observable photoemission spectrum is a surface-sensitive weighted superposition of the differently aligned peak positions of several molecular layers and in result a broader peak is obtained, see Fig. 2.6(b). Moreover, band bending is caused by the presence of charged molecules that exhibit a further contribution that might alter the peak-shape and in particular the broadening. This aspect is important for chapter 5.

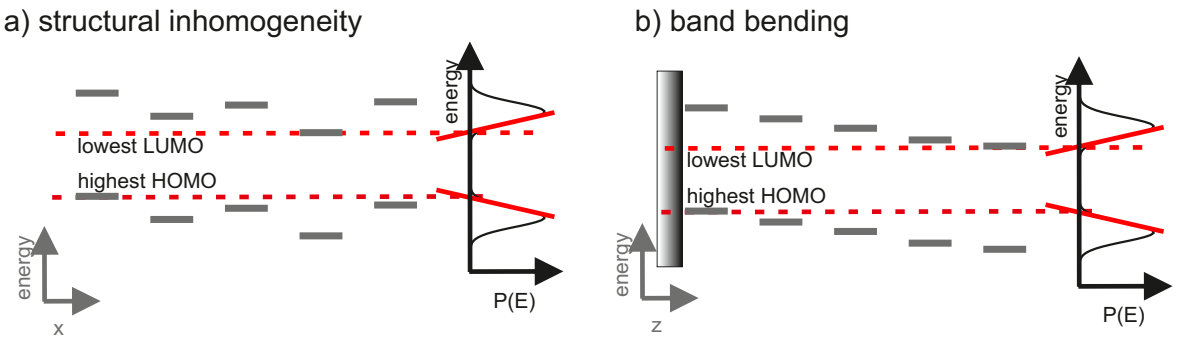

Figure 2.6.: Sketch of HOMO and LUMO levels, which are distributed in energy (a) statistically due to structural inhomogeneity within a certain layer or (b) according to band bending along the thickness of a organic thin film. The two curves on the right represent the probability distribution $P(E)$ for a certain vicinity and the related energetic position of the HOMO or LUMO. [adapted from Ref.[92]]

6. Vibration and phonon coupling
   Vibration and phonon coupling of the photo-hole, as referred to in section 1.1.2, can significantly (by up to 200 meV [93]) increase the peak-width.

2.3. Limits and Challenges

Employing photoelectron spectroscopic techniques requires awareness when organic molecules are involved in the studied samples.

- Spatial Resolution
  In general (I)PES is a surface averaging technique because the (illuminated) analyzed sample spot size is usually in the range of at least mm^2. Accordingly, a spatial distribution of different materials or materials in different electronic states cannot be resolved.[24,166,167] Indeed one usually gets a superposition of non-resolvable individual contributions. This needs to be carefully taken into account, if discussing organic material properties most commonly on the molecular scale (see particularly the discussion in section 4.3).

- Sample Charging
  As photoholes (excess electrons) are continuously generated in the sample, when employing photoemission (inverse photoemission) techniques, it is necessary to recirculate that charge.[168] Otherwise the sample would charge up positively (negatively), with most of the charge residing at the sample surface. This results virtually in an increased (decreased) binding energy attributed to the investigated electronic states due to Coulomb attraction (repulsion). Moreover, this charging effect might additionally contribute to

the peak-broadening mechanisms related to the sketched contributions in Fig. 2.6.

- Degradation
  Large absorption cross sections have been revealed to be both advantageous and disadvantageous: They provide large signal-intensities on the one hand but can induce substantial damage on sensitive materials, in particular conjugated organic molecules, on the other hand, due to strong photon(electron)-molecule interactions. To be more precise, degradation for direct photoemission is known to originate mainly from electron-molecule interaction as well, which is caused by the inelastic scattering of photoelectrons traveling from the solid to the surface. As a result, one might obtain energy levels and their alignments that are unintentionally but strongly affected by photodegradation.[153,169]

In essence, it is of paramount importance to take great care with regard of the last two issues. Charging can often be efficiently removed, via

1. reducing the external/internal photo-current via reducing (defocussing) the irradiation (electron) source or introducing a filter. This approach should also significantly minimize any degradation process.

2. illumination with additional light (visible or laser) and thus generation of additional mobile charges via internal photoemission at the interface to the substrate.

Chapter 3.

Experimental Setup and Materials

In this chapter, the materials, the experimental setups and the experimental parameters used in this work will be described. Moreover the theoretical methods and models applied within this work, available through collaboration, are briefly introduced.

3.1. Materials & Processing

This section is divided into two parts: part one deals with the substrates, mostly metal oxides, and part two deals with subsequently deposited adsorbates.

3.1.1. Metal Oxides

In all experiments presented in this work, metal oxides serve as substrates. Based on their wide range of electronic properties, which is established from a combination of geometrical, quantum chemical and electrostatic characteristics, they are used in all type of organic electronic devices. For instance, they can be employed as dielectric insulators, defective semiconductors, Mott-Hubbard insulators and metallic conductors.[37,170]
Even so, the details of the energy-level alignment mechanisms at organic/metal-oxide interfaces are rather unexplored. To derive some general insights from a variety of specific interfaces, a series of various metal oxides is employed, listed in Tab.3.1.
According to their processing they are divided into two types of metal-oxide substrates:

a. **Supplied Substrates**
   Indium tin oxide (ITO) covered glass substrates (sheet resistance 15-30 Ω) were obtained with a layer thickness of $\sim$ 150 nm and had a roughness of about 20 nm (rms). Prior to any further treatment, they were washed, scrubbed in an Extran solution (Merck), thoroughly rinsed with deionized (Milipore) water and dried in a nitrogen flow. Afterwards, the ITO substrates were immersed

Table 3.1.: Name, acronym, source and preparation process of the substrates employed in this work.

Name	Acronym	Source	Prep.
Indium Tin Oxide	$ITO_{sol.cl.}$ ITO	Thin Film Devices Inc.	solvent cleaning +UHV-cleaning
Titaniumdioxide	$TiO_2(110)$	CrysTec GmbH	UHV-cleaning
Samariumoxide	SmOx	GoodFellow	UHV-preparation
Molybdenum(VI)oxide	MoO_3_e MoO_3_cl	Sigma-Aldrich	UHV-preparation + UHV-cleaning
gold	Au(111)	MaTeck GmbH	UHV-cleaning

in acetone, sonicated at room temperature for 5 min and dried by nitrogen again; this step was then repeated in isopropanol. If not directly used for further sample processing, they remained stored in sealed pure isopropanol. If used without further treatment, this ITO substrate will be referred to as "solvent-cleaned" $ITO_{sol.cl.}$.

Both the thus pretreated ITO as well as the supplied *Titaniumdioxide* (rutil) polished single crystals (110) have been cleaned in UHV by repeated cycles of Ar^+-sputtering and annealing, until XPS showed clean metal-oxide surfaces and UPS established a reproducible work function equal to that reported in the literature. In general, this status was established after 3 cycles of 30 min sputtering at 0.5 keV (1 $\mu A/cm^2$, $\sim$ 300 K) followed by an annealing step at 700 K. To prevent depletion of oxygen due to preferential sputtering within the metal oxide,[171] the last annealing step was finalized by dosing oxygen (10 min at 10^{-6} mbar) prior to the sample was set to cool down. During the cooling-phase, Φ of the metal oxides was found to vary with the amount of time that had been elapsed since the last annealing step, as exemplified for ITO in Fig. 3.1.

This is rationalized by chemisorption of OH groups at "native" oxygen vacancy defects. This chemisorption might be photochemically activated.[172,173] A temperature dependent amount of hydrogen-termination and reconstruction of the metal-oxide surfaces can also be considered.[174,175] To establish highest reproducibility of the investigated surfaces, each study was accordingly started with a time delay of about 2 h to account for this time-dependent variation.

b. **Evaporated Films**

Molybdenum(VI)oxide (MoO_3) powder as well as *Samarium* (Sm) pellets were evaporated from resistively heated crucibles using a rate of about 2 Å/min. Nominal film-mass-thicknesses (MoO_3 density: 4.7 g/cm^3; Sm

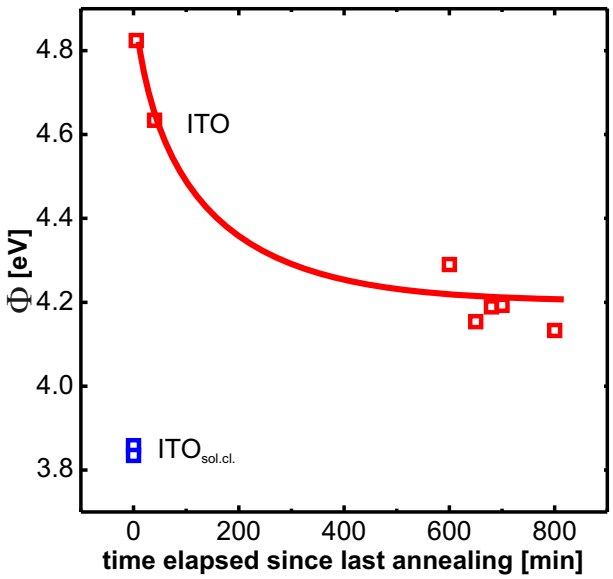

Figure 3.1.: Evolution of the ITO's Φ as a function of time elapsed since the last annealing step.

density: 7.5 g/cm^3) were monitored using a quartz crystal microbalance. To ensure a SmO_x-surface termination, the freshly exposed metal Sm films were exposed to 10^{-5} mbar oxygen for 20 min.
Both of those *in-situ* prepared substrates were free from any carbon contaminations and no further cleaning procedure was applied.
In addition, a MoO_3-termination consisting of a manifold of (not refillable by the mentioned oxygen-annealing process) oxygen vacancies was established by applying the Ar^+-sputtering/annealing-cycles mentioned previously. This surface termination results in a different work function and the sample is thus particularly labeled by MoO_3_cl.

An Au(111) single crystal, see bottom of Tab.3.1, is used to provide a most homogenous and well-defined metal-supported MoO_3-substrate. This single crystal has been cleaned in UHV by repeated cycles of Ar^+-sputtering and annealing, until XPS showed no carbon contamination and UPS established a reproducible work function equal to that reported in literature.[140] In general, this status was established after 4-5 cycles of 30 min sputtering at 0.5 keV (3 $\mu A/cm^2$, $\sim$ 300 K) followed by an annealing step at 750 K.

3.1.2. Molecules

As outlined before, a main task within this work is to establish a thorough understanding of organic/metal-oxide interfaces. Therefore a variety of distinctly different classes of molecules (summarized in Tab.3.2) is employed in order to test and/or confirm the validity of well-established concepts of organic-metal interfaces at organic/metal-oxide interfaces:

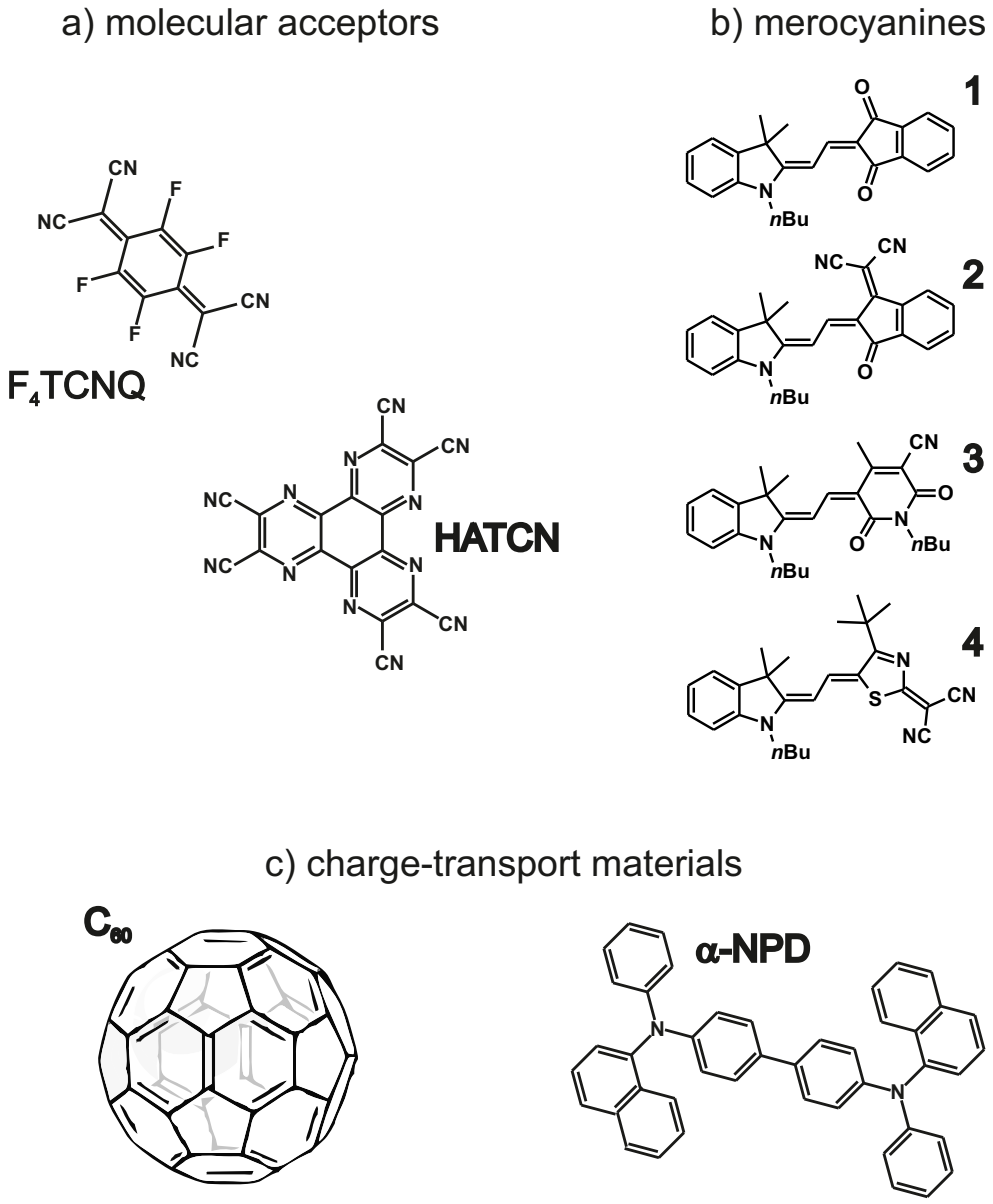

Figure 3.2.: Chemical structure of the investigated molecules in this work: (a) molecular acceptors, (b) merocyanines and (c) typical charge-transport materials. The molecular's full names are listed in Tab. 3.2.

a. **Strong Molecular Acceptor**
This class of molecules is employed as interlayers in order to significantly alter and adjust the energy-level alignment of subsequently deposited organic materials. They are known to undergo a strong charge transfer with the substrate to increase the work function of a certain metallic substrate and thereby exceeding the counteracting pushback effect: the case of HATCN and F_4TCNQ. Most importantly, the electronic coupling between molecule and metal oxide is to be studied, whereas it is well established between those molecules and metals. [HDS+13] [39,79,176]

b. **Strongly Dipolar Molecules**
Merocyanine dyes are molecules consisting of a donor (D) and an acceptor (A) part providing a strongly dipolar character. Despite their high absorption coefficients and tunable electronic character from polyene- to polymethine-type chromophores,[177–179] which make merocyanines naturally attractive for application in organic photovoltaics and particularly dye-sensitized solar cells (DSSCs)[180–185], strongly dipolar molecules are generally avoided in organic electronic devices.[186] In organic thin films, dipolar groups are known to generate a random electrostatic potential leading to a large energetic disorder decreasing the charge carrier mobility.[187,188] The discovery of highly dipolar merocyanine dyes self-assembling into dimer aggregates with vanishing dipole moments encouraged their further study in OPVCs furthermore.[189–191]

A series of merocyanines is employed to study the energy-level alignment to metal oxides. This may be characterized by their strongly dipolar character and/or by the possible reactivity of terminal functional groups with the metal-oxide substrates.

c. **Charge transport materials**
To ensure the ability of the employed interlayer (molecular classes a. and b., as referred to in section 1.2.3) to change and adjust the energy-level alignment, a typical hole transport material is subsequently deposited. The use of α-NPD is naturally attractive since due to its amorphous bulk structure the HOMO-position and consequently Δ_h is not affected by an orientation dependence of the ionization energy. Furthermore, it is expected to be rather inert with respect to potential chemical interactions to metal oxide due to its bulky sidegroups.

The typical electron transport material C_{60} was employed to facilitate the detection of potentially low concentration of molecules due to its high orbital degeneracy (HOMO:5, LUMO:3), that should come along with a significant

enhancement of signal intensity.
This is related to the fact that C_{60} in particular possesses extremely high symmetry, which allows access to an experimental and theoretical understanding on a fundamental level. It is meanwhile well suited based on its molecular structure to be rather inert. The wealth of gained insights on the electronic structure of pristine and doped C_{60} molecules can be found in excellent references. [80,81,83–85,103,192–211] [NAW+12,ANW+13]

Table 3.2.: Acronym, molecular formula, name and source of the molecular adsorbates investigated in this study. For their molecular structure, see Fig. 3.2

Acronym	Formula	Name	Source
1	$C_{25}H_{25}NO_2$	2-[2-(1-Butyl-3,3-dimethyl-1,3-dihydro-indol-2-ylidene)ethylidene]-indan-1,3-dione	Uni Würzburg (Würthner)
2	$C_{28}H_{25}N_3O$	2-{2-[2-(1-n-Butyl-3,3-dimethyl-1,3-dihydro-indol-2-ylidene)-ehtylidene]-3-oxo-indan-1-ylidene}-malononitrile	Uni Würzburg (Würthner)
3	$C_{27}H_{33}N_3O_2$	1-Butyl-5-[2-(1,3-dihydro-1-butyl-3,3-dimethyl-2H-indol-2-ylidene)ethylidene]-4-methyl-2,6-dioxo-1,2,5,6-tetrahydropyridine-3-carbonitrile	Uni Würzburg (Würthner)
4	$C_{26}H_{30}N_4S$	2-{4-tert-Butyl-5-[2-(1-butyl-3,3-dimethyl-1,3-dihydro-indol-2-ylidene)-ethylidene]-5H-thiazol-2-ylidene}-malononitrile	Uni Würzburg (Würthner)
α-NPD	$C_{44}H_{36}N_2$	N-N'-Bis-(1-naphthalenyl)-N,N'-bis-phenyl-(1,1'-biphenyl)-4,4'-diamine	Sigma-Aldrich
C_{60}	C_{60}	(C_{60}-I_h)[5,6]fullerene	Sigma-Aldrich
F_4TCNQ	$C_{12}F_4N_4$	2,3,5,6-Tetrafluoro-7,7,8,8-tetracyanoquinodimethane	Sigma-Aldrich
HATCN	$C_{18}N_{12}$	1,4,5,8,9,12-Hexaazatriphenylene-hexacarbonitrile	MPI (Müllen)

Thin film preparation of the molecules was performed via sublimation from resistively heated quartz crucibles using a rate of about 0.2 - 2 Å/min. The film mass thickness of F_4TCNQ (density: $1.64\ g/cm^3$), HATCN (density: $1.6\ g/cm^3$ [212]), α-NPD (density: $1.23\ g/cm^3$), merocyanines (density: $1.35\ g/cm^3$) and C_{60} (density: $1.6\ g/cm^3$) was monitored using a quartz crystal microbalance.

3.2. (Inverse) Photoemission Setup

The photoemission spectroscopy data presented in this work has been recorded either (i.) using the SurIcat end-station at the synchrotron light source BESSY II (Berlin, Germany) or (ii.) using a commercially available UHV system (Omicron) at the Humboldt-University Berlin.

i. The SurIcat-chamber is connected to the beamline PM4, which allowed beam energies ranging from 18 to 2000 eV. The spot size at the sample position was approximately 1 mm^2, which is equal to the acceptance area of the hemispherical electron energy analyzer Scienta SES 100. For recording the valence-level spectra the core-level spectra 21 and 620 eV were used, respectively. The resolution power of $E/\Delta E$ 4000 for the 360 lines per mm grating was determined, thus yielding the beamline resolution for the respective energies as depicted in Tab. 3.3. For all the spectra, an analyzer pass energy E_{pass} of 20 eV was used, expect of the SECO spectra (E_{pass} = 5 eV). The SECO spectra were moreover recorded with the sample biased at -10 V, in order to clear the analyzer work function.

   The experimental UHV-setup consisted of interconnected organic evaporation (base pressure $< 10^{-8}$ mbar), sample preparation (base pressure $< 10^{-10}$ mbar), and split analysis chambers (base pressure $< 10^{-10}$ mbar). The organic evaporation chamber was equipped with a fast-entry load lock, three positions for evaporation sources, two quartz crystal microbalances (QCM) and a sample storage system for up to four samples. In both the sample preparation and the upper part of the analysis chamber, Ar^+-sputtering and annealing of the sample of up to 600 $°C$ was possible. Furthermore, a LEED was mounted at the upper part of the the analysis chamber. The bottom part of the analysis chamber was equipped with the electron energy analyzer and connected to the storage ring via the beamline PM4. The angle between analyzer and the incident beam was fixed at 60°, while the angle between the sample and the analyzer was adjustable. This angle is specified as the take-off angle between the surface normal and the analyzer, which is 0° in all the recorded spectra. This corresponds to an angle of 60° between surface normal and the incident beam. All spectra were recorded angle-integrated with an acceptance angle of 10°.

ii. At the Humboldt-University a commercially available UHV apparatus (Omicron) consisting of interconnected sample preparation (base pressure $< 10^{-9}$ mbar) and analysis (base pressure $< 10^{-10}$ mbar) chambers, was used. The preparation chamber was connected to a fast-entry load lock. It is

Table 3.3.: Photon beam energies used in the experiments, corresponding line-widths, satellite-intensities and estimated photonfluxes according to the respective experimental setups. At the Beamline PM4, the grid 360 l/mm was used for both valence and core-level regions. Additional values for the commercial setup at HU Berlin were taken from literature.[152,213]

Photon-Source	Energy (eV)	Width (meV)	Intensity (%)	photonflux (1/(s*mm^2))
BESSY II (PM4, 360 l/mm)	21	5.3		10^{10}/(100 mA)
BESSY II (PM4, 360 l/mm)	620	8.7		10^{12}/(100 mA)
He Iα	21.218	5	100	10^{12}
He Iβ	23.087		2	
He Iγ	23.742		0.5	

equipped with facilities for metal substrate cleaning (Ar-ion sputtering and annealing up to 750 K), a mass spectrometer, up to four evaporator sources and a quartz crystal microbalance for monitoring the nominal evaporation rates. The analysis chamber is equipped with a multi-channel-plate LEED (Omicron) a scanning tunneling/atomic force microscope (VT-STM/AFM, Omicron), a twin-anode (Al, Mg) X-ray source ($h\nu_{(Al_{K\alpha})}$ = 1486.6 eV; $h\nu_{(Mg_{K\alpha})}$ = 1253.6 eV, Specs), a differentially pumped He-discharge UV source (Specs) and a hemispherical analyzer (Specs, PHOIBOS-150). To enable IPES-measurements the chamber was further equipped with a low electron energy source (FWHM$\sim$0.25 eV, as derived from a BaO-cathode) and a bandpass detector incorporating a NaCl-coated photocathode as high-pass filter and the transmission cutoff of a SrF2-window as low-pass filter.[148]

For recording UPS spectra, a pass energy of 5-10 eV was used, whereas for the SECO spectra the sample was biased at -10 V and a pass energy of 1-2 eV was used. XPS spectra were only recorded to verify the cleanliness of the substrates. In this case, either Mg Kα ($h\nu$ = 1253.6 eV) or Al Kα ($h\nu$ = 1486.6 eV) were used.

3.2.1. Experimental Details

Thickness-dependent measurements are recorded incrementally. After each deposition step, UPS and/or XPS spectra were recorded and compared to the previous in order to monitor the evolution of the valence-level and/or core-level features with increasing film thickness. Usually the material's mass thickness of each deposition step was read from a quartz crystal microbalance (QCM).

Consequently all values for the material coverage in this work correspond to a nominal film thickness. No correction was made for possible differences in the sticking coefficient between the different substrates and the QCM.

Most UPS and XPS experiments were performed at the SurICat end-station at BESSY II. IPES and additional UPS spectra were recorded at Humboldt University. After recording, the spectra were divided by the number of sweeps and the effective ring current to normalize them. In the case of the experiments at the Humboldt University, the spectra were just divided by the number of sweeps. XPS-peak fitting is done employing WINSPEC (University of Namur) using Gaussian peak shapes and Shirley-type backgrounds and yield a experimental resolution of 648 meV for a pass energy of 20 eV at $h\nu$=620 eV, as depicted in Fig. 3.3(a).

The Fermi level in the occupied (UPS) and unoccupied (IPES) valence-level spectra of metallic substrates was obtained according to the following fitting procedure and assuming that the experimental broadening is Gaussian-type.[215,216] The spectral intensity I(E,σ) can be represented by a convolution of the Fermi-Dirac distribution (F(E, T, E_F)) and a Gaussian function (G(E ,σ)), multiplied by the

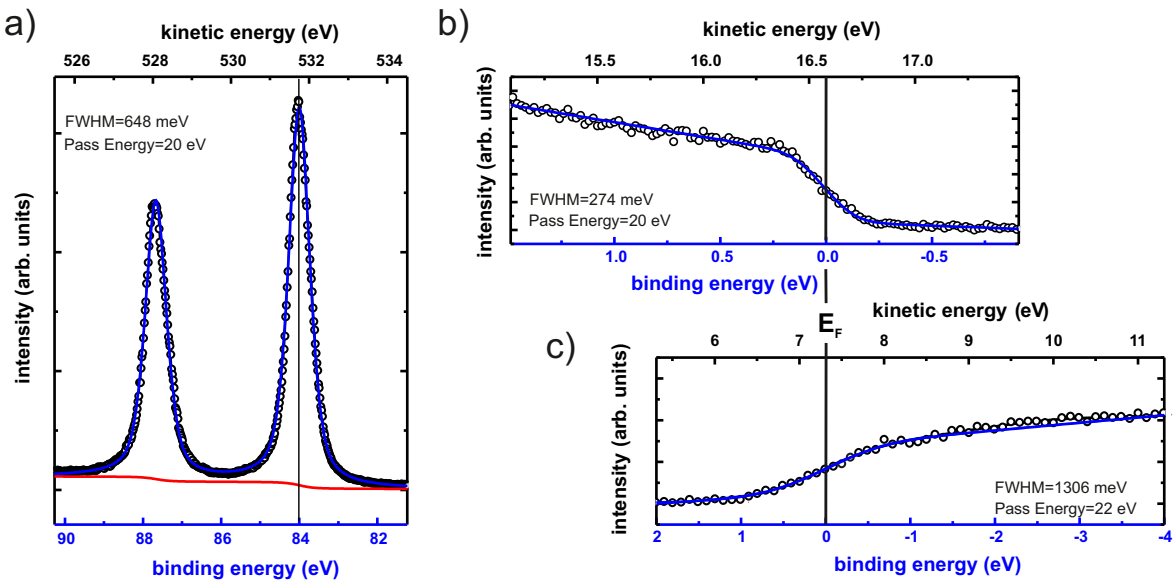

Figure 3.3.: (Inverse) photoemission spectra of clean Au(111) singly crystal: (a) Au 4f core-level spectrum ($h\nu$ = 620 eV), that has been used to convert the measured kinetic into binding energy by referencing to the binding energy of Au 4f 7/2 peak at 84 eV BE. The energy resolution was obtained by the FWHM of this peak.
Valence-level spectra for (b) the occupied and (c) the unoccupied states, in which E_F is set to 0 eV BE in order to convert kinetic into binding energy. In both cases the experimental resolution was obtained from following the fitting procedure according to Ref.[214]. Here, a Fermi-function is convoluted with a Gaussian function,[215,216] whose FWHM accounts for the experimental resolution; see text for more details.

density of states $\rho(E)$.

$$I = \rho \cdot (F * G) \tag{3.1}$$

Making use of the approximation, proposed by Weinhardt,[214] an approximated value for the spectral intensity I' can be derived:

$$I' = \frac{a \cdot E + b}{2} \left(1 - erf\left(\frac{E_F - E}{\sigma\sqrt{2}}\right)\right) + c \cdot E + d \tag{3.2}$$

The density of states is approximated to be linear around E_F and thereby dependent on the fitting parameters a and b. Accounting furthermore for a linear background depending on c and d, one can then derive the position of E_F and the variance σ could be determined. The experimental broadening FWHM$_{exp}$ was then calculated by:

$$FWHM_{exp} = 2\sqrt{2ln2} * \sigma \tag{3.3}$$

For UPS, FWHM$_{exp}$ of 274 meV for a pass energy of 20 eV and $h\nu$=21 eV (Fig. 3.3(b)), for IPES, FWHM$_{exp}$ of 1306 meV for a pass energy of 22 eV (Fig. 3.3(c)) were obtained.
For all three photoemission spectra, kinetic energy is converted to binding energy (BE) making use of a clean polycrystalline gold reference, which was measured prior to the first measurement. This is depicted in Fig. 3.3(a-c): The Au4f 7/2 peak was used as energy reference for 84 eV BE (XPS spectra) and the fitted value for the Fermi level (E_F) was used as reference for 0 eV BE (UPS and IPES spectra). The error of the binding energies and SECO positions is estimated to be $\pm$0.05 eV, if obtained by XPS and UPS, and $\pm$0.1 eV, for IPES.

3.3. Experimental Challenges

3.3.1. Degradation and Stability

High photon fluxes can charge the sample if the conductivity of the material is too low. High UV-light intensities can also irreversibly damage the organic films changing Φ and the valence-level position. This applies for the solvent-cleaned ITO substrates ($\Phi_{ITO_{sol.cl.}}$=3.9 eV), which appear less stable against UV-light than the UHV-cleaned ITO substrates. Indeed, one observes up to 0.2 eV Φ-shifts before and after recording a valence-level spectra.
Therefore a very low photon flux is mandatory for the investigation of organic thin films. As can be seen in Tab. 3.3 the light intensity changes as a function of photon energy. Even though the photon flux of 21 eV excitation energy is

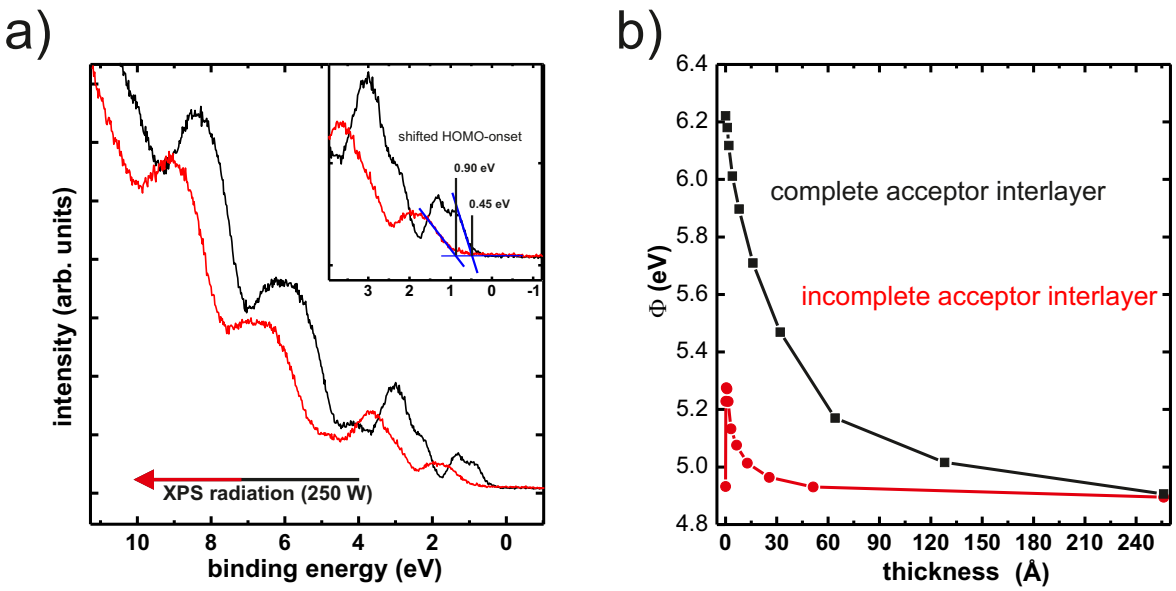

Figure 3.4.: (a) XPS-radiation induced energy-level shifts, as obtained by valence-level spectra. In addition some features are significantly broadened, which is strongly indicative of degradation. (b) Evolution of the work function upon deposition of α-NPD, as obtained for a completely and incompletely acceptor-layer covered substrate. The saturated work function is equal (beyond 20 nm) for both experiments. This strongly indicates experimental issues associated to unintentional co-evaporation. For more details, see text.

two orders of magnitude lower than of 620 eV excitation energy, the flux needs to be further reduced. Therefore a 150 nm thick Al foil is inserted in the beam after the monochromator, which decreases the photon flux and consequently the electron emission by about 85% at BESSY. At the HU-Berlin an attenuation filter (factor 100) was inserted between UV-lamp and sample.

Changing the excitation energy to XPS, for core-level analysis, the hitherto used filters to reduce the photonflux in UV are transparent for X-ray photons.

The XPS-radiation induced changes can be monitored by subsequently recording the valence-region spectra, as depicted in Fig. 3.4(a). The valence-level features are energetically shifted to higher binding energies, resulting in a different HOMO-onset position. Furthermore the shape of the valence-level spectra has slightly changed, i.e. some features are broadened or lost. The origin of this photo-induced degradation effect is mainly attributed to the avalanche of secondary photoelectrons.[153] Many organic compounds are sensitive to low-energy electrons, which makes experimental techniques, such as IPES or low-energy electron diffraction (LEED), so challenging.[217]

Accordingly valence region spectra and the sample work functions using low excitation energies are measured before the core-level analysis or at different sample positions, as referred to a small beamspot at the synchrotron facility.

3.3.2. Co-evaporation

A further experimental artifact related to the preparation of hetero-layered structures in UHV is the undesired co-evaporation of different materials. This is particularly emphasized in the case of the deposition of F_4TCNQ as first layer in *submonolayer* coverages. This rather elusive molecule has a rather low sublimation point in UHV (<100°C) and, as a consequence, is not directly sticking, when hitting the wall of the preparation chamber, but causing a permanent F_4TCNQ partial background pressure for at least 1 day. Thereby the submonolayer covered ITO substrate cannot stay in the preparation chamber, otherwise it would be fully monolayer covered.
Even if one adjourns further depositing the different molecular layers in the same preparation chamber by storing the sample in the connected analysis chamber until the partial F_4TCNQ pressure is reduced to zero, one has to face the next problem: Subsequently evaporating another material with a particularly larger sublimation point on top of this F_4TCNQ layer. The walls of the chamber which are covered with F_4TCNQ and in close vicinity to the now running evaporator, are getting warm as well and F_4TCNQ is co-evaporated.
Consequently, the second material is doped with F_4TCNQ. In the case of rather amorphous materials like α-NPD serving as second molecular layer in the heterostructure, F_4TCNQ is known to diffuse towards the substrate and thereby to modify the buried surface potential, leading to an energy-level alignment of the α-NPD-layer reminiscent of that of a full F_4TCNQ-layer.[218] This is depicted in Fig. 3.4(b): For submonolayer-coverages of F_4TCNQ deposited on ITO (Φ_{sub}=4.9 eV) subsequent deposition of the hole-transport material α-NPD results in an increase of Φ, which is rationalized by co-evaporation and subsequent diffusion towards the substrate of F_4TCNQ. When the F_4TCNQ-monolayer is completed at this buried interface, the work function, being representative of the energy-level alignment of α-NPD thick film (here: 25 nm), coincides with that of the one obtained for depositing α-NPD directly on a full F_4TCNQ-layer, as depicted in Fig. 3.4(b).

This problem has been solved in order to obtain reliable results in section 4.3.1. First, F_4TCNQ submonolayer covered substrates were prepared and stored in the analysis chamber. Afterwards, the F_4TCNQ evaporator was removed and the preparation chamber was properly baked to ensure proper UHV conditions. Finally, α-NPD was deposited on top of those stored F_4TCNQ submonolayer covered ITO substrates.

3.4. Theoretical Calculations and Modeling

Throughout this thesis the experimental observations are repeatedly supported by theoretical calculations. Gas phase molecular properties and structures were calculated using the program package Gaussian (Gaussian Inc., version 03[219]) in order to provide the localization of the molecular frontier orbital distributions (HOMO and LUMO) along the molecular structure of strongly dipolar molecules in section 4.3.2.
In particular, all other density-functional theory (DFT) calculations, as presented in chapter 5, were performed by G.Heimel (HU-Berlin). Moreover the electrostatic modeling was performed by M. Oehzelt (HZB Berlin).

3.4.1. Density-Functional Theory Calculations on Neutral and Cationic C_{60}

DFT calculations on isolated C_{60} molecules were performed with a hybrid exchange-correlation functional[220] mixing the generalized-gradient approximation developed by Perdew, Burke and Ernzerhof[221] with a fraction α of Hartree-Fock (HF) exchange. In the spirit of Refs.[222–224], α was determined by imposing Janak's theorem[225], that is, by requiring that the total-energy difference between a neutral and a positively charged molecule (at the neutral-molecule equilibrium structure) equals the eigenvalue of the highest occupied molecular orbital of C_{60}. To capture the screening of the excess hole on the fullerene by the environment (MoO_3 and surrounding molecules), a polarizable continuum model[226] with 3.5 as relative dielectric constant was employed. After repeatedly cycling through the determination of α and the geometry relaxation of the neutral molecule, an optimal value of $\alpha = 0.3147$ finally emerged. The so-obtained hybrid-functional was then employed to relax the fullerene also to its (symmetry-broken) cation equilibrium geometry. All calculation were performed with Gaussian 09, Rev. A.028[227] using the triple-ζ polarized 6-311G** contracted-Gaussian basis set[228] for geometry optimization and one set of additional diffuse functions (6-311+G**) for single-point calculations[229].
The core-level density of states (DOS) was obtained by broadening the entire manifold of C1s-related eigenvalues with area-normalized Gaussians of full-width at half-maximum (FWHM) of 0.7 eV. The valence DOS was produced by first broadening each valence-orbital eigenvalue with an area normalized Gaussian of standard deviation $\sigma = 0.22$ eV to emulate disorder, by subsequent multiplication with a room-temperature Fermi function (UPS) or one minus a Fermi function (IPES), and by finally convoluting the result with an area-normalized Gaussian

of $\sigma = 0.14$ eV (UPS) or $\sigma = 0.34$ eV (IPES) to account for detector broadening. For the spin-polarized cations, possessing one more spin-up than spin-down electrons, two possible spin-multiplicities (singlet and triplet) in the final state of the UPS/IPES experiment were taken into account: Removing a further spin-down electron from the cation by UPS (or adding another spin-up electron in IPES) results in one of three possible triplet states, while removing a spin-up electron by UPS (or adding a spin-down electron in IPES) results in a singlet final state. Therefore, the spin-down DOS for UPS (and the spin-up DOS in IPES) has been multiplied by a factor three before adding the spin-up DOS for UPS (and the spin-down DOS for UPS) to yield the final result displayed in Fig. 5.7, Fig. 5.9, Fig.5.10 and Fig. 5.11 in chapter 5.

3.4.2. Electrostatic Modeling of Band Bending in C_{60}

The model from Refs.[34, 103] is applied to the Au/MoO_3/C_{60}-heterostructure. There, the metal substrate is regarded as an electron reservoir with fixed chemical potential (i.e., E_F) and the MoO_3 interlayer as a perfect insulator with known thickness and dielectric constant (ϵ MoO_3 = 14.0[34,230]). The DOS of each molecular layer (ϵ (C_{60}) = 4.4[231]) is modeled by two Gaussians of experimentally determined width ($\sigma = 0.25$ eV), with onsets at the measured IE = 6.4 eV and EA = 4.4 eV, taking into account the respective orbital degeneracy (HOMO: 5 and LUMO: 3).[232]

The pushback effect is known to occur upon the organic monolayer formation on oxide surfaces, which amounts to $\sim$ 0.3 eV.[37] This effect is taken into account adding a linear interface-dipole contribution of 0.33 eV in the monolayer regime.[WFS+13] Therefore, instead of the measured pristine substrate work function of 6.8 eV, $\sim$6.45 eV is effectively taken into account prior applying the electrostatic model.[103]

Initially, the thusly constructed DOS is vacuum-level aligned to the "pushback-corrected" work function (6.45 eV) of the gold supported MoO_3-layer. The self-consistent calculation then starts by occupying all molecular layers in the fullerene film according to Fermi-Dirac statistics. With the values for the distance (d) between two consecutive C_{60} layers ($d = 0.82$ nm) and the density of molecules within one layer ($n_D = 1.1410^{18}$ molecules/m^2),[103] one obtains the (one-dimensional) charge density within the fullerene film (assuming lateral homogeneity). As overall charge neutrality demands, the integral over the charge density of the entire C_{60} film is compensated by a surface charge density of opposite sign on the metal. Taking into account the linear potential drop across the dielectric interlayer, the 1D-Poisson equation is numerically integrated on a

grid with steps of height d to calculate the layer-resolved electrostatic potential profile within the entire fullerene film. Subsequently, the DOS of each molecular layer is shifted in energy by the value of the potential in that layer. The second iteration then starts by, again, occupying the (now individually shifted) DOS of each layer up to the common Fermi level. The procedure is cycled until a stationary solution for charge density and electrostatic potential is reached, and is repeated for all considered film thicknesses.

III. Results and Discussion

As outlined in part I, the aim of the present work and consequently its outcome is subdivided into two parts.

Chapter 4. The first part deals with E_F-pinning at interfaces between metal-oxide electrodes and organic materials. In particular, it is demonstrated that besides the induced charge-transfer phenomenon and the general occurrence of a pushback effect at those interfaces, the organic/metal-oxide interface can be indeed characterized to be rather weakly interacting, if the organic material is appropriately chosen, i.e. functional groups of the molecules are widely avoided or at least not terminal and sterically shielded.

Chapter 5. In the second part, the spectral signature of charged molecules is obtained by employing an experimental approach involving an ultrahin metal-oxide interlayer to electronically decouple the molecular semiconductor from a metallic substrate.
Supported by DFT-calculations, performed by Georg Heimel, the common perceptions on the energy levels of molecular semiconductors comprising polarons were revised. The respective molecular-orbital level is not cut by E_F of the system, but rather subdivided by the on-site Coulomb repulsion U into one occupied and one unoccupied sub-level. By invoking inter-site Coulomb interactions, a complete picture of the energy landscape of charge carriers is derived as well as the principal accessibility of optical transitions by employing (inverse)photoemission.

Chapter 4.

Energy-level Alignment at Organic/Metal-Oxide Interfaces

In section 1.2, several properties of organic/metal interfaces that collectively determine the energy-level alignment have been introduced. In the following, these concepts will be adapted in order to characterize organic/metal-oxide interfaces complementary. In section 4.1 the discussion is started with the valence electronic structure of the individual materials involved; metal oxides and organic molecules. Subsequently, various types of interface-formation processes are discussed with a focus on the substrate-work-function-induced charge transfer, referred to as E_F-pinning. Section 4.2 deals with interfaces between a pure organic material and a metal oxide. Afterwards, the complexity is increased involving either a mixture (section 4.3.1) or a layered-structure (section 4.3.2) of two rather different organic materials deposited on metal oxides.
Parts of this chapter have been published in Ref.[WFS$^+$13] and Ref.[WFA$^+$14].

4.1. Valence Electronic Structure of Selected Materials

Even though the nature of interactions and likewise the energy-level alignment at many interfaces cannot be predicted, at least it can be educatedly guessed. In the case of physisorption, the adsorbed molecule binds to the substrate through rather weak physical forces (Van-der-Waal-forces) and the energy-level alignment is appropriately predictable by accounting for simple electrostatics, as referred to vacuum-level alignment or E_F-pinning. Regarding chemisorption, however, a prediction is rather difficult. At this point, it would be advantageous to be at least able to predict which of both distinct adsorption channels dominates.
It is obvious that this issue is strongly linked to the reactivity of the involved materials. Several concepts and parameters have been introduced and used in order to predict the reactivity of a molecule with respect to its molecular structure, particularly with respect to its terminal functional groups.[233–237] They have been

shown to be of enourmous value in order to quantify intermolecular interactions. Hunter[238] categorized these intermolecular interactions into five components that can be adapted for *molecule-substrate* interactions: Coulomb repulsion of electron densities at close distances of approach *(pushback effect)*; induction interactions between permanent charge distribution of one material and induced changes in the charge distribution of the other molecule or substrate *(image charge effect)*; dispersion interactions between mutually induced dipoles depending on the polarisabilities of the respective materials;[131,239,240] electrostatic interactions between the permanent charge distribution of the two materials, for instance the likelihood of a positive charge on the chemical bond donor and a negative charge on the chemical bond acceptor in terms of hetero-chemical bond formation, as referred to the electronegativity;[241,242] and charge-transfer interactions (E_F-*pinning*).
Prior to introducing the organic molecules according to their molecular structure and their valence electronic structure obtained by UPS, an outline of the used metal oxides serving as substrates is given.

4.1.1. Metal Oxides

This study focuses on the electronic structure of the organic/metal-oxide interfaces. It is well known that details concerning e.g. surface reconstruction and surface termination of metal oxides might significantly alter the electronic structure of the metal oxide surface and hence the organic/metal-oxide interface formation. However, in order to approximate the metal oxide's complexity to one simple derivable value, i.e. the work function of the metal oxide Φ_{ox}, a reproducible surface-preparation procedure was established, as can be found in section 3.1. This enables highest reproducibility of the recorded spectra and in consequence

Table 4.1.: Energetics of metal oxides employed as substrates: Φ_{ox}; valence band onset, as obtained experimentally and in comparison to literature values; band gaps from references and accordingly calculated conduction band onsets.

substrate	Φ_{ox} (eV)	VB-onset (eV)	literature (eV)	band-gap (eV)	calculated CB onset (eV)
MoO_3_e	7.0	2.5	2.83-2.5[37,243–245]	3.0[246]	0.5
MoO_3_cl	6.0	2.5		3.0[246]	0.5
TiO_2	5.25	3.3	2.8[37]	3.4[247]	0.1
ITO	4.2	3.1	3.2[248]	4.0[249]	0.9
Sm_2O_3	2.3	3.9	2.3[250]	4.33[251]	0.43

highest reproducibility of the surface composition.
A variety of metal oxides serves as substrates within this study. For all employed metal oxides, Fig. 4.1 depicts the photoemission onset, from which the vacuum level of the surface can be determined, and the valence-band region close to E_F, from which the valence-band onset can be determined. All of the valence-band spectra have in common the fact that they are dominated by spectral intensity originating from O2p-levels.[37,170,244,252] The energetics of MoO_3_e, MoO_3_cl, TiO_2, ITO and Sm_2O_3 are summarized in Tab.4.1 and show good agreement with the results in literature.

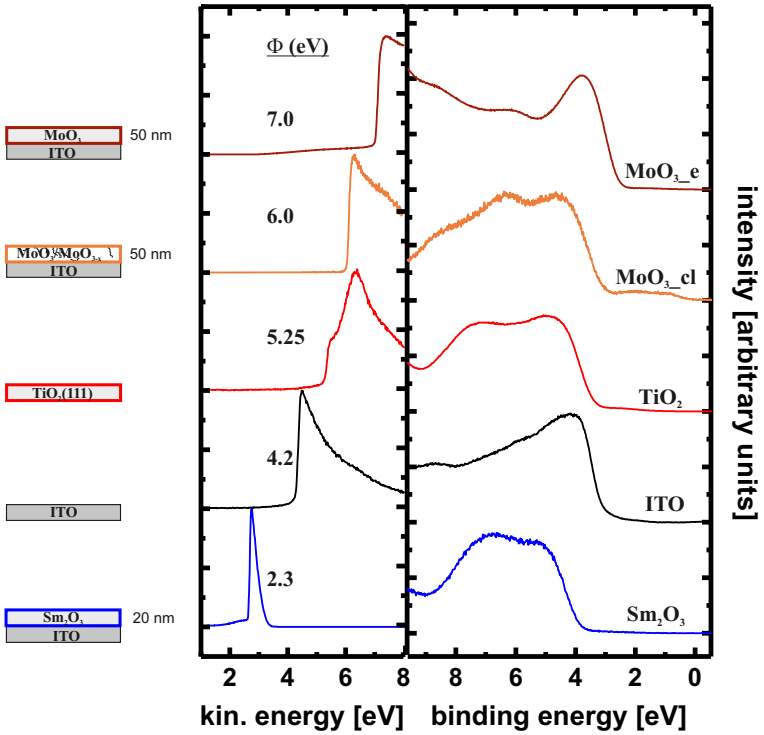

Figure 4.1.: From left to right: Pictograms for the metal oxides employed as substrates, valence electronic structure of these substrates as obtained by UPS is shown respectively: SECO and valence-level spectra.

4.1.2. Molecules

α-NPD

Along with it's molecular structure, α-NPD's valence-level region obtained by UPS is depicted in Fig. 4.2. Due to the very low basicity of the tertiary amino groups that are (i.) in conjugation with and (ii.) sterically shielded by the vicinal

aryl-groups, α-NPD is characterized to be rather chemically inert. Moreover, α-NPD exhibits an amorphous bulk structure and is known to grow in a layer-by-layer fashion on various substrates at room temperature.[31,253,254] Therefore, it is well suited as charge-transport material, sice it is not affected by any orientation-dependent effects (see section 2.2.3).

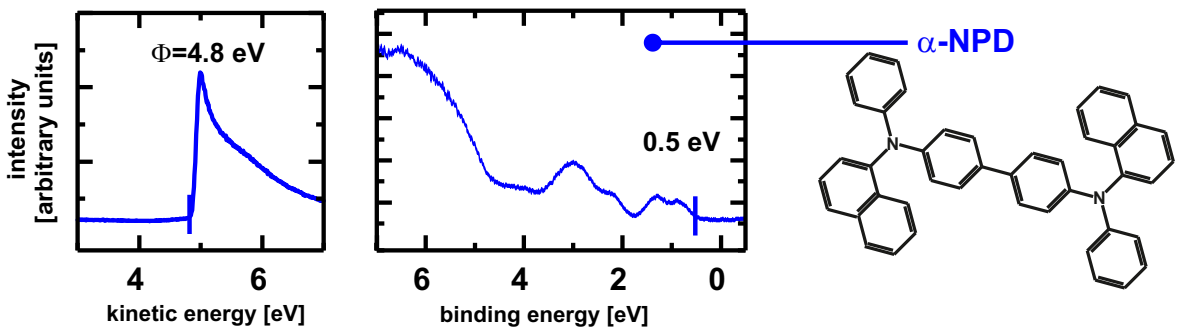

Figure 4.2.: Molecular structure of α-NPD and its valence electronic structure obtained by UPS.

From the spectrum in Fig. 4.2, the HOMO onset of a thick (50 Å) α-NPD film can be found at 0.5 eV below E_F. In sum with the work function of 4.8 eV, this yields the ionization energy of 5.3 eV, as well established in literature.[31,255]

Molecular Acceptors

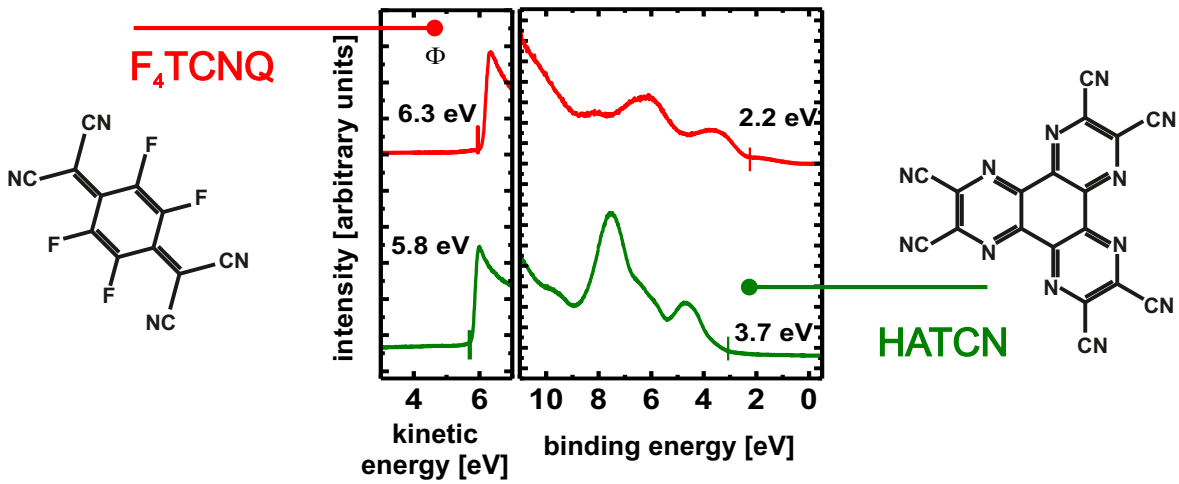

Figure 4.3.: Molecular structures of the acceptors F_4TCNQ and HATCN, as well as their valence electronic structure obtained by UPS.

The valence-level region for F_4TCNQ and HATCN nominal thick films is depicted in Fig. 4.3. From the onset of the HOMO-derived levels, marked by ticks, the ionization energy can be determined to be 9.5 eV for HATCN and 8.5 eV for F_4TCNQ. These values are larger than the literature values $IE_{Ag,HATCN} = 9.1$ eV and $IE_{Ag,F_4TCNQ} = 8.1$ eV.[150] The main difference is that the literature values were obtained for molecules on metals, where screening[87,256,257] should play a much larger role than on a metal oxide[258] thus reasoning the by 0.4 eV larger ionization energies in the present case.
Regarding their molecular structure comprising terminal cyano-groups, they are known to chemically couple to the substrate when deposited on metal surfaces. Here it was shown that the cyano-groups bend down to the metallic substrate.[259,260] Therefore they can be employed to evidence whether and to which amount metal oxides are involved in chemical interface formation as well.

Merocyanines

Next to their molecular structure, depicted in Fig. 4.4(a), thick film (50 Å) valence-level spectra of all employed (**1**-**4**) merocyanines deposited on TiO_2 are depicted in Fig. 4.4(b). A remarkable similarity between all of these spectra is observed. This applies not only to the location of the HOMO onset with respect to E_F but also and in particular to the shape of the photoemission spectra. Taking the molecular structure and the strong push-pull character of the molecules into account, the distribution of the HOMO is predominantly located on the donor moiety of the molecules (see also Fig. 4.22 in section 4.3.2), which is equal in all of these molecules. Note that in contrast the acceptor moiety varies considerably and therefore the corresponding spectra of the unoccupied levels is expected to be rather different as well. Small deviations, i.e. an increasing broadening of the HOMO-feature with increasing intramolecular

Table 4.2.: Summary of the energetics of the merocyanines used in this study: dipole moment, ionization energy, fundamental gap and the full width at half maximum of the obtained HOMO-level feature ($FWHM_{HOMO}$).

MC	dipole moment (D)[153]	IE (eV)	gap (eV)[153]	$FWHM_{HOMO}$ (eV)
1	3.8	5.3	2.24	0.59
2	6.2	5.4	1.90	0.59
3	11.1	5.3	2.09	0.67
4	13.3	4.9	1.75	0.68

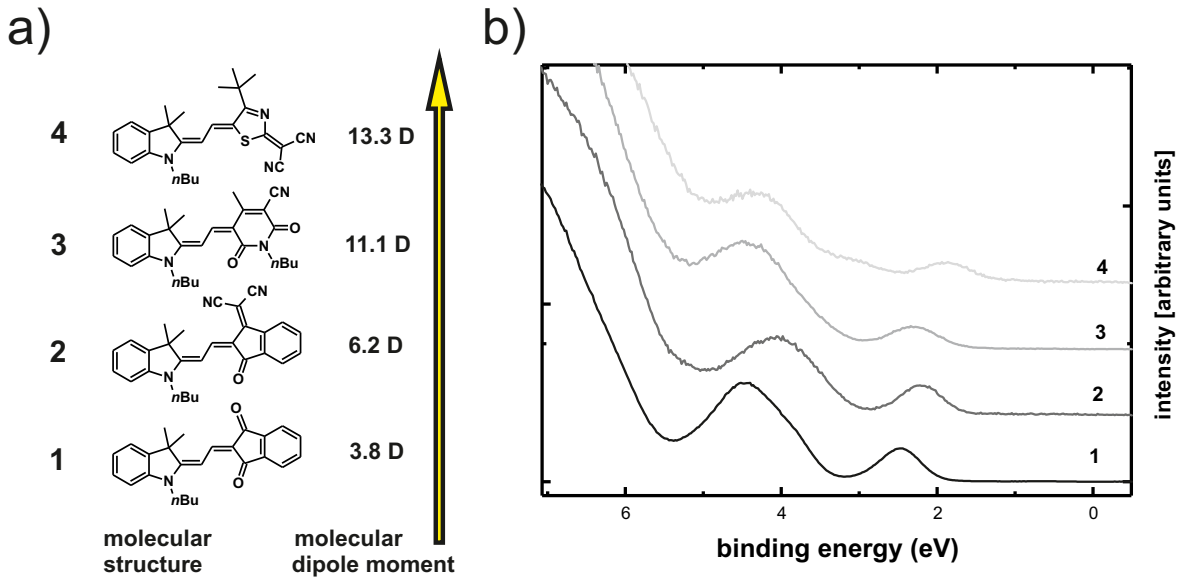

Figure 4.4.: (a) Chemical structures of the four investigated merocyanine dyes **1**-**4**. All consist of the same donor part with varying acceptor moiety. Values for their ground state dipole moments,[153] as determined by electro-optical absorption spectroscopy, are given next to the structure. (b) Valence-level spectra of **1**-**4**, as obtained from 50 Å thick films deposited on TiO_2. With increasing dipole moment, the HOMO feature becomes broader, that is related to increasingly coupling in a dipole-dimer arrangement.[153]

dipole moment are obtained nevertheless. This might be related to the presence of two translationally nonequivalent molecules of the same species per unit cell of an organic crystal[261] causing two distinct HOMO-features and thereby a level broadening[262] (associated with Davydov-splitting).
One could further think of strong intermolecular electronic coupling[263–265] caused by dimerization of the strongly dipolar molecules.[153] With increasing molecular dipole moment, one finds a stronger coupling, resulting in an increasing HOMO-level splitting, which in turn is obtainable via increasing peak width of the thin film's HOMO, summarized in Tab.4.2.

4.2. Two-Layered Structure

In section 4.2.1, α-NPD (widely established to be rather inert and based on this fact also selected by Greiner et al.[37]) is deposited on ITO and TiO_2. The results on the energy-level alignment can be arranged in conjunction with the conclusions drawn in Ref.[37]: an interface dipole arises, which is attributed to the pushback effect. Afterwards, section 4.2.2 deals with molecular acceptors, which do not only need to undergo a charge-transfer process in order to establish electronic equilibrium but also might form a chemical bond to the surface. This bond formation is related to their molecular structures comprising functional

groups in analogy to their chemical adsorption on metals.[259] Beyond that, a series of strongly dipolar molecules is studied on a variety of different metal oxides covering a substrate-Φ range between 2.3 eV and 7.0 eV in order to study dipolar molecules in a E_F-pinning induced charge-transfer process.

4.2.1. α-NPD on Metal Oxides

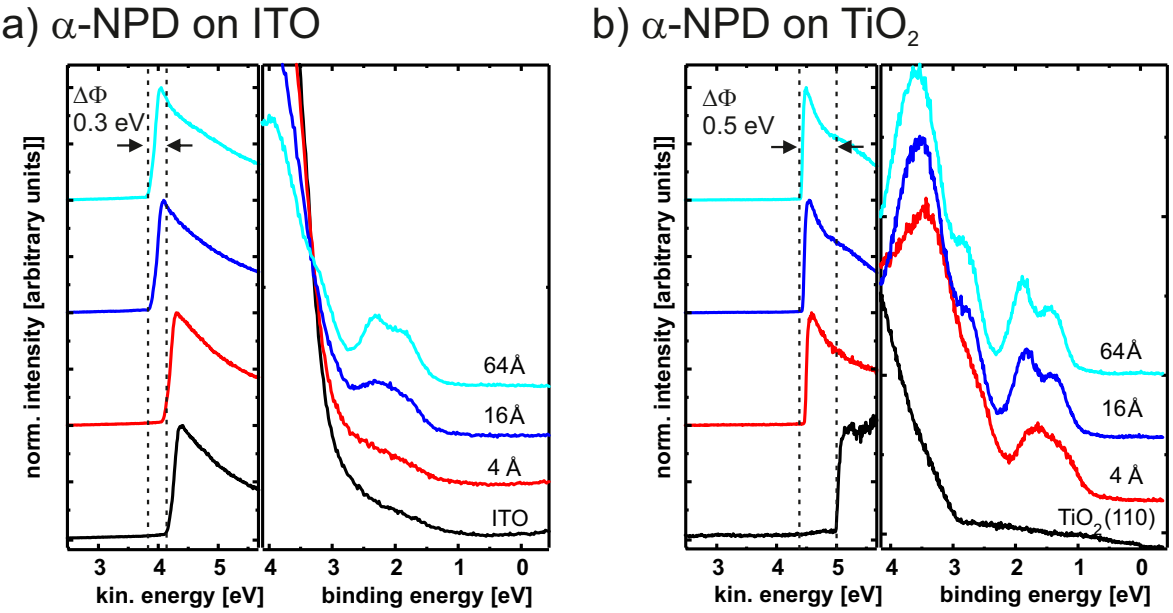

Figure 4.5.: The valence electronic structure of sequentially deposited α-NPD on (a) ITO and (b) TiO_2 as obtained by UPS is shown: SECO-spectra and valence band spectra.

α-NPD has been deposited sequentially on ITO and TiO_2. The corresponding spectra are plotted in Fig. 4.5(a, ITO) and (b, TiO_2) for various coverages. With increasing nominal coverage of α-NPD, the molecule derived features appear in the spectra. At 64 Å nominal coverage the substrate photoemission features are fully attenuated, which is attributed to the amorphous growth mode associated with their molecular structure. The saturated work function Φ=3.9 eV/4.4 eV and the HOMO onset at 1.4 eV/0.9 eV binding energy is obtained by deposition of α-NPD on ITO/TiO_2.

The evolution of Φ versus the nominal α-NPD coverage is plotted in Fig. 4.6. In accordance witj Ref.[37], one finds a work-function decrease of 0.3 eV assigned to the pushback phenomenon for α-NPD on ITO. As referred to in section 1.2.3, this is rationalized by invoking that the "soft", i.e. high polarisable, electron density at the metal oxides surface is pushed back by the presence of the "hard", i.e. low polarisable, electron density of the deposited molecules. Indeed, this

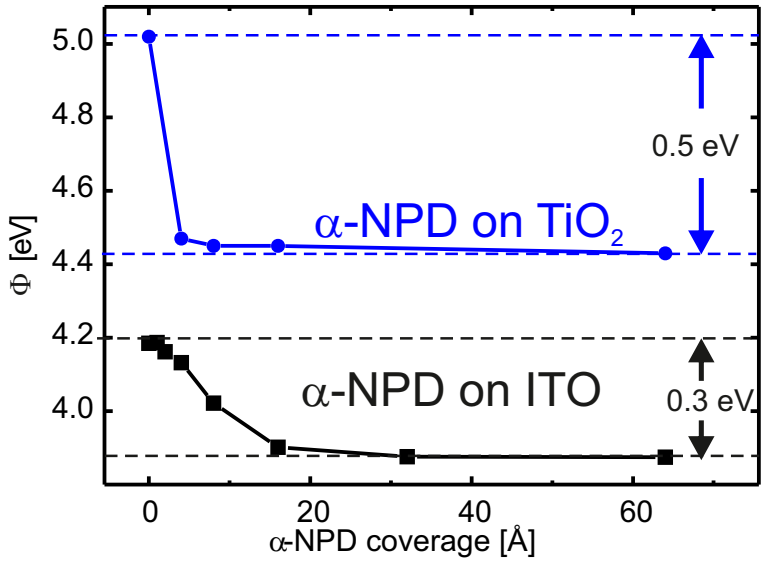

Figure 4.6.: Evolution of Φ as a function of α-NPD nominal coverage on ITO and TiO_2, as obtained from UPS.

effect is not as prominent as the one obtained for organic/metal interfaces where the difference between the hard and soft matter is more pronounced.[132]

The work function decrease of 0.5 eV for α-NPD on TiO_2 deviates from this correlation. For this observation, both of the following explanations can be considered. On the one hand, the TiO_2 surface might constitute a significant larger amount of surface defects, i.e. oxygen vacancies, whose decoration by α-NPD might result in a larger work function decrease. This is associated with a chemical bond formation at those reactive sites.[266,267] On the other hand, pinning of α-NPD's HOMO level at deep gap states[268–270] derived from TiO_2's low lying conduction band could be considered; see Tab.4.1. Those states cause the saturation of α-NPD's HOMO-onset position of 0.9 eV below E_F, which is significantly larger than the usual value of about 0.5 eV for α-NPD's HOMO pinned at E_F.[255,271] In addition to the "pristine" pushback contribution, this pinning induces a further contribution summing to the experimentally obtained value of $\Delta\Phi$.

4.2.2. Molecular Acceptors on ITO

The evolution of Φ versus the nominal acceptor coverage Θ_{acc} is plotted in Fig. 4.7(a). The bare work function is 4.2 eV for in-situ cleaned ITO substrates. When depositing the acceptor molecules, an almost linear increase of Φ to maximum values of 5.8 eV (HATCN) and 6.3 eV (F_4TCNQ) is observed. This corresponds to a work function increase of $\Delta\Phi = 1.6$ eV (HATCN) and $\Delta\Phi = 2.1$ eV (F_4TCNQ). For higher acceptor coverages Φ remains constant. The saturation

is attributed to the completion of a full monolayer, and acceptor multilayer formation does not further influence Φ. This is related to the fact that the observed ΔΦ is attributed to a pristine interface phenomenon originating from charge-transfer complex formation between acceptor molecule and metal-oxide substrate.[107] Molecules adsorbed in consecutive layers (multilayer) are vacuum-level aligned. Note that a saturated Φ-value for HATCN is obtained at nominal coverages of about 40 Å because Φ appears still slightly increasing between 20 Å and 40 Å, due to island-growth.[150]

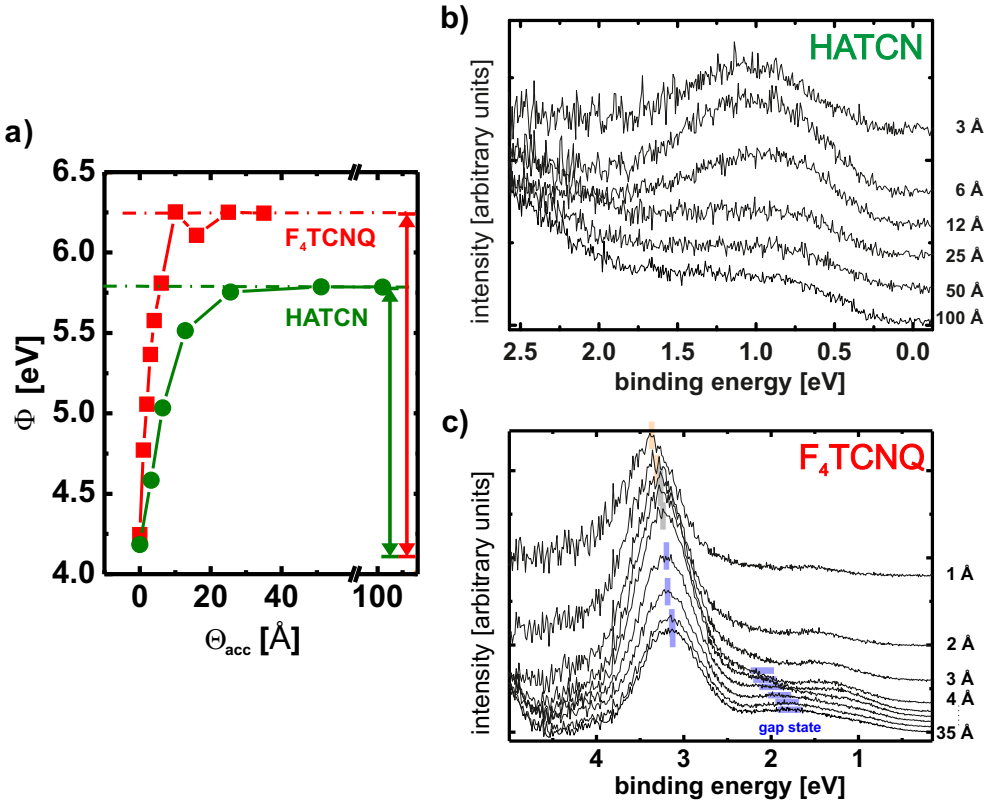

Figure 4.7.: (a) Evolution of Φ for ITO as a function of F_4TCNQ/HATCN nominal coverage Θ_{acc} obtained from UPS; (b) the evolution of differential spectra of HATCN deposited on ITO clearly shows additional photoelectron intensity within the energy gap of the molecule and thereby indicates the presence of charged molecules. (c) The evolution of F_4TCNQ differential spectra on ITO clearly shows a molecular peak shift to lower binding energies and thereby indicates the occurrence of charge transfer.

Referring to the established understanding of metal/organic-interfaces,[107,259] the origin of the pronounced work-function increase upon acceptor-layer formation on metal oxides (here: ITO) surfaces is to be discussed. Therefore, the submonolayer valence-level spectra are examined by carefully subtracting a suitably scaled substrate contribution. The remaining photoelectron intensity, depicted in

Fig. 4.7(b) and (c), is thus clearly associated with molecular acceptor-derived features.
For HATCN, one finds an additional photoelectron intensity within the gap of the semiconductor, located close to E_F and associated with the filled LUMO level. It is moreover already visible in the 3 Å HATCN valence-level spectrum and has its maximal intensity at nominal thicknesses around 6 Å and 12 Å, as depicted at the top of Fig. 4.7(b). This thickness directly correlates to the nominal film-thickness attributed to the completion of a ML. Deposition of thicker HATCN-films leads to an attenuation of this feature confirming it to be an interface phenomenon, with its origin from charged molecules localized at the interface. As this feature is attenuated but not vanished for large coverages (100 Å), island growth beyond ML-formation is further corroborated in the case of HATCN, as this monolayer-derived feature is detectable also for multilayer coverages (islands).
Although it is not possible to identify an additional photoelectron intensity located at E_F in such convincing manner for F_4TCNQ, which might be related to a bad photoelectron cross section[272] and/or particularly low amount of charged molecules, evidence of an underlying charge transfer process can be deduced. Note that due to the high volatility of F_4TCNQ, which is related to the material's low vapour pressure as referred to in section 3.3, a multilayer growth of F_4TCNQ is not expected to occur. Instead, beyond monolayer completion the sticking coefficient for further F_4TCNQ deposition is expected to decrease to zero. The discussion of the electrostatics associated with the charge-transfer process for F_4TCNQ is thereby more appropriately discussed considering the monolayer.
The evolution of the differential spectra upon incrementally increasing F_4TCNQ-coverage is shown in Fig. 4.7(c). Clearly a shift of the most prominent feature at about 3.2 eV to lower binding energies is obtained. Concomitantly a small feature within the molecular gap, which is attributed to the chemical complex formation,[32,33] [MHW+15] shifts in parallel. This electrostatic shift is caused by the Coulomb repulsion between excess electrons in the molecular monolayer, induced by the underlying charge-transfer mechanisms. At lowest F_4TCNQ coverages, this Coulomb repulsion is found to be at lowest, resulting in the HOMO level to be found at largest binding energies. With increasing submonolayer coverage up to the completion of the full acceptor monolayer, the Coulomb repulsion is increased[ANW+13] [273] and the electron binding energy of the HOMO level is found to be at increasingly lower values.

4.2.3. Merocyanines on Metal Oxides

For conventional organic semiconductors, which typically have no or very small dipole moments, the concepts introduced in sections 1.2.1 - 1.2.2 can sufficiently explain how a proper matching of the electrode Fermi level to the charge transport levels can be obtained to establish low resistance electrical contacts (i.e. by E_F-pinning). In contrast, merocyanines have substantial molecular dipoles, and it is thus necessary to take the considerations given in section 1.2.3 into account. Regarding the merocyanine's application, i.e. dye-sensitizing electrodes in solar cells (see also section 4.3.2), where low charge injection/extraction offsets are required, the interplay of intramolecular dipole moments and E_F-pinning is of particular interest and yet unexplored.
In order to ensure E_F-pinning at occupied and unoccupied levels of a series of merocyanines with varying molecular dipole moments, a wide range of substrate-Φ from 2.3 eV to 7.0 eV is employed. The gained insights are then arranged in order to categorize a certain dye/electrode-heterostructure either to be favourable for electron or for hole extraction in photovoltaic cells. The concluding remarks are followed by some outlook considerations on the role of frontier orbital distribution on molecules, when they are found in E_F-Pinning, and whether and how the molecular film's IE is affected by the presence of accumulated charges.

Merocyanine in E_F-Pinning

To study a strongly dipolar molecule in E_F-pinning, merocyanine **1** [see Fig. 4.4(a)] is chosen as test molecule, as it is the most planar molecule within the studied series of merocyanines and steric hindrance should therefore play only a minor role with respect to dimerization and substrate interaction.
Fig. 4.8 shows the evolution of the work function (Φ) and the HOMO-onset position (E_{HOMO}) [i.e., hole injection barrier (HIB)] in dependence of the nominal film thickness (Θ) of **1** on the different metal-oxide substrates, which have been introduced in section 4.1.1.
The IE of **1** for thick films ($\sim$5 nm) is 5.50 eV on all substrates, as can be derived from the sum of the respective values for E_{HOMO} and Φ in Fig. 4.8(b). As the orientation of the molecular dipole moment with respect to the surface normal has a significant effect on the observable IE of molecular films[38,163] (see section 1.2.3), the same IE of **1** on all substrates (see Fig. 4.8) moreover indicates the same structure and molecular orientation beyond a film thickness of $\Theta = 30$ Å. Since Φ also remains constant for thick films of **1**, the molecular dipoles are either oriented parallel to the surface or the molecules arrange themselves in such a way that neighboring dipoles cancel each other and no net dipole moment is

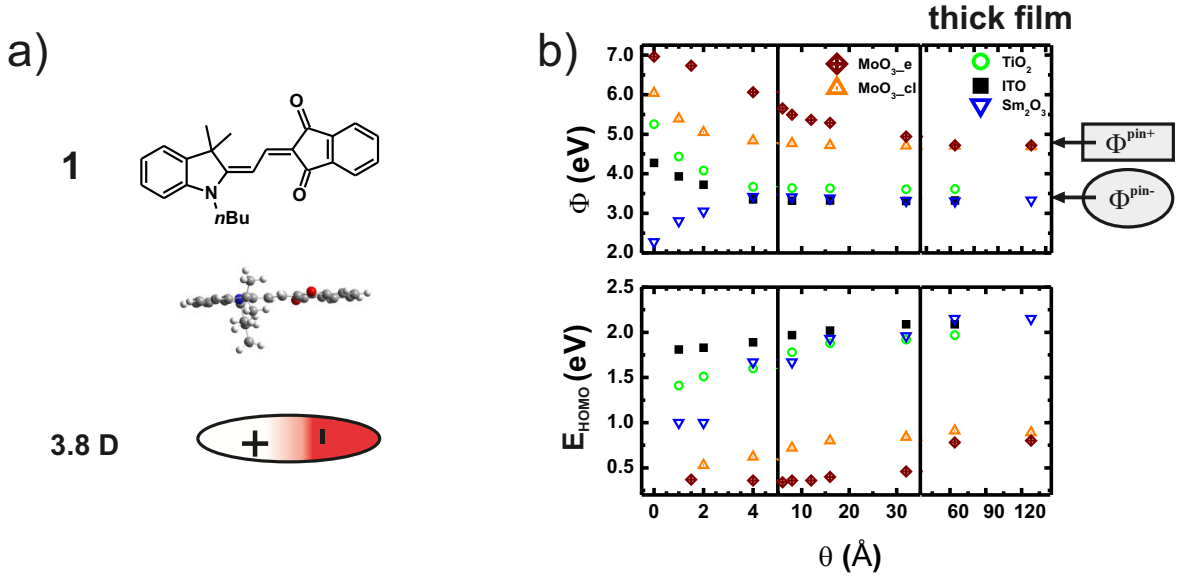

Figure 4.8.: (a) Chemical structure of **1** (b) Work function (Φ) and HOMO-onset position (E_{HOMO}) depending on the nominal film thickness (Θ) of **1** on Sm_2O_3 (blue triangles down), ITO (black squares), TiO_2(111) (green circles), MoO_3_cl (orange triangle up) and MoO_3_e (wine diamonds). The expected critical work function values Φ^{pin+}/Φ^{pin-} are marked by arrows.

obtained.[274–276] In Fig. 4.9, the corresponding energy-level schemes for thick films of **1** are depicted. By subtracting the optical gap of 2.25 eV[153], one can provide an upper limit for the EA of 3.25 eV; the exciton binding energy - so far not determined experimentally for **1** - must be taken into account for a more accurate EA value (as outlined in section 1.1.2).

In the low Θ regime, the deposition of **1** significantly changes Φ by about 1 eV and more for all studied systems, ruling out vacuum-level alignment. As a saturation value Φ_{sat} occurs close to $\Theta = 8$ Å, it is reasonable to assume that the molecular monolayer is closed at this nominal coverage.[107] Only for MoO_3_e a fairly higher Θ of ca. 30 Å is required for reaching the saturation value Φ_{sat}.

This effect is related to the occurrence of energy-level bending at the **1**/MoO_3_e-interface due to strong E_F-pinning (vide infra).[277] The initially striking fact, that in contrast energy-level bending is not observed at the approximately very similar **1**/MoO_3_cl-interface, highlights the tremendous meaning of the exact nature of interface formation on the occurrence of energy-level bending (band bending).

If strong molecular substrate interactions result in substrate-induced gap states, i.e. a pronounced mixing of substrate and molecular states, band bending collapses into a localized interface dipole.[34,103] In this regard, one can deduce that the "hybridisation" of adsorbate and substrate states occurs at the in-situ cleaned MoO_3_cl-surface. This can be rationalized by invoking the enhanced

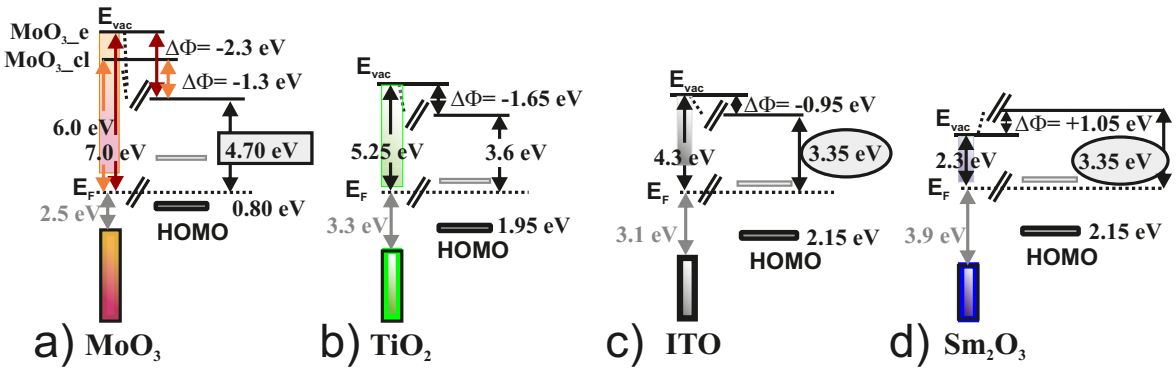

Figure 4.9.: Energy-level schemes of **1** adsorbed on (a) MoO_3 - band gap: 3.0 eV[246], (b) TiO_2 - band gap: 3.4 eV[247], (c) ITO - band gap: 4.0 eV[249] and (d) Sm_2O_3 - band gap. 4.33 eV[251]. The optical gap 2.25 eV was used to estimate the LUMO level of **1** and the band gaps of the oxides were used to estimate the CB-onset position. The critical work function values Φ^{pin+}/Φ^{pin-} are highlighted by a square/circle surrounding the corresponding numbers.

reactivity of the MoO_3_cl-surface, which is related to an increased amount of defects sites. These sites are assigned to oxygen vacancies caused by the sputtering process.[171]*

For molecules deposited on the freshly evaporated surface (MoO_3_e) this mixing of adsorbate and substrate states is obviously suppressed, thus resulting in the occurrence of band bending. Accordingly, the freshly evaporated metal-oxide film can be termed as rather inert interlayer.

MoO_3_cl/MoO_3_e (Φ_{ox}= 6.0 eV/7.0 eV, respectively) and Sm_2O_3 (Φ_{ox}= 2.3 eV) exhibit the extreme Φ_{ox}-values, as it is either larger than the IE or lower than the EA of **1**. Consequently, in the case of Sm_2O_3 the LUMO level is pinned at E_F, which results in a Φ increase of 1.05 eV giving a final Φ_{sat} of 3.35 eV for the **1** thick film. Likewise, the HOMO level is E_F-pinned for both employed MoO_3 substrates, resulting in the observed Φ decrease of 1.3 eV and 2.3 eV, respectively, giving a final Φ_{sat} of 4.7 eV. In contrast to common expectations[26,30,31,35,40,41] outlined in chapter I, additional valence spectral features upon charge transfer cannot be observed close to E_F, as depicted in Fig. 4.10. However, the density of charged molecules is typically very low and below the detection limit of our experimental setup.

Nevertheless, following the typical procedure, the such obtained Φ_{sat} values of 3.35 eV and 4.7 eV are considered to be synonymous with the critical Φ_{ox}-values, i.e. Φ^{pin-} and Φ^{pin+}, at which pinning sets in.

Turning to ITO (Φ_{ox}=4.3 eV) and TiO_2 (Φ_{ox}= 5.25 eV) as substrates, one would

* An increasing amount of these oxygen vacancies is known to result in an increasing metallicity of the surface[112] and might also result in a different initial orientation of the molecules[278].

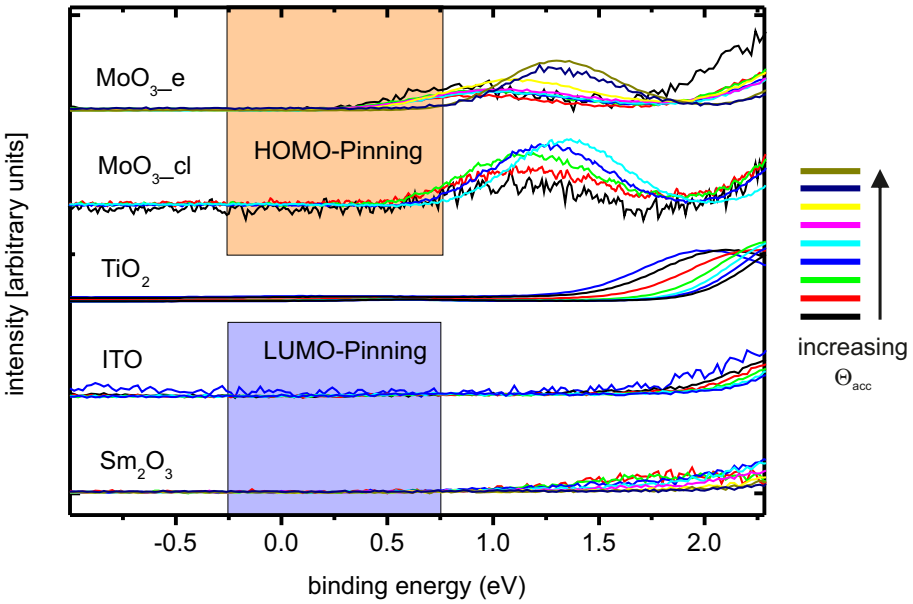

Figure 4.10.: Thickness (Θ) - dependent evolution of the differential spectra for **1** deposited on the employed metal-oxide substrates. The typical energy region for the spectral signature of molecular HOMO levels to be pinned at E_F is shaded in orange. The typical energy region for a (partially) filled LUMO level (LUMO-level pinning) is shaded in blue. No additional photoelectron intensity originating from a charge-transfer induced state is obtained, which is related to the low density of charged molecules.

therefore expect vacuum-level alignment to be established at the **1**/ITO interface, as the work function of ITO falls into the interval given by Φ^{pin+} and Φ^{pin-}, which is highlighted as grey shaded area in Fig. 4.11(a). For the $\mathbf{1}/TiO_2$ interface, Φ_{ox} falls outside this interval and a relatively small $\Delta\Phi$ of ca. 0.55 eV is expected to establish the saturation value Φ_{sat} of 4.7 eV. Clearly, the observed results differ from these expectations (see Fig. 4.8 and 4.9). For **1**/ITO an interface dipole decreases Φ_{ox} to Φ^{pin-} (3.35 eV), and for $\mathbf{1}/TiO_2$ Φ_{ox} is decreased to 3.6 eV, which is much lower than Φ^{pin+} (4.7 eV).

To visualize their interdependence,[41,279] Φ_{sat} of **1** is plotted versus the respective pristine substrate Φ_{ox} in Fig. 4.11(a). Based on the outlined expectations according to vacuum-level alignment [grey shaded area, Fig. 4.11(a)], the saturated work function value Φ_{sat} of **1** in both pinning situations (Sm_2O_3 and MoO_3) should coincide with the critical substrate work function Φ_{ox} values (Φ^{pin+} and Φ^{pin-}), at which pinning sets in.[35,41,255] In marked contrast, however, the Φ_{ox}-interval between both critical work function values is shifted by $\sim$ 1 eV to higher values.

This behavior is rationalized by invoking an interface dipole, whose various possible contributions are discussed for ITO and TiO_2 more explicitly next. One contribution is the push-back effect (see section 1.2.3 and 1.2.4), which was

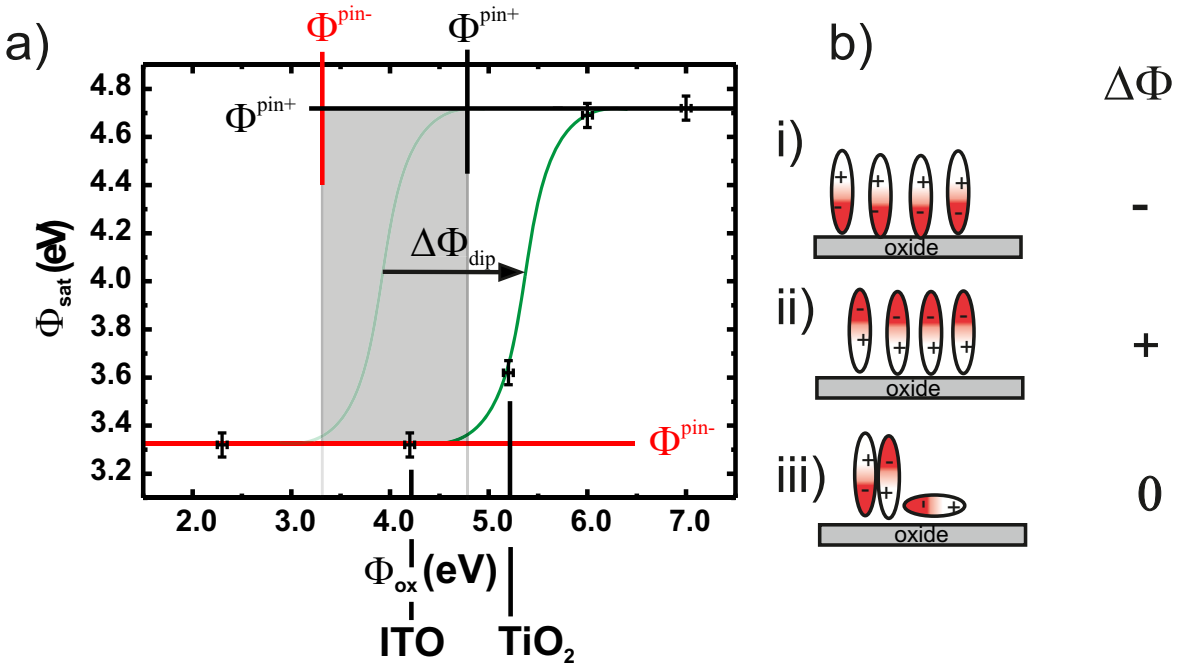

Figure 4.11.: (a) Φ_{sat} measured for thick films of **1** as function of pristine substrate Φ_{ox}. The region, where critical substrate Φ_{ox} values for pinning and Φ_{sat} values are expected to coincide (and where vacuum-level alignment is typically observed), is shaded in gray. For **1**, this region is shifted (arrow) by ca. 1 eV to higher Φ_{ox} values. This is attributed to the preferential orientation of the molecular dipole moments that cause a shift $\Delta\Phi_{dip}$. (b) Effect of the preferential orientation of molecular dipole moments on $\Delta\Phi_{dip}$.

found to generally amount to $\Delta\Phi_{PB} \approx 0.3$ eV for organic materials deposited on oxides.[WFS+13] [37] Apparently, this value is much smaller than the obtained $\Delta\Phi$-values [see Fig. 4.9(b-c)] and therefore cannot be the sole cause. In addition, one needs to consider a preferential orientation of the molecular dipoles of **1** in the monolayer (ML), leading to a work function change $\Delta\Phi_{dip}$. In this regard, the three limiting cases of possible dipole moment orientations within the ML can be considered: The electron poor (rich) part faces the vacuum side, inducing a Φ decrease (increase) [see Fig. 4.11(b, i) and (b,ii)]. If instead all molecules are lying on the surface, or if they form dimers with anti-parallel orientation of dipoles (known to often be the case for merocyanines[153,280]) $\Delta\Phi$ yields zero [see Fig. 4.11(b, iii)]. It is now important to recall that the electron-withdrawing carbonyl and/or cyano groups can act as anchoring groups as they are known to form weak coordination bonds to metal atoms.[112,138,281] This anchoring induces a vertical orientation of the intermolecular dipole moment in the monolayer, with the negative pole pointing towards the metal-oxide surface [situation (i) in Fig 4.11(b)], which reduces Φ.

To estimate the contribution of the oriented dipole moments $\Delta\Phi_{dip}$ to the total interface dipole $\Delta\Phi$, the Helmholtz equation was used assuming a compact layer of vertically aligned **1** molecules,

$$\Delta\Phi_{dip} = \frac{e n_D \mu_\perp}{\epsilon_r \epsilon_0} \tag{4.1}$$

where e is the elementary charge and ϵ_0 is the vacuum permittivity. One further uses a packing density $n_D = 2 * 10^{14}\ cm^{-2}$ [189], a relative permittivity of $\epsilon_r = 3$ of the ML, and the vertical contribution of the intramolecular dipole moment $\mu_\perp$= 3.8 D [153]. Accordingly, $\Delta\Phi_{dip}$ was found to be $\sim$ -1 eV. Taking into account both already mentioned contributions, i.e., $\Delta\Phi_{PB}$ and $\Delta\Phi_{dip}$, Φ_{ox} of pristine TiO_2 (5.25 eV) can be reduced to 3.95 eV due to the deposition of a ML of **1**. This value is in the range of - but still higher than - the measured Φ_{sat} of 3.60 eV. However, obviously a further contribution is involved, which most likely results from the chemical coordination [112,138,281] of **1** to the TiO_2 surface. This leads to an overall $\Delta\Phi$ of -1.65 eV, which is assumed to be equal for all investigated substrates from first approximation as long as pinning-induced charge transfer does not occur in addition.

Noteworthy is the fact that in the case of ITO this overall $\Delta\Phi$ is too large to explain the actually observed -0.95 eV work function shift. $\Delta\Phi$ for ITO may well differ because of different molecular tilting (thus changes of $\mu_\perp$), less dense packing, or different chemical coordination. As in this case Φ_{sat} coincides exactly with the Φ_{sat}-value obtained for Sm_2O_3, oxide-to-organic charge transfer is obviously involved. This charge transfer counteracts the interface dipole contribution of $\Delta\Phi_{dip}$ and thus limits the magnitude of the observable work function shift. [126].

Summarizing, the critical work function value at which LUMO-pinning sets in (Φ^{pin-}) is at least 0.95 eV higher than the Φ_{sat} value in a LUMO-pinned situation. On the other hand, E_F-pinning of the HOMO level was ruled out at the **1**/TiO_2-interface (Φ_{ox} = 5.25 eV). Instead one observes E_F-pinning of the HOMO level for Φ_{ox} = 6.0 eV (MoO_3_cl). Therefore, the critical value at which HOMO-pinning sets in (Φ^{pin+}) is at most 1.3 eV higher than the Φ_{sat} value found for the clear HOMO-pinned situation. Accordingly, the observed delay of E_F-pinning can be determined to be between 0.95-1.3 eV.

The main cause for this delayed E_F-pinning is the preferential orientation of molecules on the oxide surfaces, which reduces the effective work function by ca. 1.0 eV compared to the pristine surfaces. This situation is somewhat reminiscent of molecules deposited on atomically clean metal surfaces, where the push-back effect (in the absence of chemical bonding of the molecules) lowers the effective

work function "seen" by the molecules, and also leads to a "delayed" E_F-pinning.[44]

Evolution of the Ionization Energy

Having established that the dipolar layer formation has a tremendous impact on the occurrence of E_F-pinning, the question arises in what manner the pinning-induced charge transfer has an impact on the properties of the formed organic layer. This question particularly addresses the exact nature of excess charge arrangement (localization or delocalization) within this layer. To do so, Fig. 4.8(b) is reconsidered. Recalling the fact that the thick film's IE has been determined to be 5.50 eV on every employed substrate, it is now necessary to turn to the low Θ-regime from monolayer to thick film coverage.†.

The evolution of **1**'s IE is depicted in Fig. 4.12(a) as result of employing the simple relation:

$$IE_{film} = \Phi_{film} + \Delta_{h,film} \tag{4.2}$$

IE_{film} values still change beyond monolayer formation, which was determined at about 8 Å in coincidence with the saturated work function value. To explain the observed ionization energy changes, it is possible to invoke a molecular reorientation of the organic layer from first to multilayer. Indeed, turning the dipolar orientation from situation (i.) to situation (ii.) in Fig. 4.11, the experimental accessible ionization energy changes in accordance with the observed work-function change[38,163] (see section 2.2.3). As, however, the chemical coordination between the merocyanine's acceptor unit and the metal-oxide surface essentially determines the orientation of the molecules to be similar on all employed metal-oxide substrates, the evolution of the ionization energy for **1** deposited on the various metal oxides should be similar as well.

In contrast, however, one finds rather different ionization energy evolutions on the different metal oxides. For instance, the increase in IE of **1** deposited on Sm_2O_3 is found to be significantly larger than that for **1**/ITO and even larger than for **1**/TiO_2. This is somehow contradictory if considering a similar orientation dependence that is independent of the metal oxide. Therefore, it is necessary to invoke another effect: the charge transfer.

At the **1**/Sm_2O_3-interface, E_F-pinning at the dye's LUMO was deduced to occur. Accordingly, the molecular monolayer is doped with electrons.[NAW+12] On the other hand, one finds E_F-pinning of the molecular's HOMO at the **1**/MoO_3_cl-interface and due to that hole-doping of the molecular film.

† Note that below monolayer-formation the determination of an ionization energy is not appropriate, because the work function is an average value comprising covered and uncovered surface areas.(see section 4.3.1 for a comprehensive discussion)

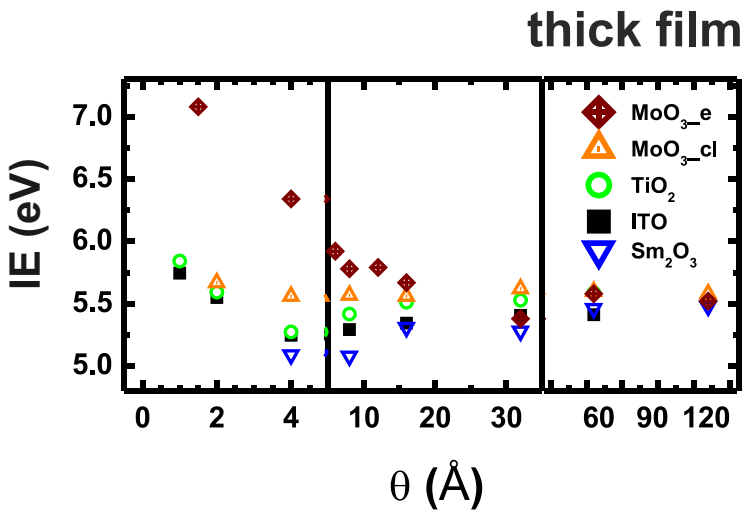

Figure 4.12.: Evolution of the IE depending on the nominal film thickness (Θ) of **1** on Sm_2O_3 (blue triangles down), ITO (black squares), TiO_2(111) (green circles), MoO_3_cl (orange triangle up) and MoO_3_e (wine diamonds). The middel panel in particular shows the evolution of the IP between monolayer- and multilayer-formation.

In this context, intercalated doped molecular films with strong electron acceptor materials (e.g. MoO_3, acceptors[32,282]) or strong electron donors (alkali atoms[283]) as dopants are invoked. Here, the host matrix's IE is found to be dependent on the doping degree. In these studies, the IEs are systematically found to decrease upon "electron doping" and to increase for "hole doping".
Obviously, the energy to remove an electron from a system comprising excess electrons is smaller than from a neutral one. In analogy, one finds the energy required for ionization of a system comprising excess holes to be larger than for a neutral one.
And indeed, as depicted in Fig. 4.13, one finds a linear relation between IE_{film} of various film thicknesses and Φ_{ox}, which is indicative of the strength of the E_F-Pinning situation from LUMO-pinning (electron-doping) to HOMO-pinning (hole-doping) via vacuum-level alignment (no doping). Moreover, the slope of this linear relation decreases with increasing dye-film-thickness to zero to establish a Φ_{ox} independent IE of the merocyanine bulk of 5.5 eV, as depicted in Fig. 4.12. This clearly indicates that the effect is related to an interface phenomenon.
On the basis of single molecular units, the experimental observation can be rationalized by invoking the on-site Coulomb repulsion (see section 1.1.1). Regarding this, one would experimentally probe neutral molecules providing a certain ionization energy next to charged molecules providing a different ionization energy. Moreover, it is reasonable to consider: The larger the electron (hole)-excess, i.e. the stronger the specific pinning situation, in the molecular film, the more dominant is the spectral contribution of the charged molecules. Despite the fact

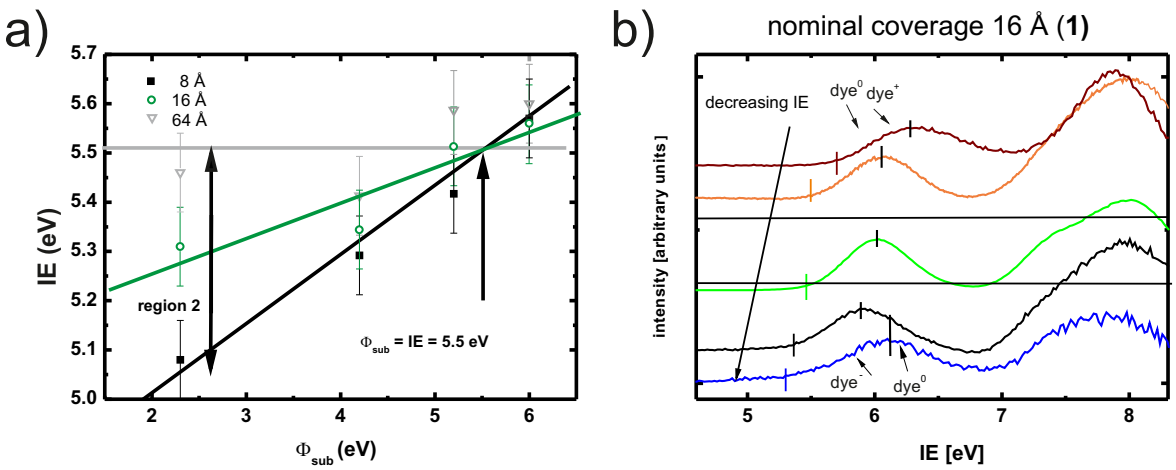

Figure 4.13.: (a) A linear increase of the organic thin film's IE in dependence of the pristine substrate work function Φ_{ox}. The observed slope is decreasing with increasing film -thickness (8 Å, 16 Å) down to S=0 for a thick film (120 Å), representing the bulk IE fo 5.5 eV. (b) valence-level signature for a 16 Å nominal film thickness as obtained for the different employed substrates and referenced to E_{vac}. The sharpest HOMO feature is obtained for the non E_F-pinned situation $\mathbf{1}/TiO_2$-interface. The pronounced broadening for the HOMO-features in both (HOMO and LUMO)-pinning situations indicates the coexistence of charged (dye$^+$/dye$^-$) and neutral (dye^0) molecules.

that individual spectral contributions cannot be properly resolved, as depicted in Fig. 4.12(b), Coulomb repulsion should be taken into account when discussing electron or hole-doped thin films. On the one hand, one finds a pronounced broadening of **1**'s HOMO-feature of a nominal 16 Å film, which indicates the presence of splitting into two HOMO-features in the case of HOMO-Pinning (dye$^+$ and dye^0) and for LUMO-Pinning (dye$^-$ and dye^0) and is attributed to both the charged and neutral molecules, respectively (see chapter 5 for more details). Unfortunately, this assignment suffers from the limited UPS-resolution.

Molecular dipole strength

To investigate the influence of the dipole moment magnitude on the energy-level alignment, the series of merocyanines was extended by **2**-**4** with the molecular dipole moment now covering the range from 3.8 D to 13.3 D. The most application-relevant metal oxides ITO and TiO_2 were chosen as substrates.
The thickness-dependent evolutions of Φ when depositing **1**-**4** on TiO_2 and ITO are shown in Fig. 4.14, along with the corresponding energy-level diagrams. Upon deposition of the different merocyanines, Φ saturates at different mass-thicknesses. This is most likely related to different growth modes of the different merocyanines, which provide a decreasing planarity of their molecular structure with increasing dipole moments (see Fig. 4.22 in section 4.3.2). Nevertheless,

it is striking that the Φ_{sat} values are very similar for all molecules on ITO (Φ_{sat}= 3.35-3.50 eV) and slightly higher on TiO_2 (Φ_{sat}=3.60-3.85 eV). Indeed, no apparent correlation of Φ_{sat} to the magnitude of the molecular dipole moment can be found. Based on the knowledge obtained in the previous discussion, one suggests that E_F-pinning at the molecules' LUMO occurs on ITO for all **1**-**4** merocyanines and furthermore that no E_F-pinning occurs on TiO_2. The fact that no correlation was found between the molecular dipole moment and the final work function in the case of E_F-pinning (ITO) can be understood from the fact that electronic equilibrium needs to be established and the impact of

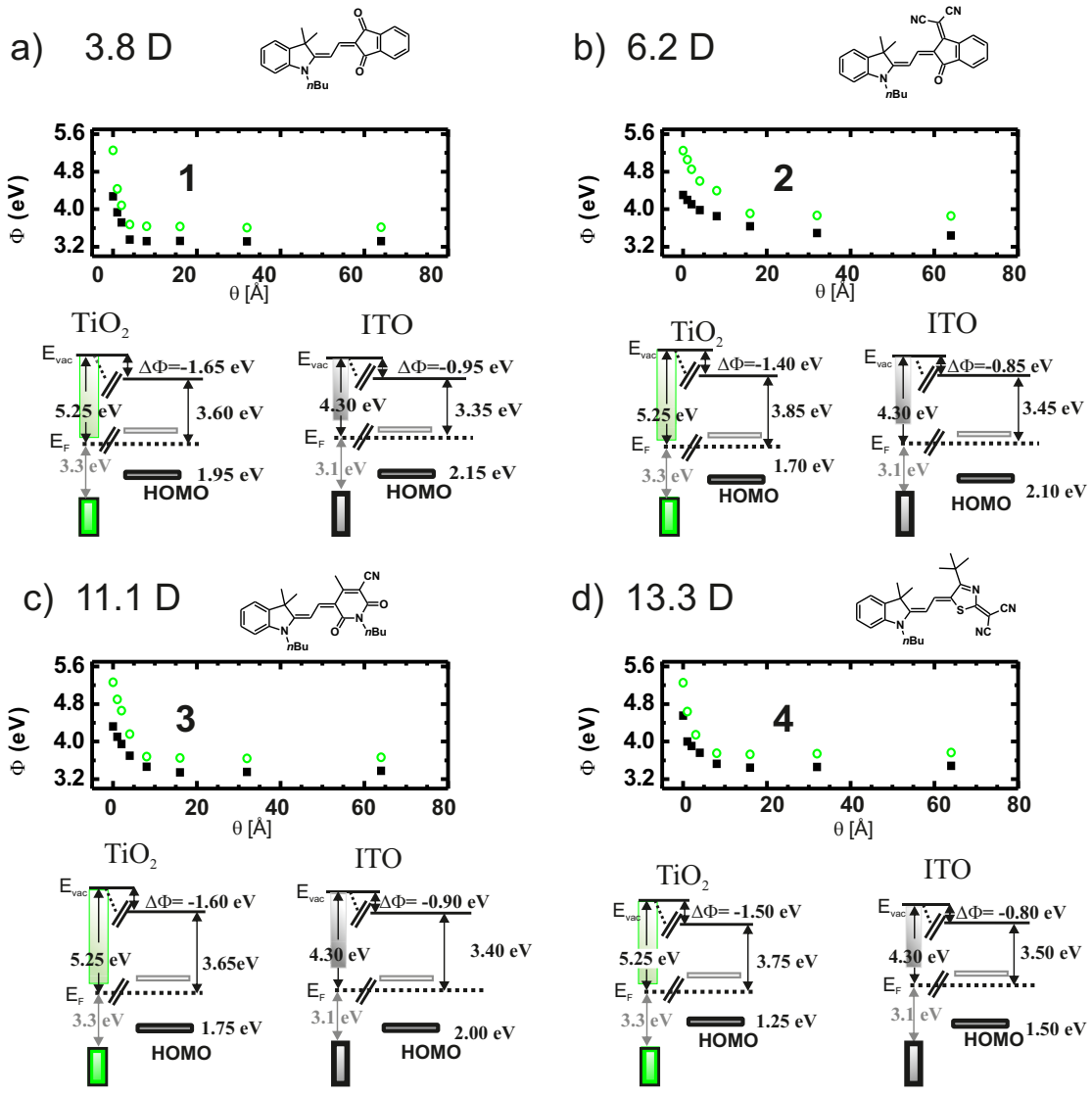

Figure 4.14.: Φ-evolution in dependence of the film coverage on ITO (black squares, band gap: 4.0 eV[249]) and TiO_2(111)-surface (green circles, band gap: 3.4 eV[247]) for the merocyanine dyes (a) **1**, (b) **2**, (c) **3**, and **4**. In conjunction the energy-level schemes are provided, where the molecules' optical gaps 2.23 eV, 1.90 eV, 2.10 eV and 1.75 eV were used to provide the LUMO-positions.[153]

$\Delta\Phi_{dip}$ (and accordingly the impact of the molecular dipole moment) becomes negligible.[126] For the merocyanine/TiO_2-interface, at which E_F-pinning is ruled out, the absence of any correlation to the dipole strength may be attributed to an increasing dimerization tendency[153,177,189,280] of the molecules. This dimerization tendency increases with increasing dipole moment and is suggested to counteract the substrate-anchoring induced arrangement of the molecules as a dipolar layer already in the monolayer. Also, molecules with larger molecular dipole moments may have an increasing tendency to lie flat on the oxides, which would reduce the magnitude of $\Delta\Phi_{dip}$ as well.

4.3. Three-Layered Structure

Designing hybrid heterojunctions for efficient charge injection in organic (opto-) electronic devices requires control of the energy-level alignment at interfaces. To ensure a proper matching of the electrode's Fermi level (E_F) to the charge transport levels of the organic semiconductor,[41,42,45] electrode materials are chosen in a way to minimize that mismatch.
In this regard, section 4.2 dealt with the employment of different electrode materials, whose appropriate choice facilitates the establishment of E_F-pinning of the molecule's HOMO or LUMO level, respectively.
Sticking instead to a specific electrode material, the use of thin interlayers that introduce tailored interface dipoles is considered as a strategy to establish E_F-pinning and thusly proper matching of (E_F) with the respective frontier orbital. Based on the previous sections, it is reasonable to make use of the pronounced interface dipoles, when employing either molecular acceptors or merocyanines providing strong intramolecular dipole moments. By insertion of these material interlayers, one can substantially alter the energy-level alignment at organic/metal-oxide (here: α-NPD/ITO) interfaces.
The impact of the modified electrode-Φ on the energy-level alignment of subsequently deposited organic materials is discussed exploring the limit(s) of the interval $[\Phi^{pin-}, \Phi^{pin+}]$, beyond which E_F-Pinning sets in. The work function at which E_F-pinning sets in is in principle an intrinsic material parameter. However, for one organic semiconductor often different values for pinning have been reported.[284] For organic/metal-oxide interfaces, for example, this is linked to the occurrence of interface dipoles, as discussed in the previous section.
Nevertheless, research on E_F-pinning in organic semiconductors has started only quite recently, and more than one mechanism may be at work to determine the energetics of pinning, and thus more detailed information about the relation between substrate work function and energy-level pinning is needed. Consequently,

this has motivated the following study.

4.3.1. α-NPD/Acceptor/Metal Oxide

One way to adjust the work function Φ_{sub} prior to subsequent material deposition to an optimal value is to use thin interlayers of strong molecular acceptors[45] (donors[108]) that form tailored interface dipoles to increase (decrease) Φ_{sub}. In doing so, one can significantly alter the level alignment towards any organic semiconductor on top of these interlayers, and therefore the charge-injection properties at the interface. On metals, Φ_{sub} increases upon the deposition of an acceptor, such as F_4TCNQ[259,285] or HATCN[260]. Likewise, acceptors like F_4TCNQ can also be used to increase the work function of conductive oxides, such as indium-tin-oxide (ITO).[286] [CWB+14]
To investigate in detail the transition point between vacuum-level alignment and E_F-pinning at Φ^{pin+}, varying molecular acceptor coverages Θ_{acc} (for both HATCN and F_4TCNQ) were employed to increase Φ_{sub} incrementally.

Determination of Φ^{pin+}

Subsequent deposition of 5 nm (corresponding to about 5 layers) thick films of α-NPD on interlayers comprising of either a full layer of F_4TCNQ or HATCN, the HOMO-onset of multilayer α-NPD is found to be pinned 0.5 eV below E_F and

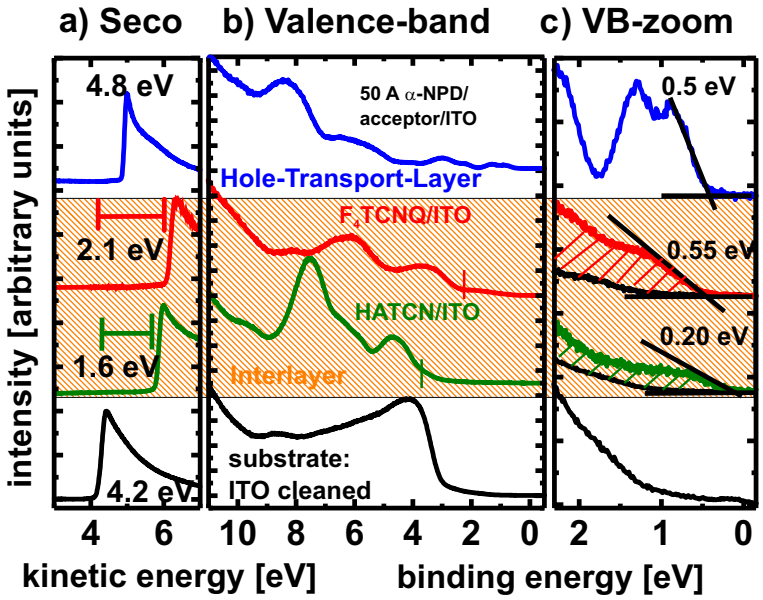

Figure 4.15.: (a) SECO, (b) valence-level spectra and (c) zoom into the near E_F-region of the investigated heterostructure comprising ITO, an interlayer (HATCN or F_FTCNQ) and subsequently deposited α-NPD.

a saturated work function $\Phi_{\alpha-NPD}$ of 4.8 eV is measured, as deduced from the spectrum in the top panel of Fig. 4.15(a-c). Assuming vacuum-level alignment, pinning is thus expected to set in at Φ_{sub} of 4.8 eV, as also reported in other studies.[255] Consequently, with each of the molecular acceptor precovered (varying from zero to one full monolayer) ITO substrates, introduced in section 4.2.2 (Fig. 4.7), one can access the range of interest around Φ^{pin+}=4.8 eV. This is the expected transition value to drive α-NPD from vacuum-level alignment to E_F-pinning.
Fig. 4.16(b) displays the work function of such thick α-NPD films ($\Phi_{\alpha-NPD}$) as well as its HOMO-onset position (E_{HOMO}) as a function of the effective work function Φ_{sub} of the acceptor pre-covered substrate. When depositing α-NPD on bare ITO the work function is found to be reduced by 0.3 eV to a saturated value of $\Phi_{\alpha-NPD} = 3.9$ eV. This interface dipole has already been attributed to the pushback effect,[37] as referred to in section 4.2.1. α-NPD HOMO-onset is found at 1.4 eV binding energy (BE). The sum of both values yields an ionization energy of 5.3 eV for α-NPD. An increase of Φ_{sub} rigidly shifts the α-NPD HOMO to lower BE until pinning sets in. From there on, α-NPD HOMO-onset is pinned 0.5 eV below E_F, with a final work function $\Phi_{\alpha-NPD}$ of 4.8 eV. Even if these saturated values show excellent agreement with the results obtained for depositing α-NPD on a multitude of different substrates (contaminated electrodes, conductive polymers) covering a wide interval of Φ_{sub},[255] Φ^{pin+} is strikingly found to be at 5.2 eV and thusly larger than expected, as depicted in Fig. 4.16(a). This strongly indicates that an interface dipole is at play. To explain this discrepancy of 0.4 eV, a model is involved, which takes into account the non-uniformity of the acceptor pre-covered substrate (comprising coexisting covered and uncovered areas next to each other) as well as the pushback effect of α-NPD on bare ITO. In essence, this model considers the different local work function on bare ITO and acceptor-covered ITO surface patches, which together yield the surface averaged effective Φ_{sub}.

As a prerequisite first the two limiting cases of uniform surfaces are discussed, i.e., (i) zero and (ii) full acceptor coverage, as illustrated in Fig. 4.16(b, i & ii).

i. When depositing α-NPD on bare ITO with pristine ITO work function (Φ_{ITO}) of 4.2 eV the work function is reduced by 0.3 eV [triangle, Fig. 4.16(a)], which is attributed to the pushback effect.[37]

ii. For the acceptor monolayers (HATCN/F_4TCNQ: Φ_{sub} = 5.8 eV/6.3 eV) the α-NPD-HOMO onset pins at 0.5 eV BE and the work function is reduced by 1.0 eV/1.5 eV.

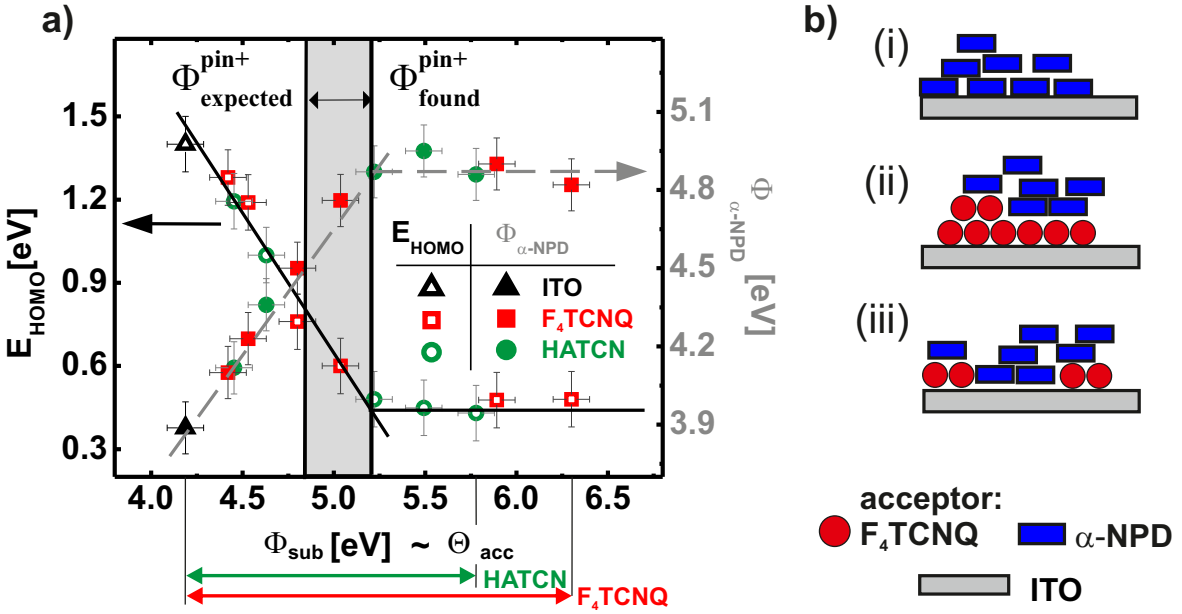

Figure 4.16.: (a) Evolution of the HOMO-onset BE for nominal 5 nm thick α-NPD-films and the sample work function $\Phi_{\alpha-NPD}$ as a function of Φ_{sub}. To adjust Φ_{sub}, different Θ_{acc} has been used, as referred to in Fig. 4.7. E_F-pinning occurs at 0.4 eV higher initial work function ($\Phi_{sub} = \Phi^{pin+} = 5.2$ eV) than initially expected (4.8 eV). (b) Illustration of the different (modified) ITO samples serving as substrates for subsequent α-NPD-deposition: the limiting cases (i) zero and (ii) full acceptor coverage, as well as (iii) the intermediate case of acceptor-submonolayer coverage.

For the intermediate effective substrate work function cases, i.e. α-NPD on submonolayers of acceptor molecules, some of the deposited α-NPD molecules adsorb on bare ITO as well as on top of the acceptor molecules, as illustrated in Fig. 4.16(b,iii). The fraction of α-NPD molecules sticking directly on ITO causes the pushback effect. The second process involved is electron transfer from those α-NPD molecules that reside on acceptor molecules, as the local work function there is already beyond that needed for pinning.

For the relative contribution of both processes to the overall work function change, the growth mode governs the quantitative behavior. For instance, in case of large coexisting domains of bare ITO and acceptor-covered areas, α-NPD molecules in the second layer would align either to the local low ITO-related work function or the local high work function related to acceptor-covered patches, as indicated in Fig. 4.17(a). As a result one would observe a superposition of two differently aligned α-NPD species. If, on the other hand, acceptors adsorb on ITO in a "hit-and-stick" fashion, i.e., bare and acceptor-covered ITO areas coexist on a molecular length scale, see Fig. 4.17(b), the second layer of α-NPD already aligns to the averaged work function of the first mixed layer.[24,166,167,267] As depicted in Fig. 4.17(c), the spectral shape variations of the α-NPD-HOMO as a function of Φ_{sub} (and Θ_{acc} likewise) are negligible. Consequently local work function

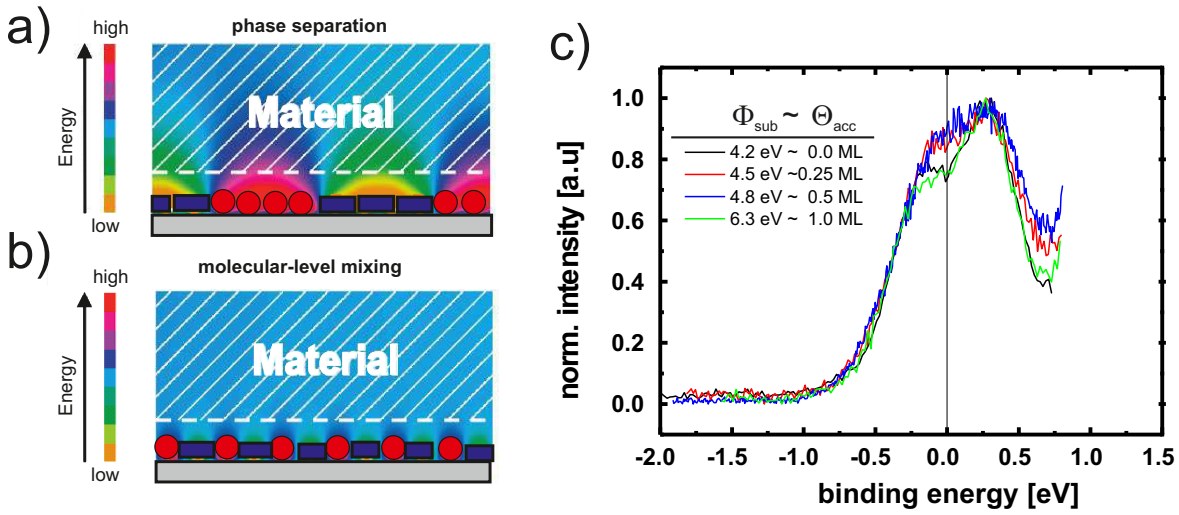

Figure 4.17.: Illustration of the energy-level alignment, if the precovered substrate consists of (a) phase-separated large patches of acceptor-covered and uncovered areas (b) bare and acceptor-covered areas mixed on a molecular length scale. (c) Spectral shape variations of the HOMO emission of about 1 layer α-NPD depending on $\Phi_{sub}(\sim \Theta_{acc})$. All spectra are aligned to each other to demonstrate the difference/similarity. Although a slight broadening for values close to $\Phi^{pin+} \sim \Theta_{acc} = 0.5$ ML can be found, there is no indication of differently aligned α-NPD species, which confirms a uniform acceptor distribution on a molecular length scale. [(a) and (b) are adapted from Ref.[167].]

variations of acceptor-covered and bare ITO patches are assumed to occur on a molecular length scale, according to the illustration in Fig. 4.17(b).
Summing up, two effects are at play when depositing α-NPD on incomplete acceptor layers: the work function shift due to α-NPD E_F-pinning $\Delta\Phi_{pin}$ on acceptor-covered areas and the remaining pushback effect (PB_{rem}) on bare ITO, whose relative contributions to the overall work function shift depend on Θ_{acc}. PB_{rem}, caused by the α-NPD molecules adsorbing on ITO areas not covered by acceptor molecules, should thus be the origin of the delayed set-in of E_F-pinning, as observed in Fig. 4.16(a).

Modeling the Dependence of Φ^{pin+} on Θ_{acc}

To test the proposition of the interplay of $\Delta\Phi_{PB}$ and $\Delta\Phi_{pin}$ upon α-NPD-deposition, a simple model is applied, which is based on electrostatics and assumes electronic equilibrium between the different layers.[37,287] To account for PB_{rem}, a linear correlation between acceptor coverage and pushback is assumed up to a maximum value of $\Delta\Phi_{PB}$=0.3 eV (as derived from α-NPD on bare ITO). This is justified by the almost linear dependence of Φ_{sub} on Θ_{acc} in Fig. 4.7(a) and thus PB_{rem} yields: $PB_{rem} = (1 - \Theta_{acc})\Delta\Phi_{PB}$.
The work function change upon α-NPD-deposition ($\Delta\Phi_{\alpha-NPD}$) is the sum of the work function change due to pinning ($\Delta\Phi_{pin}$) and the remaining pushback

(PB_{rem}):

$$\Delta\Phi_{\alpha-NPD} = \Delta\Phi_{pin} + PB_{rem} \tag{4.3}$$

$\Delta\Phi_{pin}$ at submonolayer acceptor coverages is the only experimentally inaccessible parameter, but depends on the number of electrons Q transferred (due to E_F-pinning) from the α-NPD layer to the substrate, related via the Helmholtz equation:

$$\Delta\Phi_{pin} = \frac{Qed}{\epsilon_r} \tag{4.4}$$

where d = 0.3 nm is used as the thickness of one organic layer, e the elementary charge, and ϵ_r=3.35 [276] as relative permittivity. At the premises of electronic equilibrium the number of charges itself is given by Fermi-Dirac statistics:

$$Q = \frac{en_D}{1 + exp(E_{HOMO}/(k_B T))} \tag{4.5}$$

where n_D is the number density of molecules per layer, T the temperature, k_B the Boltzmann constant, and E_{HOMO} the final α-NPD HOMO-onset position.
As a last step, the final α-NPD HOMO-onset position is given by its initial position before adsorption (which is the effective work function of the substrate minus the ionisation energy of α-NPD) minus the total work function change $\Delta\Phi_{\alpha-NPD}$:

$$E_{HOMO} = \Phi_{sub} - IE - \Delta\Phi_{\alpha_{NPD}}. \tag{4.6}$$

Also for Φ_{sub} the acceptor pre-coverage has to be taken into account with $\Phi_{sub} = \Phi_{ITO} + \Theta_{acc}\Delta\Phi_{acc}$, where Φ_{ITO} is the work function of bare ITO and $\Theta_{acc}\Delta\Phi_{acc}$ is the coverage-dependent fraction of work function increase induced by a full acceptor monolayer ($\Delta\Phi_{acc}$).
Inserting eq.(4.6) in eq.(4.5) and combining with eq.(4.4), one can solve for $\Delta\Phi_{pin}$ (and $\Delta\Phi_{\alpha-NPD}$ likewise according to eq.(4.3)) self consistently.

$$\frac{en}{1 + exp(\frac{\Phi_{sub} - IE - (\Delta\Phi_{pin} + PB_{rem})}{(k_B T)})} = \frac{\Delta\Phi_{pin}\epsilon_r}{ed} \tag{4.7}$$

In comparison to the corresponding experimental data in Fig. 4.18 (a), the results of this model are plotted in Fig. 4.18(b) for multilayer α-NPD as a function of Θ_{acc} (which is also proportional to Φ_{sub}). The contributions of PB_{rem} and $\Delta\Phi_{pin}$ are depicted separately. Increasing Θ_{acc} ($\sim \Phi_{sub}$), and therefore reducing the bare ITO area, leads to a linear decrease of $\Delta\Phi_{\alpha-NPD}$, which originates from the remaining pushback effect. It dominates as long as Φ^{pin+} is not reached. When the effective Φ_{sub} exceeds Φ^{pin+} the pinning induced interface

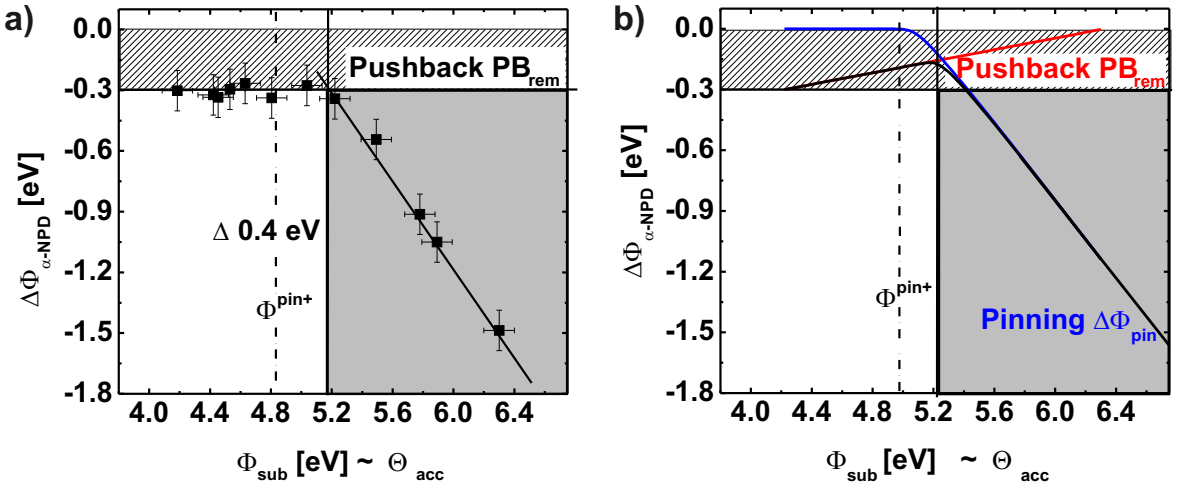

Figure 4.18.: (a) Evolution of $\Delta\Phi_{\alpha-NPD}$ of a 5 nm thick α-NPD film as a function of Φ_{sub}. A constant shift of 0.3 eV persists until pinning is established. (b) The modeled evolution of a thick α-NPD film as a function of Φ_{sub} comprises the contributions $\Delta\Phi_{pin}$ (blue line) and PB_{rem} (red line).

dipole $\Delta\Phi_{pin}$ starts to overcompensate the pushback effect and dominates for higher Φ_{sub}. The offset between the fundamental Φ^{pin+} and the effective Φ_{sub} at which pinning is observed experimentally (0.4 eV in the present case) can be reconciled by comparing $\Delta\Phi_{\alpha-NPD}$ (including the pushback contribution) with $\Delta\Phi_{pin}$ (no pushback contributions). This clearly shows that the origin of the delayed E_F-pinning for acceptor-submonolayer coverages is caused by the remaining pushback effect of α-NPD. The competing effects that contribute to effective work-function changes at non-uniform substrates must therefore be carefully included in the discussion and quantification of E_F-pinning for such organic semiconductor interfaces. This is of particular relevance to real devices. Here the surfaces are generally affected by local inhomogeneities due to unavoidable contaminations caused by e.g. the process of solvent-preparation. In this regard, the following paragraph deals with the comparison between the amount of the mentioned interfacial effects ($\Delta\Phi_{pin}$ and $\Delta\Phi_{PB}$) at UHV-cleaned and solvent-cleaned surfaces.

Contaminated Substrates

In comparison to the UHV-cleaned ITO surfaces, which have been considered so far, solvent-processed ITO substrates need to be regarded as contaminated substrates, whose surface needs to be considered to be non-uniform.

- At the α-NPD/contaminated-ITO surface $\Delta\Phi_{\alpha-NPD}$=0 was obtained. This is assigned to vacuum-level alignment and in total agreement with the

findings of vacuum-level alignment observed for organic semiconductors deposited on ambient-contaminated metals and conductive oxides.[101] Indeed one repeatedly finds a work function of 3.9 eV for solvent-cleaned (contaminated) ITO surfaces, strongly indicating that the pristine UHV-cleaned surface with $\Phi_{ox} = 4.2$ eV, is already covered by an undefined layer, which has already induced the pushback effect. The interface between an organic layer deposited on such a contamination layer, i.e. "sealing" layer, is quite non-interacting and thus vacuum-level alignment is established.

- At the F_4TCNQ/contaminated ITO-surface, one finds the amount of work function increase to be rather reduced (by $\sim$ 1.1 eV) compared to that obtained at the pristine ITO-surface (2.1 eV), as depicted in Fig. 4.19(a).

Accordingly, the comparison between interfacial phenomena regarding pristine and contamined ITO-surfaces reveals that any substrate-molecule interaction is significantly reduced due to the presence of an (in)complete "sealing" contamination-interlayer that inhibits the interfacial phenomena to occur to its full amount. Obviously, Δ_{PB} is totally surpressed.
On the other hand, the driving force to establish electronic equilibrium at the interface (E_F-pinning) is unaffected by the exact surface composition. It remains

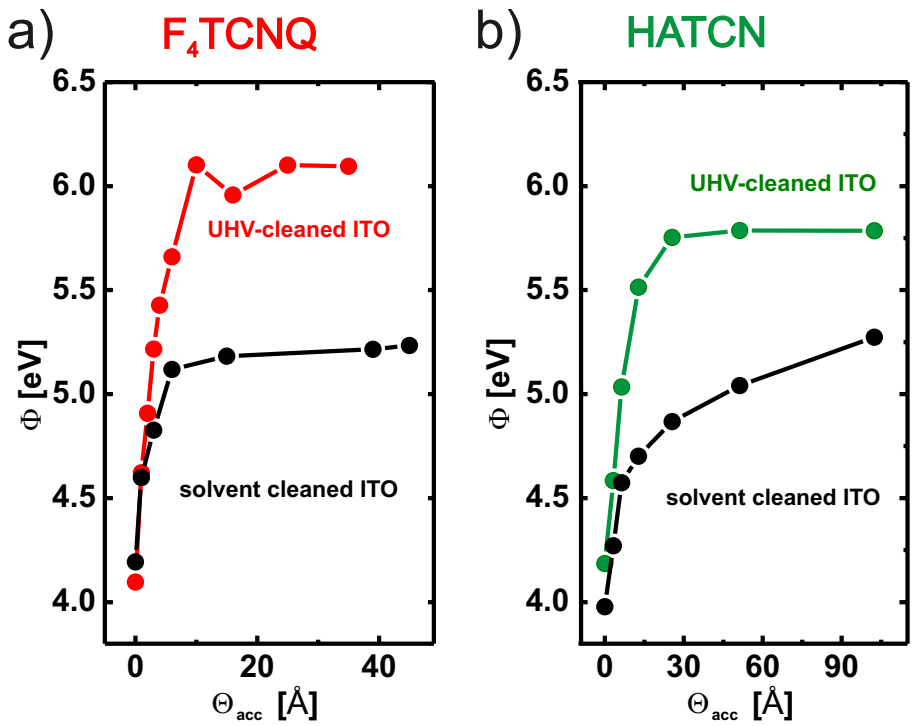

Figure 4.19.: The coverage dependent evolution of Φ is shown for acceptor deposition on proper in-situ cleaned (colour) and solvent-cleaned (black) ITO substrates. (a) F_4TCNQ and (b) HATCN.

only to question, how the electron equilibrium is established, i.e. whether a hybridisation of molecular and substrate states is involved, as referred to in section 1.2.
In this regard, the different values for $\Delta\Phi$ upon F_4TCNQ monolayer formation obtained at the pristine ITO-surface and the contaminated ITO-surface strongly indicate that the nature of interaction differs at both interfaces. Essentially, E_F-pinning cannot be the sole contribution at the pristine ITO-surface, instead a further component associated with interfacial chemistry relying on the intimate molecule-substrate contact must be involved. At the interface with the contaminated ITO-surface, intimate F_4TCNQ-substrate contact is (at least) reduced by the presence of the (in)complete sealing interlayer. This is illustrated in the top panels of Fig. 4.20, where the pristine and "reactive" substrate area is proposed to be reduced by an (in)complete contamination layer, and concomitantly the molecular-substrate interaction is reduced as well. This illustration is reminiscent of the precoverage-dependency that was observed for $\Delta\Phi_{PB}$ of α-NPD on sub-monolayer precovered ITO. Still it is not clear if the volatile and mobile F_4TCNQ molecules diffuse[218] fractionally through the sealing-layer and hence form a chemical bond (see section 3.3).

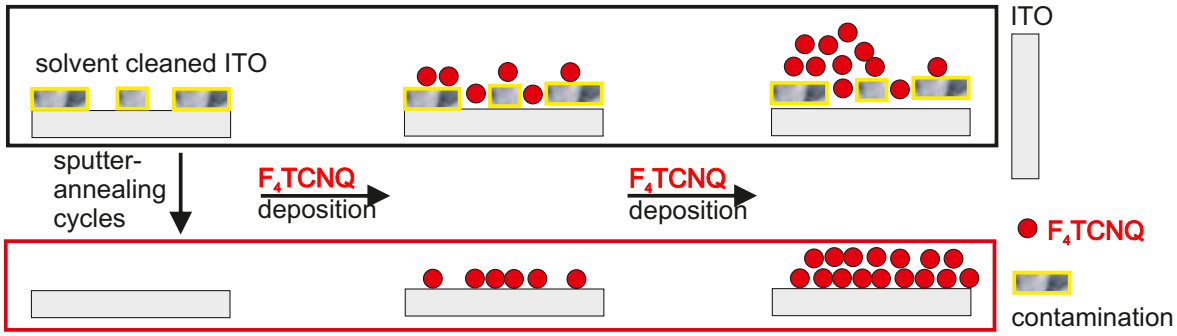

Figure 4.20.: Illustration of the suggested F_4TCNQ growth-mode on (a) *in-situ* cleaned and (b) solvent-cleaned ITO.

Notably for HATCN even $\Delta\Phi$ evolves differently on differently prepared ITO-substrates. Even for high HATCN-coverages Φ does not saturate if deposited on contaminated substrates. Related to HATCN being a high molecular acceptor, i.e. less volatile, the tendency to diffuse through the (in)complete contamination layer to the pristine ITO surface is thereby significantly reduced. Even a rather porous contamination-interlayer serves as full sealing layer due to the immobility of the HATCN molecules. Accordingly the observed $\Delta\Phi$-evolution is related to the observation of band bending, as already referred to in section 4.2 at the merocyanine **1**/ MoO_3_e-interface. At both surfaces, the contaminated ITO-surface as well as the MoO_3_e-surface, E_F-pinning is established. Beyond that,

the observation of band bending in both cases strongly suggests the absence of any mixing of molecular and substrate states, but integer charge transfer. Note that strong interactions would suppress the observation of band bending, as in that case it collapses to a localized interface dipole,[103] as referred to in section 1.2.
This reasoning highlights the importance of the exact nature of molecule-substrate interaction in the context of E_F-pinning. If simple electrostatic effects[34,103] can be ruled out as sole contribution to the observed $\Delta\Phi$-increase, as they are independent from the degree of contamination, chemisorption is to be considered, which contributes to the energy-level alignment at the interface. Due to the undefined nature of the contamination-layer concerning the aspect (in)completeness, $\Delta\Phi$ might be rather an interplay of $\Delta\Phi_{pin}$ and other contributions arising from complex and hard to quantify phenomenons related to mixing of substrate and molecular states.[HDS+13] [39]

4.3.2. α-NPD/Merocyanines/Metal-Oxide - A Device Perspective

A further possibility to adjust Φ_{sub} to a certain value is to use thin dipolar interlayers. Depending on the orientation, packing and dipole moment of the molecules forming such an interlayer, interface dipoles can be tailored. In principle, control of dipolar layer formation is facilitated by introducing substrate-anchoring groups and varying the intrinsic molecular dipole moment employing task-specific strong electron-withdrawing and -donating groups. Nevertheless, the details on molecular orientation and packing are sensitive to preparation conditions and therefore only trends can be predicted.
Regarding, however, the device perspective on merocyanine/metal-oxide interfaces, energy-level alignment is frequently predicted with respect to the simplest model of vacuum-level alignment.[189–191]
Meanwhile, the key importance for efficient charge collection at dye/electrode interfaces requires a detailed control of the energy-level alignment at those interfaces.[288–294] In consequence, the significant deviations from vacuum-level alignment, i.e. occurrence of interface dipoles (as discussed in section 4.2), have a profound impact when correlating the interface electronic properties with device performances.[189–191]
In fact, it turns out that the hole injection barrier (labelled as E_{HOMO} in Fig. 4.8) between the merocyanines HOMO and the electrode is rather high when employing ITO or TiO_2, which is in marked contrast to a-priori expectations (vacuum-level alignment) that have initially motivated the use of ITO as hole-extraction contact

for merocyanine serving as donor combined with C_{60} serving as acceptor in a heterojunction.[189]

Due to interface dipoles, which have been shown to occur at merocyanine/metal-oxide electrodes, the merocyanine/ITO interface is rendered to be favourable for electron extraction. Indeed the merocyanine's LUMO is found to be E_F-pinned. Only when substituting ITO(Φ_{ox}=4.2 eV) by a large work-function material, e.g. a MoO_3($\Phi_{ox} \geq$6 eV) interlayer, E_F-pinning at the dye's HOMO is established, resulting in a close to resonant matching with the metal oxide's E_F and thereby serving as hole-extraction electrode.

Otherwise, and also for TiO_2 (Φ_{ox}=5.3 eV), large interface dipoles result in large offsets between the dye's HOMO and the electrode's E_F. Interestingly, this means - in turn - particularly low offsets between the dye's LUMO and the electrode's E_F, which is essentially favorable for electron-extraction. This is particularly relevant for application in hybrid solar cells, e.g. dye-sensitized solar cells (DSSCs), where electrons are to be collected in the TiO_2 conduction band.[295–297]

For the ultimate single junction solar cell, the electron's energy associated to a certain open-circuit voltage (eV_{OC}) can be conceived to be equivalent to the optical bandgap.[299] In a "real" DSSCs, however, there are a manifold of losses, although only the ones related to energy-level alignment will be considered, as depicted in Fig. 4.21(a).

In analogy to the donor/acceptor heterojunction in a organic photovoltaic cell, the maximum attainable eV_{OC} at a hybrid heterojunction in a DSSCs is essentially given by the conduction band onset of the metal oxide and the HOMO level of the dye, i.e. the photovoltaic gap.[301,302] Considering the electron-extraction channel at the dye-electrode interface, a close to resonant matching of the dyes' LUMO to the metal oxide's conduction-band, i.e. the dye's LUMO to the metal oxide's E_F ($\Delta_{LUMO(D)-E_F}$) considering considerable doping ratios, is known to be favorable for the performance of a DSSC, as it exploits eV_{OC}. Considering on the other hand the dye regeneration, which is followed by the transport of holes to the back contact of the DSSCs by ions in an electrolyte, a close to-resonant matching of the dye's HOMO with the electrolyte's redox potential (e.g. I^-/I^{3-})[180,181,298,299] is essential as well. This offset has been shown to be the largest single source loss-in-potential in conventional DSSCS, and has been addressed by alternatively employing an appropriately chosen hole-transport layer in a *solid-state* DSSCs,[300,303–307] and thereby saving a few important meV.

With respect to the results in section 4.2, one can conclude that upon dye-sensitization ITO and TiO_2-surfaces are excellently suited as anode in a DSSCs regarding the energy-level alignment. In accordance to the structure of a solid-state dye-sensitized solar cell, the energy-level alignment of a subsequently

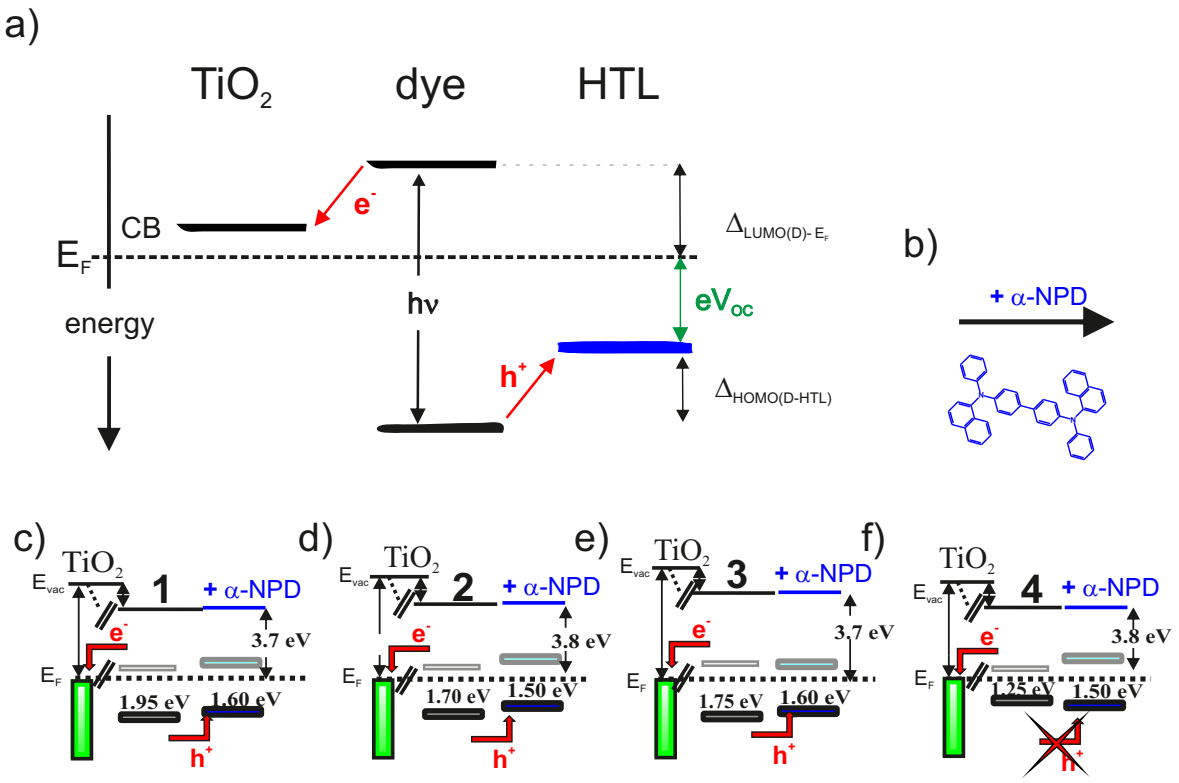

Figure 4.21.: (a) Schematic diagram of the important energy levels in a solid-state DSSC, as referred to in Refs.[298–300]: an exciton is generated ($h\nu$) on the dye and splitted by electron-transfer into the TiO_2's conduction band, i.e. E_F. This process is driven by an "overpotential" $\Delta_{LUMO(D)-E_F}$. Hole-transfer to the HTL's HOMO is driven by an "overpotential" $\Delta_{HOMO(D-HTL)}$. Accordingly the offset between TiO_2's E_F and HTL's HOMO is the estimated maximal attainable eV_{OC}.(b) illustration of the employment of subsequently deposited α-NPD as HTL on the merocyanine/metal-oxide heterojunctions depicted in Fig. 4.14. (c)-(f) full energy-level diagrams at the TiO_2/merocyanine(**1-4**)/$\alpha - NPD$ heterostructure, $\Delta_{HOMO(D-HTL)}$ and eV_{OC} values at the ITO/merocyanine(**1-4**)/$\alpha - NPD$ are summarized in Tab.4.3

deposited hole-transport material (α-NPD) is studied. In particular, this is performed for the dye-sensitization of all 4 investigated merocyanines (**1-4**) on both substrates (ITO and TiO_2) that might be suitable to be employed in such a hybrid solar cell. First of all, vacuum-level alignment is found to be established at any dye/α-NPD-interface. Therefore the offset between the dye's HOMO and that of the hole transport layer $\Delta_{HOMO(D-HTL)}$ is established to be independent of the substrate work function Φ_{ox}, as summarized in Tab.4.3.

In contrast, the estimated maximal attainable eV_{OC} - derived with respect to Fig. 4.21(a) - is shown to be particularly dependent on Φ_{ox} and significantly enhanced when employing the lower Φ_{ox} (ITO). This is a consequence of the lower Φ_{sat} value, obtained for the dye in LUMO-Pinning and according to a rigid shift of all energy levels of subsequently deposited (and vacuuum-level aligned) materials. The largest maximal attainable eV_{OC}-values can naturally be obtained

Table 4.3.: The loss-in-potential $\Delta_{HOMO(D-HTL)}$ between merocyanine and α-NPD is substrate-independent because vacuum-level alignment is established at the α-NPD/merocyanine-interface. Instead, the estimated maximal attainable eV_{OC} is dependent on the substrate work function Φ_{ox}, as this determines a further source loss-in-potential $\Delta_{LUMO(D)-E_F}$

	1 (TiO_2/ITO)	**2** (TiO_2/ITO)	**3** (TiO_2/ITO)	**4** (TiO_2/ITO)
$\Delta_{HOMO(D-HTL)}$ (eV)	0.35/0.35	0.2/0.2	0.15/0.15	-0.25/-0.25
estimated eV_{OC} (eV)	1.60/1.90	1.50/1.80	1.60/1.90	X/X

for the LUMO-pinned merocyanines **1** and **3**, which provide the largest energy gap (see Tab. 4.2) and an ionization energy only slightly larger than that of $\alpha - NPD$. This, in essence, sums up to the largest α-NPD's HOMO offset of the metal oxide's E_F in LUMO-Pinning, as illustrated in Fig. 4.21(a).

$$eV_{OC} = E_{HOMO,dye} - \Delta_{HOMO(D-HTL)} \tag{4.8}$$

If, in contrast, the $\alpha - NPD$'s IE is larger than that of the sensitizing merocyanine, as observed for **4**, the driving force for hole-transport in this hybrid solar cell is missing, as illustrated in Fig. 4.21(f).

The Role of Frontier Orbital Distribution in E_F-Pinning

In a final step, it is worth mentioning the aspect of frontier orbital distribution in the context of device architecture. Therefore it is to reconsider that HOMO pinning of the merocyanines should be favorable when combined in a typical planar or bulk heterojunction with a strong molecular acceptor. Here, they are employed either as donor in a typical donor/acceptor heterostructure or as dye-sensitizer for the underlying cathode. Aside from this, dyes can also sensitize anodes, where E_F-pinning of the LUMO would be favourable. At both the interfaces donor/acceptor and donor/cathode excitons can be generated. Depending on which channel dominates, the solar cell is termed either as heterojunction or DSSC.

It is also worth mentioning the frontier orbital distribution along the dipolar layer, i.e. the donor-unit (predominant HOMO-distribution) of the merocyanine and the acceptor-unit (predominant LUMO-distribution). Besides providing strong intramolecular dipole moments, the employed series of merocyanines is also characterized by a distinct separation of the HOMO and LUMO distribution on the molecular backbone. In general the merocyanine's HOMO is located on the donor-unit, whereas the LUMO is located predominantly on the acceptor-unit,[308] as depicted in Fig. 4.22.

Regarding a typical organic solar cell device-structure, it should additionally be

advantageous to establish large material's orbital overlap, i.e. the transfer integral t, between those particular orbitals that are involved in the respective charge transfer process. A large overlap should significantly reduce any loss-in-potentials. The largest orbital overlap should be accomplished by employing either one of the following heterostructures, illustrated in Fig. 4.23: The donor-unit (predominant HOMO-distribution) should either directly contact the cathode or the hole-transport-materials. For the acceptor unit (predominant LUMO-distribution) an orientation towards the electron-transport materials or a direct contact to the anode should be favourable.

Thus a dipolar layer, formed by anchoring the acceptor-unit on the metal oxide, is excellently arranged for dye-sensitizing an anode. The LUMO-distribution is

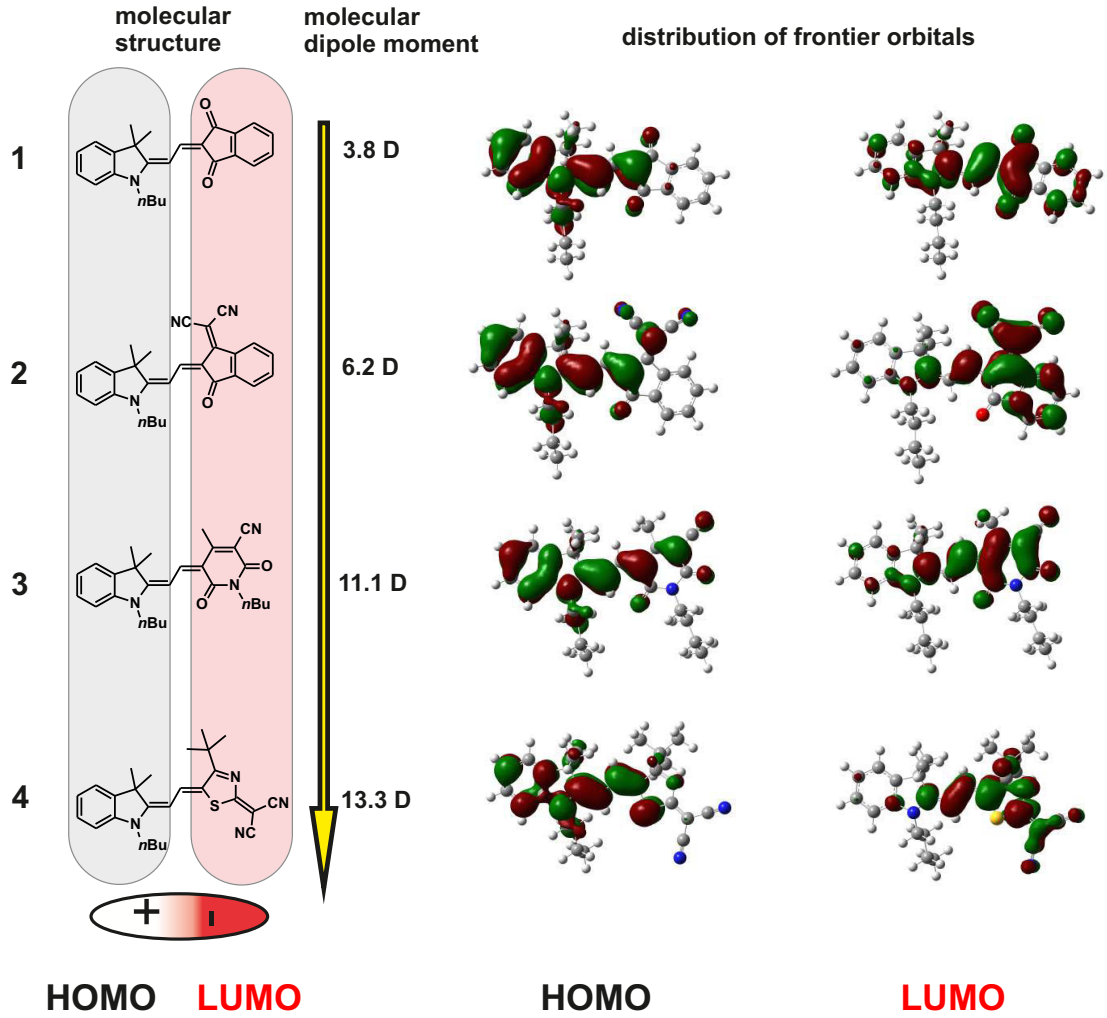

Figure 4.22.: Chemical structure of the investigated series of merocyanines **1-4** along with their intramolecular dipole moment [153]. The localization of the molecular frontier orbital distributions (HOMO and LUMO) are depicted, strongly indicating an assignment of the HOMO to the merocyanine's donor- and the LUMO to the acceptor-unit.

directly coupled to the metal oxide in order to inject electrons and the HOMO is in intimate contact to the hole-transport-material. In contrast, when using these merocyanines as donor-materials in a planar or bulk heterojunction solar cell, where holes are transferred into the metal-oxide substrate, the mentioned frontier orbital location should be disadvantageous.
Anchoring the donor-unit to the metal-oxide substrate, one would yield an improved device architecture for the mentioned donor-acceptor bulk or planar-heterojunction, combining the merocyanine with e.g. C_{60}. This configuration coincides moreover with solid-state dye-sensitization of a cathode,[295] as illustrated in Fig. 4.23(b). Unfortunately, typical anchoring-groups (oxygen, cyano,..) of a simple dipolar structure are most commonly given by the molecule's acceptor-unit and proper anchoring of the donor-unit is a synthetic issue to address in terms of an optimal design of a dye-sensitized cathode.

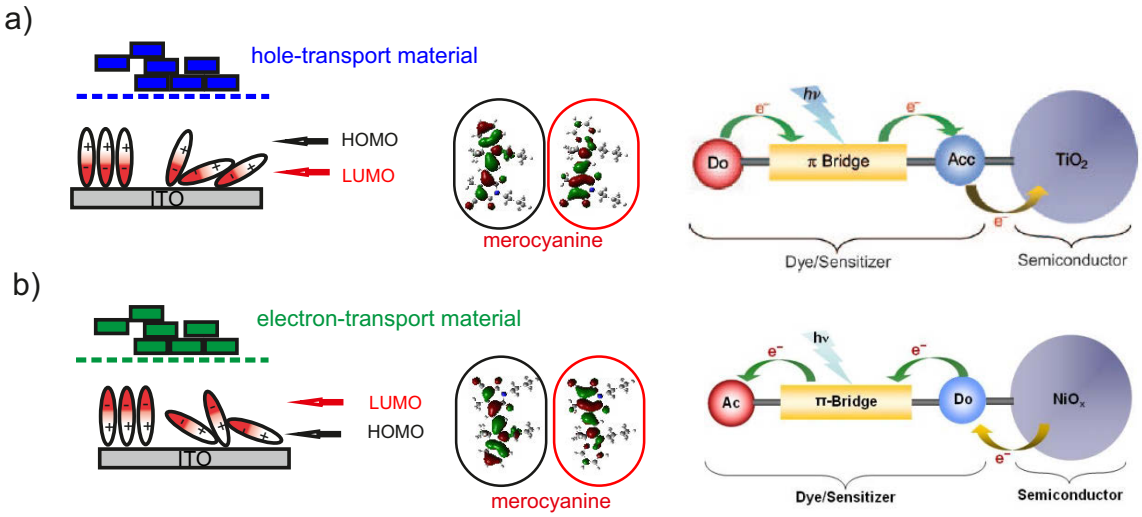

Figure 4.23.: Illustration of the aspect of frontier orbital localization concerning dye-sensitized electrodes: (a) acceptor-unit anchored to the solar cell's anode enabling the establishment of one clear defined direction for electron-transfer from (the hole-transport-material to) the donor unit across the acceptor to the anode. (b) donor-unit anchored to the solar cell's cathode enabling to establish one clear defined direction for electron transfer from the cathode across the donor to the acceptor (and electron-transport-material). (adapted from Ref.[295])

4.4. Conclusion

Employing photoemission in order to monitor the energy-level alignment at the selected organic/metal-oxide interfaces, the following conclusion can be drawn:

- Φ_{sub} can be continuously tuned between 4.2 eV and 6.3 eV as a function of strong molecular acceptor (HATCN and F_4TCNQ) coverage on ITO. Employing varying (sub)monolayer coverages of these acceptors, the HOMO-onset BE of α-NPD deposited on top of such modified electrodes can be adjusted, and pinning of the HOMO-onset is found to be 0.5 eV below E_F.

  In this regard, E_F-pinning of α-NPD's HOMO sets in at a critical substrate work function Φ^{pin+} of 5.2 eV, which is in contrast with the commonly expected Φ^{pin+} value of 4.8 eV for this particular hole-transport material. This "delayed" pinning is rationalized by taking into account the pushback effect induced by α-NPD itself, when adsorbed on bare ITO surface patches (before complete acceptor monolayer formation). This contributes to work function changes in addition to those induced by HOMO-level pinning of α-NPD, when α-NPD adsorbs on acceptor-covered surface patches. The overall behavior of the work function is successfully described with an electrostatic model that accounts for both mechanisms that change the work function upon α-NPD deposition on a non-uniform substrate, i.e. a mixture of acceptor-covered and uncovered ITO patches. The superposition of local work function values of dissimilar surface areas can fully explain the "delayed" pinning, which, with a value of 0.4 eV in the present case, can be substantial.

  Moreover, the gained insights are applied on interface formations at contaminated substrates. Here, contaminations can be treated as "sealing" layers with varying degree of completeness. These sealing layers can prevent the pushback effect to occur as well as any strong molecule-substrate interactions caused by intimate contact formation between an adsorbent and the pristine metal-oxide surface.

- At merocyanine/metal-oxide interfaces, the importance of the molecular dipole moments for the energy-level alignment is revealed. A coordination bond formation of the merocyanines with the oxide surfaces leads to a preferred orientation of molecular dipoles in the monolayer, which decreases the work function, while dimerization in the multilayer regime does not further impact Φ due to the antiparallel alignment of neighboring molecular dipole moments.

As a consequence, E_F-pinning of the molecular frontier energy levels does not set in at that substrate work function values Φ_{ox} , which coincide with the Φ_{sat} in the respective E_F-pinning situation, because substantial interface dipoles arise upon the merocyanine-monolayer formation, which cause a "delay" of E_F-pinning by ca. 1 eV.

Moreover, caused by this dipolar layer formation, one finds very large hole-injection barriers for the series of studied merocyanines on ITO ($\Phi = 4.3$ eV) and TiO_2 ($\Phi = 5.25$), which is in strong contrast to general expectations. To achieve, however, good electrical contact for injection/extraction of holes at a merocyanine/metal-oxide interface, very high Φ_{ox} ($\geq$ 6 eV)-oxides are required, e.g. MoO_3.

On the other hand, ITO and TiO_2 are ideally suited as anodes, at which electrons need to be extracted from these merocyanines. This type of merocyanine/metal-oxide interfaces is therefore recommended to be employed as dye-sensitized anodes. Towards solid-state dye-sensitized solar cells, they might be combined with a hole-transport material like α-NPD, estimated to show maximal attainable open circuit voltages of up to 1.9 eV.

- Regarding the role of the substrate within the series of employed studies, the observation of band bending is revealed to be a strong indication for the absence of strong electronic coupling between molecules and substrate, i.e. mixing of molecular and surface states. Indeed, those strong interactions rely on (i.) reactive surfaces and/or (ii.) reactive molecular side-groups.

  (i.) Band bending was obtained for HATCN on sealed/contaminated (and thereby rather inert) ITO-surfaces, as well as for merocyanine **1** deposited on freshly-evaporated MoO_3, which is essentially assumed to be free from reactive defect sites. In contrast, for HATCN on UHV-cleaned ITO-surfaces or merocyanine **1** deposited on sputtered MoO_3-surfaces, one obtains a collapse of band bending into a localized interface dipole. This is related to strong mixing of substrate and molecular states, which is obviously enhanced on UHV-cleaned metal oxides comprising a significant amount of defect sites, i.e oxygen-vacancies.

  (ii.) Apart from the employed hole-transport material $\alpha - NPD$, all investigated molecules provide at least one potentially reactive side-group that might eventually couple to a metal-oxide surface, as has been in particular observed for the series of merocyanines deposited on metal oxides. The implementation of metal oxides as interlayers to inhibit

strong molecule/substrate coupling is accordingly not straightforward. It is however possible if one relies on particularly inert molecules that basically do not provide any potential reactive side groups.

Despite the repeated observation of band bending, the spectral signature of charged molecules could not be observed in the (sub)monoloayer regime. This is mostly related to the fact that the density of charged molecules at the investigated interfaces is smaller than the experimental detection limit. To target this critical issue, the metal-oxide interlayer thickness needs to be significantly reduced in the final sample concept.

Chapter 5.

Spectral Signature of Polarons in Molecular Semiconductors

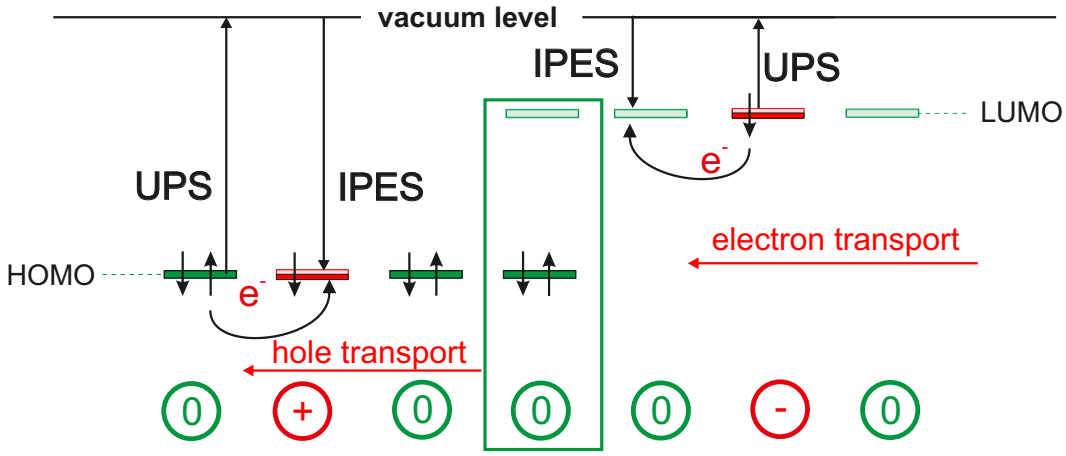

Figure 5.1.: Schematic illustration of hole- and electron-hopping transport through a molecular semiconductor, corresponding to a complementary employment of UPS and IPES.

As outlined in chapter I, it is of paramount importance to gain a detailed understanding of the nature of charge carriers *in*, and their propagation *through* molecular semiconductors. Those are widely established to be polarons formed by strong electron (or hole) coupling to (inter- and intra-) molecular vibrations[40,41,50,89,309]. To gain further insights, key parameters that enter models for hole-transport, e.g. the geometrical reorganization energy λ[8–10], have been shown to be accessible by means of ultraviolet photoelectron spectroscopy (UPS), when probing the occupied manifold of single-particle states, particularly the highest occupied molecular orbital (HOMO) states, in neutral molecules.[14,16] The left panel of Fig. 5.1 sketches the hole-transport process: electron hopping from the doubly occupied HOMO onto the singly occupied HOMO of the neighboring molecule. This corresponds to making use of UPS on a neutral molecule and inverse photoemission (IPES) on a positively charged molecule in close vicinity. Conversely, electron transport is illustrated in the right panel of Fig. 5.1: electron hopping from the singly occupied LUMO into the unoccupied LUMO

of a neighboring molecule corresponds to making use of UPS on the negatively charged molecule and IPES on the neutral molecule in immediate vicinity.

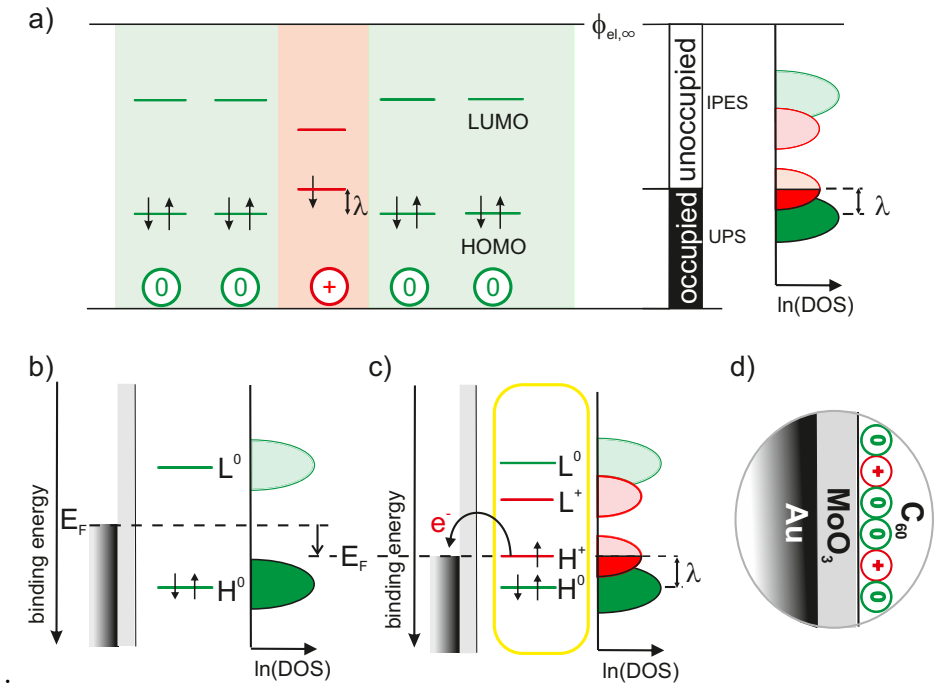

Figure 5.2.: (a) Single-particle energy levels for neutral molecules (green) surrounding a cation (red), their experimental accessibility to (inverse) photoelectron spectroscopyy depending on their occupancy and the resulting ln(DOS) as proposed in Ref.[30] (b) Single-particle energy-level diagrams for a neutral molecule on an intermediate and (c) a high work-function substrate causing electron-transfer that results in cations.[31,35,40,41,310] The latter is realized in the Au/MoO_3/C_{60}-heterostructure, shown in (d).

Unfortunately, photoemission studies on the charge carrying molecule in the solid phase have turned out to be rather challenging, as is explored in detail later. Consequently, a model for the energy levels associated with charge carriers, i.e. polarons, was conceived[27,30,40,41,47,311] due to the lack of proper experimental evidence by UPS/IPES. According to those commonly accepted perceptions, Fig. 5.2(a) shows the relevant single-particle energy levels and their occupancies considering a positive polaron. Removing an electron from the HOMO of a neutral molecule leads to geometrical relaxation and a concomitant shift by the reorganization energy λ of the now singly occupied state into the energy gap of the organic semiconductor.[40] Fig. 5.3(a) depicts the analogue situation for a negative polaron, where occupation of the LUMO of the neutral molecule by an additional electron leads to a geometrical relaxation and a concomitant shift by λ of the now singly occupied state into the energy gap of the organic semiconductor.

Based on this picture, it has been proposed in Refs.[27, 30, 31, 310] that (i) the doubly occupied states should be experimentally accessible by UPS, (ii) the unoccupied states by IPES and (iii) the singly occupied state by means of *both* UPS and IPES.

These expectations are illustrated in the right panels of Fig. 5.2(a) and Fig. 5.3(a), as referred to e.g. in Ref.[30]. So far, the observed UPS information assigned to the singly occupied LUMO, referring to the negative polarons, has been discussed applying this "polaron picture".[26–29] However, despite large efforts by means of UPS[31,269], clear spectral evidence for the singly occupied HOMO-derived level associated with positive polarons is still missing. This might be either related to a misconception of the established model or that of the experiments. To target this issue, a new experimental approach needs to be considered, one that enables the generation and experimental detection of cations in a matrix of neutral but otherwise identical molecules.

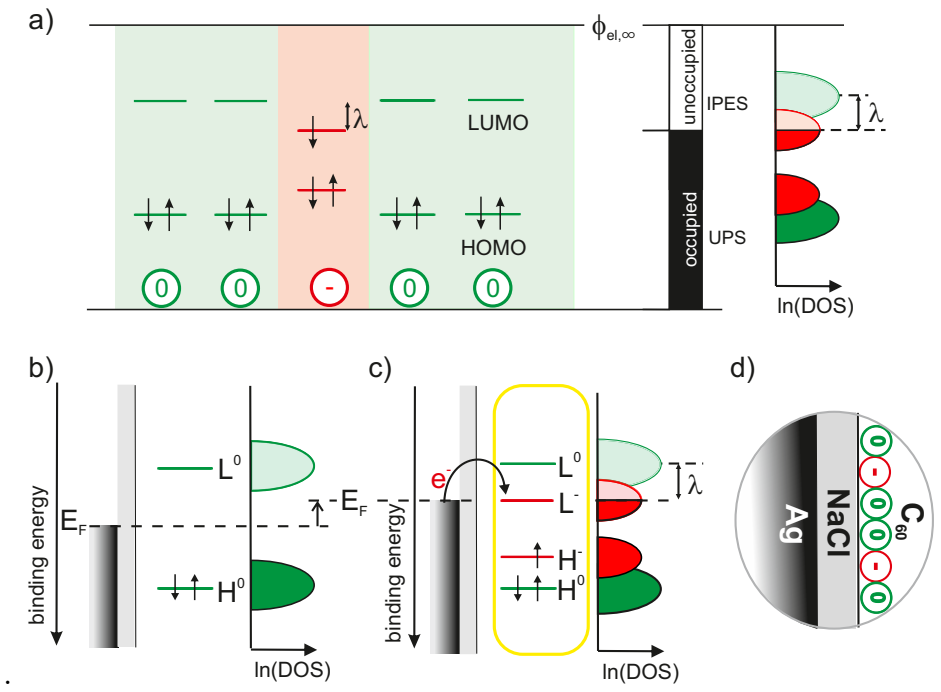

Figure 5.3.: (a) Single-particle energy levels for neutral molecules (green) surrounding a anion (red), their experimental accessibility to (inverse) photoelectron spectroscopyy depending on their occupancy and the resulting ln(DOS) as expected in Ref.[30] (b) Single-particle energy-level diagrams for a neutral molecule on an intermediate and (c) a low work-function substrate causing electron-transfer that results in anions.[31,35,40,41,310] The latter was realized in the Ag/NaCl/C_{60}-heterostructure.[103]

When generated upon p-doping (e.g. halides, F_4TCNQ), the new singly occupied HOMO-derived states can hardly be distinguished from the filled lowest unoccupied atomic orbital or LUMO of the dopant [31] and, moreover, strong electronic coupling, i.e. hybridization, between molecular HOMO and dopant LUMO cannot be excluded. [32,33] [MHW+15] Likewise, electronic coupling to atomically clean metal surfaces is known not to yield integer-charged molecules but to result in pronounced mixing of metal and molecular states instead. [39,79,312–314] [HDS+13]

This hybridization with the metal, however, can be inhibited by inserting a passivating interlayer (e.g. a metal oxide, see chapter 4) between metal and molecules, reminiscent of the situation in a p-type organic field-effect transistor [315–317] under applied (negative) gate voltage.
Following this approach, cations are generated by employing a metal-supported, ultra-thin dielectric with a final work function (Φ) larger than the ionization energy (IE) of subsequently deposited molecules as depicted in Fig. 5.2(b-c). Thereby, the Fermi level (E_F) of the underlying metal is moved into the occupied density of states (DOS) of the molecules, causing the necessity for electron transfer from the molecules across the insulator into the metal.

In the present study, this is realized with an Au-supported thin ($d = 1.2$ nm) MoO_3 layer (ϵ_r=9, Φ=6.8 eV). This particular material combination is chosen in a way that also targets the critical issue of sufficient charge carrier density. One can easily deduce that Φ should be as large as possible and the buffer layer as thin (d) as possible to receive the largest amount of charge carrier quantity (Q) per area (A).

$$\frac{Q}{A} = \Delta E \cdot \frac{\epsilon_0 \epsilon_r}{d} \qquad \Delta E = \Phi - IE \quad \text{if} \quad IE < \Phi \tag{5.1}$$

Here ΔE is the energy difference between the substrate-Φ and the IE of the molecular semiconductor (for IE<Φ).
The use of C_{60} (IE=6.4 eV < Φ) as hole-accumulation material has a wealth of significant benefits. (i) The detectability of the potentially low polaron concentrations is enhanced due to its high orbital degeneracy (HOMO:5, LUMO:3). (ii) The issue of (inverse) photoemission induced degradation (see section 3.3) is disarmed, as C_{60} provides a high robustness related to its closed cage-like molecular structure. (iii) This unique molecular structure moreover targets the critical issue of undesirable molecule-substrate interactions, as it provides no functional groups. Those have been elaborated to be potentially reactive when deposited on metal oxides, as referred to in chapter 4. The full sample structure is sketched in Fig. 5.2(d).

In analogy, the inverse approach was recently established to generate anions in order to study band bending in organic semiconductors,[103] see Fig. 5.3(b-d). However, this previous study did not focus on the full electronic structure of the generated anions by exclusively making use of UPS and thereby probing only the occupied states. The following findings on molecular cations, where a combination of UPS and IPES is employed, will therefore be qualitatively applied on the anions, to draw a comprehensive picture of the energy levels associated with (positive and negative) polarons in molecular semiconducting films.
Parts of this chapter have been published in Ref.[WAF+15].

5.1. Multilayer

The multilayer-evolution of C_{60} is discussed first in order to study band bending,[34,103,318] whose occurrence is established to prove the presence of integer-charged molecules as well as the absence of strong molecular-substrate interaction, as has been elaborated in the previous chapter 4.
Fig. 5.4 depicts the evolution of the entire electronic structure of C_{60} deposited on the metal-supported MoO_3 substrate. Upon increasing C_{60} deposition, molecular

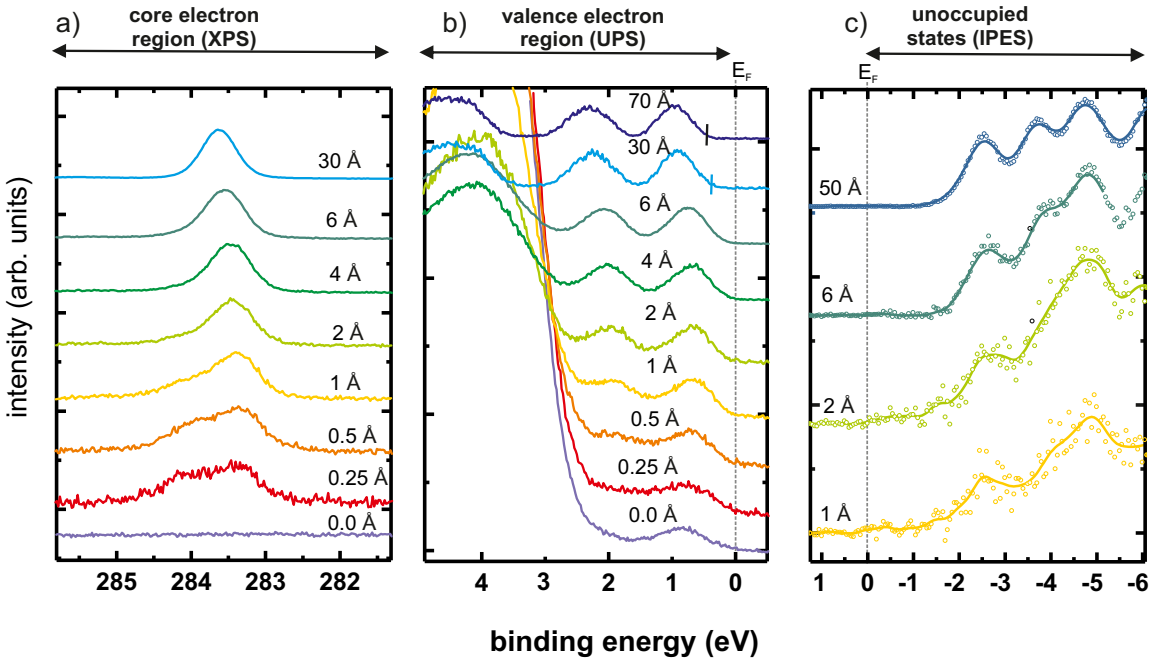

Figure 5.4.: Evolution of the C_{60}-coverage dependent (inverse) photoelectron spectra (a) C1s core level, (b) occupied valence levels. Concerning the unoccupied states (c) depicts the differential spectra obtained by IPES; see Fig. 5.10 for details.
(Note that the spectral evolution beyond a nominal layer thickness of about 7 nm is not considered, due to the observation of charging beyond that C_{60}-thickness, as will be discussed in further detail later.)

features increasingly emerge in the core-level region [Fig. 5.4(a)], the occupied [Fig. 5.4(b)], and the unoccupied [Fig. 5.4(c)] valence-level region until at about 30 Å nominal C_{60}-coverage, the typical spectral signature of C_{60} [84,192] is obtained. Noteworthy, the UPS feature assigned to the HOMO level of C_{60} is not found to be intersected by E_F, which strongly indicates that the system is not metallic. This is in clear contrast to the outlined perceptions and previous studies of C_{60} in E_F-pinning of the LUMO *vice versa*, [ANW+13,NAW+12] [103] where the spectral signature assigned to the filled LUMO was observed directly at E_F. Prior to discussing this striking observation in more detail in section 5.2, the electrostatics across the molecular semiconductor are analyzed, invoking the C_{60}-dependent evolution of Φ.

5.1.1. Work Function Evolution

Upon formation of 1.2 nm MoO_3/Au(111), Φ increases from 5.4 eV [sputter-cleaned Au(111)] to 6.8 eV. As MoO_3 should not interact with the inert Au(111)-surface, the underlying processes need to be attributed to a "pushback" of the metal electrons spilling out from the surface into the vacuum and an electrostatic contribution attributed to E_F-pinning, due to the high EA of MoO_3 (6.8 eV [246]). The evolution of Φ upon subsequently deposited C_{60} is shown in Fig. 5.5. Φ decreases to 6.2 eV for the completeness of about one monolayer ($\approx$ 8 Å), estimated with respect to one C_{60} layer-thickness of 0.82 nm. [103]
Beyond this thickness, one finds further decreases of Φ, even for higher C_{60} coverages, demonstrating the band bending within the bulk C_{60}, in conjunction with the results found by Irfan et al. in Ref.[318]. For the inverse case of LUMO-pinning, band bending has been recently shown to occur by Wang et al. in Ref.[103] for C_{60}/NaCl/Ag(111).

5.1.2. Band Bending

The continuous and parallel shifts of the HOMO level, of the C1s level and of the vacuum level with increasing nominal C_{60}-thickness are depicted in Fig. 5.5 and indicate the evolution of the electrostatic potential across the C_{60}-layers. It is rationalized by invoking the occurrence of band bending, which is modeled by adapting an electrostatic model that has been successfully applied to a molecular semiconductor. [34,103]
There, the metal substrate is regarded as electron reservoir with fixed chemical potential and the dielectric interlayer as perfect insulator with known thickness (1.2 nm) and relative permittivity ($\epsilon_r = 9$). The DOS of each molecular layer (thickness = 0.82 nm [103]) is modeled according to section 3.4.2. Note in this

regard that the fraction of charged molecules per layer decreases rapidly with increasing distance from the dielectric layer.
In contrast to the case of C_{60} on NaCl[103], where pinning is the sole contribution for establishing the energy-level alignment, a further contribution needs to be considered at the C_{60}/MoO_3-interface. A push-back effect[37] [WFS+13] is established to occur upon molecular monolayer formation on oxide surfaces, which amounts to 0.3 eV, independent of the exact surface constitution and stoichiometry (see section 1.2.3 and chapter 4). To account for this in the applied model, a linear increasing pushback effect is added exclusively for the organic monolayer completion (0-8 Å) from 0 to 0.33 eV to find the highest agreement with the experimentally observed work function changes in the submonolayer regime (see Fig. 5.5).
Most importantly, the model is in near-perfect quantitative agreement with the experimentally determined evolution of the work function (with respect to Δ_{PB}=0.33 eV) with increasing C_{60} thickness on 1.2 nm MoO_3 on Au(111). Even the C1s spectrum of neutral C_{60} follows the electrostatic potential. This coincidence beyond the ML is remarkable but limited by a C_{60} thickness of about 7 nm, at which increasing deviations between model and experiment are obtained.

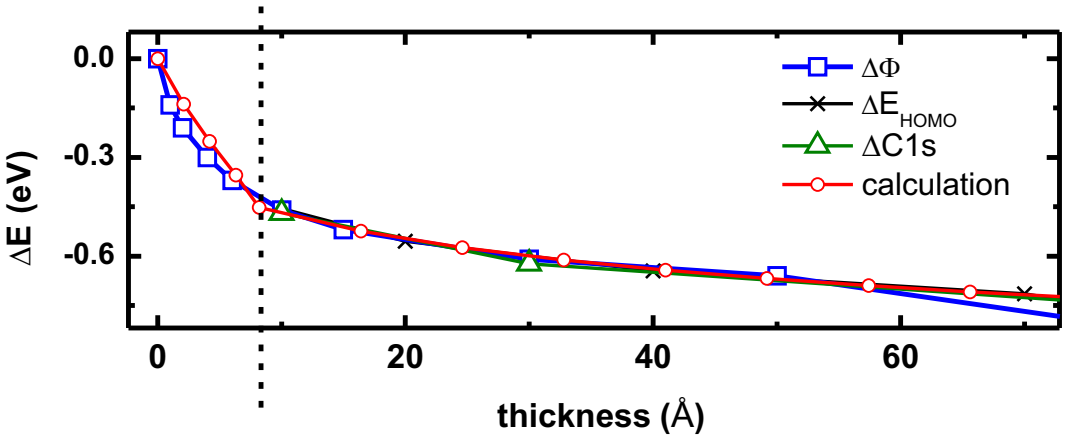

Figure 5.5.: Evolution of the measured work function shift ($\Delta\Phi$), the HOMO-level shift (ΔE_{HOMO}) and the C_{60}-core-level shift in comparison to the calculated potential decrease across the C_{60}-film.

5.1.3. Charging

Fig. 5.6 displays an extension of Fig. 5.5. It clearly shows a sudden change in the continuous evolution of all experimentally determined energy-level shifts (ΔC1s, ΔE_{HOMO}, $\Delta\Phi$) at a nominal C_{60}-coverage of 7 nm (experimentally reproduced). Due to the fact that PES is a photo-hole creating technique, it is therefore

possible to attribute this effect to charging, although a reduced photon flux (defocus of the beamline & insertion of a beam-filter) was used and no broadening of spectral features was observed.
Interestingly, for the inverse situation C_{60}/NaCl/Au(111) [103], i.e. LUMO-pinning, such phenomenon has not been observed (using the very same experimental setup) within the studied range up to 80 nm C_{60}-coverage. This discrepancy elucidates the main difference between the former [103] and the present study: For LUMO-pinning at E_F the molecular semiconductor is electron-doped at the interface. Photo-holes can thusly be refilled by surrounding negatively charged molecules, which are well coupled to the metal-substrate due to the pinning-induced charge-transfer phenomenon. For HOMO-pinning at E_F, however, the molecular semiconductor is hole-doped at the interface. Generated photo-holes need to pass this hole-accumulation layer to the metallic ground. This charge-transfer induced Coulomb barrier is supposed to result in the observed charging process already at comparable low C_{60}-coverages.

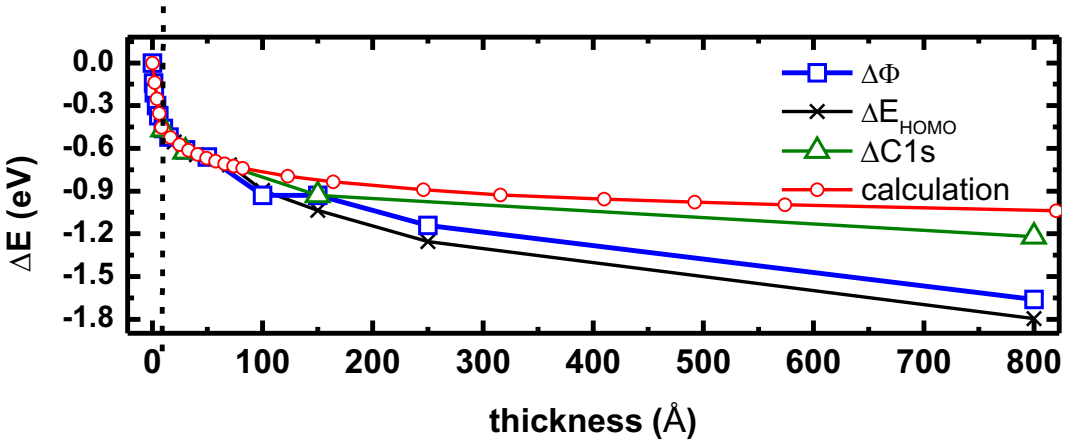

Figure 5.6.: Evolution of the measured work function shift ($\Delta\Phi$), the HOMO-level shift (ΔE_{HOMO}) and the C_{60}-core-level shift in comparison to the calculated potential decrease across the C_{60}-film. Beyond 70 Å the measured values increasingly deviate from the calculation; thus indicating the occurrence of charging.

In conjunction with this charging disadvantage for *direct* photoemission spectroscopy on hole-doped systems, one might benefit from the accumulated holes, when applying inverse photoemission spectroscopy. Following these simple considerations, a hole-doped system should be much less affected by charging and charging-induced degradation, which is a general problem for conventional IPES-studies on organic semiconductors.

5.2. (Sub)monolayer

Having established that the molecular semiconductor is electrically doped with holes at the interface, and that the molecules do not strongly interact with the MoO_3-substrate due to the occurrence of band bending, it is time to search for the spectral signature of these cations. This has highest prospects of sucess in the (sub)monolayer region, as the charge density rapidly decreases with increasing distance from the semiconductor/dielectric interface,[34,103,273] [ANW+13] as has been mentioned already, when modeling band bending. In consequence, a detailed analysis and discussion of the obtained (sub)monolayer spectra is accomplished in order to reveal the spectral signature associated with positive polarons. This is supported by DFT-calculations (see section 3.4.1) on isolated C_{60} molecules (neutral or cationic state), whereby the screening of the excess hole on the fullerene by the environment (MoO_3 and surrounding molecules) is captured by a polarizable continuum model[226] with 3.5 as relative dielectric constant.

5.2.1. Core Electronic Structure

At first, XPS is used to ensure the presence of a sufficient, i.e. detectable, amount of C_{60}-cations in the heterostructure. This is feasible because the C1s core-level features are known to be at different binding energies for molecules in their neutral and cationic state.[213] The choice of C_{60} in this context is rather sophisticated, as the molecule in its neutral state consists of 60 chemical identical carbon atoms that cause only one signal C1s feature in the core-level region.
Fig. 5.7(a) shows the evolution of the C1s spectra with increasing C_{60} coverage, together with the results of the applied fitting procedure. First of all, the clear absence of any carbon species is found for the pristine MoO_3 surface. Upon subsequent C_{60} deposition, two distinct C1s peaks [283.4 eV (red) and 284.1 eV BE (green)] emerge, which are split by ~ 0.7 eV and clearly show the coexistence of charged (high binding energy) and neutral (low binding energy) molecules at the very interface. This assignment is in accordance to literature[213] and fully in line with the expectation of a decreasing fraction of charged molecules with increasing submonolayer coverage[34,103,273] [ANW+13] (molecule/cation ratios are summarized in Tab. 5.1).
Already at 1 Å nominal coverage a (third) multilayer-contribution (blue feature in the figure) arises, which indicates island growth as illustrated in Fig. 5.7(b). While its presence is of no further consequence for the discussion below, it supports the notion of hole accumulation within the first layer, as it is energetically aligned according to the electrostatics of energy-level bending.[34,103,318]

Regarding the electrostatics resulting from the hole-accumulation within the (sub)monolayer itself, it is important to note that, here, each neutral molecule observed in XPS resides within the Coulomb well created by a nearby cation, [ANW+13]

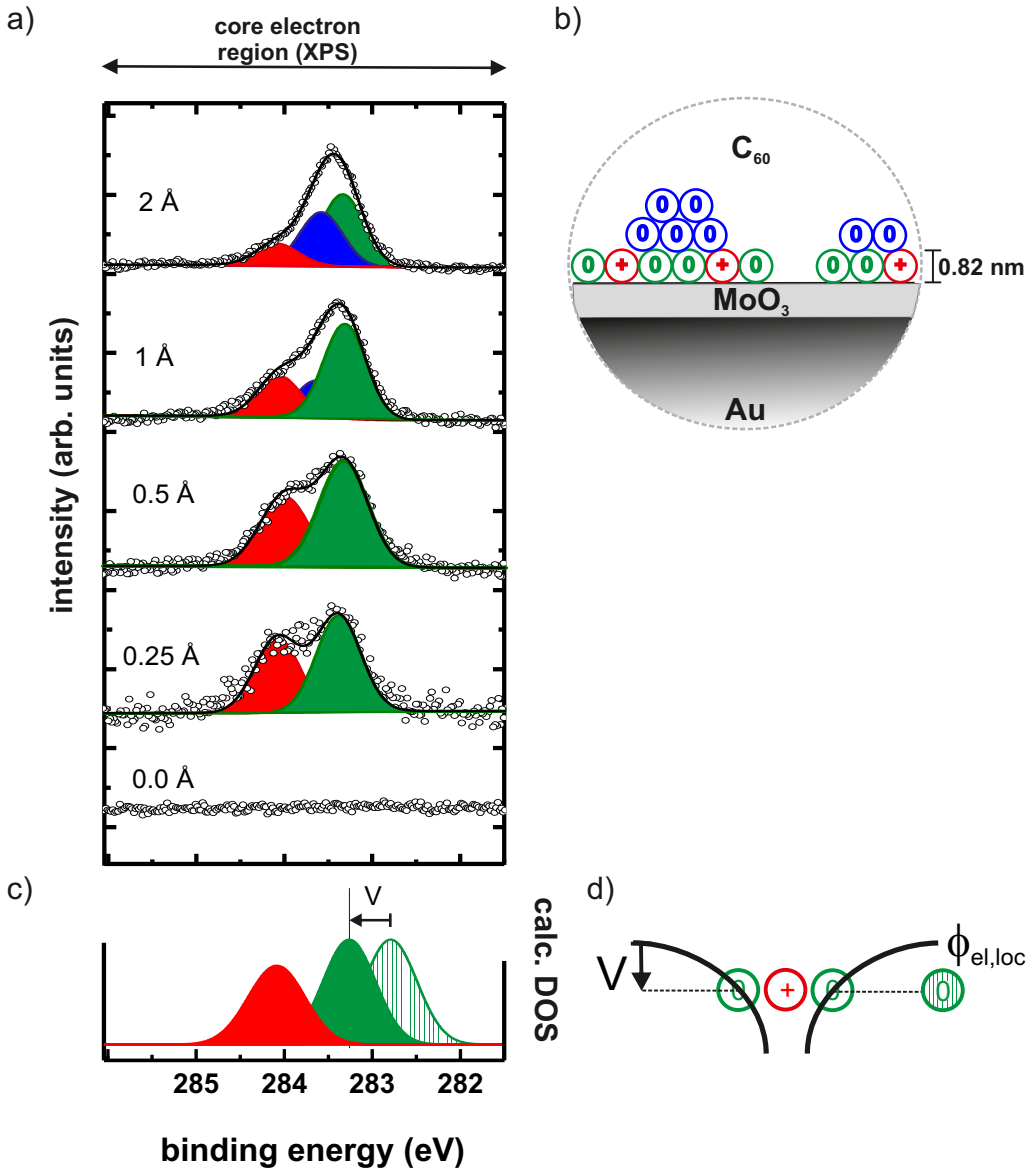

Figure 5.7.: (a) C_{60}-submonolayer-coverage dependent C1s core-level spectra. The experimental curves (black circles) are fitted with either two or three Gaussian singlet peaks (FWHM: $\sim 0.6 - 0.7$ eV) attributed to the charged (red spectra) and neutral (green spectra) C_{60} molecules within the monolayer, plus the second layer contribution (blue spectra) from 1 Å nominal coverage on. The formation of multilayer moreover induces a photo-hole screening effect [87] of about 0.2 eV on both monolayer-contributions. In b) the supposed growth mode is illustrated at the C_{60}/MoO_3-interface. c) shows the corresponding DFT-calculated DOS of the neutral (green striped) and positively charged (red) molecules. Both were rigidly shifted in energy so that the cation features match experiment. To account for the potential well created by the cations (d), the calculated DOS of the neutral molecules is shifted by V=0.5 eV to higher binding energies.

Table 5.1.: Summary of ratios between charged (C_{60}^{+}), neutral (C_{60}^{0}) and multilayer (C_{60}^{ml}) molecules in dependence of nominal C_{60}-film thickness obtained by XPS, UPS and IPES.

nominal	XPS			UPS			IPES		
film thickness (Å)	C_{60}^{+}	C_{60}^{0} (%)	C_{60}^{ml}	C_{60}^{+}	C_{60}^{0} (%)	C_{60}^{ml}	C_{60}^{+}	C_{60}^{0} (%)	C_{60}^{ml}
0.25	44	56	-	43	57			-	
0.5	40	60		35	65			-	
1	25	58	17	19	60	21	15	56	29
2	15	49	36	13	52	35	13	52	35
6	9	20	71	6	32	62	12	36	52
30/50	-	100		-	100		-	100	

as sketched in Fig. 5.7(d). Thereby, all energy levels of these neutral C_{60} molecules are shifted to higher binding energies (by an amount V). This ensures that their (fully occupied) HOMO-levels now come to lie entirely below E_F, thus preventing them from undergoing electron transfer to the underlying metal and, consequently, becoming cations themselves. The magnitude of V can be estimated by comparing the experimentally obtained core-level shift to that calculated by density functional theory (DFT)(see section 3.4.1) for a single C_{60} molecule in both its neutral and its charged state. Because the DFT-procedure does not account for mutual Coulomb interaction present in the experiment, the theoretically obtained C1s binding-energy difference of ~ 1.2 eV suggests a value of $V \sim 0.5$ eV.

5.2.2. Valence Electronic Structure

Having established the presence of a sufficient amount of cations at the interface by XPS, it is now time to turn to the valence levels of C_{60}, as measured by UPS. In order to properly assess the electronic valence-level structure of (sub)monolayer C_{60}, the following established procedure[36,103] is performed, in which the individual spectral contributions attributed to the distinct materials within the investigated heterostructure, i.e. the substrate and the molecules, are deconvoluted. From a C_{60} submonolayer spectra the pristine MoO_3-spectrum is subtracted, scaled such that the subtraction yields no negative intensity, as depicted exemplary for the 0.25 Å C_{60}-coverage in Fig. 5.8(a). The remaining spectral intensity is attributed to the adsorbed C_{60} molecules. This is reconstructed[103] [NAW+12,ANW+13] by employing two thick film C_{60} spectra, scaled in intensity (as determined from XPS, see Tab. 5.1) and shifted appropriately, as depicted in Fig. 5.8(b). Noteworthy, invoking only one C_{60}-component, one cannot reproduce the C_{60}-residual. Nevertheless, the superposition of both com-

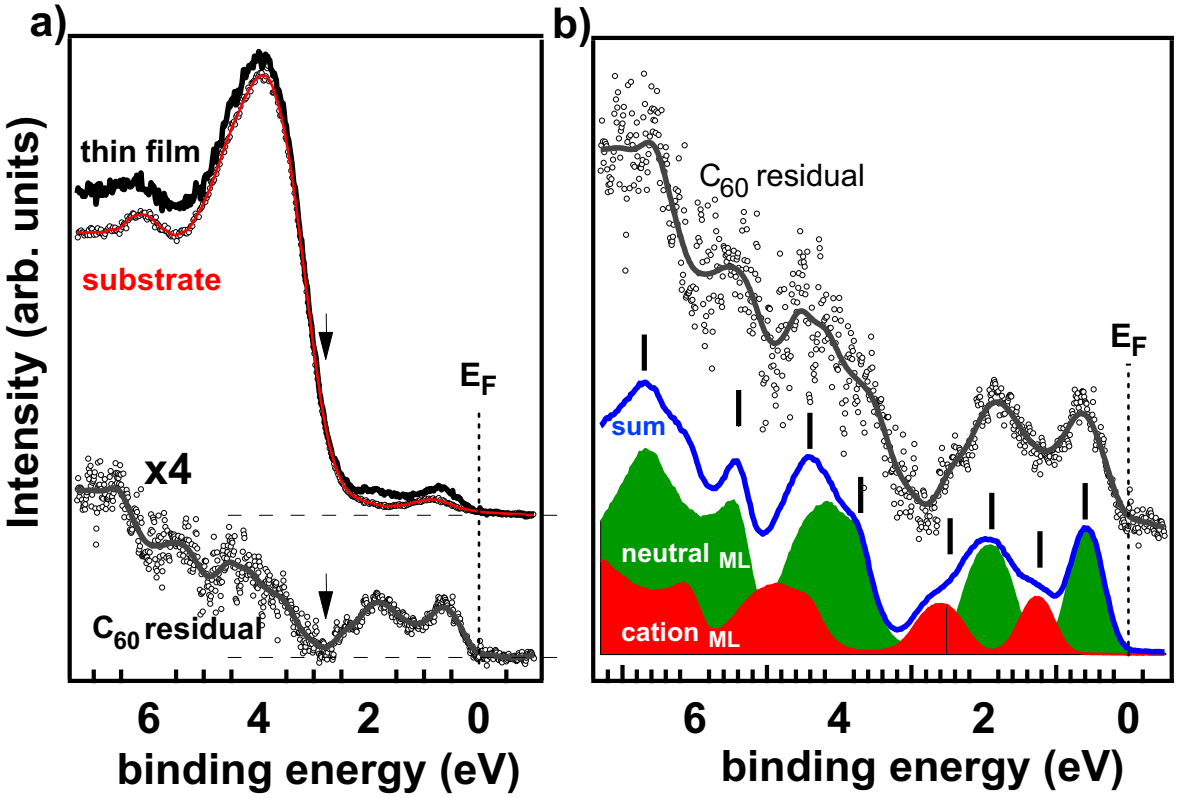

Figure 5.8.: Illustration of the applied valence band-deconvolution procedure: (a) From a 0.25 Å C_{60}-spectrum (black) a suitably scaled substrate contribution (red) is subtracted, yielding a C_{60}-derived residual spectrum (dark grey). An even larger pristine substrate contribution would cause negative spectral intensity in the residual spectrum at about 3 eV binding energy (marked by the arrows). (b) Summing two thick-film C_{60}-contributions, split by 0.7 eV (red: cations, green: neutral molecules), results in the blue spectrum, which agrees remarkably well with the obtained C_{60}-residual.

ponents, which correspond to the neutral and charged C_{60} molecules within the monolayer, shows remarkable agreement with the C_{60}-residual. Justification to take C_{60}-thick-film spectra for both C_{60}-features is given by the DFT-calculations, which confirm the shape of the cation-DOS to be almost identical with that of the neutral molecule, as shown in the bottom of Fig. 5.9(a) and (b).

Fig. 5.9(a) depicts the spectral evolution upon C_{60} (sub)monolayer deposition from 0 to 2 Å. Because here the high binding-energy contribution decreases with increasing submonolayer coverage (compare XPS, see also Tab. 5.1), the assignment - fully supported by DFT (corrected by V) - of these two C_{60} species has to be the following: the *low* binding-energy contribution corresponds to the neutral molecules (green) and the contribution at 0.8 eV *higher* binding energy corresponds to the cations (red). This is in clear contrast to the commonly accepted model and the resulting implications for UPS on the positive polaron outlined and depicted in Fig. 5.2(a,c). To further examine the appropriateness of

this model[27,30,40,41,47,311], the complementary spectroscopic technique IPES is applied conversely.

5.2.3. Unoccupied States

Studying (sub)monoloyer-coverages, the C_{60}-derived features as measured in IPES are relatively faint but become observable by subtracting a suitably scaled substrate contribution from the thin film spectrum. This is shown in Fig. 5.10(a) for 1 Å C_{60}. The intensity of the substrate is normalized, as for UPS, such that no negative intensity appears in the C_{60}-derived residual spectrum. This residual intensity is attributed to the C_{60} molecules adsorbed on the surface. As can be further seen in Fig. 5.10(a), this remaining intensity shows excellent agreement with the theoretical DOS (red spectrum), as obtained from DFT.
This residual is consequently deconvoluted by employing thick film C_{60} IPE-spectra scaled in intensity (according to the fit of the C1s spectra, see Tab. 5.1) and shifted appropriately. In Fig. 5.10(b), the green and red components correspond to the neutral and charged C_{60} molecules within the monolayer, plus the (blue) multilayer contribution. Their sum yields the blue spectrum which agrees well with the C_{60}-residual spectrum in the binding-energy region $\leq$-1 eV.
Fig. 5.9(b) depicts the evolution of the thusly obtained differential spectra for 1 and 2 Å C_{60}-coverages; for lower coverages the IPES signal suffers from the inherently low photon yield, which causes poor statics of the resulting spectra.
Most importantly, however, both experiment and theory reveal the presence of an *unoccupied* HOMO-derived state of the cation, attributed to 1 of 10 electrons missing in the fivefold degenerated HOMO of neutral C_{60}. This feature is located closely above E_F (IPES: -0.25 ± 0.25 eV), as deduced from the magnified comparison of calculated DOS and experimental spectrum in Fig. 5.9(b) (1 Å) and Fig. 5.10(b).

5.2.4. Implications on the Spectral Signature of Hole-Doped C_{60}

By combining UPS and IPES, supported by DFT, it is now possible to derive a comprehensive picture of the energy levels of a molecular semiconductor comprising polarons. To do so, Fig. 5.11 summarizes the experimental findings upon reassembling the DFT-calculated DOS representatively. It can be easily deduced that confusingly the IPES results fulfill the outlined expectations, depicted in Fig. 5.2(a), while the UPS results are in strong contrast. In order to elucidate this striking discrepancy, the implications on the spectral signature of hole-doped

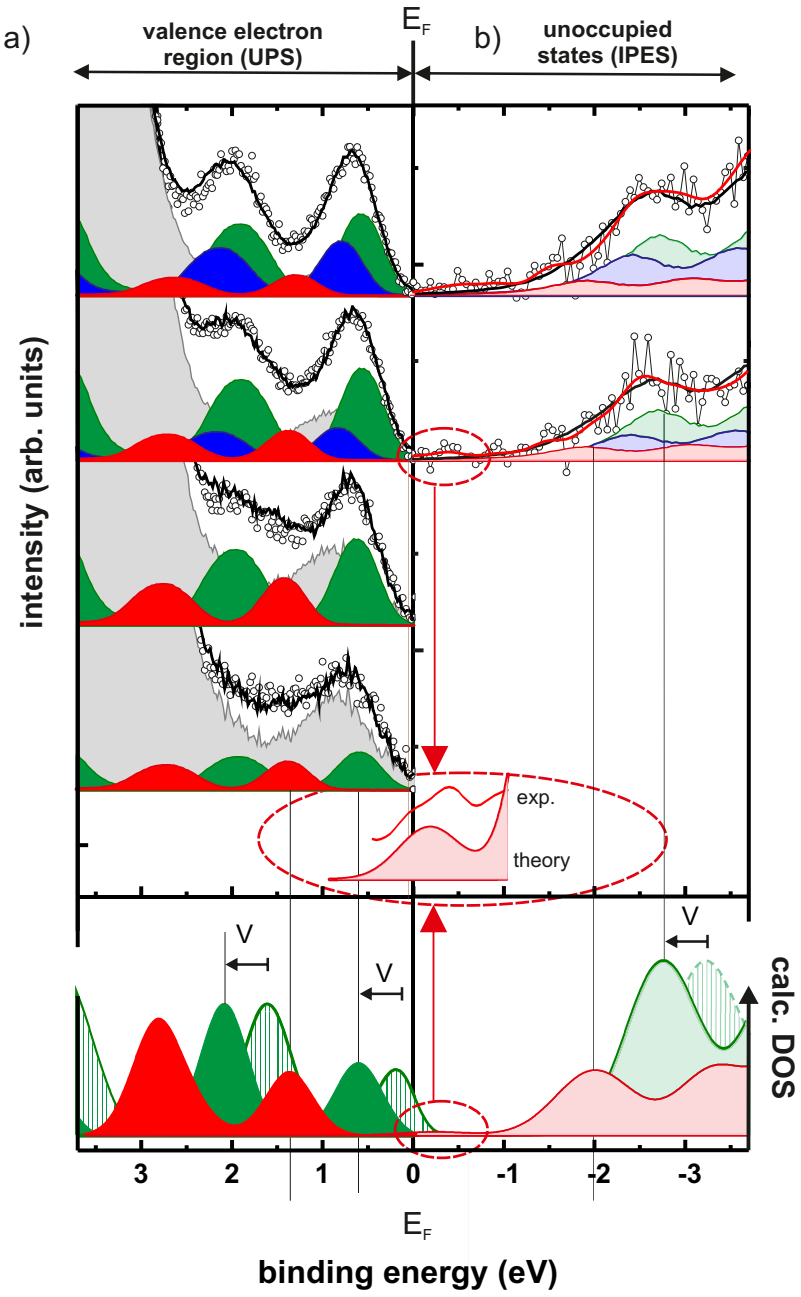

Figure 5.9.: (a) C_{60}-submonolayer-coverage dependent (inverse) photoelectron spectra of (a) occupied and (b) unoccupied valence states. The experimental curves (black circles) can be reconstructed by a superposition (black line) of accordingly shifted and scaled thick-film C_{60} spectra for charged (red), neutral monolayer (green), and multilayer (blue) contributions with a background of bare MoO_3/Au(111) (grey curve for UPS, see Fig. 5.10 for unoccupied states). Bottom of (a) and (b) shows the DFT-calculated DOS of the neutral (green striped) and positively charged (red) molecules. Both were rigidly shifted in energy so that the occupied cation features match the experiment. To account for the Coulomb potential well created by nearby cations, the calculated DOS of the neutral molecules is further shifted by V=0.5 eV to higher binding energy. The magnification highlights experimental and theoretical evidence for an unoccupied HOMO-derived state slightly above E_F.

C_{60} is comprehensively discussed in the following. On the basis of this discussion, it is moreover shown how a number of material properties, as e.g. the on-site Coulomb repulsion (U) and the optical gap (Δ_{opt}), can be derived when employing a combined photoemission on electrically doped molecular systems.

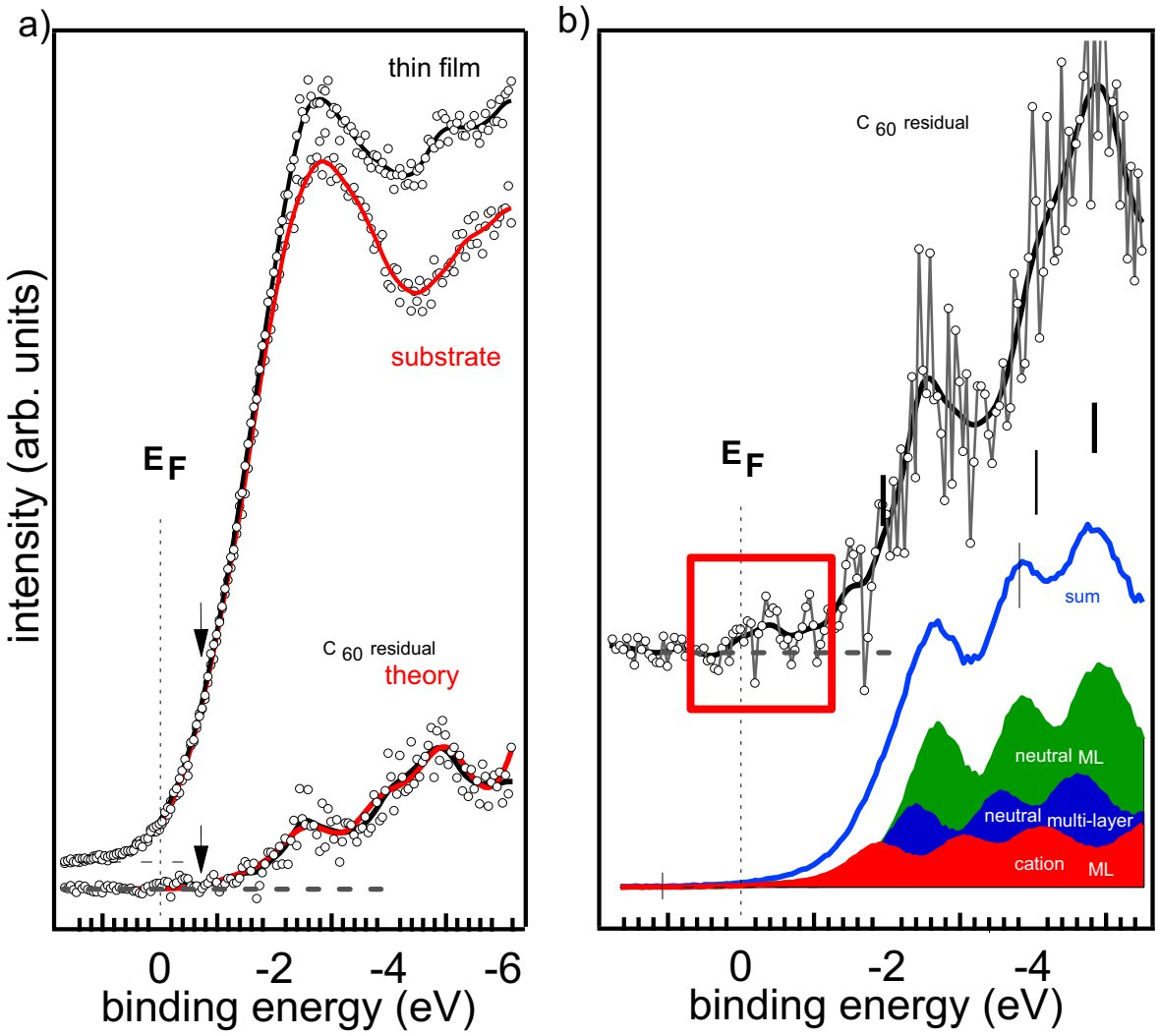

Figure 5.10.: Illustration of the applied deconvolution procedure for IPES: (a) From a 1 Å C_{60}-spectrum (black) a suitably scaled pristine substrate contribution (red) is subtracted, yielding a C_{60}-derived residual spectrum (grey), which agrees remarkably well with the calculated C_{60}-DOS (red, superposition of cation and neutral molecule contributions scaled in accordance to XPS); A larger pristine substrate contribution would yield negative spectral intensity in the residual at about -1 eV binding energy (marked by the arrows.). (b) Summing the cation-(red) neutral molecules in the monolayer-(green) and the multilayer-(blue) contributions, invoking the ratios that are obtained by XPS-fitting at the same C_{60}-coverage (Tab. 5.1), results in a (blue) sum spectrum. This shows good agreement with the obtained C_{60}-derived residual. The inverse photoelectron intensity at E_F (red circled) highlights experimental evidence for an unoccupied HOMO-derived state slightly above E_F for the 1 Å spectrum.

Revision of the polaron picture

The discussion starts with the left panel of Fig. 5.12(a): The energy required to remove an electron from an isolated neutral molecule (IE^0) via UPS to infinity equals the energy gain upon returning it onto the isolated cation (EA^+) via IPES plus the reorganization energy λ.[16,89,186]

$$EA^+ = IE^0 - \lambda \tag{5.2}$$

Notably, the ionization energy IE^+ of the cation, i.e., the *second* ionization energy of the neutral molecule, is larger than the *first* ionization energy IE^0. This is related to the on-site Coulomb interaction between electrons in the HOMO, commonly referred to as Hubbard U[58,70,84](see section 1.1.1), directly determined here to be $U = 1.4$ eV for a valence hole in C_{60} (peak-to-peak split between the occupied and unoccupied HOMO-derived sub-level of the cation obtained by UPS and IPES, respectively).

$$U = IE^+ - EA^+ \tag{5.3}$$

Accordingly, the upper unoccupied HOMO-derived sub-level (corresponding to EA^+) is found to be shifted by λ *into* the gap of the neutral molecule and, thereby, comes to lie above the HOMO of the neutral molecule in energy, as referred to in eq.(5.2). The lower occupied HOMO-derived sub-level appears at $U - \lambda$ *outside* the gap of the neutral molecule, that is, below the HOMO of the

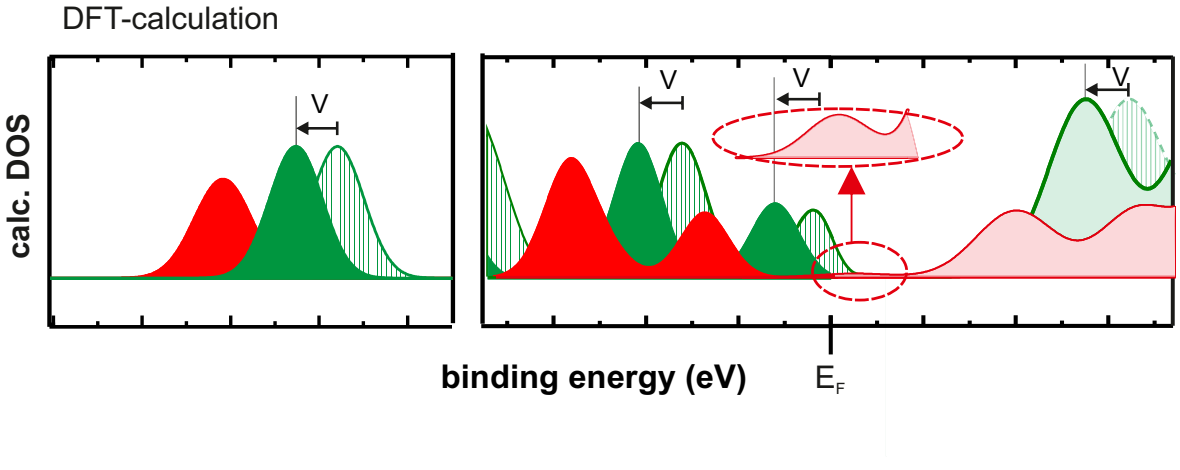

Figure 5.11.: Reassembling of the DFT-calculated DOS for neutral (green striped) and positively charged (red) molecules. Both were rigidly shifted in energy so that the occupied cation features match experiment. To account for the Coulomb potential well created by nearby cations (present in the experiment), the calculated DOS of the neutral molecules is further shifted by V to higher binding energy. The magnification highlights experimental and theoretical evidence for an unoccupied HOMO-derived state slightly above E_F.

neutral molecule in energy.

$$IE^{+} = IE^{0} + U - \lambda \tag{5.4}$$

Completing the picture in the middle panel of Fig. 5.12(a), the energy levels of neutral molecules residing in the Coulomb well ($\phi_{el,local}$) of the cation are shifted to *higher* binding energies by (up to) V, a quantity that can now, in analogy to U, be related to the inter-site Coulomb interaction[11,12,319](for further details, see following subsection).
Based on these findings, the rightmost panel of Fig. 5.12(a) provides a simplified

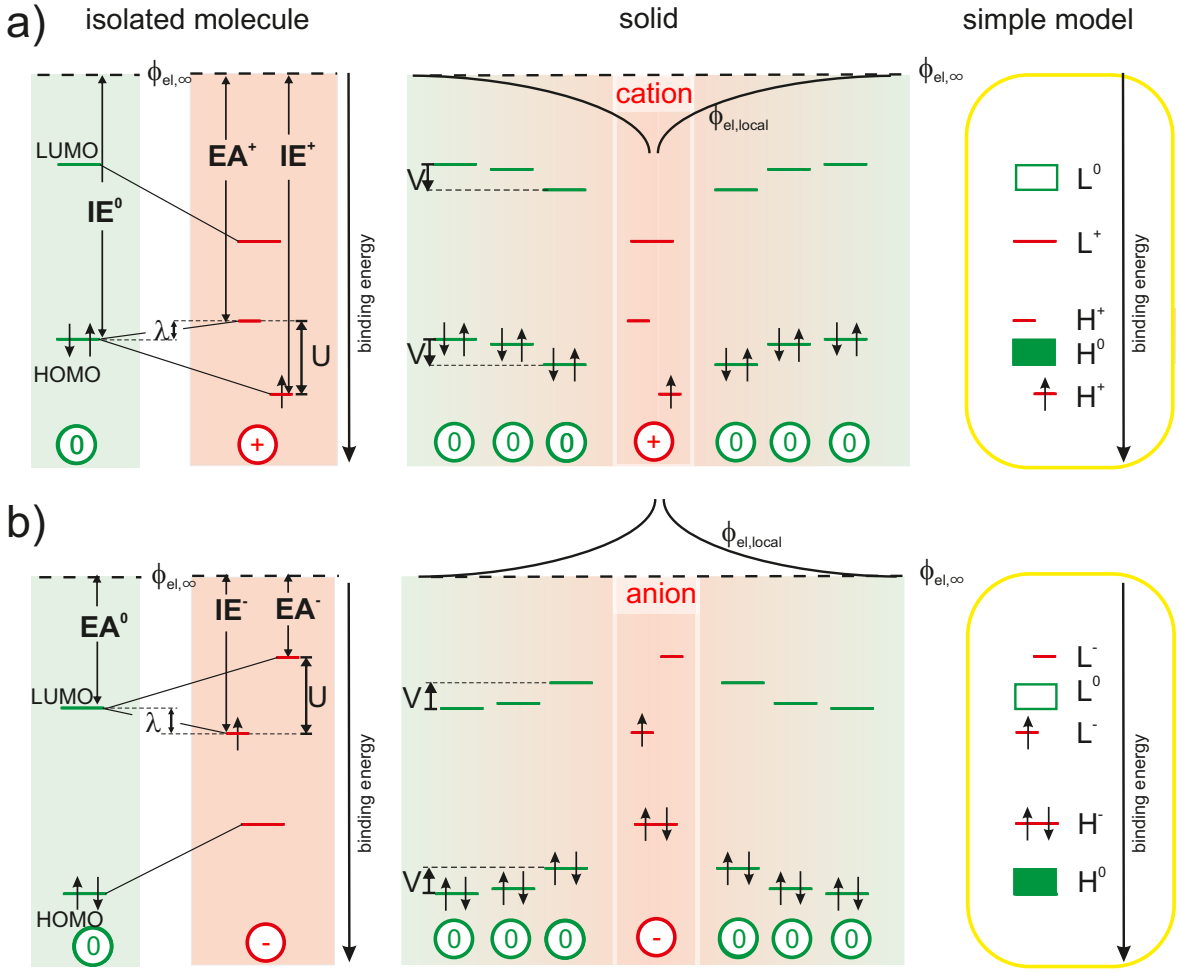

Figure 5.12.: (a) Origin of the experimentally observable spectral signature of cations from left to right: The reorganization energy λ of an isolated molecule equals the difference between IE^0 and EA^+; the on-site Coulomb interaction U causes a splitting into two HOMO-derived sub-levels, EA^+ and IE^+, while inter-site Coulomb interaction V causes an energy-level shift to higher binding energies of the neutral molecules in close vicinity to the cations; The rightmost panel shows a simplified projection revising Fig. 5.2(a,c)
(b) Analogous to (a) for negative polarons, with the rightmost panel revising Fig. 5.3(a,c)

picture of the single-particle energy levels associated with positive polarons in a molecular film, which is suggested to replace the hitherto followed one in Fig. 5.2(c).
In full analogy, Fig. 5.12(b) revises the expectations for the negative polaron as referred to in Fig. 5.3.[27,40,41,310] The energy gained from adding an electron onto an isolated neutral molecule (EA^0) by IPES equals the ionization energy of the thus generated anion (IE^-) minus the reorganization energy λ.

$$IE^- = EA^0 + \lambda \tag{5.5}$$

The electron affinity of the anion (EA^-), i.e., the *second* electron affinity of the neutral molecule, is now lower than the *first* electron affinity EA^0. This is again caused by the on-site Coulomb interaction between electrons in the LUMO.

$$U = IE^- - EA^- \tag{5.6}$$

Therefore, the upper unoccupied LUMO-derived sub-level lies by $U - \lambda$ *outside* the gap of the neutral molecule.

$$EA^- = EA^0 - (U - \lambda) \tag{5.7}$$

The lower occupied LUMO-derived sub-level appears shifted by λ *into* the gap of the neutral molecule, as referred to in eq.(5.5).
In the solid state the energy levels of neutral molecules within Coulomb interaction range of nearby anions are now shifted to *lower* binding energies by an amount V, which depends again on the distance to the anion.
The emerging full picture for the negative polaron, a simplified version of which is provided in the rightmost panel of Fig. 5.12(b), implies that also literature-based expectations[27,310] on the spectral signature of anions should be revised accordingly.

On-site and Inter-site Coulomb Interaction

In order to illustrate the terminology of and the relation between the *on-site* and *inter-site*[320,321] Coulomb interaction, first of all Fig. 5.13 is considered. A single-molecule energy-level scheme of reduced complexity (depicting only HOMO and LUMO level) in Fig. 5.13 shows the electron occupation configurations with increasing number of electrons; they are assigned to the doubly(E^{++}) & singly (E^+) positively charged configurations, neutral (E^0) configuration and singly (E^-) & doubly (E^{--}) negatively charged configurations of a molecule. For the

sake of simplicity the *reorganization energy* λ *is neglected* for now.

In a second step, the 1-electron (radiative) irradiative transitions from an initial state to a final state associated with (inverse) photoelectron spectroscopy are recalled with respect to section 2.1. In particular, transferring an electron from a bound initial state of a N-electron system to a final state in the infinite, and thereby leaving a $N-1$-electron-system, requires the corresponding ionization energy (IE). Transferring an electron from an initial state in the infinite to a N-electron system, and thereby creating a $N+1$-electron-system, provides the corresponding electron affinity (EA).

In this regard, Fig. 5.14(a) depicts the mentioned 1-electron-transitions between the mentioned molecular configurations E^{++}, E^{+}, E^{0}, E^{-}, E^{--}, which serve as initial and final states respectively. Moreover, the respective transitions are correlated to the electron-binding energies ϵ_H and ϵ_L with respect to the vacuum level for an electron occupying either the HOMO or LUMO level; $\epsilon_H > \epsilon_L$.
Starting from the initial state E^0, i.e. zero-hole occupation of the HOMO and zero-electron occupation of the LUMO, IE^0 corresponds to an increase (+1) of the occupation number of holes in the HOMO ($E^0 \rightarrow E^+$) and EA^0 corresponds to an increase (+1) of electrons in the LUMO ($E^0 \rightarrow E^-$). The difference between both transitions $IE^0 = \epsilon_H$ and $EA^0 = -\epsilon_L$ naturally yields the transport gap Δ_{trans} (see eq.(1.20) and section 1.1).
A further increase of the occupation number of holes in the HOMO ($E^+ \rightarrow E^{++}$) results in a final state of paired holes. This transition does not simply require the electron-binding energy ϵ_H, but the additional on-site Coulomb repulsion U (here: ≈ 1.4 eV) accounting for hole-hole repulsion in the HOMO. Accordingly, the molecule's second ionization energy is always larger than the first one.
Increasing the occupation number of electrons in the LUMO ($E^- \rightarrow E^{--}$) results in a final state of paired electrons. The respective transitions (EA^-) amounts for ϵ_L and the Coulomb repulsion U, which accounts for the electron-electron-

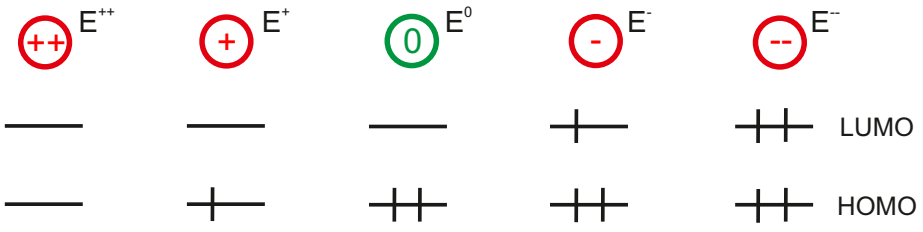

Figure 5.13.: Electron occupation configurations for the frontier energy levels (HOMO and LUMO) of a single molecule. The electron number is incrementally increased, starting from a doubly positively charged molecule (E^{++}) and ending at the doubly negatively charged molecule (E^{--}).

repulsion in the LUMO. As a result, the second electron affinity is always smaller than the first one.
In a second step, these assignments are applied to a two-molecule picture. This is because an isolated-molecule treatment (as is used in the DFT-calculations) does not properly explain the obtained (inverse) photoemission results on hole-doped C_{60}. Indeed mutual Coulomb interactions $V(r)$ are at play. In particular, neutral molecules reside within the Coulomb well ($\phi_{el,local}$) created by a hole q^+ in a cation at a distance r. Therefore the determined binding energy of the detected

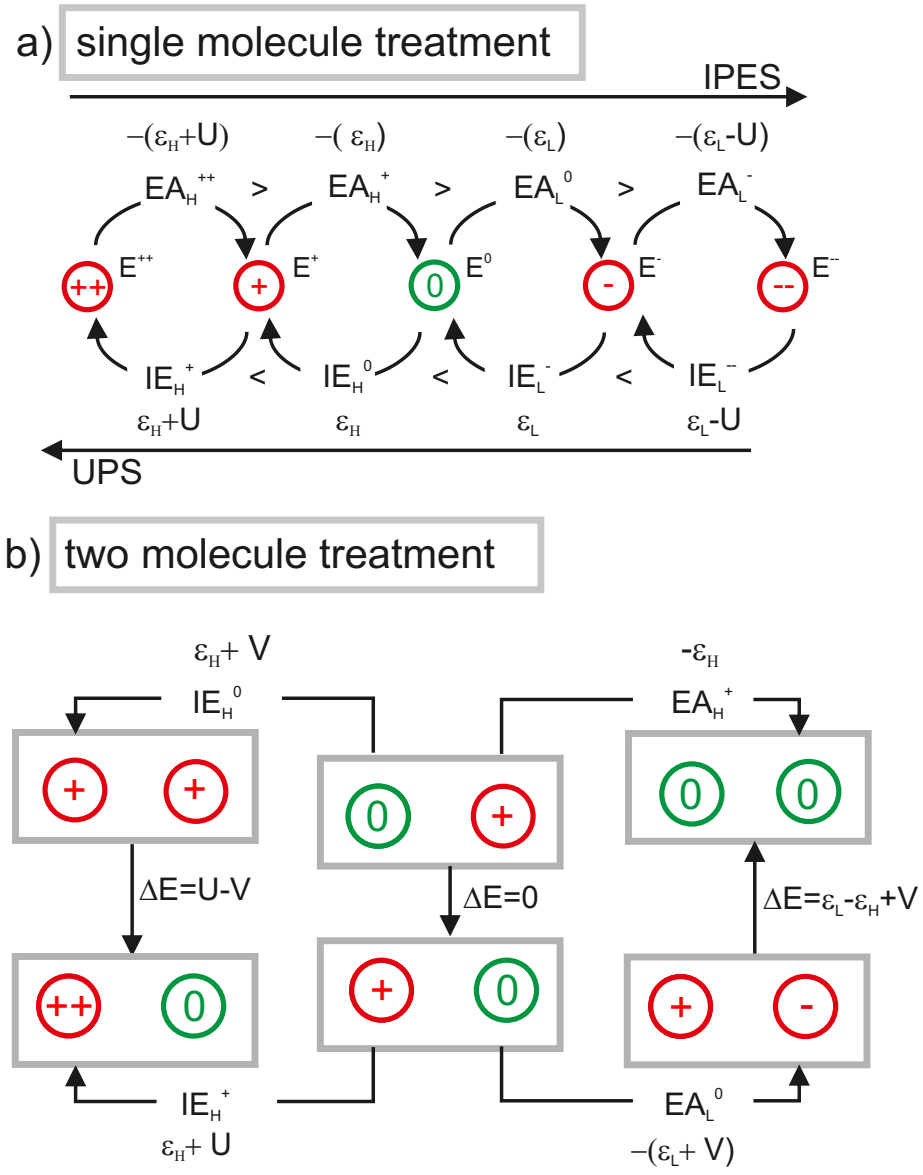

Figure 5.14.: Illustration of the (inverse) photoemission HOMO-($_H$) and LUMO($_L$)-derived transitions in (a) a single-molecule picture and (b) a two-molecule picture. The comparison between both pictures illustrates the correlation between the on-site (U) and inter-site (V) Coulomb repulsion.
For the electron binding energies ϵ_H and ϵ_L, see text.

(photo)electron q is affected by this electric field $\phi_{el,local}(r)$ via the simple relation:

$$\begin{aligned} V(r) &= q \cdot \phi_{el,local}(r) \\ V(r) &= \frac{1}{4\pi\epsilon_0\epsilon_r}\frac{qq^+}{r} \end{aligned} \tag{5.8}$$

Considering an electron "feeling" the electric field $\phi_{el}(r)$ given by a positive point charge, the electron's binding energy is increased by an amount $V(r)$ (here: ≈ 0.5 eV). As boundary conditions one further obtains:

$$\begin{aligned} V(r \to \infty) &= 0 \\ 0 < V(r \neq \infty, \neq 0) &< U \\ V(r = 0) &= U \end{aligned} \tag{5.9}$$

Fig. 5.14(b) depicts all possible photoemission 1-electron-transitions starting from an initial state comprising a neutral and a single positively charged site at a finite distance r. For the ionization of the cation neighboring a neutral molecule, one can refer to the single-molecule picture according to Fig. 5.14(a): $IE^+ = \epsilon_H + U$. As final state, one obtains a double positively charged molecule neighboring a neutral one that can be seen as part of a dielectric medium.
When, however, ionising the neutral molecule, IE^0 is affected by the positive point charge nearby. As final state for IE^0 two holes are paired on two different sites next to each other. In analogy to the on-site Coulomb repulsion (U), where holes are paired on the same site, this Coulomb interaction is termed inter-site Coulomb repulsion (V), resulting in $IE^0 = \epsilon_H + V$.

Conversely, all possible inverse photoemission 1-electron-transitions on that two-molecule initial state can be discussed. For the electron acceptance of the cation neighboring a neutral molecule, again, the single-molecule treatment according to Fig. 5.14(a) can be applied: $EA_H^+ = -\epsilon_H$.
The final state for $EA_L^0 = -(\epsilon_L + V)$ yields an electron-hole pair located on two adjacent sites, reminiscent of a charge-transfer exciton. Here the observed transition EA_L is affected by $V(r)$, which accounts for the inter-site Coulomb attraction ($-V$).

So far all available 1-electron (inverse) photoemission transitions starting from an initial state comprising a cation and an adjacent neutral molecule are discussed and illustrated by the horizontal arrows in Fig. 5.14(b). The next step is to discuss the electron-transfer transitions from one site to the other, which are illustrated by the vertical arrows in Fig. 5.14(b).

Hole-transfer from the cation to the neutral molecule sums up to an energy

$\Delta E = 0$. This is because simultaneously oxidizing the neutral site (changing the number of electrons, $E^0 \rightarrow E^+$) and reducing the cationic site (changing the number of electrons, $E^+ \rightarrow E^0$) does not change the electron configuration in this two-molecule system.

$$C_{60}{}^{+}C_{60}{}^{0} \rightarrow C_{60}{}^{0}C_{60}{}^{+} \qquad \Delta E = 0 \tag{5.10}$$

In contrast, hole-transfer from one cation to another cation sums up to $\Delta E = U - V$. Here simultaneous oxidation of one cationic site ($E^+ \rightarrow E^{++}$) and reduction of the other cationic site ($E^+ \rightarrow E^0$) changes the electronic configuration of this two-molecule system. The system is changed from two holes paired on two adjacent sites, into two holes paired on the same site; this *requires* the on-site Coulomb repulsion and *provides* the inter-site Coulomb repulsion. From this relation one can deduce that the configuration of a dication, i.e. bipolaron [26,41,310] (E^{++}), can only be preferred against the pairing of two holes on adjacent sites if $V > U$.

$$C_{60}{}^{+}C_{60}{}^{+} \rightarrow C_{60}{}^{0}C_{60}{}^{++} \qquad \Delta E = U - V \tag{5.11}$$

Moreover, hole-transfer from a cation to an adjacent anion sums up to $\Delta E = \epsilon_L - \epsilon_H + V$. That is because simultaneously reducing the cationic site ($E^+ \rightarrow E^0$) and oxidizing the anionic site ($E^- \rightarrow E^0$) changes the electronic configuration of this two-molecule system. Indeed, the system is changed from a Coulombically bound electron-hole-pair configuration on adjacent sites to a configuration that is free from any mutual Coulomb interaction (two neutral molecules next to each other). This process of exciton recombination provides the energy $\epsilon_L - \epsilon_H$, reduced by the inter-site Coulomb attraction ($-V$). Accordingly, this attraction can be termed as exciton-binding energy of an electron-hole pair located on two adjacent sites.

$$C_{60}{}^{+}C_{60}{}^{-} \rightarrow C_{60}{}^{0}C_{60}{}^{0} \qquad \Delta E = -(\epsilon_H - \epsilon_L) + V \tag{5.12}$$

In total analogy to the given explanations on a cation neighbouring a neutral molecule, one can consider the 1-electron transitions starting from an initial state comprising an anion adjacent to a neutral molecule, i.e. a n-doped system.

Following equations (5.10)-(5.12), one can derive:

$$\begin{aligned} {C_{60}}^{-}{C_{60}}^{0} &\rightarrow {C_{60}}^{0}{C_{60}}^{-} \qquad \Delta E = 0 \\ {C_{60}}^{-}{C_{60}}^{-} &\rightarrow {C_{60}}^{0}{C_{60}}^{--} \quad \Delta E = U - V \\ {C_{60}}^{-}{C_{60}}^{+} &\rightarrow {C_{60}}^{0}{C_{60}}^{0} \qquad \Delta E = -(\epsilon_H - \epsilon_L) + V \end{aligned} \tag{5.13}$$

Excited states

In conjunction with the electron-hole pair located on two adjacent sites (charge-transfer exciton), which have been assessed as final state discussing inverse photoemission transitions on hole-doped C_{60} in a two-molecule picture, the electron-hole pair located on one single site can be assessed as final state reconsidering the single-particle picture.
In the previous discussion, the electronic ground state configurations of the neutral molecule (E^0) have been termed as final state upon electron acceptance of the cation's HOMO (EA_H^+) as referred to in Fig. 5.14(a).

$$EA_H^+ = E^0 - E^+ \tag{5.14}$$

This is now extended by invoking excited states as potential final states. Fig. 5.15(a) illustrates the inverse photoemission process of adding an electron to the cation's LUMO (EA_L^+), which yields an on-site electron-hole pair as final state being reminiscent of a Frenkel exciton. As depicted in Fig. 5.15(c) this final state can have either singlet (E^1) or triplet (E^3) configuration and represents the first excited state of the molecule.

$$EA_L^+ = E^1 - E^+ \tag{5.15}$$

As can be easily derived from eq.(5.14) and eq.(5.15), probing a hole-doped molecular system one has access to the neutral electronic ground state as well as the excited state, and thereby to the optical gap Δ_{opt}. Essentially Δ_{opt} correlates both of these states:

$$\Delta_{opt} = E^1 - E^0 \tag{5.16}$$

In accordance to the illustration in Fig. 5.15(a), this can be rewritten accounting for eq.(5.14) and eq.(5.15):

$$EA_L^+ - EA_H^+ = E^1 - E^0 = \Delta_{opt} \tag{5.17}$$

In total analogy, considering an n-doped system photoemission of the former

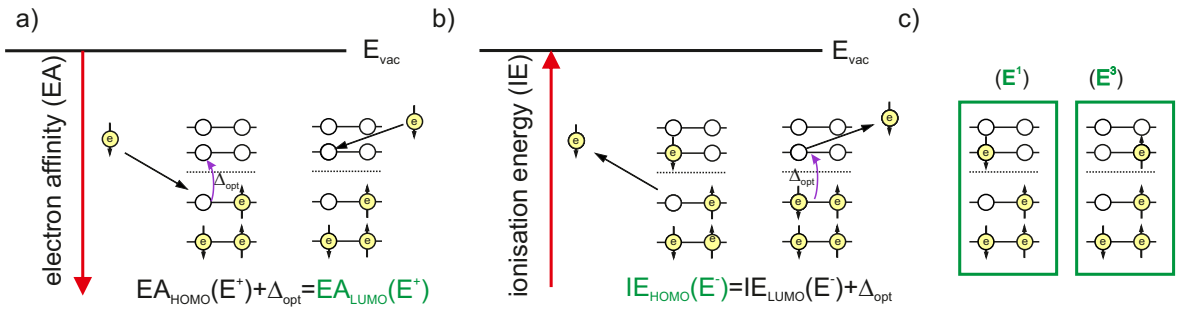

Figure 5.15.: Scheme associated with (a) eq.(5.17) and (b) eq.(5.20) illustrating the simultaneous experimental access of neutral ground (E^0) and excited state (E^1 and E^3), which serve as final states when employing (a) inverse photoemission on a hole doped system and (b) direct photoemission on an electron-doped system. Conclusively, Δ_{opt} can be easily derived.

HOMO level of an anion (IE_H^-) results in a neutral excited state E^1 as final state.

$$IE_H^- = E^1 - E^- \tag{5.18}$$

This corresponds to the first excited state[140] (Frenkel exciton), as depicted in Fig. 5.15(b). Accounting additionally for the process of removing an electron from the anion's LUMO (IE_L^-) in order to assess E^0,

$$IE_L^- = E^0 - E^- \tag{5.19}$$

one obtains in accordance to eq.(5.17):

$$IE_H^- - IE_L^- = E^1 - E^0 = \Delta_{opt} \tag{5.20}$$

Noteworthy, λ has been neglected on purpose for the sake of simplicity since starting out the detailed discussion on the on-site and inter-site Coulomb repulsion invoking the two-molecule picture. Now it is time *to invoke* λ again in order to elucidate the derivability of Δ_{opt} comparing the transitions starting from the neutral configurations with that starting from the charged ones. Regarding particularly an electrically doped system, namely correlating the transitions IE_H^0 and EA_L^+, EA_L^0 and IE_L^- respectively.

To do so, one needs to consider eq.(5.2) and (5.5) on the one hand and the pronounced mutual Coulomb interaction on the other hand, as previously discussed. Accounting for all that, eq.(5.17) and eq.(5.20) can be rewritten:

$$\begin{aligned} EA_L^+ + IE_H^0 &= \Delta_{opt} + V + \lambda \\ IE_H^- + EA_L^0 &= \Delta_{opt} + V + \lambda \end{aligned} \tag{5.21}$$

Assembling the Spectral Features

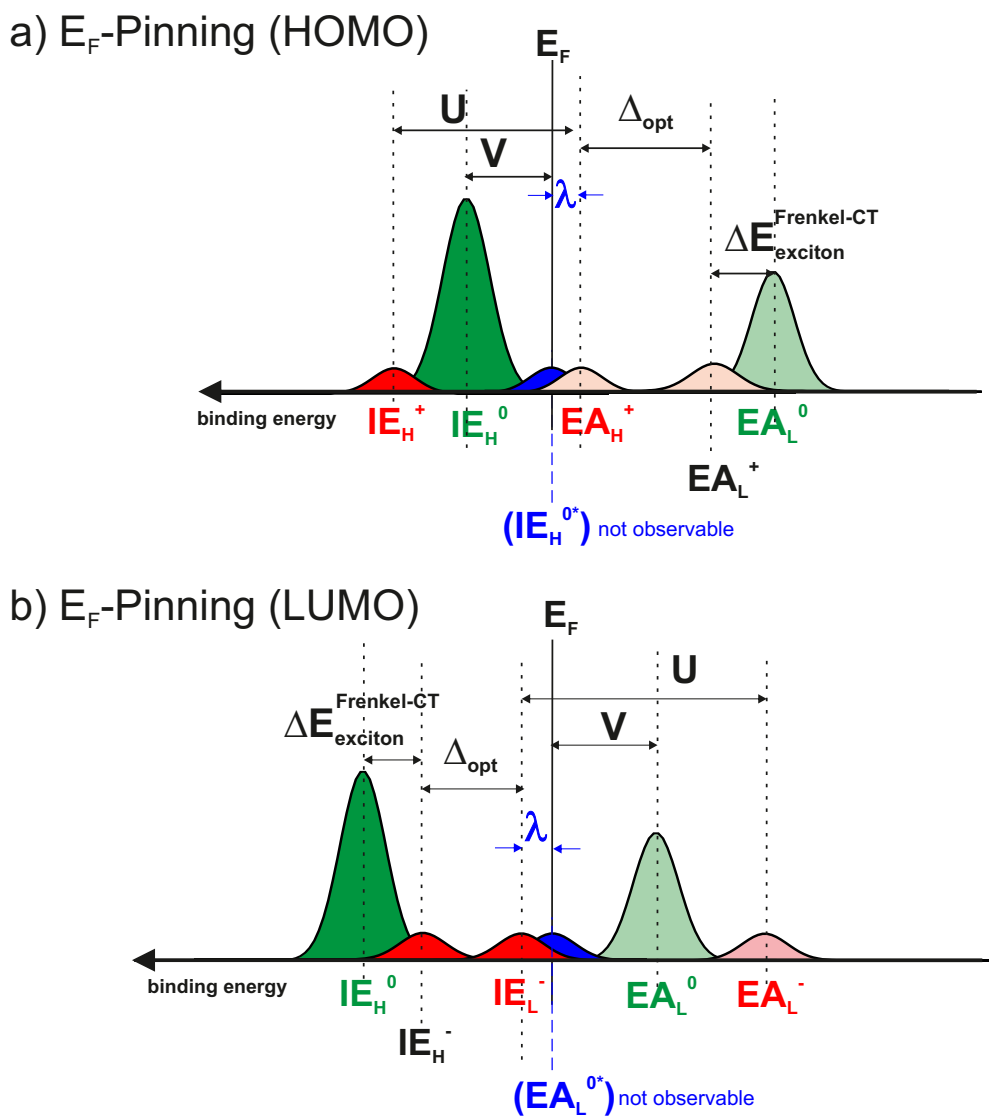

Figure 5.16.: Schematic illustration of the photoemission and inverse photoemission spectra of the HOMO ($_H$)- and LUMO ($_L$)-derived ionization (IE) and affinity (EA) levels of $C_{60}{}^0(C_{60}{}^+/C_{60}{}^-)$ in both E_F-Pinning- situations: (a) HOMO-level pinning, (b) LUMO-level pinning. U, Δ_{opt} and Δ_{trans} are to be read out directly. Assuming the energy-level shift associated to the HOMO relaxation (λ_H) to be equal to that associated to the LUMO relaxation (λ_L), one yields $\Delta_{trans} = \Delta_{opt} + U$ and accordingly $E_{exciton} = U$.
It is worth highlighting that the geometrical reorganization energy λ should be for directly read in such an experiment. Even though the Coulomb-interaction-free virtual (a) IE_H^{0*}, (b) EA_L^{0*} cannot be measured, the associated electron binding energy necessarily needs to coincide with E_F from simple electrostatics. Consequently (a) λ_H upon ionising the neutral molecule, (b) λ_L upon electron acceptance of the neutral molecule equals the energy associated to (a) EA_H^+, (b) IE_L^- with respect to E_F.

Collecting the insights of the previous subsections, Fig. 5.16 sketches the spectral

signature of (a) a hole-doped and (b) an electron-doped molecular film, when combining direct and inverse photoelectron spectroscopy. This spectral signature is moreover recalled to be deconvolutable into two contributions due to the different oxidation states. For the hole-doped system, as depicted in Fig. 5.16(a), those are $C_{60}{}^0$ (green) and $C_{60}{}^+$ (red) contributions; for the electron-doped system, as depicted in Fig. 5.16(b), those are $C_{60}{}^0$ (green) and $C_{60}{}^-$ (red) contributions. Accordingly, the individual features to the (inverse) photoelectron transitions can be assigned, as depicted at the bottom of Fig. 5.16(a) and (b). The relations between the ionization-level and affinity-level features obtained for the hole-doped C_{60} system, illustrated in Fig. 5.16(a), are moreover summarized in Tab. 5.2. According to these interrelations, the following material parameters can be derived from the entire spectral signature, as sketched in Fig. 5.16: transport gap Δ_{trans}, optical gap Δ_{opt}, on-site (U) and inter-site (V) Coulomb interaction and reorganization energy λ.

Table 5.2.: Summary of the relations between the observable ionization-level and affinity-level features, from which one can derive $U \approx 1.4$ eV, $\Delta_{opt} \approx 1.6$ eV, $\Delta_{trans} \approx 3.2$ eV, $\Delta E_{exciton}^{Frenkel-CT} = 0.65$ eV, $V = 0.5$ eV, $\lambda = \lambda_H \approx \lambda_L \approx 0.25$ eV

transitions	IE_H^0	IE_H^+	EA_H^+	EA_L^0	EA_L^+
IE_H^0	-	$U-(V+\lambda)$	$V+\lambda$	Δ_{trans}	$\Delta_{opt}+U-(V-\lambda)$
IE_H^+	$U-(V+\lambda)$	-	U	$\Delta_{trans}+U-(V+\lambda)$	$\Delta_{opt}+U$
EA_H^+	$V+\lambda$	U	-	$\Delta_{opt}+U-(V+\lambda)$	Δ_{opt}
EA_L^0	Δ_{trans}	$\Delta_{trans}+U-(V+\lambda)$	$\Delta_{opt}+U-(V+\lambda)$	-	$\Delta E_{exciton}^{Frenkel-CT}$
EA_L^+	$\Delta_{opt}+U-(V-\lambda)$	$\Delta_{opt}+U$	Δ_{opt}	$\Delta E_{exciton}^{Frenkel-CT}$	-

<u>λ **&** V</u> - The energy required to remove an electron from an isolated neutral molecule (IE^0) via UPS equals the energy gain upon returning it onto the isolated

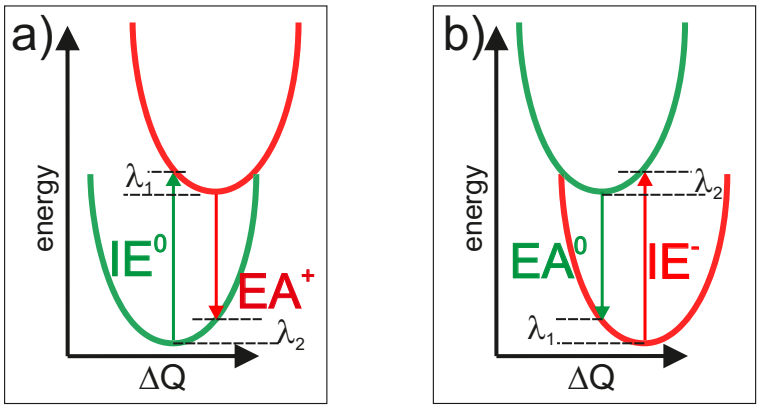

Figure 5.17.: The reorganization energy λ of an isolated molecule, the difference between IE^0 (EA^0) and EA^+ (IE^-), is composed of two relaxation energies: λ_1 after charging and λ_2 after returning to the neutral state.[16,89,186]

cation (EA^+) plus the reorganization energy λ, the sum of the two relaxation energies when a molecule changes its geometry from neutral to ionized (λ_1) and from ionized back to neutral (λ_2),[16,89,186] as depicted in Fig. 5.17(a).

$$\lambda = \lambda_1 + \lambda_2 \approx 2\lambda_2 \quad \text{if} \quad \lambda_1 \approx \lambda_2 \tag{5.22}$$

As the determination of IE^0 is affected by mutual Coulomb interaction (V), λ is not directly assessable. Indeed one obtains:

$$IE^0_H - EA^+_H = \lambda + V \tag{5.23}$$

In order to determine a value for λ, however, one can rely on the following reasoning: The pinning-induced cations originate from those neutral molecules whose HOMO levels are energetically aligned directly at E_F, as the metal acts as an electrical dopant. Those neutral molecules have already undergone the pinning-induced charge transfer, thusly are cations, and thereby only have a virtual IE^{0*}_H, depicted as blue feature in Fig. 5.16(a). This virtual IE^{0*}_H is unaffected by V, as the surrounding molecules are neutral. The energy difference between this virtual IE^{0*}_H, which indeed coincidences with E_F, and EA^+_H thus yields λ.

$$IE^{0*}_H - EA^+_H = \lambda \qquad \lambda = 0.25 \pm 0.25 \text{ eV} \tag{5.24}$$

In the present study the energy difference corresponding to λ was determined to be 0.25 ± 0.25 eV for C_{60}. Consequently, V ($= 0.5$ eV) can be directly determined by the energy difference between IE^0_H and virtual IE^{0*}_H (that is in coincidence with the E_F).

$$IE^0_H - IE^{0*}_H = V \qquad V = 0.5 \text{ eV} \tag{5.25}$$

$\underline{U}$ - As previously discussed, the on-site Coulomb interaction U, determined to be 1.4 eV for the valence hole in C_{60} in the present study, is defined as follows:

$$U = IE_H^+ - EA_H^+ \qquad U = 1.4 \text{ eV} \tag{5.26}$$

$\underline{\Delta_{opt}}$ - Furthermore, the optical gap Δ_{opt} can be readily accessed, as illustrated in Fig. 5.15 and according to Fig. 5.16(a), and yields:

$$\Delta_{opt} = EA_H^+ - EA_L^+ \qquad \Delta_{opt} = 1.6 \text{ eV} \tag{5.27}$$

Here, it is determined to be 1.6 eV for C_{60}.
As previously discussed, electron population of the LUMO of the cation can result either in the singlet (E^1) or triplet (E^3) excited state. This population is driven by simple statistics: the triplet state (1.55 eV for C_{60} [322]) is three times more populated than the singlet state (1.87 eV for C_{60} [322]). Concerning the inverse photoemission results obtained here, where cations are the minority, it is obvious, that E^1 cannot be resolved. The obtained value of $\approx$ 1.6 eV for Δ_{opt} in C_{60} accordingly needs to be attributed to E^3 and agrees very well with Ref.[322].

$\underline{\Delta_{trans}}$ - The difference between IE_H^0 and EA_L^0 yields the well known transport gap Δ_{trans}, which is determined (peak to peak) to be $\approx$ 3.2 eV for C_{60}.

$$\Delta_{trans} = IE_H^0 - EA_L^0 \qquad \Delta_{trans} = 3.2 \text{ eV} \tag{5.28}$$

One can subdivide Δ_{trans} further in the following contributions: Δ_{opt}, V, λ and a further contribution. According to Fig. 5.16(a) this is the energy difference between EA_L^+ and EA_L^0 (referring to Fig. 5.16(b) this is the energy difference between IE_H^- and IE_H^0), whose meaning regarding the exciton binding energy ($E_{exciton}$) is elucidated in the following paragraph.

$\underline{E_{exciton}}$ - Fig. 5.18 illustrates that the energy difference between EA_L^+ and EA_L^0 should in principle correspond to the exciton binding energy $E_{exciton}$ of an exciton, which is located on one single site (Frenkel exciton). This is related to the fact that, according to the given illustration, the incoming electron is either Coulombically bound to a hole in the HOMO of the same molecule in its final state (EA_L^+) or there is no Coulomb interaction at play at all (EA_L^0).
In the present case of a hole-doped C_{60} system, however, indeed mutual Coulomb interactions are at play. As final state, the electron in the LUMO of the formerly neutral molecule is Coulombically bound to the hole in the nearby cation. Thus the EA_L^0-transition results in a charge-transfer exciton, as mentioned earlier in

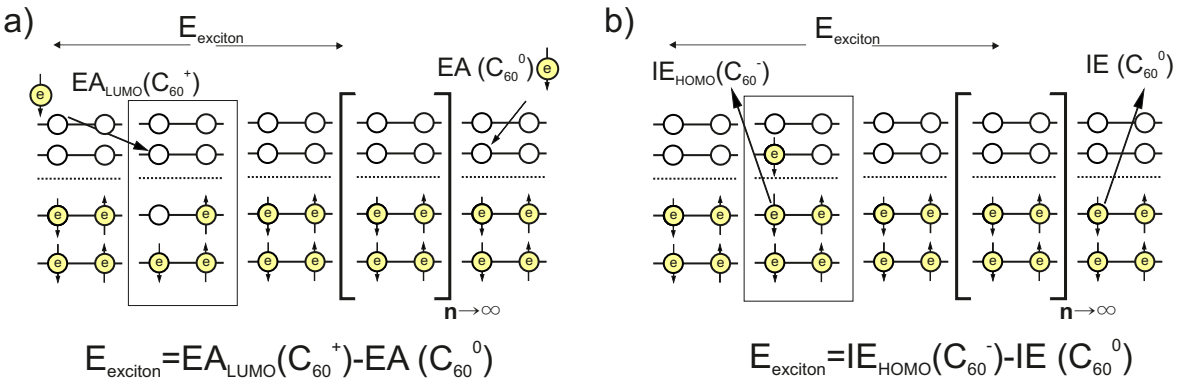

Figure 5.18.: The principle of deriving the exciton binding ($E_{exciton}$) energy from (a) inverse photoemission on hole-doped systems and (b) photoemission on electron-doped systems. Experimentally, neither EA_L^0 nor IE_H^0 are obtainable in a large (at infinity) distance, because they are affected by mutual Coulomb interactions. Accordingly, one has exclusive access to $\Delta E_{exciton}^{Frenkel-CT}$, representing the energy difference between the exciton to be either located on one single site or on adjacent sites.

the discussion. Accordingly, the energy difference between a "charge-transfer" and a "Frenkel" exciton $\Delta E_{exciton}^{Frenkel-CT}$ in a hole-doped system yields:

$$\Delta E_{exciton} = EA_L^+ - EA_L^0 \qquad \Delta E_{exciton}^{Frenkel-CT} = 0.65 \text{ eV} \tag{5.29}$$

Relying on the definition $\Delta_{trans} = \Delta_{opt} + E_{exciton}$ [93,94] one can further determine the charge transfer exciton binding energy $E_{exciton}^{CT}$

$$E_{exciton}^{CT} = \Delta_{trans} - \Delta_{opt} - \Delta E_{exciton}^{Frenkel-CT} \qquad E_{exciton}^{CT} = 0.95 \text{ eV} \tag{5.30}$$

According to Fig. 5.16 in this regard one also derives:

$$E_{exciton} = V + \lambda + \Delta E_{exciton}^{Frenkel-CT} \qquad E_{exciton}^{CT} = V + \lambda \tag{5.31}$$

Recalling the common expression of $E_{exciton} = U$, [80,86] that is often referred to in this context, one can now deduce that this expression is indeed valid, if $\Delta E_{exciton}^{Frenkel-CT} = U - V - \lambda$. In that case equation (5.28) can be rewritten:

$$\Delta_{trans} = \Delta_{opt} + U \tag{5.32}$$

The as discussed strong relation between the obtained values on the different types of Coulomb interactions, i.e. *repulsion* and *attraction*, is obvious: On the one hand there is the on-site (U) and inter-site (V) Coulomb repulsion, and on the other hand there is the on-site (Frenkel exciton) and inter-site (charge-transfer

exciton) Coulomb attraction between a hole in the HOMO of one site and an electron in the LUMO of the same or neighboring site.
Yet, specific attention has to be drawn to the particular differences that inhibit their equivalent usage. Indeed the strength of Coulomb interaction between charges in different orbitals, as referred to for Coulomb attraction between a hole in the HOMO level and an electron in the LUMO level, does not necessarily amount to the same value as when equivalent charges repel each other in the same orbital, as referred to for two holes in the HOMO. One would need to discriminate between Coulomb interaction between electrons in the same orbital and in two different orbitals, respectively.[11] Moreover, the energy shift upon reorganization due to charging does not necessarily affect two different orbitals in the same manner, i.e. $\lambda_H \neq \lambda_L$. This is related to the exact distribution of the respective orbitals and might induce significant deviations for non-spherical and rather electronically asymmetric molecular structures: molecules with strong intramolecular dipole moments, as referred to in section 4.3.2. However, for C_{60} the equivalent usage of exciton binding energies and Coulomb repulsion is expected to be quite appropriate due to the extraordinary high molecular symmetry.

5.3. Conclusion

Cations can be generated by employing a metallic substrate with a work function (Φ) larger than the ionization energy (IE) of the molecular adsorbate. Thereby, the Fermi level (E_F) of the underlying metal is moved into the occupied density of states (DOS) of the molecules, inducing electron transfer from the molecules into the metal to establish electronic equilibrium (E_F-pinning). Unfortunately, however, for molecule-metal interfaces, one often finds hybridization of molecular and metallic states in the first monolayer, which is well known to *not* yield integer-charged molecules. This hybridization, moreover, causes a "collapse" of the entire band bending region into a localized interface dipole.
By employing a dielectric interlayer, the formation of metal-induced gap states is suppressed, integer charge transfer occurs resulting in a mixture of clearly distinguishable charged and neutral molecules in the monolayer and band bending is observed for multilayer coverages.
In the present direct and inverse photoelectron spectrsocopy (XPS, UPS, IPES) study, this is realized with an Au-supported thin (d = 1.2 nm) MoO_3-layer ($\epsilon_r = 9$, $\Phi = 6.8$ eV) and C_{60} as molecular semiconductor. The thusly obtained results can be summarized as follows:

1. **Multilayer**
   C_{60}-cations accumulation at the C_{60}/MoO_3-interface indeed induces band bending in the subsequently deposited C_{60}-multilayer. The evolution of the electrostatic potential (as obtained by the evolution of Φ, E_{HOMO}, C1s simultaneously) throughout the C_{60}-layers was rationalized using a simple electrostatic model, which additionally accounts for a linear pushback effect in the (sub)monolayer regime.
   Due to this hole accumulation, unusual photo-induced charging apparently occurs at comparably low C_{60}-coverages ($\approx$ 70 Å) when employing direct photoemission, which is in marked contrast to most photoemission studies on C_{60}-films.

2. **(Sub)monolayer**
   In the (sub)monolayer regime, the superimposed spectral contributions of neutral molecules and cations in the molecular semiconductor could be clearly deconvoluted over the entire energy region for the first time. Supported by DFT calculations, the energy-level shift in neutral molecules due to inter-site Coulomb interaction with nearby cations was estimated to be $\approx$ 0.5 eV. Naturally, the on-site Coulomb interaction (Hubbard U) exceeds that value and was experimentally determined here to amount to

1.4 eV for the valence hole in the C_{60}-film. Most importantly, this term causes the ionization energy of cations to be larger than that of the respective neutral molecules. This implies the need for a fundamental revision of the widely established picture of polarons in molecular semiconductors. Instead of one single, singly occupied state within the gap of the neutral molecules, the respective frontier molecular orbital (i.e., the HOMO for positive and the LUMO for negative polarons) is split by on-site Coulomb repulsion in an upper unoccupied sub-level (EA_H^+) and a lower occupied sub-level (IE_H^+). For UPS and IPES, this implies that the spectral intensity of a polaron does not necessarily appear cut by E_F. Indeed molecular films are not metallic, as long as U dominates over the weak molecule-molecule and molecule-substrate interactions. This is generally the case for molecules in the bulk film or deposited on passivated or weakly interacting substrates.

The obtained UPS/IPES results cannot properly be explained by a single-particle treatment due to mutual Coulomb interaction. Consequently a two-particle treatment is needed. In accordance direct photoemission on a hole-doped film, i.e. an initial state comprising of a cation and an adjacent neutral molecule, results in hole-pairing on either one single site or two adjacent sites. On the other hand, inverse photoemission results in either a pair of two neutral molecules or an electron-hole pair, located on adjacent sites (charge-transfer exciton).
Accordingly, the charge-transfer exciton is considered as final state upon electron-occupation of the LUMO of a neutral molecule in close distance to a cation (EA_L^0). Likewise, the Coulombically bound electron-hole pair on one site (Frenkel exciton) is rationalized as final state upon electron-occupation of a cation's former LUMO (EA_L^+). Comparing both values, the energy difference between the exciton binding energy of a Frenkel and a charge-transfer (CT) exciton ($\Delta E_{exciton}^{Frenkel-CT} \approx 0.65$ eV) is experimentally accessible. With respect to the determined transport gap (peak-to-peak: $\Delta_{trans} = IE_H^0 - EA_L^0 = 3.2$ eV) and optical gap (peak-to-peak: $\Delta_{opt} = EA_L^+ - EA_L^+ = 1.6$ eV), one can accordingly estimate the exciton binding energy of a Frenkel exciton to be 1.6 eV and that of charge-transfer exciton to be 0.95 eV.

IV. Summary and Outlook

The aim of the present work was to explore the spectral signature of charge carriers in molecular semiconductors, in particular that of positive polarons. Following a comprehensive experimental approach combining XPS, UPS, and IPES, complementary information on both occupied and unoccupied states was gathered. Finally, this allowed revising the standard model for the energy levels of molecular semiconductors comprising polarons, which has been trusted for decades.

As a first step, a sample structure was identified that allows deliberately generating charged molecules and applying the photoemission techniques to assess the associated energetics. This sample concept relies on E_F-pinning, which occurs for molecular layers exhibiting either an ionization energy (IE) larger, or an electron affinity (EA) lower than the work function (Φ) of the supporting substrate. Consequently, charge transfer occurs between the molecule and the substrate to establish electronic equilibrium. Concomitantly, strong electronic coupling between the adsorbed molecules and the underlying metal surfaces might significantly alter the spectral information obtained via photoemission, as it suppresses the occurrence of localized charges on the molecules. To ensure the generation of "pure" cations, i.e. without affecting the respective molecular DOS, a passivating interlayer was employed. In this regard it was necessary to verify that the molecules physically adsorb on the implemented metal-oxide interlayer. Therefore, a number of molecular adsorbates on metal-oxide substrates were characterized via photoemission. As a result, the degree of undesired interaction between molecule and metal oxide could be quantified by determining the critical substrate work function (Φ_{crit}), at which E_F-pinning sets in.

Φ_{crit} is an intrinsic material parameter for any subsequently deposited material, if no interface dipole $\Delta\Phi_{ID}$ arises upon monolayer formation or, in other words, if the process of E_F-pinning is exclusively ruled by the individual material parameters, that is, the substrate-Φ and IE/EA of the adsorbate.

In order to drive a certain adsorbate beyond Φ_{crit} into E_F-Pinning, both of the following strategies were pursued to cover a large range of substrate work functions: (a) various metal-oxide substrates were employed that covered a work function range from 2.3 eV to 7.0 eV, and (b) the substrate work function of one particular metal oxide (ITO) was tuned from 4.2 eV to 6.3 eV by varying the submonolayer coverage of interlayers formed by strong molecular acceptors. The shifted onset of E_F-pinning observed in both studies is at odds with the expected

scenarios following simple electrostatics, as mentioned above. This finding could be rationalized by additionally taking into account further interfacial phenomena that cause interface dipoles $\Delta\Phi_{ID}$ and, thus, determine the electronic structure at a given interface:

(a) Upon deposition of strongly dipolar merocyanines, their LUMO level is found E_F-pinned at unexpectedly high substrate-Φ values of 4.3 eV, which is exceedingly larger than the molecule's EA$\approx$2.0 eV. Moreover, extraordinary high Φ-values of 6.0 eV, that is, much larger than the molecule's IE $\approx$ 5 eV, need to be employed in order to establish E_F-pinning of the merocyanine's HOMO. This is rationalized by the occurrence of an interface dipole mainly attributed to chemical coordination of the molecular functional groups and the thusly induced dipolar layer formation. As result, the surface potential is significantly altered. In essence, this chemically driven interface formation is *non predictable* with respect to the individual material parameters (the molecular IE/EA and the substrate Φ).

    Indeed, predictions neglecting such interface dipoles have led to the wrong assumption that such interfaces were advantageous for charge-extraction in organic electronic devices, although the exact opposite is in fact the case.

(b) For incompletely acceptor-precovered substrates, the HOMO level of a subsequently deposited material is found to be E_F-pinned if the molecule adsorbs at the acceptor-precovered surface patches, while for molecules on the pristine ITO substrate portion, the pushback effect is induced. Such an energetically mixed monolayer determines the surface potential for subsequent layers in multilayer growth, and, hence, the occurrence of E_F-pinning, such that the critical pinning work function is "delayed". This finding highlights the fact that the superposition of local work functions of dissimilar surface areas results from a highly complex interplay of different effects upon molecular monolayer formation. Thus, the energy-level alignment at real (non-uniform) interfaces remains *hardly predictable*, if only the individual (macroscopically averaged) material parameters are considered.

These findings could be rationalized either by a partial pushback effect or by chemical interaction driven by a specific functional group in the molecular structure of the deposited material, whereby the latter induces a bond dipole and dipolar layer formation.
The pushback effect itself was identified to be a phenomenon affecting the surface electron density of the metal oxide rather than the molecular monolayer and, as such, inevitably occurs at molecule/metal-oxide interfaces. This effect is not

causally linked to the mixing of molecular and substrate electronic states and, therefore, can be *predictably* quantified to lower the surface potential in general by 0.3 eV.

Clearly, *non-predictable* and, as such, undesired interfacial phenomena are to be avoided, as they might affect the spectral signature of polarons. In order to ensure the generation of "pure" cations, C_{60} was chosen as molecular adsorbate, as it exhibits an inherently inert molecular structure without functional groups that could participate in chemical interactions with the substrate.

As result of these efforts, the following sample concept based on E_F-pinning was identified to not only account for a sufficient amount of charge carriers to be detectable by photoemission techniques but also to exclude undesired molecule-substrate interactions: C_{60} (IE = 6.4 eV) /ultrathin MoO_3 (Φ = 6.8 eV) /Au(111)-heterostructure.

The spectral signature of C_{60}-cations, as obtained for this particular system, allowed revising the generally accepted model for the energy levels of organic semiconductors comprising polarons, which was outlined in part I (Fig. I.2). In contrast to the common perception, the HOMO level of neutral C_{60} is *not* necessarily cut by E_F of the system, but, rather, subdivided by a Coulomb term U (here: 1.4 eV) into one occupied and one unoccupied HOMO-derived sub-level, as depicted in the left panel of Fig. IV.1.

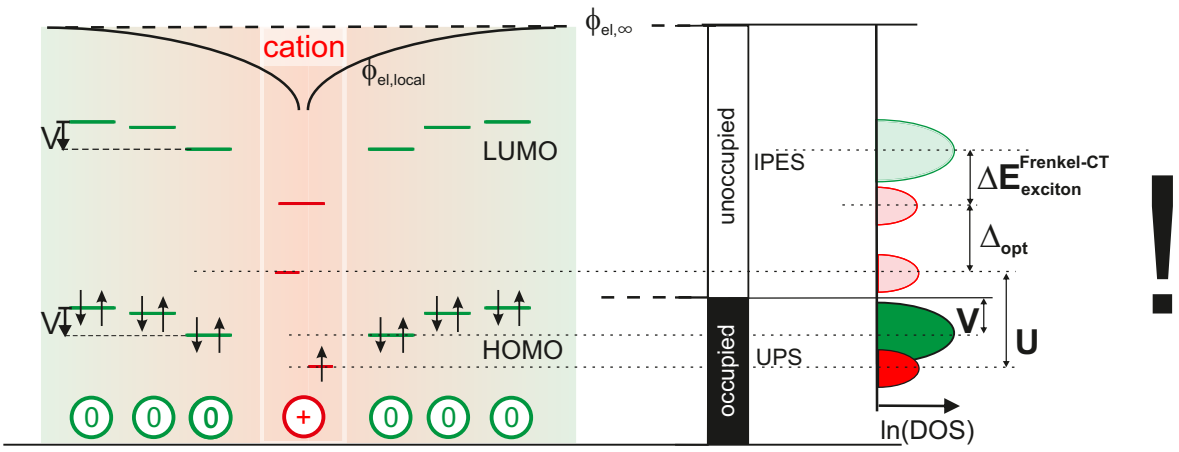

Figure IV.1.: From left to right: revision of the single-particle energy levels for neutral molecules (green) surrounding a cation (red) with respect to a common vacuum level, their experimental accessibility to (inverse) photo-electron spectroscopy depending on their electron occupancy and the corresponding density of states (DOS) on a logarithmic scale, ln(DOS). The on-site Coulomb repulsion U causes a splitting into two HOMO sub-levels of a molecular cation, while the inter-site Coulomb repulsion V induces an energy-level shift to higher binding energies of the neutral molecules in close vicinity to the cation. The rightmost panel further illustrates the on-site (U) and inter-site Coulomb repulsion V, the optical (Δ_{opt}) and the transport gap Δ_{trans}, as well as the energy difference between an on-site and inter-site exciton $\Delta E^{Frenkel-CT}_{exciton}$.

In this context, previous experimental observations could be elucidated with respect to the key importance of the substrate. Only in the special case of charge delocalization predominant in a molecular layer, as e.g. promoted by the presence of an underlying metal substrate, is the spectral feature associated with the charge-transport level indeed cut by E_F. The molecular layer then shows metallic behaviour, as the Coulomb term becomes negligible (U=0). However, in the general case where no metallic substrate is employed and no further effects promoting charge delocalization are at work, weakly interacting molecular systems are associated with a significant U-value and accordingly are not metallic. Clearly, this emphasizes that the present fundamental revision of the polaron model is essential to complement the general understanding of excess charge in molecular semiconductors, concerning the opposite trends of delocalization and localization of these charges in particular.
By further including the inter-site Coulomb interaction between charged and neutral molecules, a complete picture of the energy levels of molecular semiconductors comprising excess charge was derived. Due to these interactions, the hitherto used isolated-molecule treatment is not capable of properly explaining the observed spectral signature of hole-doped C_{60}. In contrast, this necessitates to consider a multi-site system to account for inter-site interaction, for which a two-molecule system comprising one molecular cation in the vicinity of a neutral molecule was chosen for the sake of simplicity. As depicted in Fig. IV.2, employing direct photoemission on such an initial state yields two available final states: on the one hand, two paired holes on the same site and on the other hand, two paired holes on adjacent sites can be obtained. The difference between both ionization energies then equals the difference between the *on-site* Coulomb repulsion U ($\approx$ 1.4 eV) and the *inter-site* Coulomb repulsion V ($\approx$ 0.5 eV).

Figure IV.2.: Illustration of two possible final states resulting from direct photoemission on a two-molecule system comprising a cation and a neutral molecule in its vicinity. Both ionization energies differ by an energy $U - V$.

In full analogy, inverse photoemission spectroscopy (IPES) was employed. The electron occupation of the neutral molecule's LUMO results in a Coulombically bound *inter-site* electron-hole pair that is reminiscent of a charge-transfer (CT) exciton. The electron-occupation of a molecular cation's LUMO results in a Coulombically bound *on-site* electron-hole pair, which is reminiscent of a

Frenkel exciton. The energy difference between these two was determined to be $\Delta E_{exciton}^{Frenkel-CT} = 0.65$ eV.
In addition to increasing the fundamental understanding of the molecular energy levels associated with polarons, the present thesis demonstrates an application of (inverse) photoemission techniques beyond simply determining the transport gap of a molecular semiconductor (Δ_{trans}=3.2 eV for C_{60}). Employing IPES on hole-doped molecular systems, optical transition energies can be directly derived: Upon comparing the electron affinity of the HOMO-derived sub-level (EA_H^+) of the molecular cation [yielding the neutral molecule's ground state (E^0) as final state] with that of the cation's LUMO (EA_L^+) [yielding the neutral molecule's first excited triplet state (E^3)], the first excitation energy is determined to $\Delta_{opt} = 1.6$ eV for C_{60}. This is particularly relevant as this very transition is optically forbidden in C_{60}, which, therefore, renders the experimental approach of determining above energy levels a valuable experimental tool for assessing energies of forbidden optical transitions in general.
An illustration of the interrelation between above mentioned material parameters, which could be derived from the spectral signature of hole-doped C_{60}, is depicted in the right panel of Fig. IV.1

Within this work, fundamental aspects of the interfaces between metal-oxide electrodes and organic materials present in organic electronic devices such as hybrid solar cells, were addressed. On the one hand, it was demonstrated that, apart from the pushback effect at molecule/metal-oxide interfaces, *unpredictable* interface dipoles frequently arise, which are due to chemical coordination of molecular functional groups. This emphasizes the importance of further fundamental studies aiming at facilitating the quantitative prediction of such interfacial phenomena which, thereby, can significantly improve the control over the electronic properties of interfaces in organic electronic devices.
On the other hand, the new model for the energy levels associated to excess charges in molecular semiconductors aims to replace the common perceptions both in fundamental and applied research, as well as in education on the academic level in the field of organic electronics. Clearly, already the re-interpretation of existing experimental results in pertinent literature might lead to new insights. Even more importantly, however, this novel conception might inspire future experiments further addressing the fundamental properties of charge carriers in weakly interacting molecular systems, in particular of charges induced by the electrical doping of molecular semiconductors through admixing strong electron donors or acceptors.

Bibliography

[1] H. Shirakawa, E. J. Louis, A. G. MacDiarmid, C. K. Chiang, A. J. Heeger, *Synthesis of Electrically Conducting Organic Polymers: Halogen Derivatives of Polyacetylene, (CH)x*, Journal of the Chemical Society, Chemical Communications, pp. 578–580 (1977).

[2] C. K. Chiang, C. R. Fincher, Y. W. Park, A. J. Heeger, H. Shirakawa, E. J. Louis, S. C. Gau, A. G. MacDiarmid, *Electrical Conductivity in Doped Polyacetylene*, Physical Review Letters **39(17)**, 1098 (1977).

[3] A. J. Heeger, *Semiconducting and Metallic Polymers: The Fourth Generation of Polymeric Materials (Nobel Lecture)*, Angewandte Chemie International Edition **40(14)**, 2591 (2001).

[4] H. Shirakawa, *The Discovery of Polyacetylene Film: The Dawning of an Era of Conducting Polymers (Nobel Lecture)*, Angewandte Chemie International Edition **40(14)**, 2574 (2001).

[5] A. G. MacDiarmid, *"Synthetic Metals": A Novel Role for Organic Polymers (Nobel Lecture)*, Angewandte Chemie International Edition **40(14)**, 2581 (2001).

[6] D. De Rossi, *Electronic Textiles: A Logical Step*, Nature Materials **6(5)**, 328 (2007).

[7] I. Mcculloch, *Thin films: Rolling out Organic Electronics*, Nature Materials **4(8)**, 583 (2005).

[8] R. A. Marcus, *Electron Transfer Reactions in Chemistry. Theory and Experiment*, Reviews of Modern Physics **65(3)**, 599 (1993).

[9] V. Coropceanu, M. Malagoli, D. A. da Silva Filho, N. E. Gruhn, T. G. Bill, J. L. Brédas, *Hole- and Electron-Vibrational Couplings in Oligoacene Crystals: Intramolecular Contributions*, Physical Review Letters **89(27)**, 275503 (2002).

[10] J.-L. Brédas, D. Beljonne, V. Coropceanu, J. Cornil, *Charge-Transfer and Energy-Transfer Processes in π-Conjugated Oligomers and Polymers: A Molecular Picture*, Chemical Reviews **104(11)**, 4971 (2004).

[11] E. Canadell, M.-L. Doublet, C. Iung, *Orbital Approach to the Electronic Structure of Solids* (Oxford University Press, 2012).

[12] P. Fazekas, *Lecture Notes on Electron Correlation and Magnetism* (World Scientific, Singapore, River Edge, N.J, 1999).

[13] E.-G. Kim, V. Coropceanu, N. E. Gruhn, R. S. Sánchez-Carrera, R. Snoeberger, A. J. Matzger, J.-L. Brédas, *Charge Transport Parameters of the*

Pentathienoacene Crystal, Journal of the American Chemical Society **129(43)**, 13072 (2007).

[14] N. Ueno, S. Kera, *Electron Spectroscopy of Functional Organic Thin Films: Deep Insights into Valence Electronic Structure in Relation to Charge Transport Property*, Progress in Surface Science **83(10–12)**, 490 (2008).

[15] N. Ueno, S. Kera, K. Sakamoto, K. K. Okudaira, *Energy Band and Electron-Vibration Coupling in Organic Thin Films: Photoelectron Spectroscopy as a Powerful Tool for Studying the Charge Transport*, Applied Physics A **92(3)**, 495 (2008).

[16] S. Kera, H. Yamane, N. Ueno, *First-Principles Measurements of Charge Mobility in Organic Semiconductors: Valence Hole–Vibration Coupling in Organic Ultrathin Films*, Progress in Surface Science **84(5–6)**, 135 (2009).

[17] H. Yamane, S. Nagamatsu, H. Fukagawa, S. Kera, R. Friedlein, K. K. Okudaira, N. Ueno, *Hole-Vibration Coupling of the Highest Occupied State in Pentacene Thin Films*, Physical Review B **72(15)**, 153412 (2005).

[18] S. Duhm, Q. Xin, S. Hosoumi, H. Fukagawa, K. Sato, N. Ueno, S. Kera, *Charge Reorganization Energy and Small Polaron Binding Energy of Rubrene Thin Films by Ultraviolet Photoelectron Spectroscopy*, Advanced Materials **24(7)**, 901 (2012).

[19] S. Hasegawa, T. Mori, K. Imaeda, S. Tanaka, Y. Yamashita, H. Inokuchi, H. Fujimoto, K. Seki, N. Ueno, *Intermolecular Energy-Band Dispersion in Oriented Thin Films of Bis(1,2,5-Thiadiazolo)-p-Quinobis(1,3-Dithiole) by Angle-Resolved Photoemission*, The Journal of Chemical Physics **100(9)**, 6969 (1994).

[20] H. Yamane, S. Kera, K. K. Okudaira, D. Yoshimura, K. Seki, N. Ueno, *Intermolecular Energy-Band Dispersion in PTCDA Multilayers*, Physical Review B **68(3)**, 033102 (2003).

[21] G. N. Gavrila, H. Mendez, T. U. Kampen, D. R. T. Zahn, D. V. Vyalikh, W. Braun, *Energy Band Dispersion in Well Ordered N,N'-Dimethyl-3,4,9,10-Perylenetetracarboxylic Diimide Films*, Applied Physics Letters **85(20)**, 4657 (2004).

[22] N. Ueno, A. Kitamura, K. K. Okudaira, T. Miyamae, Y. Harada, S. Hasegawa, H. Ishii, H. Inokuchi, T. Fujikawa, T. Miyazaki, K. Seki, *Angle-Resolved Ultraviolet Photoelectron Spectroscopy of Thin Films of Bis(1,2,5-Thiadiazolo)-p-Quinobis (1,3-Dithiole) on the MoS2 Surface*, The Journal of Chemical Physics **107(6)**, 2079 (1997).

[23] H. Kakuta, T. Hirahara, I. Matsuda, T. Nagao, S. Hasegawa, N. Ueno, K. Sakamoto, *Electronic Structures of the Highest Occupied Molecular Orbital Bands of a Pentacene Ultrathin Film*, Physical Review Letters **98(24)**, 247601 (2007).

[24] G. Koller, B. Winter, M. Oehzelt, J. Ivanco, F. P. Netzer, M. G. Ramsey, *The Electronic Band Alignment on Nanoscopically Patterned Substrates*, Organic Electronics **8(1)**, 63 (2007).

[25] S. Kera, H. Fukagawa, T. Kataoka, S. Hosoumi, H. Yamane, N. Ueno, *Spectroscopic Evidence of Strong π-π Interorbital Interaction in a Lead-Phthalocyanine Bilayer Film Attributed to the Dimer Nanostructure*, Physical Review B **75(12)**, 121305 (2007).

[26] N. Koch, A. Rajagopal, J. Ghijsen, R. L. Johnson, G. Leising, J.-J. Pireaux, *Bipolaron: The Stable Charged Species in n-Doped p-Sexiphenyl*, The Journal of Physical Chemistry B **104(7)**, 1434 (2000).

[27] D. Steinmüller, M. G. Ramsey, F. P. Netzer, *Polaron and Bipolaronlike States in n-Doped Bithiophene*, Physical Review B **47(20)**, 13323 (1993).

[28] R. Macovez, A. Goldoni, L. Petaccia, I. Marenne, P. A. Brühwiler, P. Rudolf, *Reversible Phase Transformation and Doubly Charged Anions at the Surface of Simple Cubic RbC60*, Physical Review Letters **101(23)**, 236403 (2008).

[29] R. Macovez, M. R. C. Hunt, A. Goldoni, M. Pedio, P. Rudolf, *Surface Hubbard U of Alkali Fullerides*, Journal of Electron Spectroscopy and Related Phenomena **183(1–3)**, 94 (2011).

[30] O. Bubnova, Z. U. Khan, H. Wang, S. Braun, D. R. Evans, M. Fabretto, P. Hojati-Talemi, D. Dagnelund, J.-B. Arlin, Y. H. Geerts, S. Desbief, D. W. Breiby, J. W. Andreasen, R. Lazzaroni, W. M. Chen, et al., *Semi-Metallic Polymers*, Nature Materials **13(2)**, 190 (2014).

[31] W. Gao, A. Kahn, *Controlled p-Doping of the Hole-Transport Molecular Material N,N'-Diphenyl-N,N'-Bis(1-Naphthyl)-1,1'-Biphenyl-4,4'-Diamine with Tetrafluorotetracyanoquinodimethane*, Journal of Applied Physics **94(1)**, 359 (2003).

[32] I. Salzmann, G. Heimel, S. Duhm, M. Oehzelt, P. Pingel, B. M. George, A. Schnegg, K. Lips, R.-P. Blum, A. Vollmer, N. Koch, *Intermolecular Hybridization Governs Molecular Electrical Doping*, Physical Review Letters **108(3)**, 035502 (2012).

[33] H. Méndez, G. Heimel, A. Opitz, K. Sauer, P. Barkowski, M. Oehzelt, J. Soeda, T. Okamoto, J. Takeya, J.-B. Arlin, J.-Y. Balandier, Y. Geerts, N. Koch, I. Salzmann, *Doping of Organic Semiconductors: Impact of Dopant Strength and Electronic Coupling*, Angewandte Chemie **125(30)**, 7905 (2013).

[34] M. Oehzelt, N. Koch, G. Heimel, *Organic Semiconductor Density of States Controls the Energy Level Alignment at Electrode Interfaces*, Nature Communications **5(4174)** (2014).

[35] M. Fahlman, A. Crispin, X. Crispin, S. K. M. Henze, M. P. d. Jong, W. Osikowicz, C. Tengstedt, W. R. Salaneck, *Electronic Structure of Hybrid*

Interfaces for Polymer-Based Electronics, Journal of Physics: Condensed Matter **19(18)**, 183202 (2007).

[36] A. Wilke, P. Amsalem, J. Frisch, B. Bröker, A. Vollmer, N. Koch, *Electric Fields Induced by Energy Level Pinning at Organic Heterojunctions*, Applied Physics Letters **98(12)**, 123304 (2011).

[37] M. T. Greiner, M. G. Helander, W.-M. Tang, Z.-B. Wang, J. Qiu, Z.-H. Lu, *Universal Energy-Level Alignment of Molecules on Metal Oxides*, Nature Materials **11(1)**, 76 (2012).

[38] G. Heimel, L. Romaner, E. Zojer, J.-L. Brédas, *The Interface Energetics of Self-Assembled Monolayers on Metals*, Accounts of Chemical Research **41(6)**, 721 (2008).

[39] Y. Zou, L. Kilian, A. Schöll, T. Schmidt, R. Fink, E. Umbach, *Chemical Bonding of PTCDA on Ag Surfaces and the Formation of Interface States*, Surface Science **600(6)**, 1240 (2006).

[40] J. L. Brédas, G. B. Street, *Polarons, Bipolarons, and Solitons in Conducting Polymers*, Accounts of Chemical Research **18(10)**, 309 (1985).

[41] S. Braun, W. R. Salaneck, M. Fahlman, *Energy-Level Alignment at Organic/Metal and Organic/Organic Interfaces*, Advanced Materials **21(14-15)**, 1450 (2009).

[42] H. Ishii, K. Sugiyama, E. Ito, K. Seki, *Energy Level Alignment and Interfacial Electronic Structures at Organic/Metal and Organic/Organic Interfaces*, Advanced Materials **11(8)**, 605 (1999).

[43] D. Cahen, A. Kahn, *Electron Energetics at Surfaces and Interfaces: Concepts and Experiments*, Advanced Materials **15(4)**, 271 (2003).

[44] N. Koch, *Energy Levels at Interfaces between Metals and Conjugated Organic Molecules*, Journal of Physics: Condensed Matter **20(18)**, 184008 (2008).

[45] N. Koch, *Organic Electronic Devices and Their Functional Interfaces*, ChemPhysChem **8(10)**, 1438 (2007).

[46] J. L. Brédas, R. R. Chance, R. Silbey, *Comparative Theoretical Study of the Doping of Conjugated Polymers: Polarons in Polyacetylene and Polyparaphenylene*, Physical Review B **26(10)**, 5843 (1982).

[47] M. Lögdlund, R. Lazzaroni, S. Stafström, W. R. Salaneck, J.-L. Brédas, *Direct Observation of Charge-Induced π-Electronic Structural Changes in a Conjugated Polymer*, Physical Review Letters **63(17)**, 1841 (1989).

[48] N. Ueno, in *Physics of Organic Semiconductors*, edited by W. Brütting, C. Adachi, pp. 65–89, *Electronic Structure of Molecular Solids: Bridge to the Electrical Conduction* (Wiley-VCH Verlag GmbH & Co. KGaA, 2012).

[49] H. Bässler, A. Köhler, in *Unimolecular and Supramolecular Electronics I*, edited by R. M. Metzger, pp. 1–65, *Charge Transport in Organic Semiconductors* (Springer Berlin Heidelberg, 2012).

[50] N. Karl, *Charge Carrier Transport in Organic Semiconductors*, Synthetic Metals **133–134**, 649 (2003).

[51] M. Schwoerer, H. C. Wolf, *Organic Molecular Solids* (John Wiley & Sons, 2008).

[52] E. A. Silinsh, V. Capek, *Organic Molecular Crystals: Interacton Localization, and Transport Phenomena*, 1st ed. (American Institute of Physics, 1997).

[53] S.-i. Machida, Y. Nakayama, S. Duhm, Q. Xin, A. Funakoshi, N. Ogawa, S. Kera, N. Ueno, H. Ishii, *Highest-Occupied-Molecular-Orbital Band Dispersion of Rubrene Single Crystals as Observed by Angle-Resolved Ultraviolet Photoelectron Spectroscopy*, Physical Review Letters **104(15)**, 156401 (2010).

[54] W. Warta, R. Stehle, N. Karl, *Ultrapure, High Mobility Organic Photoconductors*, Applied Physics A **36(3)**, 163 (1985).

[55] W. Warta, N. Karl, *Hot Holes in Naphthalene: High, Electric-Field-Dependent Mobilities*, Physical Review B **32(2)**, 1172 (1985).

[56] N. Karl, J. Marktanner, R. Stehle, W. Warta, *High-Field Saturation of Charge Carrier Drift Velocities in Ultrapurified Organic Photoconductors*, Synthetic Metals **42(3)**, 2473 (1991).

[57] M. Born, R. Oppenheimer, *Zur Quantentheorie der Molekeln*, Annalen der Physik **389(20)**, 457 (1927).

[58] B. Alvarez-Fernández, J. A. Blanco, *The Hubbard Model for the Hydrogen Molecule*, European Journal of Physics **23(1)**, 11 (2002).

[59] W. Nolting, *Viel-Teilchen-Theorie*, vol. 7 of *Grundkurs Theoretisch Physik*, 7th ed. (Springer, 2009).

[60] J. C. Slater, G. F. Koster, *Simplified LCAO Method for the Periodic Potential Problem*, Physical Review **94(6)**, 1498 (1954).

[61] C. M. Goringe, D. R. Bowler, E. Hernández, *Tight-Binding Modelling of Materials*, Reports on Progress in Physics **60(12)**, 1447 (1997).

[62] W. Heitler, F. London, *Wechselwirkung neutraler Atome und homöopolare Bindung nach der Quantenmechanik*, Zeitschrift für Physik **44(6-7)**, 455 (1927).

[63] F. Hund, *Zur Deutung der Molekelspektren. IV*, Zeitschrift für Physik **51(11-12)**, 759 (1928).

[64] B. N. Finkelstein, G. E. Horowitz, *Über die Energie des He-Atoms und des positiven H2-Ions im Normalzustande*, Zeitschrift für Physik **48(1-2)**, 118 (1928).

[65] R. S. Mulliken, *Electronic Structures of Polyatomic Molecules and Valence VI. On the Method of Molecular Orbitals*, The Journal of Chemical Physics **3(7)**, 375 (1935).

[66] F. Bloch, *Bemerkung zur Elektronentheorie des Ferromagnetismus und der elektrischen Leitfähigkeit*, Zeitschrift für Physik **57(7-8)**, 545 (1929).

[67] N. F. Mott, *A Discussion of the Transition Metals on the Basis of Quantum Mechanics*, Proceedings of the Physical Society **47(4)**, 571 (1935).

[68] J. C. Slater, *The Ferromagnetism of Nickel*, Physical Review **49(7)**, 537 (1936).

[69] E. C. Stoner, *Collective Electron Specific Heat and Spin Paramagnetism in Metals*, Proceedings of the Royal Society of London. Series A - Mathematical and Physical Sciences **154(883)**, 656 (1936).

[70] J. Hubbard, *Electron Correlations in Narrow Energy Bands*, Proceedings of the Royal Society of London. Series A. Mathematical and Physical Sciences **276(1365)**, 238 (1963).

[71] J. Hubbard, *Electron Correlations in Narrow Energy Bands. II. The Degenerate Band Case*, Proceedings of the Royal Society of London. Series A. Mathematical and Physical Sciences **277(1369)**, 237 (1964).

[72] J. Hubbard, *Electron Correlations in Narrow Energy Bands. III. An Improved Solution*, Proceedings of the Royal Society of London. Series A. Mathematical and Physical Sciences **281(1386)**, 401 (1964).

[73] E. Wigner, H. B. Huntington, *On the Possibility of a Metallic Modification of Hydrogen*, The Journal of Chemical Physics **3(12)**, 764 (1935).

[74] M. I. Eremets, I. A. Troyan, *Conductive Dense Hydrogen*, Nature Materials **10(12)**, 927 (2011).

[75] U. Bovensiepen, H. Petek, M. Wolf, *Dynamics at Solid State Surfaces and Interfaces: Volume 2: Fundamentals* (John Wiley & Sons, 2012).

[76] Q. Xin, S. Duhm, F. Bussolotti, K. Akaike, Y. Kubozono, H. Aoki, T. Kosugi, S. Kera, N. Ueno, *Accessing Surface Brillouin Zone and Band Structure of Picene Single Crystals*, Physical Review Letters **108(22)**, 226401 (2012).

[77] G. Koller, S. Berkebile, M. Oehzelt, P. Puschnig, C. Ambrosch-Draxl, F. P. Netzer, M. G. Ramsey, *Intra- and Intermolecular Band Dispersion in an Organic Crystal*, Science **317(5836)**, 351 (2007).

[78] K. Seki, H. Inokuchi, Y. Harada, *Photoelectron Spectroscopy of Naphthacene and Perylene Crystals by the Rare Gas Emission Lines*, Chemical Physics Letters **20(2)**, 197 (1973).

[79] R. Temirov, S. Soubatch, A. Luican, F. S. Tautz, *Free-Electron-Like Dispersion in an Organic Monolayer Film on a Metal Substrate*, Nature **444(7117)**, 350 (2006).

[80] R. W. Lof, M. A. van Veenendaal, B. Koopmans, H. T. Jonkman, G. A. Sawatzky, *Band Gap, Excitons, and Coulomb Interaction in Solid C60*, Physical Review Letters **68(26)**, 3924 (1992).

[81] P. A. Brühwiler, A. J. Maxwell, A. Nilsson, N. Mårtensson, O. Gunnarsson, *Auger and Photoelectron Study of the Hubbard U in C60, K3C60, and K6C60*, Physical Review B **48(24)**, 18296 (1993).

[82] X. Lu, M. Grobis, K. H. Khoo, S. G. Louie, M. F. Crommie, *Charge Transfer and Screening in individual C60 Molecules on Metal Substrates: A Scanning Tunneling Spectroscopy and Theoretical Study*, Physical Review B **70(11)**, 115418 (2004).

[83] G. Dutton, X.-Y. Zhu, *Unoccupied States in C60 Thin Films Probed by Two-Photon Photoemission*, The Journal of Physical Chemistry B **106(23)**, 5975 (2002).

[84] R. Schwedhelm, L. Kipp, A. Dallmeyer, M. Skibowski, *Experimental Band Gap and Core-Hole Electron Interaction in Epitaxial C60 Films*, Physical Review B **58(19)**, 13176 (1998).

[85] L. Weinhardt, O. Fuchs, D. Batchelor, M. Bär, M. Blum, J. D. Denlinger, W. Yang, A. Schöll, F. Reinert, E. Umbach, C. Heske, *Electron-Hole Correlation Effects in Core-Level Spectroscopy Probed by the Resonant Inelastic Soft X-Ray Scattering Map of C60*, The Journal of Chemical Physics **135(10)**, 104705 (2011).

[86] M. Knupfer, *Exciton Binding Energies in Organic Semiconductors*, Applied Physics A **77(5)**, 623 (2003).

[87] E. V. Tsiper, Z. G. Soos, W. Gao, A. Kahn, *Electronic Polarization at Surfaces and Thin Films of Organic Molecular Crystals: PTCDA*, Chemical Physics Letters **360(1–2)**, 47 (2002).

[88] J. E. Norton, J.-L. Brédas, *Polarization Energies in Oligoacene Semiconductor Crystals*, Journal of the American Chemical Society **130(37)**, 12377 (2008).

[89] E. Silinsh, A. Klimkāns, S. Larsson, V. Čápek, *Molecular Polaron States in Polyacene Crystals. Formation and Transfer Processes*, Chemical Physics **198(3)**, 311 (1995).

[90] S. Kera, S. Hosoumi, K. Sato, H. Fukagawa, S.-i. Nagamatsu, Y. Sakamoto, T. Suzuki, H. Huang, W. Chen, A. T. S. Wee, V. Coropceanu, N. Ueno, *Experimental Reorganization Energies of Pentacene and Perfluoropentacene: Effects of Perfluorination*, The Journal of Physical Chemistry C **117(43)**, 22428 (2013).

[91] D. P. McMahon, A. Troisi, *Evaluation of the External Reorganization Energy of Polyacenes*, The Journal of Physical Chemistry Letters **1(6)**, 941 (2010).

[92] S. Krause, M. B. Casu, A. Schöll, E. Umbach, *Determination of Transport Levels of Organic Semiconductors by UPS and IPS*, New Journal of Physics **10(8)**, 085001 (2008).

[93] I. G. Hill, A. Kahn, Z. G. Soos, R. A. Pascal, Jr, *Charge-Separation En-*

ergy in Films of π-Conjugated Organic Molecules, Chemical Physics Letters **327(3–4)**, 181 (2000).

[94] D. R. T. Zahn, G. N. Gavrila, M. Gorgoi, *The Transport Gap of Organic Semiconductors Studied Using the Combination of Direct and Inverse Photoemission*, Chemical Physics **325(1)**, 99 (2006).

[95] B. A. Gregg, M. C. Hanna, *Comparing Organic to Inorganic Photovoltaic Cells: Theory, Experiment, and Simulation*, Journal of Applied Physics **93(6)**, 3605 (2003).

[96] P. Atkins, J. d. Paula, *Physical Chemistry, 9th Edition*, 9th ed. (W. H. Freeman, New York, 2009).

[97] K. Wandelt, J. E. Hulse, *Xenon Adsorption on Palladium. I. The Homogeneous (110), (100), and (111) Surfaces*, The Journal of Chemical Physics **80(3)**, 1340 (1984).

[98] G. Brivio, *The Adiabatic Molecule–Metal Surface Interaction: Theoretical Approaches*, Reviews of Modern Physics **71(1)**, 231 (1999).

[99] H. Ishii, H. Oji, E. Ito, N. Hayashi, D. Yoshimura, K. Seki, *Energy Level Alignment and Band Bending at Model Interfaces of Organic Electroluminescent Devices*, Journal of Luminescence **87–89**, 61 (2000).

[100] A. Kahn, N. Koch, W. Gao, *Electronic Structure and Electrical Properties of Interfaces between Metals and π-Conjugated Molecular Films*, Journal of Polymer Science Part B: Polymer Physics **41(21)**, 2529 (2003).

[101] J. Hwang, A. Wan, A. Kahn, *Energetics of Metal-Organic Interfaces: New Experiments and Assessment of the Field*, Materials Science & Engineering R-Reports **64(1-2)**, 1 (2009).

[102] A. Wan, J. Hwang, F. Amy, A. Kahn, *Impact of Electrode Contamination on the α-NPD/Au Hole Injection Barrier*, Organic Electronics **6(1)**, 47 (2005).

[103] H. Wang, P. Amsalem, G. Heimel, I. Salzmann, N. Koch, M. Oehzelt, *Band-Bending in Organic Semiconductors: the Role of Alkali-Halide Interlayers*, Advanced Materials **26(6)**, 925 (2014).

[104] H. Vázquez, F. Flores, A. Kahn, *Induced Density of States Model for Weakly-Interacting Organic Semiconductor Interfaces*, Organic Electronics **8(2–3)**, 241 (2007).

[105] L. Pauling, *The Nature of the Chemical Bond and the Structure of Molecules and Crystals: An Introduction to Modern Structural Chemistry*, 3rd ed. (Cornell University Press, 1960).

[106] H. Vázquez, F. Flores, R. Oszwaldowski, J. Ortega, R. Pérez, A. Kahn, *Barrier Formation at Metal–Organic Interfaces: Dipole Formation and the Charge Neutrality Level*, Applied Surface Science **234(1–4)**, 107 (2004).

[107] N. Koch, S. Duhm, J. P. Rabe, A. Vollmer, R. L. Johnson, *Optimized Hole*

Injection with Strong Electron Acceptors at Organic-Metal Interfaces, Physical Review Letters **95(23)**, 237601 (2005).

[108] B. Bröker, R.-P. Blum, J. Frisch, A. Vollmer, O. T. Hofmann, R. Rieger, K. Müllen, J. P. Rabe, E. Zojer, N. Koch, *Gold Work Function Reduction by 2.2 eV with an Air-Stable Molecular Donor Layer*, Applied Physics Letters **93(24)**, 243303 (2008).

[109] A. Ulman, *Formation and Structure of Self-Assembled Monolayers*, Chemical Reviews **96(4)**, 1533 (1996).

[110] F. Schreiber, *Structure and Growth of Self-Assembling Monolayers*, Progress in Surface Science **65(5–8)**, 151 (2000).

[111] J. C. Love, L. A. Estroff, J. K. Kriebel, R. G. Nuzzo, G. M. Whitesides, *Self-Assembled Monolayers of Thiolates on Metals as a Form of Nanotechnology*, Chemical Reviews **105(4)**, 1103 (2005).

[112] U. Diebold, *The Surface Science of Titanium Dioxide*, Surface Science Reports **48(5–8)**, 53 (2003).

[113] G. Heimel, L. Romaner, E. Zojer, J.-L. Brédas, *Toward Control of the Metal-Organic Interfacial Electronic Structure in Molecular Electronics: A First-Principles Study on Self-Assembled Monolayers of π-Conjugated Molecules on Noble Metals*, Nano Letters **7(4)**, 932 (2007).

[114] L. Wang, G. M. Rangger, Z. Ma, Q. Li, Z. Shuai, E. Zojer, G. Heimel, *Is there a Au–S Bond Dipole in Self-Assembled Monolayers on Gold?*, Physical Chemistry Chemical Physics **12(17)**, 4287 (2010).

[115] A. Tada, Y. Geng, Q. Wei, K. Hashimoto, K. Tajima, *Tailoring Organic Heterojunction Interfaces in Bilayer Polymer Photovoltaic Devices*, Nature Materials **10(6)**, 450 (2011).

[116] C. Schmidt, A. Witt, G. Witte, *Tailoring the Cu(100) Work Function by Substituted Benzenethiolate Self-Assembled Monolayers*, The Journal of Physical Chemistry A **115(25)**, 7234 (2011).

[117] D. M. Alloway, M. Hofmann, D. L. Smith, N. E. Gruhn, A. L. Graham, R. Colorado, V. H. Wysocki, T. R. Lee, P. A. Lee, N. R. Armstrong, *Interface Dipoles Arising from Self-Assembled Monolayers on Gold: UV-Photoemission Studies of Alkanethiols and Partially Fluorinated Alkanethiols*, The Journal of Physical Chemistry B **107(42)**, 11690 (2003).

[118] N. D. Lang, W. Kohn, *Theory of Metal Surfaces: Work Function*, Physical Review B **3(4)**, 1215 (1971).

[119] V. Sahni, J. B. Krieger, J. Gruenebaum, *Analytic Calculation of Metal Surface Dipole Moments in the Step-Potential Approximation*, Physical Review B **12(8)**, 3503 (1975).

[120] J. Bardeen, *Theory of the Work Function. II. The Surface Double Layer*, Physical Review **49(9)**, 653 (1936).

[121] V. Heine, C. H. Hodges, *Theory of the Surface Dipole on Nontransition Metals*, Journal of Physics C: Solid State Physics **5(2)**, 225 (1972).

[122] N. D. Lang, W. Kohn, *Theory of Metal Surfaces: Charge Density and Surface Energy*, Physical Review B **1(12)**, 4555 (1970).

[123] X. Crispin, V. Geskin, A. Crispin, J. Cornil, R. Lazzaroni, W. R. Salaneck, J.-L. Brédas, *Characterization of the Interface Dipole at Organic/ Metal Interfaces*, Journal of the American Chemical Society **124(27)**, 8131 (2002).

[124] S. Halas, T. Durakiewicz, *Work Functions of Elements Expressed in Terms of the Fermi Energy and the Density of Free Electrons*, Journal of Physics: Condensed Matter **10(48)**, 10815 (1998).

[125] J. R. Smith, *Self-Consistent Many-Electron Theory of Electron Work Functions and Surface Potential Characteristics for Selected Metals*, Physical Review **181(2)**, 522 (1969).

[126] D. A. Egger, E. Zojer, *Anticorrelation between the Evolution of Molecular Dipole Moments and Induced Work Function Modifications*, Journal of Physical Chemistry Letters **4(20)**, 3521 (2013).

[127] J. Uihlein, H. Peisert, M. Glaser, M. Polek, H. Adler, F. Petraki, R. Ovsyannikov, M. Bauer, T. Chassé, *Communication: Influence of graphene interlayers on the interaction between cobalt phthalocyanine and Ni(111)*, The Journal of Chemical Physics **138(8)**, 081101 (2013).

[128] G. Witte, S. Lukas, P. S. Bagus, C. Wöll, *Vacuum Level Alignment at Organic/Metal Junctions: "Cushion" Effect and the Interface Dipole*, Applied Physics Letters **87(26)**, 263502 (2005).

[129] P. S. Bagus, V. Staemmler, C. Woll, *Exchangelike Effects for Closed-Shell Adsorbates: Interface Dipole and Work Function*, Physical Review Letters **89(9)** (2002).

[130] P. S. Bagus, K. Hermann, C. Wöll, *The Interaction of C6H6 and C6H12 with Noble Metal Surfaces: Electronic Level Alignment and the Origin of the Interface Dipole*, The Journal of Chemical Physics **123(18)**, 184109 (2005).

[131] R. G. Pearson, *Hard and Soft Acids and Bases*, Journal of the American Chemical Society **85(22)**, 3533 (1963).

[132] G. Witte, K. Hänel, C. Busse, A. Birkner, C. Wöll, *Molecules Coining Patterns into a Metal: The Hard Core of Soft Matter*, Chemistry of Materials **19(17)**, 4228 (2007).

[133] M. Timpel, M. V. Nardi, S. Krause, G. Ligorio, C. Christodoulou, L. Pasquali, A. Giglia, J. Frisch, B. Wegner, P. Moras, N. Koch, *Surface Modification of ZnO(0001)–Zn with Phosphonate-Based Self-Assembled Monolayers: Binding Modes, Orientation, and Work Function*, Chemistry of Materials **26(17)**, 5042 (2014).

[134] P. J. Hotchkiss, M. Malicki, A. J. Giordano, N. R. Armstrong, S. R.

Marder, *Characterization of Phosphonic Acid Binding to Zinc Oxide*, Journal of Materials Chemistry **21(9)**, 3107 (2011).

[135] P. J. Hotchkiss, H. Li, P. B. Paramonov, S. A. Paniagua, S. C. Jones, N. R. Armstrong, J.-L. Brédas, S. R. Marder, *Modification of the Surface Properties of Indium Tin Oxide with Benzylphosphonic Acids: A Joint Experimental and Theoretical Study*, Advanced Materials **21(44)**, 4496 (2009).

[136] P. J. Hotchkiss, S. C. Jones, S. A. Paniagua, A. Sharma, B. Kippelen, N. R. Armstrong, S. R. Marder, *The Modification of Indium Tin Oxide with Phosphonic Acids: Mechanism of Binding, Tuning of Surface Properties, and Potential for Use in Organic Electronic Applications*, Accounts of Chemical Research **45(3)**, 337 (2011).

[137] Y. E. Ha, M. Y. Jo, J. Park, Y.-C. Kang, S.-J. Moon, J. H. Kim, *Effect of Self-Assembled Monolayer Treated ZnO as an Electron Transporting Layer on the Photovoltaic Properties of Inverted Type Polymer Solar Cells*, Synthetic Metals **187**, 113 (2014).

[138] M. A. Barteau, *Organic Reactions at Well-Defined Oxide Surfaces*, Chemical Reviews **96(4)**, 1413 (1996).

[139] D. R. T. Zahn, G. N. Gavrila, G. Salvan, *Electronic and Vibrational Spectroscopies Applied to Organic/Inorganic Interfaces*, Chemical Reviews **107(4)**, 1161 (2007).

[140] S. Hüfner, *Photoelectron Spectroscopy: Principles and Applications* (Springer Science & Business Media, 2003).

[141] D. Briggs, M. P. Seah, *Practical Surface Analysis: Auger and X-Ray Photoelectron Spectroscopy*, 2nd ed. (John Wiley & Sons Ltd, Chichester; New York, 1996).

[142] K. Siegbahn, *Electron Spectroscopy for Atoms, Molecules, and Condensed Matter*, Reviews of Modern Physics **54(3)**, 709 (1982).

[143] J.-E. Rubensson, J. Lüning, S. Eisebitt, W. Eberhardt, *It's Always a One-Step Process*, Applied Physics A **65(2)**, 91 (1997).

[144] V. Dose, *Momentum-Resolved Inverse Photoemission*, Surface Science Reports **5(8)**, 337 (1985).

[145] I. S. Tilinin, A. Jablonski, W. S. M. Werner, *Quantitative Surface Analysis by Auger and X-ray Photoelectron Spectroscopy*, Progress in Surface Science **52(4)**, 193 (1996).

[146] N. V. Smith, *Inverse Photoemission*, Reports on Progress in Physics **51(9)**, 1227 (1988).

[147] F. Himpsel, *Inverse Photoemission from Semiconductors*, Surface Science Reports **12(1)**, 3 (1990).

[148] F. Schedin, G. Thornton, R. I. G. Uhrberg, *Windows and Photocathodes*

for a High Resolution Solid State Bandpass Ultraviolet Photon Detector for Inverse Photoemission, Review of Scientific Instruments **68(1)**, 41 (1997).

[149] H. Yamane, E. Kawabe, D. Yoshimura, R. Sumii, K. Kanai, Y. Ouchi, N. Ueno, K. Seki, *Intermolecular Band Dispersion in Highly Ordered Monolayer and Multilayer Films of Pentacene on Cu(110)*, physica status solidi (b) **245(5)**, 793 (2008).

[150] B. Bröker, *Electronic and Structural Properties of Interfaces between Electron Donor & Acceptor Molecules and Conductive Electrodes*, Ph.D. thesis, Humboldt-Universität zu Berlin, Mathematisch-Naturwissenschaftliche Fakultät I (2011).

[151] I. Salzmann, *Structural and Energetic Properties of Pentacene Derivatives and Heterostructures*, Ph.D. thesis, Humboldt-Universität zu Berlin, Mathematisch-Naturwissenschaftliche Fakultät I (2009).

[152] M. Henzler, *Oberflächenphysik des Festkörpers*, auflage: 2. aufl. 1994 ed. (Teubner Verlag, Stuttgart, 1994).

[153] S. Krause, M. Stolte, F. Würthner, N. Koch, *Influence of Merocyanine Molecular Dipole Moments on the Valence Levels in Thin Films and the Interface Energy Level Alignment with Au(111)*, The Journal of Physical Chemistry C **117(37)**, 19031 (2013).

[154] R. Schlesinger, *in preparation.*

[155] M. P. Seah, W. A. Dench, *Quantitative Electron Spectroscopy of Surfaces: A Standard Data Base for Electron Inelastic Mean Free Paths in Solids*, Surface and Interface Analysis **1(1)**, 2 (1979).

[156] G. E. Rhead, M. G. Barthès, C. Argile, *Determination of Growth Modes of Ultrathin Films from Auger Electron Spectroscopy : An Assessment and Commentary*, Thin Solid Films **82(2)**, 201 (1981).

[157] S. R. Forrest, *Ultrathin Organic Films Grown by Organic Molecular Beam Deposition and Related Techniques*, Chemical Reviews **97(6)**, 1793 (1997).

[158] H. Bubert, J. C. Rivière, H. F. Arlinghaus, H. Hutter, H. Jenett, P. Bauer, L. Palmetshofer, L. Fabry, S. Pahlke, A. Quentmeier, K. Hinrichs, W. Hill, B. Gruska, Arthur Röseler, G. Friedbacher, in *Ullmann's Encyclopedia of Industrial Chemistry*, *Surface and Thin-Film Analysis* (Wiley-VCH Verlag GmbH & Co. KGaA, 2000).

[159] A. Jablonski, C. J. Powell, *Relationships between Electron Inelastic Mean Free Paths, Effective Attenuation Lengths, and Mean Escape Depths*, Journal of Electron Spectroscopy and Related Phenomena **100(1–3)**, 137 (1999).

[160] A. Jablonski, C. J. Powell, *The Electron Attenuation Length Revisited*, Surface Science Reports **47(2–3)**, 33 (2002).

[161] S. V. Merzlikin, N. N. Tolkachev, T. Strunskus, G. Witte, T. Glogowski, C. Wöll, W. Grünert, *Resolving the Depth Coordinate in Photoelectron Spec-*

troscopy – Comparison of Excitation Energy Variation vs. Angular-Resolved XPS for the Analysis of a Self-Assembled Monolayer Model System, Surface Science **602(3)**, 755 (2008).

[162] D. Käfer, C. Wöll, G. Witte, *Thermally Activated Dewetting of Organic Thin Films: the Case of Pentacene on SiO2 and Gold*, Applied Physics A **95(1)**, 273 (2009).

[163] S. Duhm, G. Heimel, I. Salzmann, H. Glowatzki, R. L. Johnson, A. Vollmer, J. P. Rabe, N. Koch, *Orientation-Dependent Ionization Energies and Interface Dipoles in Ordered Molecular Assemblies*, Nature Materials **7(4)**, 326 (2008).

[164] S. Soubatch, C. Weiss, R. Temirov, F. S. Tautz, *Site-Specific Polarization Screening in Organic Thin Films*, Physical Review Letters **102(17)**, 177405 (2009).

[165] H. Peisert, D. Kolacyak, T. Chassé, *Site-Specific Charge-Transfer Screening at Organic/Metal Interfaces*, Journal of Physical Chemistry C **113(44)**, 19244 (2009).

[166] I. Salzmann, S. Duhm, G. Heimel, M. Oehzelt, R. Kniprath, R. L. Johnson, J. P. Rabe, N. Koch, *Tuning the Ionization Energy of Organic Semiconductor Films: The Role of Intramolecular Polar Bonds*, Journal of the American Chemical Society **130(39)**, 12870 (2008).

[167] G. Heimel, I. Salzmann, S. Duhm, N. Koch, *Design of Organic Semiconductors from Molecular Electrostatics*†, Chemistry of Materials **23(3)**, 359 (2011).

[168] A. Opitz, J. Frisch, R. Schlesinger, A. Wilke, N. Koch, *Energy Level Alignment at Interfaces in Organic Photovoltaic Devices*, Journal of Electron Spectroscopy and Related Phenomena **190(PART A)**, 12 (2013).

[169] D. Zerulla, T. Chassé, *X-ray Induced Damage of Self-Assembled Alkanethiols on Gold and Indium Phosphide*, Langmuir **15(16)**, 5285 (1999).

[170] M. T. Greiner, Z.-H. Lu, *Thin-Film Metal Oxides in Organic Semiconductor Devices: Their Electronic Structures, Work Functions and Interfaces*, NPG Asia Materials **5(7)**, e55 (2013).

[171] J. B. Malherbe, S. Hofmann, J. M. Sanz, *Preferential Sputtering of Oxides: A Comparison of Model Predictions with Experimental Data*, Applied Surface Science **27(3)**, 355 (1986).

[172] S. Gutmann, M. Conrad, M. A. Wolak, M. M. Beerbom, R. Schlaf, *Work Function Measurements on Nano-Crystalline Zinc Oxide Surfaces*, Journal of Applied Physics **111(12)**, 123710 (2012).

[173] M. M. Beerbom, B. Lägel, A. J. Cascio, B. V. Doran, R. Schlaf, *Direct Comparison of Photoemission Spectroscopy and in situ Kelvin Probe Work Function Measurements on Indium Tin Oxide Films*, Journal of Electron Spectroscopy and Related Phenomena **152(1–2)**, 12 (2006).

[174] J. A. Chaney, P. E. Pehrsson, *Work Function Changes and Surface Chemistry of Oxygen, Hydrogen, and Carbon on Indium Tin Oxide*, Applied Surface Science **180(3–4)**, 214 (2001).

[175] P. Herrmann, G. Heimel, *Structure and Stoichiometry Prediction of Surfaces Reacting with Multicomponent Gases*, Advanced Materials **27(2)**, 255 (2015).

[176] X.-Y. Zhu, *Electronic Structure and Electron Dynamics at Molecule–Metal Interfaces: Implications for Molecule-Based Electronics*, Surface Science Reports **56(1–2)**, 1 (2004).

[177] F. Würthner, R. Wortmann, K. Meerholz, *Chromophore Design for Photorefractive Organic Materials*, ChemPhysChem **3(1)**, 17 (2002).

[178] S. R. Marder, B. Kippelen, A. K.-Y. Jen, N. Peyghambarian, *Design and Synthesis of Chromophores and Polymers for Electro-Optic and Photorefractive Applications*, Nature **388(6645)**, 845 (1997).

[179] F. Würthner, K. Meerholz, *Systems Chemistry Approach in Organic Photovoltaics*, Chemistry – A European Journal **16(31)**, 9366 (2010).

[180] M. Grätzel, *Dye-Sensitized Solar Cells*, Journal of Photochemistry and Photobiology C: Photochemistry Reviews **4(2)**, 145 (2003).

[181] A. Hagfeldt, G. Boschloo, L. Sun, L. Kloo, H. Pettersson, *Dye-Sensitized Solar Cells*, Chemical Reviews **110(11)**, 6595 (2010).

[182] T. Meyer, D. Ogermann, A. Pankrath, K. Kleinermanns, T. J. J. Müller, *Phenothiazinyl Rhodanylidene Merocyanines for Dye-Sensitized Solar Cells*, The Journal of Organic Chemistry **77(8)**, 3704 (2012).

[183] K. Sayama, K. Hara, H. Sugihara, H. Arakawa, N. Mori, M. Satsuki, S. Suga, S. Tsukagoshi, Y. Abe, *Photosensitization of a Porous TiO2 Electrode with Merocyanine Dyes Containing a Carboxyl Group and a Long Alkyl Chain*, Chemical Communications, pp. 1173–1174 (2000).

[184] W. Wu, J. Hua, Y. Jin, W. Zhan, H. Tian, *Photovoltaic Properties of Three New Cyanine Dyes for Dye-Sensitized Solar Cells*, Photochemical & Photobiological Sciences **7(1)**, 63 (2008).

[185] J. Tang, W. Wu, J. Hua, J. Li, X. Li, H. Tian, *Starburst Triphenylamine-Based Cyanine Dye for Efficient Quasi-Solid-State Dye-Sensitized Solar Cells*, Energy & Environmental Science **2(9)**, 982 (2009).

[186] V. Coropceanu, J. Cornil, D. A. da Silva Filho, Y. Olivier, R. Silbey, J.-L. Brédas, *Charge Transport in Organic Semiconductors*, Chemical reviews **107(4)**, 926 (2007).

[187] A. Dieckmann, H. Bässler, P. M. Borsenberger, *An Assessment of The Role of Dipoles on the Density-of-States Function of Disordered Molecular Solids*, The Journal of Chemical Physics **99(10)**, 8136 (1993).

[188] M. Van der Auweraer, F. C. De Schryver, P. M. Borsenberger, H. Bässler,

Disorder in Charge Transport in Doped Polymers, Advanced Materials **6(3)**, 199 (1994).

[189] A. Ojala, H. Bürckstümmer, J. Hwang, K. Graf, B. v. Vacano, K. Meerholz, P. Erk, F. Würthner, *Planar, Bulk and Hybrid Merocyanine/C60 Heterojunction Devices: A Case Study on Thin Film Morphology and Photovoltaic Performance*, Journal of Materials Chemistry **22(10)**, 4473 (2012).

[190] A. Ojala, A. Petersen, A. Fuchs, R. Lovrincic, C. Pölking, J. Trollmann, J. Hwang, C. Lennartz, H. Reichelt, H. W. Höffken, A. Pucci, P. Erk, T. Kirchartz, F. Würthner, *Merocyanine/C60 Planar Heterojunction Solar Cells: Effect of Dye Orientation on Exciton Dissociation and Solar Cell Performance*, Advanced Functional Materials **22(1)**, 86 (2012).

[191] V. Steinmann, N. M. Kronenberg, M. R. Lenze, S. M. Graf, D. Hertel, K. Meerholz, H. Bürckstümmer, E. V. Tulyakova, F. Würthner, *Simple, Highly Efficient Vacuum-Processed Bulk Heterojunction Solar Cells Based on Merocyanine Dyes*, Advanced Energy Materials **1(5)**, 888 (2011).

[192] J. H. Weaver, *Electronic Structures of C60, C70 and the Fullerides: Photoemission and Inverse Photoemission Studies*, Journal of Physics and Chemistry of Solids **53(11)**, 1433 (1992).

[193] G. Gensterblum, J. J. Pireaux, P. A. Thiry, R. Caudano, J. P. Vigneron, P. Lambin, A. A. Lucas, W. Krätschmer, *High-Resolution Electron-Energy-Loss Spectroscopy of Thin Films of C60 on Si(100)*, Physical Review Letters **67(16)**, 2171 (1991).

[194] A. J. Maxwell, P. A. Brühwiler, D. Arvanitis, J. Hasselström, N. Mårtensson, *C 1s Ionisation Potential and Energy Referencing for Solid C60 Films on Metal Surfaces*, Chemical Physics Letters **260(1–2)**, 71 (1996).

[195] B. Wästberg, S. Lunell, C. Enkvist, P. Brühwiler, A. Maxwell, N. Mårtensson, *1s X-Ray-Absorption Spectroscopy of C60: The Effects of Screening and Core-Hole Relaxation*, Physical Review B **50(17)**, 13031 (1994).

[196] A. Rosén, B. Wästberg, *Calculations of the Ionization Thresholds and Electron Affinities of the Neutral, Positively and Megatively Charged C60—''Follene-60''*, The Journal of Chemical Physics **90(4)**, 2525 (1989).

[197] M. Nyberg, Y. Luo, L. Triguero, L. Pettersson, H. Ågren, *Core-Hole Effects in X-Ray-Absorption Spectra of Fullerenes*, Physical Review B **60(11)**, 7956 (1999).

[198] E. L. Shirley, L. X. Benedict, S. G. Louie, *Excitons in Solid C60*, Physical Review B **54(15)**, 10970 (1996).

[199] E. L. Shirley, S. G. Louie, *Electron Excitations in Solid C60: Energy Gap, Band Dispersions, and Effects of Orientational Disorder*, Physical Review Letters **71(1)**, 133 (1993).

[200] F. Lin, E. S. Sørensen, C. Kallin, A. J. Berlinsky, *Single-Particle Excitation*

Spectra of C60 Molecules and Monolayers, Physical Review B **75(7)**, 075112 (2007).

[201] J. D. Sau, J. B. Neaton, H. J. Choi, S. G. Louie, M. L. Cohen, *Electronic Energy Levels of Weakly Coupled Nanostructures: C60-Metal Interfaces*, Physical Review Letters **101(2)**, 026804 (2008).

[202] C. Cepek, A. Goldoni, S. Modesti, F. Negri, G. Orlandi, F. Zerbetto, *The EEL Spectrum of the Triplet Exciton of C60 and the Theoretical Analysis of its Vibronic Structure*, Chemical Physics Letters **250(5–6)**, 537 (1996).

[203] R. Yamachika, M. Grobis, A. Wachowiak, M. F. Crommie, *Controlled Atomic Doping of a Single C60 Molecule*, Science **304(5668)**, 281 (2004).

[204] E. Ćavar, M.-C. Blüm, M. Pivetta, F. Patthey, M. Chergui, W.-D. Schneider, *Fluorescence and Phosphorescence from Individual C60 Molecules Excited by Local Electron Tunneling*, Physical Review Letters **95(19)**, 196102 (2005).

[205] G. Tian, Y. Luo, *Fluorescence and Phosphorescence of Single C60 Molecules as Stimulated by a Scanning Tunneling Microscope*, Angewandte Chemie International Edition **52(18)**, 4814 (2013).

[206] A. F. Hebard, M. J. Rosseinsky, R. C. Haddon, D. W. Murphy, S. H. Glarum, T. T. M. Palstra, A. P. Ramirez, A. R. Kortan, *Superconductivity at 18 K in Potassium-Doped C60*, Nature **350(6319)**, 600 (1991).

[207] R. C. Haddon, A. F. Hebard, M. J. Rosseinsky, D. W. Murphy, S. J. Duclos, K. B. Lyons, B. Miller, J. M. Rosamilia, R. M. Fleming, A. R. Kortan, S. H. Glarum, A. V. Makhija, A. J. Muller, R. H. Eick, S. M. Zahurak, et al., *Conducting Films of C60 and C70 by Alkali-Metal Doping*, Nature **350(6316)**, 320 (1991).

[208] O. Gunnarsson, H. Handschuh, P. S. Bechthold, B. Kessler, G. Ganteför, W. Eberhardt, *Photoemission Spectra of C60: Electron-Phonon Coupling, Jahn-Teller Effect, and Superconductivity in the Fullerides*, Physical Review Letters **74(10)**, 1875 (1995).

[209] C. B. Winkelmann, N. Roch, W. Wernsdorfer, V. Bouchiat, F. Balestro, *Superconductivity in a Single-C60 Transistor*, Nature Physics **5(12)**, 876 (2009).

[210] P.-M. Allemand, K. C. Khemani, A. Koch, F. Wudl, K. Holczer, S. Donovan, G. Grüner, J. D. Thompson, *Organic Molecular Soft Ferromagnetism in a Fullerene C60*, Science **253(5017)**, 301 (1991).

[211] S. Chakravarty, M. P. Gelfand, S. Kivelson, *Electronic Correlation Effects and Superconductivity in Doped Fullerenes*, Science **254(5034)**, 970 (1991).

[212] P. Frank, T. Djuric, M. Koini, I. Salzmann, R. Rieger, K. Müllen, R. Resel, N. Koch, A. Winkler, *Layer Growth, Thermal Stability, and Desorption Behavior of Hexaaza-Triphenylene-Hexacarbonitrile on Ag(111)*, The Journal of Physical Chemistry C **114(14)**, 6650 (2010).

[213] C. D. Wagner, *Handbook of X-Ray Photoelectron Spectroscopy: A Reference Book of Standard Data for Use in X-Ray Photoelectron Spectroscopy* (Physical Electronics Division, Perkin-Elmer Corp., 1979).

[214] L. Weinhardt, *Elektronische und chemische Eigenschaften von Grenzflächen und Oberflächen in optimierten Cu(In,Ga)(S,Se)2 Dünnschichtsolarzellen*, Ph.D. thesis, Universität Würzburg (2005).

[215] F. Reinert, S. Hüfner, *Photoemission Spectroscopy—from Early Days to Recent Applications*, New Journal of Physics **7(1)**, 97 (2005).

[216] M. G. Helander, M. T. Greiner, Z. B. Wang, Z. H. Lu, *Note: Binding Energy Scale Calibration of Electron Spectrometers for Photoelectron Spectroscopy Using a Single Sample*, Review of Scientific Instruments **82(9)**, 096107 (2011).

[217] L. Sanche, *Irradiation of Organic and Polymer Films with Low-Energy Electrons*, Nuclear Instruments and Methods in Physics Research Section B: Beam Interactions with Materials and Atoms **208**, 4 (2003).

[218] S. Duhm, I. Salzmann, B. Bröker, H. Glowatzki, R. L. Johnson, N. Koch, *Interdiffusion of Molecular Acceptors through Organic Layers to Metal Substrates Mimics Doping-Related Energy Level Shifts*, Applied Physics Letters **95(9)**, 093305 (2009).

[219] M. Frisch, G. Trucks, H. Schlegel, G. Scuseria, M. Robb, J. Cheeseman, J. Montgomery, T. Vreven, K. Kudin, J. Burant, J. Millam, S. Iyengar, J. Tomasi, V. Barone, B. Mennucci, et al., *Gaussian 03, Revision C.02* (2003).

[220] C. Adamo, V. Barone, *Toward Reliable Density Functional Methods without Adjustable Parameters: The PBE0 Model*, The Journal of Chemical Physics **110(13)**, 6158 (1999).

[221] J. P. Perdew, K. Burke, M. Ernzerhof, *Generalized Gradient Approximation Made Simple*, Physical Review Letters **77(18)**, 3865 (1996).

[222] T. Stein, H. Eisenberg, L. Kronik, R. Baer, *Fundamental Gaps in Finite Systems from Eigenvalues of a Generalized Kohn-Sham Method*, Physical Review Letters **105(26)**, 266802 (2010).

[223] S. Refaely-Abramson, R. Baer, L. Kronik, *Fundamental and Excitation Gaps in Molecules of Relevance for Organic Photovoltaics from an Optimally Tuned Range-Separated Hybrid Functional*, Physical Review B **84(7)**, 075144 (2011).

[224] V. Atalla, M. Yoon, F. Caruso, P. Rinke, M. Scheffler, *Hybrid Density Functional Theory Meets Quasiparticle Calculations: A Consistent Electronic Structure Approach*, Physical Review B **88(16)**, 165122 (2013).

[225] J. F. Janak, *Proof that dE/dni=ε in Density-Functional Theory*, Physical Review B **18(12)**, 7165 (1978).

[226] G. Scalmani, M. J. Frisch, *Continuous Surface Charge Polarizable Continuum Models of Solvation. I. General Formalism*, The Journal of Chemical Physics **132(11)**, 114110 (2010).

[227] M. Frisch, G. Trucks, H. Schlegel, G. Scuseria, M. Robb, J. Cheeseman, G. Scalmani, V. Barone, B. Mennucci, G. Petersson, H. Nakatsuji, M. Caricato, X. Li, H. Hratchian, A. Izmaylov, et al., *Gaussian 09 Revision A.02* (Gaussian Inc. Wallingford CT 2009, 2009).

[228] R. Krishnan, J. S. Binkley, R. Seeger, J. A. Pople, *Self-Consistent Molecular Orbital Methods. XX. A Basis Set for Correlated Wave Functions*, The Journal of Chemical Physics **72(1)**, 650 (1980).

[229] M. J. Frisch, J. A. Pople, J. S. Binkley, *Self-Consistent Molecular Orbital Methods 25. Supplementary Functions for Gaussian Basis Sets*, The Journal of Chemical Physics **80(7)**, 3265 (1984).

[230] M. Sayer, A. Mansingh, *Transport Properties of Semiconducting Phosphate Glasses*, Physical Review B **6(12)**, 4629 (1972).

[231] A. F. Hebard, R. C. Haddon, R. M. Fleming, A. R. Kortan, *Deposition and Characterization of Fullerene Films*, Applied Physics Letters **59(17)**, 2109 (1991).

[232] E. Manousakis, *Electronic Structure of C60 within the Tight-Binding Approximation*, Physical Review B **44(19)**, 10991 (1991).

[233] L. P. Hammett, *The Effect of Structure upon the Reactions of Organic Compounds. Benzene Derivatives*, Journal of the American Chemical Society **59(1)**, 96 (1937).

[234] C. Hansch, A. Leo, R. W. Taft, *A Survey of Hammett Substituent Constants and Resonance and Field Parameters*, Chemical Reviews **91(2)**, 165 (1991).

[235] M. H. Abraham, J. A. Platts, *Hydrogen Bond Structural Group Constants*, The Journal of Organic Chemistry **66(10)**, 3484 (2001).

[236] S. Soh, Y. Wei, B. Kowalczyk, C. M. Gothard, B. Baytekin, N. Gothard, B. A. Grzybowski, *Estimating Chemical Reactivity and Cross-Influence from Collective Chemical Knowledge*, Chemical Science **3(5)**, 1497 (2012).

[237] A. Tanaka, H. Okamoto, M. Bersohn, *Construction of Functional Group Reactivity Database under Various Reaction Conditions Automatically Extracted from Reaction Database in a Synthesis Design System*, Journal of Chemical Information and Modeling **50(3)**, 327 (2010).

[238] C. A. Hunter, *Quantifying Intermolecular Interactions: Guidelines for the Molecular Recognition Toolbox*, Angewandte Chemie International Edition **43(40)**, 5310 (2004).

[239] R. G. Parr, R. G. Pearson, *Absolute Hardness: Companion Parameter to Absolute Electronegativity*, Journal of the American Chemical Society **105(26)**, 7512 (1983).

[240] R. G. Pearson, *Absolute Electronegativity and Hardness Correlated with Molecular Orbital Theory*, Proceedings of the National Academy of Sciences **83(22)**, 8440 (1986).

[241] L. Pauling, *The Nature of the Chemical Bond. IV. The Energy of single Bonds and the Relative Electronegativity of Atoms*, Journal of the American Chemical Society **54(9)**, 3570 (1932).

[242] R. S. Mulliken, *A New Electroaffinity Scale; Together with Data on Valence States and on Valence Ionization Potentials and Electron Affinities*, The Journal of Chemical Physics **2(11)**, 782 (1934).

[243] K. Kanai, K. Koizumi, S. Ouchi, Y. Tsukamoto, K. Sakanoue, Y. Ouchi, K. Seki, *Electronic Structure of Anode Interface with Molybdenum Oxide Buffer Layer*, Organic Electronics **11(2)**, 188 (2010).

[244] J. Meyer, S. Hamwi, M. Kröger, W. Kowalsky, T. Riedl, A. Kahn, *Transition Metal Oxides for Organic Electronics: Energetics, Device Physics and Applications*, Advanced Materials **24(40)**, 5408 (2012).

[245] D. Y. Kim, J. Subbiah, G. Sarasqueta, F. So, H. Ding, Irfan, Y. Gao, *The effect of Molybdenum Oxide Interlayer on Organic Photovoltaic Cells*, Applied Physics Letters **95(9)**, 093304 (2009).

[246] M. Kröger, S. Hamwi, J. Meyer, T. Riedl, W. Kowalsky, A. Kahn, *P-Type Doping of Organic Wide Band Gap Materials by Transition Metal Oxides: A Case-Study on Molybdenum Trioxide*, Organic Electronics **10(5)**, 932 (2009).

[247] T. Uozumi, K. Okada, A. Kotani, *Electronic Structures of Ti and V Oxides: Calculation of Valence Photoemission and Bremsstrahlung Isochromat Spectra*, Journal of the Physical Society of Japan **62(8)**, 2595 (1993).

[248] I. Séguy, R. Mamy, P. Destruel, P. Jolinat, H. Bock, *Photoemission Study of the ITO/Triphenylene/Perylene/Al Interfaces*, Applied Surface Science **174(3–4)**, 310 (2001).

[249] I. Hamberg, C. G. Granqvist, *Evaporated Sn-Doped In2O3 Films: Basic Optical Properties and Applications to Energy-Efficient Windows*, Journal of Applied Physics **60(11)**, R123 (1986).

[250] T. Kuriyama, K. Kunimori, T. Kuriyama, H. Nozoye, *Adsorption of Carbon Monoxide on a SmOx Film*, Chemical Communications, pp. 501–502 (1998).

[251] A. A. Dakhel, *Dielectric and Optical Properties of Samarium Oxide Thin Films*, Journal of Alloys and Compounds **365(1–2)**, 233 (2004).

[252] K. W. Goodman, V. E. Henrich, *Assignment of a Photoemission Feature in the O-2s–O-2p Band Gaps of TiO2 and V2O5*, Physical Review B **50(15)**, 10450 (1994).

[253] T. Kato, T. Mori, T. Mizutani, *Effect of Fabrication Conditions on Photoluminescence and Absorption of Hole Transport Materials*, Thin Solid Films **393(1–2)**, 109 (2001).

[254] T. Sugiyama, Y. Furukawa, H. Fujimura, *Crystalline/Amorphous Raman Markers of Hole-Transport Material NPD in Organic Light-Emitting Diodes*, Chemical Physics Letters **405(4–6)**, 330 (2005).

[255] S. Braun, W. Osikowicz, Y. Wang, W. R. Salaneck, *Energy Level Alignment Regimes at Hybrid Organic–Organic and Inorganic–Organic Interfaces*, Organic Electronics **8(1)**, 14 (2007).

[256] M. B. Casu, *Evidence for Efficient Screening in Organic Materials*, physica status solidi (RRL) – Rapid Research Letters **2(1)**, 40 (2008).

[257] H. Peisert, M. Knupfer, T. Schwieger, J. M. Auerhammer, M. S. Golden, J. Fink, *Full Characterization of the Interface between the Organic Semiconductor Copper Phthalocyanine and Gold*, Journal of Applied Physics **91(8)**, 4872 (2002).

[258] M. G. Helander, M. T. Greiner, Z. B. Wang, Z. H. Lu, *Effect of Electrostatic Screening on Apparent Shifts in Photoemission Spectra near Metal/Organic Interfaces*, Physical Review B **81(15)**, 153308 (2010).

[259] G. M. Rangger, O. T. Hofmann, L. Romaner, G. Heimel, B. Bröker, R.-P. Blum, R. L. Johnson, N. Koch, E. Zojer, *F4TCNQ on Cu, Ag, and Au as Prototypical Example for a Strong Organic Acceptor on Coinage Metals*, Physical Review B **79(16)**, 165306 (2009).

[260] B. Bröker, O. T. Hofmann, G. M. Rangger, P. Frank, R.-P. Blum, R. Rieger, L. Venema, A. Vollmer, K. Müllen, J. P. Rabe, A. Winkler, P. Rudolf, E. Zojer, N. Koch, *Density-Dependent Reorientation and Rehybridization of Chemisorbed Conjugated Molecules for Controlling Interface Electronic Structure*, Physical Review Letters **104(24)**, 246805 (2010).

[261] M. Willenbockel, B. Stadtmüller, K. Schönauer, F. C. Bocquet, D. Lüftner, E. M. Reinisch, T. Ules, G. Koller, C. Kumpf, S. Soubatch, P. Puschnig, M. G. Ramsey, F. S. Tautz, *Energy Offsets within a Molecular Monolayer: the Influence of the Molecular Environment*, New Journal of Physics **15(3)**, 033017 (2013).

[262] N. Dori, M. Menon, L. Kilian, M. Sokolowski, L. Kronik, E. Umbach, *Valence Electronic Structure of Gas-Phase 3,4,9,10-Perylene Tetracarboxylic Acid Dianhydride: Experiment and Theory*, Physical Review B **73(19)**, 195208 (2006).

[263] I. Shirotani, H. Inokuchi, S. Minomura, *Electrical Conduction of Organic Semiconductors under High Pressure*, Bulletin of the Chemical Society of Japan **39(2)**, 386 (1966).

[264] D. A. da Silva Filho, E.-G. Kim, J.-L. Brédas, *Transport Properties in the Rubrene Crystal: Electronic Coupling and Vibrational Reorganization Energy*, Advanced Materials **17(8)**, 1072 (2005).

[265] S. Kwon, K.-R. Wee, J. W. Kim, C. Pac, S. O. Kang, *Effects of Inter-*

molecular Interaction on the Energy Distribution of Valance Electronic States of a Carbazole-Based Material in Amorphous Thin Films, The Journal of Chemical Physics **136(20)**, 204706 (2012).

[266] S. Wendt, Y. D. Kim, D. W. Goodman, *Identification of Defect Sites on Oxide Surfaces by Metastable Impact Electron Spectroscopy*, Progress in Surface Science **74(1–8)**, 141 (2003).

[267] K. Wandelt, *The Local Work Function: Concept and Implications*, Applied Surface Science **111**, 1 (1997).

[268] F. Bussolotti, S. Kera, K. Kudo, A. Kahn, N. Ueno, *Gap States in Pentacene Thin Film Induced by Inert Gas Exposure*, Physical Review Letters **110(26)**, 267602 (2013).

[269] T. Sueyoshi, H. Fukagawa, M. Ono, S. Kera, N. Ueno, *Low-Density Band-Gap States in Pentacene Thin Films Probed with Ultrahigh-Sensitivity Ultraviolet Photoelectron Spectroscopy*, Applied Physics Letters **95(18)**, 183303 (2009).

[270] H. Y. Mao, F. Bussolotti, D.-C. Qi, R. Wang, S. Kera, N. Ueno, A. T. S. Wee, W. Chen, *Mechanism of the Fermi Level Pinning at Organic Donor–Acceptor Heterojunction Interfaces*, Organic Electronics **12(3)**, 534 (2011).

[271] J. Niederhausen, P. Amsalem, J. Frisch, A. Wilke, A. Vollmer, R. Rieger, K. Müllen, J. P. Rabe, N. Koch, *Tuning Hole-Injection Barriers at Organic/Metal Interfaces Exploiting the Orientation of a Molecular Acceptor Interlayer*, Physical Review B **84(16)**, 165302 (2011).

[272] J. H. Scofield, Tech. Rep. UCRL–51326, CALIFORNIA UNIV., LIVERMORE. LAWRENCE LIVERMORE LAB. (1973).

[273] B. J. Topham, M. Kumar, Z. G. Soos, *Profiles of Work Function Shifts and Collective Charge Transfer in Submonolayer Metal–Organic Films*, Advanced Functional Materials **21(10)**, 1931 (2011).

[274] E. Ito, Y. Washizu, N. Hayashi, H. Ishii, N. Matsuie, K. Tsuboi, Y. Ouchi, Y. Harima, K. Yamashita, K. Seki, *Spontaneous Buildup of Giant Surface Potential by Vacuum Deposition of Alq3 and its Removal by Visible Light Irradiation*, Journal of Applied Physics **92(12)**, 7306 (2002).

[275] Y. Noguchi, N. Sato, Y. Tanaka, Y. Nakayama, H. Ishii (2008), vol. 7051, pp. 70510K–70510K–8, URL `http://dx.doi.org/10.1117/12.795640`.

[276] Y. Noguchi, Y. Miyazaki, Y. Tanaka, N. Sato, Y. Nakayama, T. D. Schmidt, W. Brütting, H. Ishii, *Charge Accumulation at Organic Semiconductor Interfaces due to a Permanent Dipole Moment and its Orientational Order in Bilayer Devices*, Journal of Applied Physics **111(11)**, 114508 (2012).

[277] I. Lange, J. C. Blakesley, J. Frisch, A. Vollmer, N. Koch, D. Neher, *Band Bending in Conjugated Polymer Layers*, Physical Review Letters **106(21)**, 216402 (2011).

[278] I. Biswas, H. Peisert, M. B. Casu, B.-E. Schuster, P. Nagel, M. Merz, S. Schuppler, T. Chassé, *Initial Molecular Orientation of Phthalocyanines on Oxide Substrates*, physica status solidi (a) **206(11)**, 2524 (2009).

[279] W. Osikowicz, M. P. de Jong, W. R. Salaneck, *Formation of the Interfacial Dipole at Organic-Organic Interfaces: C60/Polymer Interfaces*, Advanced Materials **19(23)**, 4213 (2007).

[280] F. Würthner, S. Yao, T. Debaerdemaeker, R. Wortmann, *Dimerization of Merocyanine Dyes. Structural and Energetic Characterization of Dipolar Dye Aggregates and Implications for Nonlinear Optical Materials*, Journal of the American Chemical Society **124(32)**, 9431 (2002).

[281] A. Y. Matsuura, T. Obayashi, H. Kondoh, T. Ohta, H. Oji, N. Kosugi, K. Sayama, H. Arakawa, *Adsorption of Merocyanine Dye on Rutile TiO2(1 1 0)*, Chemical Physics Letters **360(1–2)**, 133 (2002).

[282] M. L. Tietze, L. Burtone, M. Riede, B. Lüssem, K. Leo, *Fermi Level Shift and Doping Efficiency in p-Doped Small Molecule Organic Semiconductors: A Photoelectron Spectroscopy and Theoretical Study*, Physical Review B **86(3)**, 035320 (2012).

[283] T. Schwieger, H. Peisert, M. S. Golden, M. Knupfer, J. Fink, *Electronic Structure of the Organic Semiconductor Copper Phthalocyanine and K-CuPc Studied Using Photoemission Spectroscopy*, Physical Review B **66(15)**, 155207 (2002).

[284] S. Yogev, R. Matsubara, M. Nakamura, U. Zschieschang, H. Klauk, Y. Rosenwaks, *Fermi Level Pinning by Gap States in Organic Semiconductors*, Physical Review Letters **110(3)**, 036803 (2013).

[285] N. Koch, S. Duhm, J. P. Rabe, S. Rentenberger, R. L. Johnson, J. Klankermayer, F. Schreiber, *Tuning the Hole Injection Barrier Height at Organic/Metal Interfaces with (Sub-) monolayers of Electron Acceptor Molecules*, Applied Physics Letters **87(10)**, 101905 (2005).

[286] O. Rana, R. Srivastava, G. Chauhan, M. Zulfequar, M. Husain, P. C. Srivastava, M. N. Kamalasanan, *Modification of Metal–Organic Interface Using F4-TCNQ for Enhanced Hole Injection Properties in Optoelectronic Devices*, physica status solidi (a) **209(12)**, 2539 (2012).

[287] L. Ley, Y. Smets, C. I. Pakes, J. Ristein, *Calculating the Universal Energy-Level Alignment of Organic Molecules on Metal Oxides*, Advanced Functional Materials **23(7)**, 794 (2013).

[288] T. Edvinsson, C. Li, N. Pschirer, J. Schöneboom, F. Eickemeyer, R. Sens, G. Boschloo, A. Herrmann, K. Müllen, A. Hagfeldt, *Intramolecular Charge-Transfer Tuning of Perylenes: Spectroscopic Features and Performance in Dye-Sensitized Solar Cells*, The Journal of Physical Chemistry C **111(42)**, 15137 (2007).

[289] L. Cao, Y. Wang, J. Zhong, Y. Han, W. Zhang, X. Yu, F. Xu, D.-C. Qi, A. T. S. Wee, *Electronic Structure, Chemical Interactions and Molecular Orientations of 3,4,9,10-Perylene-Tetracarboxylic-Dianhydride on TiO2(110)*, The Journal of Physical Chemistry C **115(50)**, 24880 (2011).

[290] U. Bach, J. Krueger, M. Graetzel (2001), vol. 4108, pp. 1–7, URL `http://dx.doi.org/10.1117/12.416937`.

[291] C. Goh, S. R. Scully, M. D. McGehee, *Effects of Molecular Interface Modification in Hybrid Organic-Inorganic Photovoltaic Cells*, Journal of Applied Physics **101(11)**, 114503 (2007).

[292] S. Rühle, M. Greenshtein, S.-G. Chen, A. Merson, H. Pizem, C. S. Sukenik, D. Cahen, A. Zaban, *Molecular Adjustment of the Electronic Properties of Nanoporous Electrodes in Dye-Sensitized Solar Cells*, The Journal of Physical Chemistry B **109(40)**, 18907 (2005).

[293] E. M. J. Johansson, R. Schölin, H. Siegbahn, A. Hagfeldt, H. Rensmo, *Energy Level Alignment in TiO2/Dipole-Molecule/P3HT Interfaces*, Chemical Physics Letters **515(1–3)**, 146 (2011).

[294] S. A. Berhe, J. Y. Zhou, K. M. Haynes, M. T. Rodriguez, W. J. Youngblood, *Electron Transport in Acceptor-Sensitized Polymer–Oxide Solar Cells: The Importance of Surface Dipoles and Electron Cascade Effects*, ACS Applied Materials & Interfaces **4(6)**, 2955 (2012).

[295] A. Mishra, M. K. R. Fischer, P. Bäuerle, *Metal-Free Organic Dyes for Dye-Sensitized Solar Cells: From Structure: Property Relationships to Design Rules*, Angewandte Chemie International Edition **48(14)**, 2474 (2009).

[296] Y. Ooyama, Y. Shimada, A. Ishii, G. Ito, Y. Kagawa, I. Imae, K. Komaguchi, Y. Harima, *Photovoltaic Performance of Dye-Sensitized Solar Cells Based on a Series of New-Type Donor–Acceptor π-Conjugated Sensitizer, Benzofuro[2,3-c]Oxazolo[4,5-a]Carbazole Fluorescent Dyes*, Journal of Photochemistry and Photobiology A: Chemistry **203(2–3)**, 177 (2009).

[297] Y. Hao, X. Yang, J. Cong, X. Jiang, A. Hagfeldt, L. Sun, *Photo-Induced Electron Transfer Study of D-π-A Sensitizers with Different Type of Anchoring Groups for Dye-Sensitized Solar Cells*, RSC Advances **2(14)**, 6011 (2012).

[298] B. E. Hardin, H. J. Snaith, M. D. McGehee, *The Renaissance of Dye-Sensitized Solar Cells*, Nature Photonics **6(3)**, 162 (2012).

[299] H. J. Snaith, *Estimating the Maximum Attainable Efficiency in Dye-Sensitized Solar Cells*, Advanced Functional Materials **20(1)**, 13 (2010).

[300] P. Docampo, S. Guldin, T. Leijtens, N. K. Noel, U. Steiner, H. J. Snaith, *Lessons Learned: From Dye-Sensitized Solar Cells to All-Solid-State Hybrid Devices*, Advanced Materials **26(24)**, 4013 (2014).

[301] A. Wilke, J. Endres, U. Hörmann, J. Niederhausen, R. Schlesinger, J. Frisch, P. Amsalem, J. Wagner, M. Gruber, A. Opitz, A. Vollmer, W. Brütting,

A. Kahn, N. Koch, *Correlation Between Interface Energetics and Open Circuit Voltage in Organic Photovoltaic Cells*, Applied Physics Letters **101(23)**, 233301 (2012).

[302] K. Vandewal, K. Tvingstedt, A. Gadisa, O. Inganäs, J. V. Manca, *On the Origin of the Open-Circuit Voltage of Polymer–Fullerene Solar Cells*, Nature Materials **8(11)**, 904 (2009).

[303] D. Li, D. Qin, M. Deng, Y. Luo, Q. Meng, *Optimization the Solid-State Electrolytes for Dye-Sensitized Solar Cells*, Energy & Environmental Science **2(3)**, 283 (2009).

[304] J.-H. Yum, P. Chen, M. Grätzel, M. K. Nazeeruddin, *Recent Developments in Solid-State Dye-Sensitized Solar Cells*, ChemSusChem **1(8-9)**, 699 (2008).

[305] B. Li, L. Wang, B. Kang, P. Wang, Y. Qiu, *Review of Recent Progress in Solid-State Dye-Sensitized Solar Cells*, Solar Energy Materials and Solar Cells **90(5)**, 549 (2006).

[306] I. Chung, B. Lee, J. He, R. P. H. Chang, M. G. Kanatzidis, *All-Solid-State Dye-Sensitized Solar Cells with High Efficiency*, Nature **485(7399)**, 486 (2012).

[307] G. A. Chamberlain, P. J. Cooney, S. Dennison, *Photovoltaic Properties of Merocyanine Solid-State Photocells*, Nature **289(5793)**, 45 (1981).

[308] H. Meier, *Conjugated Oligomers with Terminal Donor–Acceptor Substitution*, Angewandte Chemie International Edition **44(17)**, 2482 (2005).

[309] M. Pope, C. E. Swenberg, *Electronic Processes in Organic Solids*, Annual Review of Physical Chemistry **35(1)**, 613 (1984).

[310] N. Koch, G. Leising, L. M. Yu, A. Rajagopal, J. J. Pireaux, R. L. Johnson, *Bipolaron Formation in para-Sexiphenyl Thin Films upon Cs Doping*, Journal of Vacuum Science & Technology A **18(2)**, 295 (2000).

[311] A. J. Heeger, S. Kivelson, J. R. Schrieffer, W. P. Su, *Solitons in Conducting Polymers*, Reviews of Modern Physics **60(3)**, 781 (1988).

[312] S. Berkebile, T. Ules, P. Puschnig, L. Romaner, G. Koller, A. J. Fleming, K. Emtsev, T. Seyller, C. Ambrosch-Draxl, F. P. Netzer, M. G. Ramsey, *A Momentum Space View of the Surface Chemical Bond*, Physical Chemistry Chemical Physics **13(9)**, 3604 (2011).

[313] P. Puschnig, E.-M. Reinisch, T. Ules, G. Koller, S. Soubatch, M. Ostler, L. Romaner, F. S. Tautz, C. Ambrosch-Draxl, M. G. Ramsey, *Orbital Tomography: Deconvoluting Photoemission Spectra of Organic Molecules*, Physical Review B **84(23)**, 235427 (2011).

[314] M. Wießner, J. Ziroff, F. Forster, M. Arita, K. Shimada, P. Puschnig, A. Schöll, F. Reinert, *Substrate-Mediated Band-Dispersion of Adsorbate Molecular States*, Nature Communications **4**, 1514 (2013).

[315] G. Horowitz, *Organic Thin Film Transistors: From Theory to Real Devices*, Journal of Materials Research **19(07)**, 1946 (2004).

[316] C. R. Newman, C. D. Frisbie, D. A. da Silva Filho, J.-L. Brédas, P. C. Ewbank, K. R. Mann, *Introduction to Organic Thin Film Transistors and Design of n-Channel Organic Semiconductors*, Chemistry of Materials **16(23)**, 4436 (2004).

[317] A. R. Murphy, J. M. J. Fréchet, *Organic Semiconducting Oligomers for Use in Thin Film Transistors*, Chemical Reviews **107(4)**, 1066 (2007).

[318] Irfan, M. Zhang, H. Ding, C. W. Tang, Y. Gao, *Strong Interface p-Doping and Band Bending in C60 on MoOx*, Organic Electronics **12(9)**, 1588 (2011).

[319] P. Hansmann, L. Vaugier, H. Jiang, S. Biermann, *What about U on Surfaces? Extended Hubbard Models for Adatom Systems from First Principles*, Journal of Physics: Condensed Matter **25(9)**, 094005 (2013).

[320] M. L. Knotek, M. Pollak, *Correlation Effects in Hopping Conduction: A Treatment in Terms of Multielectron Transitions*, Physical Review B **9(2)**, 664 (1974).

[321] R. Eder, J. van den Brink, G. A. Sawatzky, *Intersite Coulomb Interaction and Heisenberg Exchange*, Physical Review B **54(2)**, R732 (1996).

[322] A. Goldoni, C. Cepek, S. Modesti, *The Surface Triplet Exciton of C60(111)*, Synthetic Metals **77(1–3)**, 189 (1996).

Publications

[ANW+13] Patrick Amsalem, Jens Niederhausen, Andreas Wilke, Georg Heimel, Raphael Schlesinger, Stefanie Winkler, Antje Vollmer, Jürgen P. Rabe, and Norbert Koch. Role of Charge Transfer, Dipole-Dipole Interactions, and Electrostatics in Fermi-Level Pinning at a Molecular Heterojunction on a Metal Surface. *Physical Review B*, 87(3):035440, 2013.

[CWB+14] Mauro Castellani, Stefanie Winkler, Benjamin Bröker, Martin Baumgarten, Klaus Müllen, and Norbert Koch. Work function Increase of Transparent Conductive Electrodes by Solution Processed Electron Acceptor Molecular Monolayers. *Applied Physics A*, 114(2):291–295, 2014.

[HDS+13] Georg Heimel, Steffen Duhm, Ingo Salzmann, Alexander Gerlach, Anna Strozecka, Jens Niederhausen, Christoph Bürker, Takuya Hosokai, Isabel Fernandez-Torrente, Gunnar Schulze, Stefanie Winkler, Andreas Wilke, Raphael Schlesinger, Johannes Frisch, Benjamin Bröker, Antje Vollmer, Blanka Detlefs, Jens Pflaum, Satoshi Kera, Katharina J. Franke, Nobuo Ueno, José Ignacio Pascual, Frank Schreiber, and Norbert Koch. Charged and Metallic Molecular Monolayers through Surface-Induced Aromatic Stabilization. *Nature Chemistry*, 5(3):187–194, 2013.

[MHW+15] Henry Méndez, Georg Heimel, Stefanie Winkler, Johannes Frisch, Andreas Opitz, Katrein Sauer, Berthold Wegner, Martin Oehzelt, Christian Röthel, Steffen Duhm, Daniel Többens, Norbert Koch, and Ingo Salzmann. Charge-transfer crystallites as molecular electrical dopants. *Nature Communications*, 6:8560, 2015.

[NAW+12] Jens Niederhausen, Patrick Amsalem, Andreas Wilke, Raphael Schlesinger, Stefanie Winkler, Antje Vollmer, Jürgen P. Rabe, and Norbert Koch. Doping of C60 (Sub)monolayers by Fermi-Level Pinning Induced Electron Transfer. *Physical Review B*, 86(8):081411, 2012.

[NSW+13] Sebastian Nau, Niels Schulte, Stefanie Winkler, Johannes Frisch, Antje Vollmer, Norbert Koch, Stefan Sax, and Emil J. W. List. Highly Efficient Color-Stable Deep-Blue Multilayer PLEDs: Preventing PEDOT:PSS-Induced Interface Degradation. *Advanced Materials*, 25(32):4420–4424, 2013.

[NTP+13] Sebastian Nau, Roman Trattnig, Leonid Pevzner, Monika Jäger, Raphael Schlesinger, Marco V. Nardi, Giovanni Ligorio, Christos Christodoulou, Niels Schulte, Stefanie Winkler, Johannes Frisch, Antje Vollmer, Martin Baumgarten, Stefan Sax, Norbert Koch, Klaus Müllen, and Emil J. W. List-Kratochvil. All Solution Processed Blue Multi-Layer Light Emitting Diodes Realized by Thermal Layer Stabilization and Orthogonal Solvent Processing. In *SPIE Proceedings*, volume 8829, pages 88290Z–88290Z–12, 2013.

[QWN+11] Tianshi Qin, Wolfgang Wiedemair, Sebastian Nau, Roman Trattnig, Stefan Sax, Stefanie Winkler, Antje Vollmer, Norbert Koch, Martin Baumgarten, Emil J. W. List, and Klaus Müllen. Core, Shell, and Surface-Optimized Dendrimers for Blue Light-Emitting Diodes. *Journal of the American Chemical Society*, 133(5):1301–1303, 2011.

[SSK+13] Kerstin Schmoltner, Florian Schlütter, Milan Kivala, Martin Baumgarten, Stefanie Winkler, Roman Trattnig, Norbert Koch, Andreas Klug, Emil J. W. List, and Klaus Müllen. A Heterotriangulene Polymer for Air-Stable Organic Field-Effect Transistors. *Polymer Chemistry*, 4(20):5337–5344, 2013.

[STF+13] Christian Schwarz, Steffen Tscheuschner, Johannes Frisch, Stefanie Winkler, Norbert Koch, Heinz Bässler, and Anna Köhler. Role of the Effective Mass and Interfacial Dipoles on Exciton Dissociation in Organic Donor-Acceptor Solar Cells. *Physical Review B*, 2013.

[SXH+13] Raphael Schlesinger, Yong Xu, Oliver T. Hofmann, Stefanie Winkler, Johannes Frisch, Jens Niederhausen, Antje Vollmer, Sylke Blumstengel, Fritz Henneberger, Patrick Rinke, Matthias Scheffler, and Norbert Koch. Controlling the Work Function of ZnO and the Energy-Level Alignment at the Interface to Organic Semiconductors with a Molecular Electron Acceptor. *Physical Review B*, 87(15):155311, 2013.

[TFDL+11] Roman Trattnig, Teresa M. Figueira-Duarte, Dominik Lorbach, Wolfgang Wiedemair, Stefan Sax, Stefanie Winkler, Antje Vollmer, Norbert Koch, Marianna Manca, Maria Antonietta Loi, Martin Baumgarten, Emil J.W. List, and Klaus Müllen. Deep Blue Polymer Light Emitting Diodes Based on Easy to Synthesize, Non-Aggregating Polypyrene. *Optics Express*, 19(S6):A1281–A1293, 2011.

[WAF+15] Stefanie Winkler, Patrick Amsalem, Johannes Frisch, Martin Oehzelt, Georg Heimel, and Norbert Koch. Probing the energy levels in hole-doped molecular semiconductors. *Mater. Horiz.*, 2:427–433, 2015.

[WFA+14] Stefanie Winkler, Johannes Frisch, Patrick Amsalem, Stefan Krause, Melanie Timpel, Matthias Stolte, Frank Würthner, and Norbert Koch. Impact of Molecular Dipole Moments on Fermi Level Pinning

in Thin Films. *The Journal of Physical Chemistry C*, 118(22):11731–11737, 2014.

[WFS+13] Stefanie Winkler, Johannes Frisch, Raphael Schlesinger, Martin Oehzelt, Ralph Rieger, Joachim Räder, Jürgen P. Rabe, Klaus Müllen, and Norbert Koch. The Impact of Local Work Function Variations on Fermi Level Pinning of Organic Semiconductors. *The Journal of Physical Chemistry C*, 117(43):22285–22289, 2013.

[XHS+13] Yong Xu, Oliver T. Hofmann, Raphael Schlesinger, Stefanie Winkler, Johannes Frisch, Jens Niederhausen, Antje Vollmer, Sylke Blumstengel, Fritz Henneberger, Norbert Koch, Patrick Rinke, and Matthias Scheffler. Space-Charge Transfer in Hybrid Inorganic-Organic Systems. *Physical Review Letters*, 111(22):226802, November 2013.

Acknowledgments

This thesis would not have been possible without the help of many people. To be more precise, I like to thank ..

- Norbert Koch for direct supervising this work embedded in an interesting research field between chemistry and physics and his kind support. Particularly, he enabled me to meet a manifold of exciting experts in the field on national and international conferences, during collaborative work at the Synchrotron and during my research internship in Japan.

- Klaus Rademann for officially supervising this work, and guiding me concerning the task on "staying focused" during the final phase of writing this thesis.

- Thomas Chassé for immediate interest in my topic and willingness to act as referee as well as Michael M. Linscheid, Stefan Hecht and Nicola Pinna for acting as members of my committee.

- Georg Heimel for elucidating hours stimulating discussing my manifold "path-to-glory"-approaches towards the positive polaron, as well as Martin Oehzelt for countless fruitful discussions on science and the meaning of scientific literature.

- Johannes Frisch for his omnipresent support in doing and discussing science, Patrick Amsalem for elucidating beam nights and discussions and Ingo Salzmann for always being in a good spirit, spreading and sharing his motivation, when discussing and solving scientific issues.

- Stefan Krause for introducing me to the IPES-setup, as well as for mental support.

- my colleagues Raphael Schlesinger, Jens Niederhausen, Christos Christodolous, Giovanni Ligorio, Marco Nardi and Melanie Timpel especially but not only for the demanding time-schedules during beamtimes. Thanks to you it was always a great fun and good experience. You are also acknowledged for many discussions on various "highly promising" topics in the field and your support.

- Henriette Strahl for taking care of a manifold of administrative issues, as well as Timo Kropp and Paul Zybarth for solving one ore the other technical issue.

- Nobuo Ueno, Satoshi Kera, Steffen Duhm and Qian Xin for the possibility to gain some research experience abroad at Chiba University, Japan.
- Antje Vollmer, who warmly welcomed me at the synchrotron facilities.
- Matthias Stolte & Frank Würthner (University Würzburg), Joachim Räder & Klaus Müllen (MPIP) for providing the organic molecules.
- Phillipp Hermann for some general and deep insights into solid state theory.
- Kouki Akaike, Shuwen Yu, Andreas Wilke, Katrein Sauer, Berthold Wegener, Benjamin Bröker, David Egger and Oliver Monti for being valuable partners for discussions.
- Sebastian Nau, Stefan Sax, Emil List for incredible delightful beam-nights.
- Carsten Jost and Guido Schröter for being valuable lunch time partners.
- Viktoria Kneilmann, Sarah Aull, Stefan Henkel and Simone Schindler for always being patiently willing to listen to me. Thanks for cheering me up or bringing me back down on earth, if necessary.
- my family for understanding and support.

Selbständigkeitserklärung

Hiermit erkläre ich eidesstattlich, die Dissertation selbständig und nur unter Verwendung der angegebenen Hilfen und Hilfsmittel angefertigt zu haben. Ich habe mich anderweitig nicht um einen Doktorgrad beworben und besitze nicht einen entsprechenden Doktorgrad. Ferner erkläre ich die Kenntnisnahme der dem Verfahren zugrunde liegenden Promotionsordnung der Mathematisch- Naturwissenschaftlichen Fakultät der Humboldt-Universität zu Berlin.

Stefanie Winkler, Berlin, den 24.3.2015